Topology and electronic transport in Dirac systems under irradiation

Jonathan Atteia

université de BORDEAUX

LOMA UMR5798 Laboratoire Ondes et Matière d'Aquitaine

Thèse de Doctorat

Préparée au Laboratoire Ondes et Matière d'Aquitaine

pour obtenir le grade de

Docteur de l'Université de Bordeaux

École doctorale n°209
Sciences physiques et de l'ingénieur
Spécialité : Physique

Par

Jonathan ATTEIA

Topologie et transport électronique dans des systèmes de Dirac sous irradiation

---

Topology and electronic transport in Dirac systems under irradiation

Sous la direction de **Jérome CAYSSOL**

Thèse soutenue à Talence le 18 décembre 2018

devant le jury composé de :

David **DEAN**, Professeur au LOMA	Président
Jean-Noël **FUCHS**, Directeur de Recherche au LPTMC Jussieu	Rapporteur
David **CARPENTIER**, Directeur de Recherche à l'ENS Lyon	Rapporteur
Pierre **DELPLACE**, Chargé de Recherche à l'ENS Lyon	Examinateur
Jérôme **CAYSSOL**, Professeur au LOMA	Directeur

Topologie et transport électronique dans des systèmes de Dirac sous irradiation

Résumé :

Cette thèse présente un travail théorique effectué dans le domaine de la physique de la matière condensée, et plus particulièrement la physique des solides. Ce domaine de la physique décrit le comportement des électrons dans les cristaux à très basses températures dans le but d'observer des effets quantiques à l'échelle mésoscopique.

Cette thèse se situe à l'interface entre deux types de matériaux : le graphène et les isolants topologiques. Le graphène est une couche d'épaisseur monoatomique d'atomes de carbone arrangés en réseau nid d'abeilles, qui présente de nombreuses propriétés impressionnantes en optique, en mécanique et en électronique. Les isolants topologiques sont des matériaux qui sont isolants en volume et conduisent l'électricité sur les bords. Cette caractéristique découle d'une propriété topologique des électrons dans le volume. La topologie est une branche des mathématiques qui décrit des objets dans leur globalité en ne retenant que les caractéristiques invariantes par certaines déformations continues. Les états de bords des isolants topologiques sont robustes à certaines perturbations comme le désordre créé par des impuretés dans le matériau. Le lien entre ces deux sujets est double. D'une part les premiers modèles d'isolants topologiques de bande ont été formulés pour le graphène, par Haldane en 1988 et Kane et Mele en 2005, ouvrant ainsi la voie à la découverte des isolants topologiques à 2D et 3D dans des matériaux à fort spin-orbite. D'autre part, il a été prédit que le graphène, même sans spin-orbite, devient un isolant topologique lorsqu'il est irradié par une onde électromagnétique. Dans cette thèse, nous suivons deux directions en parallèle : décrire les caractéristiques topologiques d'une part et les propriétés de transport électronique d'autre part.

En premier lieu, nous passons en revue le modèle des liaisons fortes pour le graphène, puis le modèle effectif qui décrit les électrons de basse énergie comme des fermions de Dirac sans masse. Nous introduisons ensuite le modèle de Haldane, un modèle simple défini sur le réseau en nid d'abeille et qui présente des bandes non triviales caractérisées par un invariant topologique, le nombre de Chern, non nul. Du fait de cette propriété topologique, ce modèle a un état de bord chiral se propageant au bord de l'échantillon et une conductance de Hall quantifiée. Lorsque le graphène est irradié par une onde électromagnétique polarisée circulairement ayant une fréquence plus large que la largeur de bande du graphène, il acquiert un gap dynamique similaire au gap topologique du modèle de Haldane. Lorsque la fréquence est réduite, nous montrons que des transitions topologiques se produisent et que différents états de bords apparaissent.

Le travail principal de cette thèse est l'étude du transport électronique dans le graphène irradié dans un régime de paramètres réalisables expérimentalement. Une feuille de graphène est connectée à deux électrodes avec une différence de potentiel qui génère un courant. Nous calculons la conductance différentielle de l'échantillon selon le formalisme de Landauer-Büttiker étendu aux systèmes soumis à une modulation périodique. En utilisant ce formalisme simple, il nous est possible d'obtenir la conductance en fonction de la géométrie de l'échantillon et de différents paramètres tels que le potentiel chimique, la fréquence et l'intensité de l'onde.

Un autre type d'isolant topologique est l'isolant d'effet Hall quantique de spin. Ce type de phase possède deux états de bords dans lesquels les spins opposés se propagent dans des directions opposées. Le second travail de cette thèse concerne le transport électronique à travers cet état de bord irradié. Nous observons l'apparition d'un courant pompé

en l'absence de différence de potentiel. Nous distinguons deux régimes : un pompage adiabatique quantifié à basse fréquence, et un régime de réponse linéaire non quantifiée à hautes fréquences. Par rapport aux études précédentes existantes, nous montrons un effet important de la présence des électrodes de mesure.

Mots-clés :
Graphène, Isolants topologiques, Theorie de Floquet, Isolants topologiques de Floquet, Physique mésoscopique, Transport électronique, Formalisme de Landauer-Buttiker

Topology and electronic transport in Dirac systems under irradiation

Abstract :
This thesis presents a theoretical work done in the field of condensed matter physics, and in particular solid state physics. This field of physics aims at describing the behaviour of electrons in crystalline materials at very low temperature to observe effects characteristic of quantum physics at the mesoscopic scale.

This thesis lies at the interface between two types of materials : graphene and topological insulators. Graphene is a monoatomic layer of carbon atoms arranged in a honeycomb lattice that presents a wide range of striking properties in optics, mechanics and electronics. Topological insulators are materials that are insulators in the bulk and conduct electricity at the edges. This characteristic originates from a topological property of the electrons in the bulk. Topology is a branch of mathematics that aims to describe objects globally retaining only characteristics invariant under smooth deformations. The edge states of topological insulators are robust to certain king of perturbations such as disorder created by impurities in the bulk. The link between these two topics is two-fold. On one hand, the first models of band topological insulators were formulated for graphene, by Haldane in 1988 and Kane and Mele in 2005, opening the way to the discovery of 2D and 3D topological insulators in materials with strong spin-orbit coupling. On the other hand, it was predicted that graphene, even without spin-orbit coupling, turns to a topological insulator under irradiation by an electromagnetic wave. In this thesis, we follow two directions in parallel : describe the topological properties on one hand, and the electronic transport properties on the other hand.

First, we review the tight-binding model of graphene, and the effective model that describes low-energy electrons as massless Dirac fermions. We then introduce the Haldane model, a simple model defined on the honeycomb lattice that presents non-trivial bands characterised by a topological invariant, the Chern number. Due to this topological property, this model possesses a chiral edge state that propagates around the sample and a quantized Hall conductance. When graphene is irradiated by a circularly polarized electromagnetic wave with a frequency larger than the graphene bandwidth, it acquires a dynamical gap similar to the topological gap of the Haldane model. When the frequency is lowered, we show that topological transitions happens and that different edge states appear.

The main work of this thesis is the study of electronic transport in irradiated graphene in a regime of experimentally achievable parameters. A graphene sheet is connected to two electrodes with a potential difference that generates a current. We compute the differential conductance of the sample according to Landauer-Büttiker formalism extended

to periodically driven systems. Using this simple formalism, we are able to obtain the conductance as a function of the geometry of the sample and of several parameters such as the chemical potential, the frequency and the intensity of the electromagnetic wave.

Another kind of topological insulator is the quantum spin Hall insulator. This type of phase possesses two edge states in which opposite spins propagate in opposite directions. The second work of this thesis concerns electronic transport through this irradiated edge state. We observe the apparition of a pumped current in the absence of a potential difference. We observe two regimes : a quantized adiabatic at low frequency, and a non-quantized linear response regime at high frequency. Compared to previous studies, we show an important effect originating from the presence of electrodes.

Keywords : Graphene, Topological insulators, Floquet theory, Floquet topological insulators, Mesoscopic physics, electronic transport, Landauer-Buttiker formalism

---

Laboratoire Ondes et matière d'Aquitaine (LOMA)
351 cours de la Libération
33405 TALENCE CEDEX (France)

Remerciements

Tout d'abord, je tiens à remercier Jérôme, mon directeur de thèse, qui a été présent pour moi tout au long de cette thèse sans faillir. Il m'a guidé afin que je puisse m'épanouir dans la découverte de la recherche scientifique et que j'y prenne plaisir, ce qu'il a fait merveilleusement bien. Il a toujours été présent, même dans les moments difficiles ou il a toujours fait preuve de patience et de compréhension. Je souhaite ensuite remercier David Carpentier et Jean-Noël Fuchs d'avoir accepté d'être les rapporteurs de cette thèse, ainsi que Pierre Delplace et David Dean d'accepter de participer à la soutenance.

Je me souviens tout d'abord de mon stage de master 1 sous la direction de Fabio Pistolesi et Rémi Avriller qui m'ont fait découvrir la beauté de la physique de la matière condensée. Ensuite, je repense aussi à mon master 2 à l'ENS de Lyon où j'ai suivi de nombreux cours en physique quantique, théorie des champs et autres, par d'excellents professeurs. J'y ai rencontré entre autres Thibaud et Sergueï avec qui j'ai eu des stimulantes discussions sur la matière condensée. Tout ceci m'a encouragé à continuer mon parcours avec une thèse dans ce domaine très riche et stimulant.

Au début de ma thèse, je pense à Doru avec qui j'ai partagé mon bureau avec plaisir, travailleur acharné mais toujours très amical. Je pense aussi à Serguey, Gianluca, Anna et Nina pour ces nombreuses discussions autour de nombreux repas et cafés. À la fin de ma thèse, Bishal et Julie furent d'agréables partenaires de bureau et de discussions. Je remercie aussi Artur et Mikael avec qui j'ai pu partager, en autres, concerts et spectacles.

Je voudrais aussi remercier chaleureusement tout ceux qui ont été présents à mes côtés pendant ma thèse hors du labo. Je pense à Brigitte, Frédéric, Marielle, Suzanne, Anaïs, Aminta, Auriana d'autres qui m'ont soutenu durant ces années. Un grand merci à Salim pour avoir été présent inconditionnellement et pour nos longues discussions autant sur la physique que sur (tout) le reste.

Finalement, un immense merci à mes parents, qui ont toujours été présents et sans qui je ne serais jamais arrivé là. Je pense aussi à mes grand-parents, et particulièrement à mon grand-père avec qui j'ai eu mes premières discussions sur la physique quantique, qui ont stimulé mon intérêt dès le plus jeune âge, et pour encore bien longtemps.

Contents

Introduction **1**

1 Graphene **5**
1 Lattice description of graphene 6
2 Effective low-energy excitations : the Dirac equation 10
3 Discrete symmetries of the graphene lattice 13
4 Masses in the Dirac equation 20
5 Conclusion 22

2 Geometry, topology and the Haldane model **23**
1 Berry phase, quantum Hall effect and topological insulators 24
2 The Haldane model 31
3 Berry phases and Chern number in the Haldane model 34
4 Edge states 45
5 Conclusion 52

3 Floquet theory description of irradiated graphene **53**
1 Floquet formalism 54
2 Irradiated graphene : lattice description 58
3 Irradiated graphene : continuum Dirac description 66
4 Conclusion 79

4 Electronic transport in irradiated graphene **81**
1 Non-irradiated ribbon 81
2 Irradiated ribbon 89
3 Conductance of the ribbon 93
4 Experimental parameters 104
5 Conclusions 106

5 Irradiated quantum spin Hall edge state **107**
1 Quantum Spin Hall insulator 107
2 Helical edge state 108
3 Transport through the irradiated edge state 109
4 Quantized adiabatic charge pumping 117
5 Experimental parameters 120
6 Conclusion and perspectives 120

Conclusion **121**

A Symmetry constraints on the Berry phase properties **123**
1 Time-reversal symmetry 123
2 Space-inversion symmetry 124

B Kubo formula for the Hall conductivity **125**
1 General derivation 125
2 Application to a two band system 127

C Oscillating integrals **131**
1 Integral (4.21) 131
2 Integral (5.46) 132

D generalized rotatating wave approximation for graphene **135**

Introduction

Since its experimental discovery in 2004 [1], graphene has been the subject of an intense experimental and theoretical effort to synthesize [2], manipulate and characterize [3] its physical properties. Graphene has very good electrical and thermal conduction and shows striking properties in several domains such as optics, chemistry, mechanics or electronics. It can be synthesized very easily by mechanical exfoliation, meaning by pealing graphite repeatedly using tape, until only one layer subsists. It is a purely two-dimensional material with a honeycomb lattice of carbon atoms which makes it very simple to model theoretically using a tight-binding formalism. Moreover, its band structure is linear at low-energy, analogously to massless relativistic fermions in two-dimensions, which allows it to be modelled by a Dirac-Weyl like equation. Due to its two-dimensional nature, the carrier density can be tuned by electrostatic gating. All of these properties makes graphene a very promising material for technological applications and a very interesting material to study from a fundamental point of view.

Another field of physics that surged in the recent years is the one of topological insulators [4, 5]. Such materials are insulators in the bulk but conduct electricity in a robust way along their edges for two-dimensional materials or at their surface in three dimensions. These edge states are robust against disorder because they arise from a topological property of the bulk of the material. Topology aims at describing the global properties of objects which are invariant under smooth deformations. For example, a sphere and a torus are not topologically equivalent because the torus possesses one "hole" which means that it cannot be deformed continuously to a sphere without closing the hole. In the field of topological insulators, one can assign a topological invariant to the Bloch Hamiltonian of the material without edges. This topological invariant is an integer that is robust under small perturbations of the Hamiltonian as long as the gap remains open. One can thus have a topological phase transition only when the bulk gap closes and reopens. The relation between the number of the edge states and the bulk topological invariant is expressed through the bulk-boundary correspondence.

Historically, the first system to present both bulk topological invariant and robust edge states is the quantum Hall effect. A two-dimensional gas of electrons subjected to an intense magnetic field forms Landau levels, which are highly degenerated flat bands. Close to the edges of the material, the Landau levels acquire an energy dispersion and thus conduct current. When the Fermi level is in the gap, the longitudinal conductance vanishes while the Hall conductance is quantized according to :

$$\sigma_H = \nu \frac{e^2}{h}, \tag{1}$$

where e^2/h is the quantum of conductance and ν is the number of filled Landau levels. Using the linear response theory, the quantized Hall conductance was found to originate from a bulk property, which was labelled as TKNN integer according to the original

paper by Thouless, Kohmoto, Nightingale and Den Nijs [6]. Later on, it was realized that this integer ν was in fact the Chern number of the filled magnetic Bloch bands. The Chern number is a topological invariant that characterizes systems in which time-reversal symmetry is broken and counts the number of chiral edge states (which all propagate in the same direction) in the case of a two-dimensional topological insulator. However, the quantum Hall effect arises in the presence of an external magnetic field and defining the Bloch bands is non trivial in presence of a magnetic field because translational invariance is broken.

In 1988, Haldane proposed a model that exhibits a quantized Hall conductance in presence of a magnetic flux pattern with the same periodicity as the lattice. In this model, based on the graphene honeycomb lattice, defining Bloch bands is natural. The valence and conduction bands present a Chern number +1 or −1 with the Hall conductance quantized accordingly. This topological insulator was coined Chern insulator or quantum anomalous Hall insulator due its similarity with the quantum Hall effect. It was then thought that it was necessary to break time-reversal invariance to obtain non-trivial topological phases. However, in 2005, Kane and Mele [7] introduced a new type of topological insulator based on graphene with spin-orbit coupling for which time-reversal symmetry is conserved. It was also predicted to exist in HgTe/CdTe quantum well heterostructures [8]. It wasn't discovered in graphene because spin-orbit coupling is too weak, but it was observed in 2007 in the quantum well heterostructure [9]. Instead of having chiral edge states, this topological insulator possesses two counter-propagating edge states whose directions are locked to the spin of the electron. This kind of topological insulator is characterized by a $\mathbb{Z}_2$ topological invariant that counts the parity of the number of pairs of counter-propagating edge states.

More recently, it was shown that non-trivial topological phases could be generated by shining light on a trivial insulator. Irradiating graphene with a circularly polarized electromagnetic wave with a frequency larger than the bandwidth opens a mass gap similar to the Haldane model [10]. Similarly, when the irradiation is on-resonance with the conduction and valence bands of a material, band inversion occurs at the crossing between two bands which in turn leads to a non-zero Chern number associated with the band crossing [11]. These systems are called Floquet topological insulators because they are usually studied using the Floquet theorem. Floquet theory, which takes into account for the time periodicity of the driving, allows for the definition of a new quantum number, the quasi-energy, which is analogous to the quasi-momentum in Bloch bands. The spectrum is now $\hbar\omega$-periodic where ω is the frequency of the driving, and non-equivalent gaps open at $\varepsilon = 0$ and $\varepsilon = \hbar\omega/2$ which can both host edge states.

In this context, wa have studied in this thesis the transport properties of Dirac systems under irradiation. We consider two systems in particular : first, graphene irradiated by an electromagnetic wave, and second, an edge state of the quantum spin Hall insulator also under irradiation. We consider a two-terminal setting where electrons are injected in one lead and can be scattered towards both leads after having absorbed or emitted one or more photons. In the irradiated region, the electrons are dressed coherently by the driving, and we assume that the dissipation occurs solely in the leads.

The first three chapters is a review of the systems under study, while Chapters 4 and 5 represent the main work of this thesis, namely the transport properties of irradiated bulk or edge Dirac systems.

In Chapter 1, we introduce the reader to the electronic properties of graphene. We

describe the dispersion relation of graphene using the tight-binding formalism. We then derive the low-energy Hamiltonian analogous to the Dirac equation. This simple low-energy description will be used frequently in the next chapters. Graphene possesses several discrete symmetries : time-reversal symmetry, particle-hole symmetry, parity and sublattice symmetry. We derive the constraints that these symmetries impose on the Bloch Hamiltonian, and discuss several symmetry breaking terms analogous to a mass in the Dirac equation.

Chapter 2 is dedicated to the geometrical structure encoded in the Bloch wavefunctions of two-dimensional crystals, namely the Berry connection and curvature. To each point in the Brillouin zone is associated a point on the Bloch sphere corresponding to the state of a two-band model. If the phase of the wavefunction winds around the Bloch sphere as the momentum spans the Brillouin zone, the bands possess a non-trivial topology which in turn leads to a quantized Hall conductance. To picture these geometrical and topological properties, we present the Haldane model defined on the graphene lattice. Depending on the parameters of the model, different mass terms at low-energy are generated and we observe topological phases with a non-zero Chern number. In the topological phase, we obtain the dispersion relation of the edge states in a ribbon geometry using two different procedures : direct diagonalization of a tight-binding ribbon Hamiltonian, and resolution of the Dirac equation with proper boundary conditions.

In Chapter 3, we briefly review the Floquet formalism for systems driven by a time-periodic excitation. The effective Hamiltonian of graphene irradiated by a circularly polarized electromagnetic wave at high frequency can be mapped to the Haldane model. When the valence band and the conduction band are on resonance with the driving, we observe edge states bridging the non-equivalent gaps in the Floquet quasi-energy spectrum of a ribbon. When the frequency is small compared to the bandwidth of graphene, we can use the Floquet formalism applied to the Dirac equation to obtain the spectrum. We observe a set of nested gaps corresponding to anti-crossing between the valence and conduction bands corresponding to n-photon processes. We introduce a simple model to obtain the Chern number associated with a band crossing corresponding to one-photon resonance. We present results concerning the edge states of irradiated graphene obtained using the Dirac equation and a description of the associated wavefunctions.

Chapter 4 is devoted to the main work of this thesis. We investigate transport through an irradiated graphene sheet connected to two reservoirs. We use the Landauer-Büttiker formalism extended to Floquet systems to obtain the DC conductance as a function of the different parameters of the system such as the geometry of the sample, the frequency and strength of the driving, and the chemical potential in the irradiated region. We find that the conductance is identical to the conductance of the non-irradiated sheet except in the quasi-energy gaps where the conductance is significantly reduced. In these gaps, the current is carried by a set of evanescent states with different characteristic lengths corresponding to the number of photons associated to the anti-crossing. We observe a competition between these evanescent states as a function of the driving strength and the length of the sample.

Chapter 5 presents a preliminary work concerning transport through the helical edge state of the quantum spin Hall effect irradiated by an electromagnetic wave. This system was studied in Ref. [12] in the absence of leads, and a quantized pumped current was generated. We show that this pumped current is related to the topological charge pumping mechanism introduced by Thouless [13]. The novelty of our work is to include the effect of the leads on the generated photocurrent. We observe the same quantized charge pumping

at low frequency but obtain a different behavior at high frequency due to the presence of leads.

Chapter 1

Graphene

Graphene is the first available truly two-dimensional crystal. It is a one-atom thick material made of carbon atoms arranged in a honeycomb structure. Graphene has completed the series of allotropic forms of carbon : fullerenes in 0D, carbon nanotubes in 1D, and graphite in 3D. These materials are all made of the same building block : a 2D sheet of graphene. However, strictly 2D materials were expected to be thermodynamically unstable due to important thermal fluctuations. The experimental discovery of graphene in 2004 by the group of Geim and Novoselov in Manchester [1] proved that such a material was in fact stable. This discovery earned them the Nobel prize of physics in 2010 and led to the rise of graphene [14], a material that is now very widely studied in condensed matter physics due to its striking physical properties. Following this breakthrough discovery and a decade of research, a whole new family of 2D crystals was then realized in the laboratory : Van der Waals heterostructures. These materials include hexagonal Boron-Nitride, MoS_2, and other transition dichalcogenoid metals [15].

We focus here on the electronic properties of graphene [3]. The electronic band structure of graphene was first studied by Wallace [16] in 1947 as the building block of graphite. Graphene is a semi-metal, which means that the conduction band and the valence band touch at different points, called Dirac points. Around these points, the dispersion relation is linear, which corresponds to a two-dimensional gas of massless Dirac fermions [17], except that the electrons travel at the Fermi velocity v_F, which is 300 times smaller than the velocity of light. Moreover, because the unit cell is made of two sites, the wavefunction has an isospin structure, allowing to describe accurately the electron motion with the Dirac-Weyl equation in 2D. Graphene was thereby advertized as a good playground to study quantum electrodynamics in condensed matter [18].

Another fundamental interest of graphene arises because of its crystalline nature. Because the wavefunctions of the electrons in a crystal are labelled by their wavevector defined over the compact Brillouin zone, they possess a geometrical structure encoded in the phases of the corresponding Bloch wavefunctions. These properties that derive from the Berry phase [19] are the Berry connection and the Berry curvature. We will study in detail these properties in Chap. 2. The graphene lattice possesses discrete symmetries : time-reversal, space inversion, particle-hole symmetry and chiral symmetry. These symmetries have implications on the electronic band structure and on the geometrical quantities defined in momentum space.

One of the reasons that makes graphene so interesting in the scientific community is the ability to tune the carrier density in a reversible way using the electric field effect [1]. In 3D semiconductors, the doping can only be tuned chemically, which is an irreversible process

and introduces disorder in the host material. Due to the purely two-dimensional structure of graphene, it can be doped very effectively by electrostatic gating. The graphene sheet is either suspended or deposited on an insulating substrate, with a remote metallic gate located under or on top. This tunability gives an extra degree of freedom to study electrical transport in graphene in comparison to metals where the Fermi energy is large and fixed.

This chapter is organized as follows. In Sec. 1, we study the full electronic band structure of graphene using a nearest neighbours tight-binding formalism. In Sec. 2, we describe the low-energy electronic excitation which behave like massless chiral Dirac-Weyl fermions in 2D. In Sec. 3, we detail the discrete symmetries of the graphene lattice and of the Dirac Hamiltonian and explain the constraints they impose on the electronic properties. Finally, in Sec. 4 we discuss the different mass terms allowed depending on the presence or the absence of these symmetries.

1 Lattice description of graphene

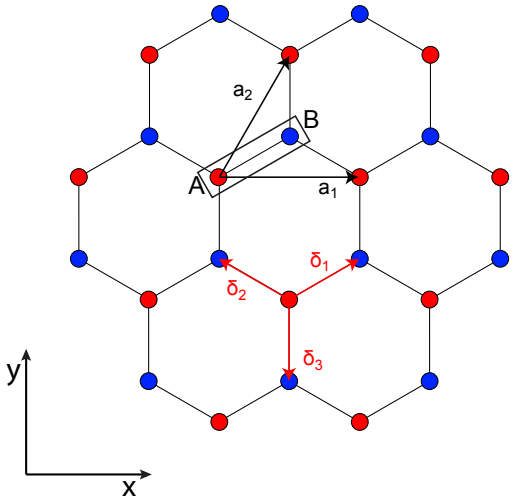

Figure 1.1 – Hexagonal lattice of graphene. The elementary unit cell (in the rectangle) is made of two atoms, the crystallographically non-equivalent A (red) and B (blue) sites. The vectors $\boldsymbol{a}_1$ and $\mathbf{a}_2$ are elementary cell vectors, and $\boldsymbol{\delta}_1$, $\boldsymbol{\delta}_2$ and $\boldsymbol{\delta}_3$ link a site A to its nearest neighbours. The distance between the nearest neighbours is $a \approx 1,42$ Å.

An isolated carbon atom has 6 electrons in the configuration $1s^2 2s^2 2p^2$, which means that the inner $1s$ orbital is filled with two electrons, and the outer $2s$ and $2p$ orbitals are also filled with two electrons each. In graphene, the $2s$, $2p_x$ and $2p_y$ orbitals hybridize in sp_2 configuration. Three covalent bonds are formed in the xy plane with an angle of 120°, and a distance between two carbon atoms of $a \approx 1,42$ Å. These bonds form the honeycomb structure of graphene which is pictured on Fig. 1.1. The remaining electron occupies the out-of-plane $2p_z$ orbital which is weakly coupled to the $2p_z$ orbitals from the other atoms. The coupling between the $2p_z$ orbitals creates the valence and the conduction bands of graphene. Because there is only one electron per $2p_z$ orbital and two spin states, the valence band is completely filled and the conduction band is empty in the absence of doping. Graphene is naturally at half-filling and the Fermi level consists in two Dirac points.

Due to the peculiar geometry of the honeycomb lattice, the different sites are not equivalent in a crystallographic point of view, because a translation of the lattice from one site to its neighbour is not a symmetry of the lattice. In fact, the elementary unit cell is composed of two sites that we call the A and B sites (see Fig. 1.1). Physically, the A and B are both made of the same orbitals and the energy of an electron is the same on both sites. Because there are two orbitals per unit cell, the band structure is composed of two bands, the valence and the conduction band.

In the next sections, we will consider second quantized Hamiltonians acting in the Fock space, that we denote by a calligraphic letter : $\mathcal{H}$. We will also consider single particle operators such as the Bloch Hamiltonian acting on a (usually two-dimensional) Hilbert space, and labelled by the quasi-momentum $\mathbf{k}$.

1.1 Tight-binding Hamiltonian of graphene

Because the outer $2p_z$ orbitals are decoupled from the in-plane orbitals, the electronic properties of graphene are very accurately described by a tight-binding model involving only $2p_z$ orbitals with no mixing with lower or higher bands. This tight-binding description makes graphene a very simple material to study analytically, and is therefore very interesting for theoreticians. Here, we only take into account hoppings between nearest neighbours, namely the A and B sites. Introducing next-nearest neighbour hoppings is not mathematically complicated but we will keep a nearest-neighbour description here for simplicity. The non-interacting second-quantized graphene Hamiltonian $\mathcal{H}$ is expressed as :

$$\mathcal{H} = t \sum_{\mathbf{r}_A} \sum_{\alpha=1}^{3} b^\dagger(\mathbf{r}_A + \boldsymbol{\delta}_\alpha) a(\mathbf{r}_A) + \text{H.c.} , \tag{1.1}$$

where $a^\dagger(\mathbf{r}_A)$ is the creation operator on a site A at position $\mathbf{r}_A$, $b^\dagger(\mathbf{r}_B)$ is the creation operator on a site B (see Fig. 1.1), and t is the interatomic matrix element that represents the coupling between neighbouring sites. *Ab initio* calculations give $t \approx -2.7$eV [20] and show that this description is accurate. Finally, $\boldsymbol{\delta}_a$ corresponds to the vectors linking a site A to it nearest neighbours B with $\alpha \in \{1, 2, 3\}$, such that :

$$\boldsymbol{\delta}_{1,2} = \pm \frac{\sqrt{3}a}{2} \boldsymbol{e}_x + \frac{a}{2} \boldsymbol{e}_y, \quad \text{and} \quad \boldsymbol{\delta}_3 = -a \boldsymbol{e}_y, \tag{1.2}$$

where a is the inter-atomic distance.

To diagonalize this Hamiltonian, we expand the operators on the plane wave basis :

$$a(\mathbf{r}_A) = \frac{1}{\sqrt{N}} \sum_{\mathbf{k}} a(\mathbf{k}) e^{i\mathbf{k}\mathbf{r}_A}, \quad \text{and} \quad b(\mathbf{r}_B) = \frac{1}{\sqrt{N}} \sum_{\mathbf{k}} b(\mathbf{k}) e^{i\mathbf{k}\mathbf{r}_B}, \tag{1.3}$$

where N is the total number of atoms and $\mathbf{k}$ is the wavevector belonging to the first Brillouin zone. Here, we have used a representation where the atoms A and B have different phases in real space because we defined the Fourier transform of the a and b operators relative to their positions $\mathbf{r}_A$ and $\mathbf{r}_B$, with $\mathbf{r}_B = \mathbf{r}_A + \boldsymbol{\delta}_1$. Another definition of the Fourier decomposition would be to choose a position $\mathbf{r}$ as the "origin" of the unit cell (e.g. $\mathbf{r}_A$ or $\mathbf{r}_B$) and operate the Fourier transform relative to this position. This choice of definition doesn't affect the observables of the system, however, one has to use the same basis to calculate measurable quantities [21].

In reciprocal space, the Hamiltonian is diagonal :

$$\mathcal{H} = t \sum_{\mathbf{k}} \sum_{\alpha=1}^{3} b^\dagger(\mathbf{k}) a(\mathbf{k}) e^{i\mathbf{k}\boldsymbol{\delta}_\alpha} + \text{H.c.} , \tag{1.4}$$

$$= \sum_{\mathbf{k}} \Psi^\dagger(\mathbf{k}) H(\mathbf{k}) \Psi(\mathbf{k}) , \tag{1.5}$$

where $\Psi^\dagger(\mathbf{k}) = (a^\dagger(\mathbf{k}), b^\dagger(\mathbf{k}))$ and $H(\mathbf{k})$ is the Bloch Hamiltonian that reads :

$$H(\mathbf{k}) = t \begin{pmatrix} 0 & \sum_\alpha e^{-i\mathbf{k}\boldsymbol{\delta}_\alpha} \\ \sum_\alpha e^{i\mathbf{k}\boldsymbol{\delta}_\alpha} & 0 \end{pmatrix}, \tag{1.6}$$

A generic two-band single-particle Bloch Hamiltonian can be expressed as :

$$H(\mathbf{k}) = \varepsilon_0(\mathbf{k})\mathbb{1} + \mathbf{d}(\mathbf{k}).\boldsymbol{\sigma}, \tag{1.7}$$

$$= \varepsilon(\mathbf{k})\mathbb{1} + d_x(\mathbf{k})\sigma_x + d_y(\mathbf{k})\sigma_y + d_z(\mathbf{k})\sigma_z, \tag{1.8}$$

$$= \varepsilon_0(\mathbf{k})\mathbb{1} + \begin{pmatrix} d_z(\mathbf{k}) & d_x(\mathbf{k}) - id_y(\mathbf{k}) \\ d_x(\mathbf{k}) + id_y(\mathbf{k}) & -d_z(\mathbf{k}) \end{pmatrix}, \tag{1.9}$$

where $\sigma_{x,y,z}$ are the Pauli matrices :

$$\sigma_x = \begin{pmatrix} 0 & 1 \\ 1 & 0 \end{pmatrix}, \quad \sigma_y = \begin{pmatrix} 0 & -i \\ i & 0 \end{pmatrix}, \quad \sigma_z = \begin{pmatrix} 1 & 0 \\ 0 & -1 \end{pmatrix}, \tag{1.10}$$

that act on the sublattice isospin (A, B). For the case of graphene, according to Eq. (1.6), we find that $\varepsilon_0(\mathbf{k}) = 0$, and the vector $\mathbf{d}(\mathbf{k})$ is equal to :

$$\mathbf{d}(\mathbf{k}) = \begin{pmatrix} t \sum_\alpha \cos(\mathbf{k}\boldsymbol{\delta}_\alpha) \\ t \sum_\alpha \sin(\mathbf{k}\boldsymbol{\delta}_\alpha) \\ 0 \end{pmatrix}, \tag{1.11}$$

We note that in that case, $d_x(\mathbf{k})$ is even in $\mathbf{k}$ while $d_y(\mathbf{k})$ is even in $\mathbf{k}$. This vector is of fundamental importance to study the underlying geometric structure of the phases of the wavefunctions, in particular around the Dirac points. We will study these geometric properties in Chap. 2.

1.2 Dispersion relation and eigenvectors

Using the fact that the Pauli matrices anti-commute with each other, it is easy to find the dispersion relation by squaring the Hamiltonian :

$$H(\mathbf{k})^2 = |\mathbf{d}(\mathbf{k})|^2 \mathbb{1} \quad \Leftrightarrow \quad E_s(\mathbf{k}) = s|\mathbf{d}(\mathbf{k})|, \tag{1.12}$$

where $s = \{+1, -1\}$ refers to the conduction and valence band respectively. The dispersion relation is therefore given by the modulus of $\mathbf{d}(\mathbf{k})$:

$$|\mathbf{d}(\mathbf{k})|^2 = t^2 \left| \sum_{a=1}^{3} e^{i\mathbf{k}\boldsymbol{\delta}_a} \right|^2 . \tag{1.13}$$

Using Eq. (1.13) combined with the vectors (1.2), we find the dispersion relation :

$$E_s(\mathbf{k}) = st\sqrt{3 + 2\cos\left(\sqrt{3}ak_x\right) + 4\cos\left(\frac{3}{2}ak_y\right)\cos\left(\frac{\sqrt{3}}{2}ak_x\right)}. \tag{1.14}$$

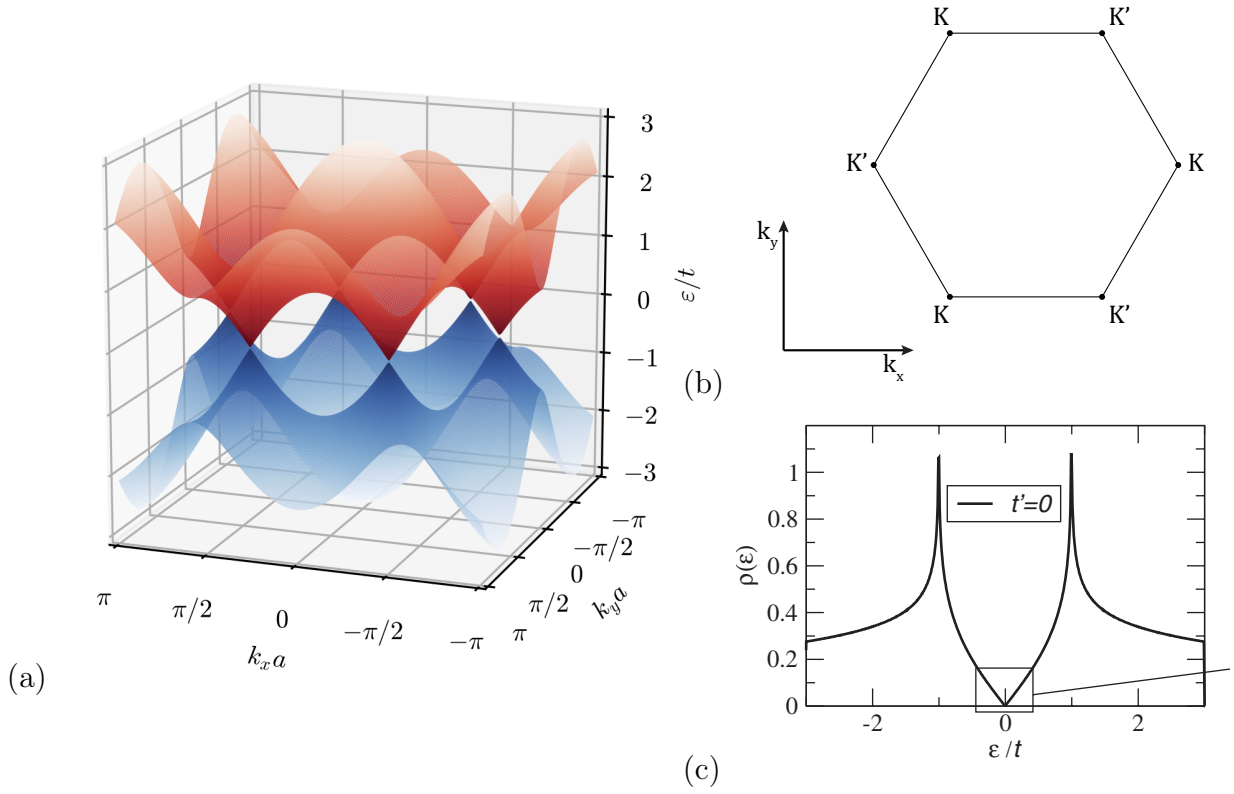

Figure 1.2 – (a) Dispersion relation of the valence (blue) and conduction (red) band. These two bands touch at the Dirac points. (b) Brillouin zone showing the location of the Dirac points K and K'. The equivalent Dirac points can be linked an elementary reciprocal unit vector. (c) Density of states of graphene. For $\varepsilon \ll t$, the density is linear in ε, and diverge at the van Hove singularity for $\varepsilon = t$. (Image taken from Castro Neto et *al* [3]).

Fig. 1.2.(a) shows the dispersion relation of graphene, and Fig. 1.2.(b) shows the first Brillouin zone of graphene. We see that the bands touch at the six corners of the Brillouin zone. These points are called Dirac points, because at low-energy, the dispersion is linear, similar to massless (or ultra-relativistic) Dirac fermions. We see 6 of them on the figure, however, only two are inequivalent because they can't be linked by the elementary vectors of the reciprocal lattice. Graphene is called a semi-metal because the valence band and the conduction band touch each other. Fig. 1.2.(c) shows the density of states of graphene. The density vanishes at the Dirac points and is linear in energy for $E \ll t$. At $E = t$, the density of states diverges, which corresponds to a van Hove singularity. At zero doping, there is only one electron on each $2p_z$ orbital so the valence band is filled, and the conduction band is empty. The fermi level is pinned at the Dirac point, also called charge neutrality point (CNP).

The eigenvectors can be expressed as :

$$|u^s_{\mathbf{k}}\rangle = \frac{1}{\sqrt{2}} \begin{pmatrix} 1 \\ s e^{i\phi_{\mathbf{k}}} \end{pmatrix}, \tag{1.15}$$

with $\phi_{\mathbf{k}} = \arctan\left(\frac{d_y(\mathbf{k})}{d_x(\mathbf{k})}\right)$, where $d_x(\mathbf{k})$ and $d_y(\mathbf{k})$ are the elements of the vector (1.11).

2 Effective low-energy excitations : the Dirac equation

The lattice model is accurate in a broad range range of energy $\pm 3t \approx 9$eV. In the range $E \ll t$, the dispersion is conical and the density of states is linear, it is therefore useful to define a low energy model around the Dirac points. In this case, the validity of the model corresponds to experimentally achievable range of Fermi energy E_F. Typical electron concentration $n \approx 10^{12}\text{cm}^{-2}$ corresponds to a Fermi energy of ≈ 100 meV.

The Dirac points are defined by the zeros of the dispersion relation (the zero of energy is defined as the common energy of the $2p_z$ orbital) :

$$|\mathbf{d}(\mathbf{K})| = 0 \quad \Rightarrow \quad d_x(\mathbf{K}) + id_y(\mathbf{K}) = \sum_{a=1}^{3} e^{i\mathbf{K}\boldsymbol{\delta}_a} = 0. \tag{1.16}$$

We see from Eq. (1.16) that if $\mathbf{K}$ is a Dirac point, then $\mathbf{K}' = -\mathbf{K}$ is also one. The valley index is denoted by ξ such that $\xi = +$ corresponds to the valley $\mathbf{K}$ and $\xi = -$ to the valley $\mathbf{K}'$. The position of the Dirac point ξ is :

$$\mathbf{K}_\xi = \xi \frac{4\pi}{3\sqrt{3}a}\mathbf{e}_x. \tag{1.17}$$

The Dirac points are located at the corners of the Brillouin zone, and it is possible to give alternate locations for equivalent Dirac points by a translation with a reciprocal unit vector as illustrated on Fig. 1.2.(b).

2.1 Massless Dirac fermions

The low-energy excitations have a momentum $\mathbf{q}$ relative to the Dirac points, such that $\mathbf{q} = \mathbf{k} - \mathbf{K}_\xi$ with $|\boldsymbol{q}| \ll |\boldsymbol{K}|$. The low-energy dispersion relation is obtained by developing $H(\mathbf{k})$ around $\mathbf{K}_\xi$:

$$\sum_{a=1}^{3} e^{i(\xi\mathbf{K}+\mathbf{q})\boldsymbol{\delta}_a} \approx -\frac{3a}{2}(\xi q_x + iq_y). \tag{1.18}$$

This dispersion relation is linear in $\mathbf{q}$ close to the Dirac points, the Hamiltonian can be written as :

$$H_{\xi\mathbf{K}}(\mathbf{q}) = -\frac{3at}{2}\begin{pmatrix} 0 & \xi q_x - iq_y \\ \xi q_x + iq_y & 0 \end{pmatrix}. \tag{1.19}$$

We introduce the velocity :

$$v = -\frac{3at}{2\hbar} = \frac{3a|t|}{2\hbar} \approx \frac{c}{300} \approx 10^6 \text{ m.s}^{-1}, \tag{1.20}$$

such that the Hamiltonian in the valley ξ can be expressed as :

$$H_\xi = v(\xi\sigma_x p_x + \sigma_y p_y), \tag{1.21}$$

where we have reinserted the momentum operator $\mathbf{p} = (p_x, p_y) = -i\hbar(\partial/\partial x, \partial/\partial y)$ for long-wavelength excitations relative to the Dirac points.

In the valley $\mathbf{K}$, the Hamiltonian can be expressed as :

$$H = v\boldsymbol{\sigma}\mathbf{p}, \tag{1.22}$$

where $\boldsymbol{\sigma} = (\sigma_x, \sigma_y)$. This equation presents similarities with the Dirac equation introduced by Dirac in 1928 to describe the motion of relativistic electrons [22] :

$$i\hbar\partial_t\Psi = (c\boldsymbol{\alpha}\mathbf{p} + \beta mc^2)\Psi, \tag{1.23}$$

where $\mathbf{p}$ is the momentum operator in 3D space, and $\boldsymbol{\alpha} = (\alpha_1, \alpha_2, \alpha_3)$ and β are 4 anti-commuting matrices. Because these matrices anti-commute with each other, the eigenvalue equation of the Dirac equation corresponds to the relativistic equation for a particle of mass m : $E^2 = p^2c^2 + m^2c^4$. These matrices are 4×4 matrices acting on the spin and particle/antiparticle space. In 2D, only three anti-commuting matrices are necessary, two for the two momentum directions and one for the mass, therefore the three Pauli matrices satisfy this condition. In the low-energy description of graphene, the Hamiltonian is analogous to the Dirac equation with 2×2 matrices acting on the sublattice isospin and with the mass set to zero. This analogy is only approximate and originates from the peculiar crystalline arrangement of the atomic sites of the graphene lattice. A term proportional to σ_z is therefore allowed in this equation that would be analogous to a mass in the Dirac equation. We will discuss in detail the different mass terms allowed in the Dirac equation in Sec. 4.

It is thus very simple to model the low-energy excitations in graphene using the massless Dirac equation. Due to the fact that the Dirac cones come in pairs, the electrons near the Dirac points come in two flavours, giving rise to a new pseudo-spin quantum number : the valley index. In the valley-isospin representation, the Dirac Hamiltonian has the expression :

$$H = v(\tau_z\sigma_x p_x + \tau_0\sigma_y p_y), \tag{1.24}$$

where τ_z is the Pauli matrix and τ_0 is the identity acting in the valley space with eigenvalues $\tau_z = \xi$. In this representation, the spinor has four components : $u = (u_{\mathbf{K}A}, u_{\mathbf{K}B}, u_{\mathbf{K}'A}, u_{\mathbf{K}'B})$. In the absence of short-range scatterers, the valley are decoupled and are two-fold degenerate : $g_v = 2$. Taking into account also the spin degeneracy, we obtain a four-fold degeneracy $g_v g_s = 4$. When making calculations using a single Dirac cone, we have to take into account this valley and spin degeneracy.

The dispersion relation is obtained by squaring the Hamiltonian $H^2 = v^2(p_x^2 + p_y^2)$, which gives us :

$$E = \pm\hbar v q, \tag{1.25}$$

where $q = |\mathbf{q}|$. In analogy with the Dirac equation, negative energy states exist for $s = -1$, which, instead of describing anti-particles, correspond here to holes in the valence band with opposite charge. The linear dispersion relation is only valid in the continuum limit, for long wavelength excitations. The wavefunction of an electron in the valley ξ is $u_\xi = (u_\xi^A, u_\xi^B)^T$, where u_ξ^A (resp. u_ξ^B) is the envelope function on the A (resp. B) sublattice. In this limit, one can ignore the lattice effects, and the electrons behave identically to massless Dirac fermions. This long-wavelength approximation is valid for wavevectors $q \ll K \approx (0.1nm)^{-1}$.

In the (A, B) basis, the eigenvectors have the expression :

$$|u_{\xi,\mathbf{q}}^s\rangle = \begin{pmatrix} 1 \\ se^{i\varphi_{\xi,\mathbf{q}}} \end{pmatrix}, \tag{1.26}$$

where $\varphi_{\xi,\mathbf{q}} = \arctan(\frac{\xi q_y}{q_x})$, and s is the valence ($s = -$) or conduction ($s = +$) band index.

Because of the 2D nature of graphene, and the linear dispersion close to the Dirac points, the density of states is also linear in E :

$$\rho(E) = \frac{2E}{\pi(\hbar v)^2}, \tag{1.27}$$

where we have taken into account the spin and valley degeneracy.

2.2 Chiral fermions

Another interesting analogy can be made between graphene and high-energy physics. The Hamiltonian (1.22) presents similarities with the Hamiltonian of the Weyl equation [23]. This equation describes massless Dirac fermions in three dimensions, as opposed to graphene where the fermions are restricted to two dimensions. When the mass is set to zero in the Dirac equation, it possible to separate it in two decoupled equations :

$$i\hbar\partial_t\Psi_L = ic\boldsymbol{\sigma}\mathbf{p}\Psi_L \tag{1.28}$$

$$i\hbar\partial_t\Psi_R = -ic\boldsymbol{\sigma}\mathbf{p}\Psi_R, \tag{1.29}$$

where $\boldsymbol{\sigma} = (\sigma_x, \sigma_y, \sigma_z)$ are the three Pauli matrices (one for each space dimension), while Ψ_L and Ψ_R are the wavefunctions of left-handed and right-handed fermions. This handedness describes a property of massless fermions : the chirality, namely the projection of its spin on its momentum. It is equal to +1 when the spin is aligned with the momentum (left-handed fermions), and −1 when it is anti-aligned (right-handed). This equation was originally used to describe neutrinos, because the mass of the neutrinos was thought to be null.

The chiral operator in the valley $\mathbf{K}$ is defined as :

$$\chi_{\mathbf{K}} = \frac{\boldsymbol{\sigma}.\mathbf{p}}{|\mathbf{p}|}. \tag{1.30}$$

This operator commutes with the Hamiltonian (1.22), it is therefore possible to define a chiral quantum number +1(−1) which tells if the isospin is parallel (anti-parallel) to the momentum. We find that :

$$\chi|u^s_{\xi,\mathbf{q}}\rangle = s|u^s_{\xi,\mathbf{q}}\rangle, \tag{1.31}$$

which tells us that electrons in the conduction band have $\chi = +1$, while holes in the valence band have $\chi = -1$. This property derives from the peculiar arrangement of the A and B sublattices which induces a coupling between the orbital momentum and the pseudospin. This property is valid because the lattice is bipartite, meaning that there are only anti-diagonal terms linking the A sublattice to the B sublattice, and no-diagonal terms. In fact, if we were to introduce a mass term proportionnal to σ_z in the Hamiltonian, the chiral operator would not commute with the Hamiltonian, and the fermions would not have a definite chirality.

The chirality has important consequences on the transport properties of graphene. The wavefunction of an electron with momentum $\mathbf{q}$ in one valley is orthogonal to the wavefunction of the electron with momentum $-\mathbf{q}$ in the same valley. This means that if we were to introduce a potential term that would commute with the chiral operator (proportional to the identity), it would not couple electrons with opposite chiralities. This property protects the fermions from back-scattering, and therefore increases the conductivity of graphene compared to other metals.

2.3 Electric field effect in graphene

When the graphene sheet is connected to Fermi reservoirs (for example leads), it is possible to change the number of particles in the graphene sheet. This can be done by applying an electric potential generated by a metalic gate parallel to the graphene sheet, such that varying the gate voltage allows to tune the chemical doping of the bands with the electric field effect [1]. Depending on the sign of the gate voltage, graphene can be doped either with electrons in the conduction band or holes in the valence band.

We consider a graphene sheet separated from the gate by a dielectric plate. The carrier density (number of electrons per unit area) in the classical picture is given by [24] :

$$n = \frac{C_g V_g}{e}, \tag{1.32}$$

where C_g is the capacitance of the dielectric substrate, V_g is the gate voltage, and e is electric charge of the electron. This limit is valid for plates thicker than a few angströms [25], when the graphene sheet can effectively screen the electrostatic potential. For thinner plates, one has to take into account for the quantum capacitance effects.

The chemical potential (or Fermi level) is the energy required to add one electron in the system. The Fermi-Dirac distribution for the population of the bands in a solid has the expression :

$$f(E) = \frac{1}{1 + e^{\beta(E-\mu)}}, \tag{1.33}$$

where μ is the chemical potential, and β is the inverse temperature. Using the expression for the density of states (1.27) close to the Dirac point, we find that the electron density is equal to :

$$n = \int_0^\infty \rho(E) f(E) dE = \int_0^\mu \rho(E) dE = \frac{\mu^2}{\pi(\hbar v)^2} \quad \Rightarrow \quad \mu = \hbar v \sqrt{\pi n}, \tag{1.34}$$

where we have set $T = 0$.

We choose a convention where the fermi level is located at $E = 0$ which gives us the expression of the low-energy Bloch Hamiltonian as :

$$H = v\boldsymbol{\sigma}\mathbf{p} - \mu\mathbb{1}, \tag{1.35}$$

so that the spectrum is :

$$E_s(\mathbf{q}) = s\hbar v q - \mu. \tag{1.36}$$

This doping modifies the spectrum only by a shift of μ in energy, while the Fermi level is located at zero energy. The eigenvectors are left unchanged by the presence of this doping since it is independent of the momentum.

3 Discrete symmetries of the graphene lattice

A system is said to be invariant under a certain transformation when its Hamiltonian remains invariant under this transformation. The second quantized Hamiltonian is invariant under a unitary or anti-unitary transformation $\mathcal{U}$ if it commutes with the operator corresponding to this transformation :

$$\mathcal{U} \text{ is a symmetry of the system} \quad \Leftrightarrow \quad [\mathcal{H}, \mathcal{U}] = 0, \tag{1.37}$$

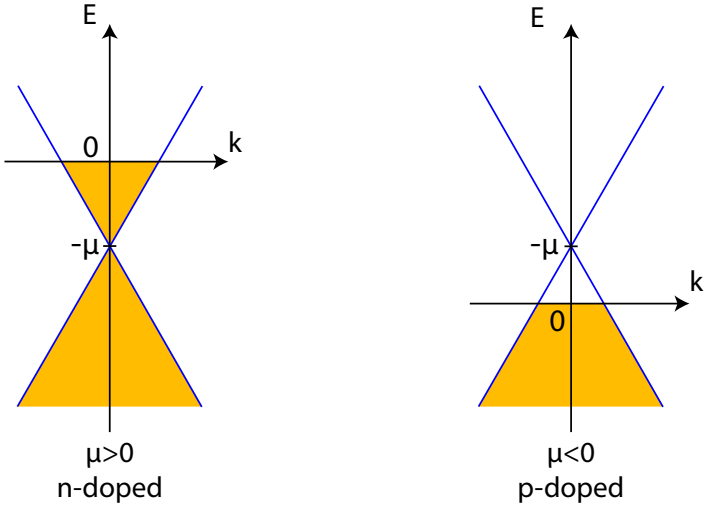

Figure 1.3 – Doping of a Dirac cone for positive doping (left) and negative doping (right). The orange regions corresponds to filled state. The Fermi level is always at $E = 0$.

where $\mathcal{U}$ acts in the Fock space of the system.

In quantum mechanics, basic transformations such as rotations or translations are described by unitary operators with continuous parameters. However, there also exists symmetries described by anti-unitary (and anti-linear) operators, such as time-reversal ($\mathcal{T}$) and charge conjugation ($\mathcal{C}$) symmetries. An anti-unitary operator is the product of a unitary operator times the complex conjugate operation denoted K such that $Kc = c^*K$ where c is a complex number and c^* is its complex conjugate. Here, we will study the effect of the discrete symmetries of graphene and the restriction it imposes on different properties of the electrons such as the Hamiltonian or the wavefunctions. We will consider the three fundamental symmetries, time-reversal, charge conjugation and chiral symmetry, denoted by the operators $\mathcal{T}$, $\mathcal{C}$ and $\mathcal{S}$ respectively. These fundamental symmetries are useful when studying Anderson localization or in the classification of topological insulators as we will see in Chap. 2. In certain scenarios, breaking the symmetries can turn graphene into a topological insulator. We will also consider space-inversion symmetry (also named parity), which is less fundamental because it is broken in the presence of disorder. However, in our case, we will consider clean crystals and we will consider the constraints of the symmetries on the Bloch Hamiltonian for simplicity.

When applying a transformation on the spinor fields, it can mix the different components of the spinor. Its action on the field operators can thus be expressed as :

$$\mathcal{U}\Psi_\alpha\mathcal{U}^{-1} = U_{\alpha\beta}\Psi_\beta, \tag{1.38}$$

where the indices α and β run over the lattice sites i for spinless particles or (i,σ) for spinfull particles where $\sigma = \pm$ corresponds to the spin of the particle, and U is a matrix acting on these indices. In order to see the action of these transformations on the Bloch Hamiltonian, we will assume translationnal invariance. Eq. (1.38) can be generalized to the case where the transformation mixes the creation and annihilation operators, such as the case of particle-hole symmetry. Under a transformation $\mathcal{U}$, the state $|\psi\rangle$ transforms into $|\psi^{\mathcal{U}}\rangle$ as :

$$|\psi^{\mathcal{U}}\rangle = \mathcal{U}|\psi\rangle. \tag{1.39}$$

3.1 Time-reversal symmetry

The time-reversal operation reverses the direction of the arrow of time. It is described by the anti-unitary operator $\mathcal{T}$. This operation reverses the direction of propagation of a particle, the angular momentum, and thus also the spin. The time-reversal operation leaves the position of the particle unchanged :

$$\mathcal{T}\Psi_\alpha(\mathbf{r})\mathcal{T}^{-1} = (U_T)_{\alpha\beta}\Psi_\beta(\mathbf{r}), \tag{1.40}$$

where α runs over the (A, B) sites and the spin degree of freedom $(\uparrow, \downarrow)$ sites, and we have used the einstein summation rule over same indices. If we consider spinless fermions, the time-reversal operation acts only in sublattice space without affecting the sublattice index and thus has the expression :

$$U_T = \sigma_0 s_0, \tag{1.41}$$

where σ_0 is the identity matrices in sublattice space and s_0 is the identity in spin space. In the case of spinfull fermions, the time-reversal operation reverses the spin of the electron and according to the usual expression for the time-reversal operation [26], we have :

$$U_T = i s_y \sigma_0, \tag{1.42}$$

where s_y is the Pauli matrix acting in spin space. In $\mathbf{k}$-space, the field operators are transformed as :

$$\mathcal{T}\Psi_\alpha(\mathbf{k})\mathcal{T}^{-1} = \frac{1}{\sqrt{N}}\sum_{\mathbf{r}} \mathcal{T}\Psi_\alpha(\mathbf{r})\mathcal{T}^{-1}\mathcal{T}e^{i\mathbf{kr}}\mathcal{T}^{-1} = \frac{1}{\sqrt{N}}\sum_{\mathbf{r}}(U_T)_{\alpha\beta}\Psi_\beta(\mathbf{r})e^{-i\mathbf{kr}} \tag{1.43}$$

$$= (U_T)_{\alpha\beta}\Psi_\beta(-\mathbf{k}). \tag{1.44}$$

Here, to describe the operation in $\mathbf{k}$-space, we have used the fact that the system is translationaly invariant. However, it is more general than that, because if we consider a disordered lattice, the matrix U_T is extended to the whole space of the lattice sites and doesn't need translationnal invariance. In the disorded case, U_T is much more complicated, so for simplicity we consider translationaly invariant system. Applying the time-reversal operation twice on a single-particle state gives :

$$\mathcal{T}^2|u_\mathbf{k}\rangle = \mathcal{T}^2\Psi^\dagger(\mathbf{k})|0\rangle = \mathcal{T}^2\Psi^\dagger(\mathbf{k})\mathcal{T}^{-2}\mathcal{T}^2|0\rangle, = U_T^* U_T|u_\mathbf{k}\rangle \tag{1.45}$$

In the case of spinless fermions, according to Eq. (1.41), we have :

$$U_T^* U_T = 1 \quad \Leftrightarrow \quad \mathcal{T}^2 = 1. \tag{1.46}$$

For spinfull fermions, using Eq. (1.42), we find :

$$U_T^* U_T = -1 \quad \Leftrightarrow \quad \mathcal{T}^2 = -1. \tag{1.47}$$

In the case of graphene in the absence of spin-orbit coupling, the Bloch Hamiltonian (1.6) acts in sublattice space and the real spins are always degenerate. Thus, for simplicity, we consider spinless fermions with the property $\mathcal{T}^2 = 1$ and omit s_0 in Eq. (1.41). The second quantized Hamiltonian in momentum space :

$$\mathcal{H} = \sum_{\mathbf{k}}\sum_{\alpha\beta}\Psi^\dagger_\alpha(\mathbf{k})H_{\alpha\beta}(\mathbf{k})\Psi_\beta(\mathbf{k}), \tag{1.48}$$

transforms as :

$$\mathcal{T}\mathcal{H}\mathcal{T}^{-1} = \sum_{\mathbf{k}}\sum_{\alpha\beta}(\mathcal{T}\Psi^{\dagger}_{\alpha}\mathbf{k})\mathcal{T}^{-1})H^{*}_{\alpha\beta}(\mathbf{k})(\mathcal{T}\Psi_{\beta}(\mathbf{k})\mathcal{T}^{-1}), \tag{1.49}$$

$$= \sum_{\mathbf{k}}\sum_{\gamma\delta}\Psi^{\dagger}_{\gamma}(\mathbf{k})(U^{\dagger}_{T}H^{*}(-\mathbf{k})U_{T})_{\gamma\delta}\Psi_{\delta}(\mathbf{k}). \tag{1.50}$$

Therefore, the Hamiltonian is invariant under time-reversal if :

$$[\mathcal{H},\mathcal{T}] = 0 \quad \Leftrightarrow \quad U^{\dagger}_{T}H^{*}(\mathbf{k})U_{T} = H(-\mathbf{k}) \tag{1.51}$$

which gives :

$$H^{*}(\mathbf{k}) = H(-\mathbf{k}) \tag{1.52}$$

for the case of spinless fermions in graphene.

We can see that from Eqs. (1.6) and (1.22) that this condition is fullfilled, which is consistent with the fact that graphene is time-reversal invariant. We can see that the time-reversal operation relates the Hamiltonian at $\mathbf{k}$ to the one at $-\mathbf{k}$, because as we said earlier, the operation reverses the direction of the velocity of the particle. If we consider the effect of time-reversal in the low energy description of graphene, we see that the time-reversal operation exchanges the valleys. Thus, in the 4×4 valley-isospin representation, the time reversal operation acts as :

$$U_{T} = \sigma_{0}\tau_{x}, \tag{1.53}$$

where τ_x is the Pauli matrix acting in valley space. The condition for time-reversal invariance reads :

$$\tau_{x}H^{*}(\mathbf{q})\tau_{x} = H(-\mathbf{q}), \tag{1.54}$$

where $\mathbf{q} = \mathbf{k} - \xi\mathbf{K}$ is the wavevector relative to the Dirac points. We can see that Eq. (1.24) respect this condition.

The single particle states are obtained as :

$$|u_{\mathbf{k}}\rangle = \Psi^{\dagger}(\mathbf{k})|0\rangle, \tag{1.55}$$

where $|0\rangle$ is the vaccum state. Upon time-reversal, the single particle states transform as :

$$\mathcal{T}|u_{\mathbf{k}}\rangle = \mathcal{T}\Psi^{\dagger}(\mathbf{k})\mathcal{T}^{-1}\mathcal{T}|0\rangle, \tag{1.56}$$

$$= U^{*}_{T}\Psi^{\dagger}(-\mathbf{k})K|0\rangle, \tag{1.57}$$

$$= U^{*}_{T}K|u_{-\mathbf{k}}\rangle, \tag{1.58}$$

where K is the complex conjugation operation. From the eigenvalue equation we have :

$$H(\mathbf{k})|u_{\mathbf{k}}\rangle = E(\mathbf{k})|u_{\mathbf{k}}\rangle \quad \Rightarrow \quad H(-\mathbf{k})\mathcal{T}|u_{\mathbf{k}}\rangle = E(\mathbf{k})\mathcal{T}|u_{\mathbf{k}}\rangle, \tag{1.59}$$

which tells us that $\mathcal{T}|u_{\mathbf{k}}\rangle$ is an eigenstate of the Hamiltonian $H(-\mathbf{k})$ with the eigenvalue $E(\mathbf{k})$. Therefore, for every state in the Brillouin zone, there always exist an eigenstate at momentum $-\mathbf{k}$ which is degenerate. The spectrum is thus symmetric under inversion of the momentum :

$$E(\mathbf{k}) = E(-\mathbf{k}). \tag{1.60}$$

This property is responsible for the fermion doubling of electrons in a lattice : when TR is conserved, the Dirac point always come in pairs.

3.2 Particle-hole symmetry

Particle-hole symmetry, also called charge conjugation in high-energy, expresses the symmetry between a particle and its anti-particle. Under charge conjugation, the charge of the particle is reversed while space and time variables are kept unchanged. In condensed matter systems, the antiparticle of an electron in the valence band is a hole in the conduction band. The charge conjugation operator $\mathcal{C}$ is also anti-unitary and can square to +1 or −1. The case of $\mathcal{C}^2 = -1$ happens usually in Bogoliubov-de Gennes Hamiltonians of superconductors, so we are not concerned here. Once again, the charge conjugation symmetry is valid in the presence of disorder, but we consider here a space-inversion invariant Hamiltonian for simplicity. The charge conjugate partner of an electron of momentum $\mathbf{k}$ in the conduction band is a hole of momentum $-\mathbf{k}$ in the valence band, because the velocity of the electron and of the hole have the same direction. The action of the charge conjugation operator on the field operators can thus be expressed as :

$$\mathcal{C}c_+^\dagger(\mathbf{k})\mathcal{C}^{-1} = c_-(-\mathbf{k}), \tag{1.61}$$

$$\mathcal{C}c_+(\mathbf{k})\mathcal{C}^{-1} = c_-^\dagger(-\mathbf{k}), \tag{1.62}$$

where the operator $c_+^\dagger$ creates an electron in the conduction band, and c_- annihilates an electron in the valence band, which is equivalent to creating a hole in the valence band.

We now need to find the expression of the charge conjugation on the creation operators $a(\mathbf{k})$ and $b(\mathbf{k})$ on the A and B sublattices respectively (defined in Eq. (1.3)). This can be done by the change of basis using the expression for the eigenstates (1.15). We get :

$$a^\dagger(\mathbf{k}) = c_+^\dagger(\mathbf{k}) + c_-^\dagger(\mathbf{k}), \tag{1.63}$$

$$b^\dagger(\mathbf{k}) = e^{-i\phi_\mathbf{k}}(c_+^\dagger(\mathbf{k}) - c_-^\dagger(\mathbf{k})). \tag{1.64}$$

The action of the charge conjugation on the operators $a(\mathbf{k})$ and $b(\mathbf{k})$ is therefore :

$$\mathcal{C}a^\dagger(\mathbf{k})\mathcal{C}^{-1} = a(-\mathbf{k}), \tag{1.65}$$

$$\mathcal{C}b^\dagger(\mathbf{k})\mathcal{C}^{-1} = -b(-\mathbf{k}), \tag{1.66}$$

that can be written in matrix form :

$$\mathcal{C}\Psi_\alpha^\dagger(\mathbf{k})\mathcal{C}^{-1} = (U_C)_{\alpha\beta}\Psi_\beta(-\mathbf{k}), \tag{1.67}$$

with :

$$U_C = \sigma_z \tag{1.68}$$

The simple expression of the matrix U_C comes from the fact that we have considered here the case of graphene with no term in σ_z. However $\mathcal{C}$ can also be defined for more general quadratic Hamiltonians and U_C has a more complicated expression that depends on $\mathbf{k}$.

When acting on the Hamiltonian, we obtain :

$$\mathcal{C}\mathcal{H}\mathcal{C}^{-1} = \sum_\mathbf{k}\sum_{\alpha\beta}\mathcal{C}\Psi_\alpha^\dagger(\mathbf{k})\mathcal{C}^{-1}H_{\alpha\beta}^*(\mathbf{k})\mathcal{C}\Psi_\beta(\mathbf{k})C^{-1}, \tag{1.69}$$

$$= \sum_\mathbf{k}\sum_{\alpha\beta\gamma\delta}(U_C)_{\alpha\gamma}\Psi_\gamma(-\mathbf{k})H_{\alpha\beta}^*(\mathbf{k})(U_C^*)_{\beta\delta}\Psi_\delta^\dagger(-\mathbf{k}), \tag{1.70}$$

$$= -\sum_\mathbf{k}\sum_{\alpha\beta\gamma\delta}\Psi_\delta^\dagger(\mathbf{k})(U_C^\dagger H^*(-\mathbf{k})U_C)_{\delta\gamma}\Psi_\gamma(\mathbf{k}) \tag{1.71}$$

where we have used the anti-commutation relations of the electron field operators in the third line. The particle-hole symmetry is thus expressed on the Bloch Hamiltonian as :

$$[\mathcal{H},\mathcal{T}] = 0 \quad \Leftrightarrow \quad U_C^\dagger H^*(-\mathbf{k})U_C = -H(\mathbf{k}) \quad \rightarrow \quad \sigma_z H^*(-\mathbf{k})\sigma_z = -H(\mathbf{k}). \tag{1.72}$$

Because of the minus sign in front of the Bloch Hamiltonian, this symmetry is rather a reality condition on the Bloch Hamiltonian than a symmetry in the traditionnal sense. Once again, we can see that this condition is satisfied from Eqs. (1.19) and (1.22) for the case of graphene. The charge-conjugate of a state in the conduction band is :

$$\mathcal{C}|u_{\mathbf{k}}^+\rangle = \mathcal{C}\Psi^\dagger(\mathbf{k})\mathcal{C}^{-1}\mathcal{C}|0\rangle, \tag{1.73}$$
$$= U_C\Psi(-\mathbf{k})K|0\rangle, \tag{1.74}$$
$$= U_C K|u_{-\mathbf{k}}^-\rangle, \tag{1.75}$$

where we have used the fact that the vacuum is made of a full valence band and an empty conduction band. Therefore the charge conjugate of a state in the valence band (+) is a hole in the condution band (-). Particle-hole symmetry implies the condition on the spectrum :

$$E(\mathbf{k}) = -E(-\mathbf{k}) \tag{1.76}$$

3.3 Chiral symmetry

Time-reversal and particle-hole symmetries are two anti-unitary symmetries that relate the matrix elements of the Hamiltonian to their complex conjugate. Combining these two symmetries gives another symmetry called chiral or sublattice symmetry. Its particularity is that it can be present even when time-reversal and particle-hole symmetry are not. The chiral operator is :

$$\mathcal{S} = \mathcal{C}\mathcal{T}. \tag{1.77}$$

Its action on the field operators has therefore the expression :

$$\mathcal{S}\Psi_\alpha^\dagger(\mathbf{k})\mathcal{S}^{-1} = (U_S)_{\alpha\beta}\Psi_\beta(\mathbf{k}), \tag{1.78}$$

with :

$$U_S = U_C U_T = \sigma_z \tag{1.79}$$

in the case of spinless fermions in graphene. We don't need to go through the derivation to find the constraints it imposes on the Bloch Hamiltonian as just need to combining Eqs. (1.51) and (1.72). We find that :

$$[\mathcal{H},\mathcal{T}] = 0 \quad \Leftrightarrow \quad U_S^\dagger H(\mathbf{k})U_S = -H(\mathbf{k}) \quad \Leftrightarrow \quad \{H(\mathbf{k}),\sigma_z\} = 0, \tag{1.80}$$

where $\{A,B\}$ corresponds to the anticommutator of the operators A and B. This condition is valid for graphene since its Hamiltonian involves only σ_x and σ_y terms. The chiral conjugate of the state $u_{\mathbf{k}}$ is :

$$\mathcal{S}|u_{\mathbf{k}}\rangle = \sigma_z|u_{\mathbf{k}}\rangle, \tag{1.81}$$

which means that this transformation reverses the sign of the wavefunction on the B lattice. If $|u_{\mathbf{k}}\rangle$ is an eigenstate with energy E, then $\mathcal{S}|u_{\mathbf{k}}\rangle$ is an eigenstate with energy $-E$. The spectrum of a chiral symmetric system is thus symmetric over the plane $E = 0$. For every momentum $\mathbf{k}$, there are two eigenvalues in the conduction and valence band. A term ε_0 proportional to the identity will trivially break chiral symmetry by shifting the origin of

the energy, but if its independent of $\mathbf{k}$, the spectrum will still be symmetric about $E = \varepsilon_0$. Eq. (1.80) is fulfilled because we have chosen the energy of the $2p_z$ orbital in graphene as the origin of the energy. This symmetry is also not exact because second nearest neighbour hopping terms introduce a $\mathbf{k}$-dependent term proportional to the identity [3].

The crucial consequence of chiral symmetry in graphene is :

$$d_z(\mathbf{k}) = 0. \tag{1.82}$$

This symmetry is characteristic of fermions on bipartite lattices (two sites per unit cell), with only nearest neighbour hoppings. This is the case for graphene where only the nearest-neighbour hoppings are taken into account. This constraint has important consequences when considering the topological properties of a material, as we will see in Chap. 2.

The analogy with the Weyl fermions considered in Sec. 2.2 can thus be extended to the lattice description of graphene. Chiral symmetry forbids the σ_z term analogous to a mass in the Dirac equation, which implies that chirality is a good quantum number. The action of the operator $\mathcal{S}$ reverses the chirality of the particle while the eigenvalue of χ gives the chirality of the particle.

3.4 Parity

The parity operation consists in reversing the space coordinates, which implies also reversing the momentum of the particle. Parity is a unitary operation, and therefore doesn't affects complex numbers. Considering the graphene lattice on Fig. (1.1), we can choose the center of inversion either at the center of a hexagon, or in the middle of a bond between two site. This transformation inverts the A and B sublattices such that :

$$\mathcal{P}a(\mathbf{r})\mathcal{P}^{-1} = b(-\mathbf{r}), \tag{1.83}$$

$$\mathcal{P}b(\mathbf{r})\mathcal{P}^{-1} = a(-\mathbf{r}). \tag{1.84}$$

This transformation can be expressed in the reciprocal space using the operators $a(\mathbf{k})$ and $b(\mathbf{k})$ defined in Eq. (1.3) :

$$\mathcal{P}a(\mathbf{k})\mathcal{P}^{-1} = \frac{1}{\sqrt{N}}\sum_{\mathbf{r}}\mathcal{P}a(\mathbf{r})\mathcal{P}^{-1}e^{i\mathbf{kr}} = \frac{1}{\sqrt{N}}\sum_{\mathbf{r}}b(\mathbf{r})e^{-i\mathbf{kr}} = b(-\mathbf{k}), \tag{1.85}$$

and similarly $\mathcal{P}b(\mathbf{k})\mathcal{P}^{-1} = a(-\mathbf{k})$. In matrix representation, we find the transformation of the field operator :

$$\mathcal{P}\Psi_\alpha(\mathbf{k})\mathcal{P}^{-1} = (U_P)_{\alpha\beta}\Psi_\beta(-\mathbf{k}), \quad \text{with} \quad U_P = \sigma_x \tag{1.86}$$

We now consider how the second quantized Hamiltonian transforms under the action of the parity operator. Therefore, the system remains invariant under space inversion if the Bloch Hamiltonian obeys the relation :

$$U_P^\dagger H(\mathbf{k})U_P = H(-\mathbf{k}) \quad \Leftrightarrow \quad \sigma_x H(\mathbf{k})\sigma_x = H(-\mathbf{k}), \tag{1.87}$$

while the eigenvectors transform as :

$$|u_\mathbf{k}\rangle^\mathcal{P} = \sigma_x|u_{-\mathbf{k}}\rangle, \tag{1.88}$$

From Eq. (1.11), we deduce that graphene is invariant under space inversion because $d_x(\mathbf{k})$ is even and $d_y(\mathbf{k})$ is odd. In the valley-isospin representation, the parity operation also reverses the valleys :

$$U_P^\dagger H(\mathbf{q})U_P = H(-\mathbf{q}) \quad \text{with} \quad U_P = \sigma_x\tau_x \tag{1.89}$$

3.5 Summary

In this section, we have derived the expression for the symmetry operators of graphene and the constraints they impose on the Bloch Hamiltonian. Graphene is a two-dimensional material with two sites per unit cell and is therefore described by a two-band Bloch Hamiltonian as introduced in Eq. (1.7). We have considered the generic symmetries time-reversal $\mathcal{T}$, charge conjugation $\mathcal{C}$ and chiral symmetry $\mathcal{S}$ that are independent of disorder. They are defined for a lattice for which the Bloch theorem is not necessarily applicable. However, we will not consider disordered systems, so we have studied their expression on the Bloch Hamiltonian. The symmetries $\mathcal{T}$, $\mathcal{C}$ and $\mathcal{S}$ have the expression for graphene :

$$\mathcal{T} : H^*(\mathbf{k}) = H(-\mathbf{k}), \tag{1.90}$$

$$\mathcal{C} : \sigma_z H^*(\mathbf{k})\sigma_z = -H(-\mathbf{k}), \tag{1.91}$$

$$\mathcal{S} : \sigma_z H(\mathbf{k})\sigma_z = -H(\mathbf{k}). \tag{1.92}$$

As we will see later, these symmetries allow to classify the topological insulators and their topological invariants according to their symmetries. Space inversion, in contrary, is present only on clean materials where the Bloch theorem applies. It has the expression for graphene :

$$\mathcal{P} : \sigma_x H(\mathbf{k})\sigma_x = H(-\mathbf{k}) \tag{1.93}$$

In the next section, we consider the presence of mass terms in the graphene Hamiltonian, and what are the constraints imposed by the symmetries on the massive Hamiltonian.

4 Masses in the Dirac equation

Relativistic electrons in free space are described by the Dirac equation which is a 4×4 matrix equation that lives in the spin and particle/antiparticle space. At low-energy, electrons in graphene are described by a 2×2 Hamiltonian made of the Pauli matrices that presents similarities with the Dirac equation. Instead of acting on the real spin, the Pauli matrices in the graphene Hamiltonian act on the sublattice space. In two dimensions, only two anti-commutating Pauli matrices are needed to obtain the massless dispersion relation $E^2 = p^2c^2$, namely the matrices σ_x and σ_y of Eq. (1.22). This fact opens the possibility to introduce a term proportional to σ_z that anti-commutes with σ_x and σ_y to obtain the massive Dirac dispersion relation $E^2 = p^2c^2 + m^2c^4$.

However, we have seen that there are two non-equivalent Dirac cones labelled by their valley index. The low-energy graphene Hamiltonian can thus be expressed in a 4×4 space that includes the valley index such as in Eq. (1.24). In that space, there exists additional anti-commuting matrices that can generate mass-like terms in the low-energy description of graphene. There exists 16 4×4 matrices acting in the valley-sublattice space that can be denoted as :

$$\alpha_{ij} = \sigma_i \otimes \tau_j, \tag{1.94}$$

where σ_i and τ_j with $i, j \in \{0, x, y, z\}$ are Pauli matrices acting in the sublattice and valley indices respectively and σ_0 and τ_0 are the identity. In order to generate mass-like term at low-energy, the matrices α_{ij} must anticommute with the matrices α_{xz} and α_{y0} of the Hamiltonian (1.24). There exists only 4 matrices that satisfy this condition [27], namely :

$$\alpha_{z0}, \quad \alpha_{zz}, \quad \alpha_{xx} \quad \text{and} \quad \alpha_{xy}. \tag{1.95}$$

The first is called the Semenoff mass, the second is the Haldane mass and the other two are generated by a Kekule distortion. The Semenoff and the Haldane mass are diagonal in valley space, while the Kekule distorsion mixes the valleys. We will not analyze in detail the Kekule distortion as it is not of interest in this thesis.

Because the Semenoff and Haldane masses are diagonal in valley space, it is possible to define a mass term in each valley. In the Hamiltonian (1.8), the mass at the **K** point is equal to $M_+ = d_z(\mathbf{K})$, while at $\mathbf{K}'$, we have $M_- = d_z(\mathbf{K}')$. The presence of space-inversion given by Eq. (1.87) imposes the constraint :

$$\mathcal{P}\mathcal{H}\mathcal{P}^{-1} = \mathcal{H} \quad \Leftrightarrow \quad d_z(\mathbf{k}) = -d_z(-\mathbf{k}) \quad \rightarrow \quad M_+ = -M_-, \tag{1.96}$$

whereas from Eq. (1.51), we see that time-reversal invariance imposes :

$$\mathcal{T}\mathcal{H}\mathcal{T}^{-1} = \mathcal{H} \quad \Leftrightarrow \quad d_z(\mathbf{k}) = d_z(-\mathbf{k}) \quad \rightarrow \quad M_+ = M_-. \tag{1.97}$$

We can see that the combination of $\mathcal{P}$ and $\mathcal{T}$ implies that $d_z(\mathbf{k}) = 0$ which protects the degeneracy of the Dirac point [28]. To generate a mass term, it is thus necessary to break one of them. The Semenoff mass term has identical sign in both valleys and therefore breaks space-inversion symmetry, while the Haldane mass term has opposite sign in the different valleys and thus breaks time-reversal invariance. In Sec. 4.1 we consider the microscopic origin of the Semenoff mass, while in sec. 4.2, we introduce the Haldane mass.

4.1 Semenoff mass

In 1984, in context of simulation of gauge theories on a lattice, Semenoff [29] introduced an additionnal term on the graphene Hamiltonian. This term corresponds to on-site energies $+M$ and $-M$ on the A and B sublattices respectively :

$$\mathcal{H} = \mathcal{H}_0 + \mathcal{M} \tag{1.98}$$

$$\mathcal{M} = m \sum_{\mathbf{r}_A, \mathbf{r}_B} (a(\mathbf{r}_A)^\dagger a(\mathbf{r}_A) - b(\mathbf{r}_B)^\dagger b(\mathbf{r}_B)), \tag{1.99}$$

where $\mathcal{H}_0$ is the bare graphene Hamiltonian and $\mathcal{M}$ is the additionnal mass term. This term generates a term $d_z(\mathbf{k}) = m$ in the Bloch Hamiltonian which breaks explicitely space inversion symmetry. This is coherent with the fact that the A and B sublattices are no longer identical. This term is diagonal in **k**-space, so we can obtain directly the expression of the low-energy graphene Hamiltonian in the valley spinor representation :

$$H = v(\tau_z \sigma_x p_x + \sigma_y p_y) + m\sigma_z \tau_0, \tag{1.100}$$

where τ_0 is the identity in valley space. The mass term $m\sigma_z\tau_0$ is identical in both valleys, which respects time-reversal invariance (1.97). Such a mass term is not present in graphene, but is present in hexagonal Boron-Nitride for example.

4.2 Haldane mass

In 1988, Haldane [30] proposed a model that possesses a non-zero Hall conductance in the absence of an external magnetic field. He introduced complex next-nearest neighbour hopping terms on the honeycomb lattice, which is realized by an alterning magnetic flux threading the unit cell with a zero total magnetic flux. The alterning magnetic flux has

the same period that the lattice, so this model is invariant under space-inversion and we can define Bloch states. Because of the presence of a magnetic flux, time-reversal is broken. According to the symmetry conditions from Eqs. (1.96) and (1.97), close to the Dirac points, the mass term has the expression :

$$d_z(\mathbf{q}) = m\sigma_z\tau_z, \tag{1.101}$$

which means that the sign is opposite in the different valleys. Although it is not realized in a condensed matter context, this model is very interesting because it is the first example of a topological insulator. Due to the presence of a mass gap, the system is insulating but it possesses a metallic state that propagates at the edge of the material. We will analyze with more detail this model in Chap. 2.

5 Conclusion

In this chapter, we studied the tight-binding model of graphene. We find that the spectrum is made of two bands that touch in two non-equivalent points in the Brillouin zone. These points are called Dirac points and the dispersion is linear around these points. At low-energy, we find that the excitations can be described by a Dirac-Weyl equation for massless fermions in two-dimensions. These fermions are chiral and have the property to be protected against backscattering.

We have derived the discrete symmetries : time-reversal, charge conjugation, sublattice symmetry and space-inversion of graphene and found the constraints they impose on the Bloch Hamiltonian. In certain conditions, breaking these symmetries allows to generate mass-like terms that can turn graphene into an insulator. In the case of spinless fermions, two mass terms are of importance : the Semenoff mass that breaks space-inversion symmetry, and the Haldane mass that breaks time-reversal symmetry and is at the origin of a non-trivial topological phase. These two mass terms will be analyzed in detail in Chap. 2.

If we take into account for the real spin of the electron, the Dirac equation lives in a 8×8 space and 16 mass terms are allowed [27]. Only one of them respects time-reversal invariance : the Kane-Mele mass term. This term consists of a Haldane mass term with opposite sign for each spin species, namely :

$$m\sigma_z\tau_z s_z, \tag{1.102}$$

where s_z is the Pauli matrix acting in spin space. The Kane-Mele model possess two counter-propagating edge states locked to their spin orientation. We will consider this model with more detail in Chap. 5.

Chap. 2, will be devoted to the Haldane model. We will analyze the geometrical and topological properties encoded the Berry phase, while Chap. 3 will show how a Haldane mass term can be generated by irradiation.

Chapter 2

Geometry, topology and the Haldane model

Physicists have always strived to classify the states or phases of matter according to the parameters of the system. Landau theory of phase transitions [31] relies on a symmetry breaking mechanism between phases with different local order parameters. The ferromagnetic or paramagnetic phases are described by a particular orientation of spin originating from the interaction between neighbouring atoms. This ferromagnetic phase is characterized by the absence of invariance of the system under arbitrary spin rotations. Superconductivity is characterized by the breaking of $U(1)$ gauge symmetry. Another way of classifying electronic states in crystals was introduced by Bloch with his famous Bloch theorem [32]. Electrons in a crystal are arranged in a band structure and are indexed by their quasi-momentum in the reciprocal space called Brillouin zone. Depending on the filling or these bands, the crystal can be a metal, an insulator or a semi-conductor.

In the modern theory of bands, a new kind of phase of matter has been discovered which emerges from a global characteristic of the Bloch wavefunctions in the Brillouin zone. These materials, called topological insulators [4, 5], possess a topological quantum number that characterizes the winding of the phase of the wavefunction when the wavevector spans the whole Brillouin zone. This ordering is robust in the sense that the topological number, which is an integer, is a global property of the band that can only be changed by closing the gap. It is therefore possible to classify the different Hamiltonians according to characteristic classes, labelled by a topological invariant. The Hamiltonians of a same class can be deformed continuously into each other. When the Fermi level is in the gap, the material is an insulator and has a quantized Hall conductivity which is proportional to this topological invariant. The Hall conductivity is carried by gapless metallic states located at its edges which are robust to moderate disorder. The connection between the topological invariant of the bulk states and the number of edge states is expressed in the bulk-boundary correspondence, which is a mathematical theorem that can be formulated for various systems, such as the quantum Hall effect [33, 34], chiral symmetric systems [35], Dirac Hamiltonians [36] or in the presence of interactions [37]. The presence of edge states can be understood intuitively by considering the vacuum as a trivial insulator. At the interface between a non-trivial insulator and a trivial one, the gap has to interpolate continuously between the two domains and therefore has to close at the boundary.

The discovery of the existence of such topological phases in materials started with the experimental discovery of the quantum Hall effect in the eighties. It was realized

by Thouless *et al.* [13] that the quantization of the Hall conductance arose from the impossibility to have a well-defined and continuous phase for the wavefunction of the electron across the Brillouin zone. The phase of the wavefunction is encoded in geometrical properties such as the Berry connection and the Berry curvature. In the case of the quantum Hall effect, the topological invariant is the Chern number which is expressed as the integral of the Berry curvature over the Brillouin zone. However, in the presence of an external magnetic field, the Bloch theorem can be applied only under specific conditions and the band structure is a complex fractal called the Hofstadter butterfly[38].

The first example of a topological insulator to present a non-zero Chern number without the application of an external magnetic field was introduced by Haldane in 1988 [30]. This model based on the graphene lattice possesses a chiral edge state that propagates along one direction at its boundary and therefore breaks time-reversal symmetry. The Haldane model has not been realized experimentally in graphene but it anticipated the field of topological insulators. However, later on, it has been realized in thin Bi_2Te_3 films with induced ferromagnetism [39], and in cold atoms systems [40]. Another example of a topological insulator, called quantum spin Hall insulator, was predicted to exist in graphene when the spin-orbit interaction is present [7]. Spin-orbit opens a gap and two counterpropagating edge states cross the gap such that the spin is locked to the direction of propagation. Backscattering between these edge states is forbidden as long as time-reversal symmetry is present. This effect was not observed in graphene because spin-orbit is too weak, however it was realized in 2007 in HgTe/CdTe quantum wells structures [41], or more recently in WTe_2 two-dimensional crystals [42].

In this section, we focus mainly on the Haldane model as a prototype of a two-dimensional topological insulator with time-reversal symmetry breaking. In Sec. 1, we introduce the different geometrical and topological aspects of the Bloch wavefunction defined over the Brillouin zone using the Berry phase as a starting point. In Sec. 2, we introduce the Haldane model. In Sec. 3, we investigate the Berry connection, the Berry curvature and the Chern number of the Haldane model as a function of the different parameters of the model. Finally, in Sec. 4, we calculate the dispersion relation of ribbons and observe the presence of edge states crossing the gap.

1 Berry phase, quantum Hall effect and topological insulators

In a seminal paper, Berry [43] introduced a phase factor accumulated by the wavefunction of a particle when the parameters of its Hamiltonian are evolved in an adiabatic manner. Originally, this phase factor was neglected because it could be redefined by a gauge transformation and was thought to be not measurable. However, if the system comes back to its original state after a closed path in parameter space, this phase becomes gauge independent and can therefore be measured. This phase does not depend on the duration of the path but only on the geometry of the path. It can thus be expressed as a line integral of a vector potential called the Berry connection along the path, or as the flux of the Berry curvature through the surface enclosed by the path. We see that an elegant geometrical interpretation of Berry's phase has emerged in parameter space. These geometrical aspects are physical expressions of the mathematical field of fiber bundles.

Berry's phase was subsequently found to have a broad range of applications in both classical and quantum physics. The Foucault pendulum is a prime example of a classical

geometric phase [44], while the Aharonov-Bohm effect was shown to originate from a Berry phase effect. After Berry's discovery, several experiments were performed to measure this phase. At a classical level, this phase appeared in the rotation of the angle of polarisation of photons in optical fibers [45], whereas at the quantum level, it was observed in magnetic resonance spectra [46, 47].

Geometrical phases have also important applications in condensed matter systems, as was first pointed out by Zak [48] who noticed that the Bloch quasi-momentum could serve as parameter for the Bloch Hamiltonian. It allowed to establish a modern theory of polarization which stated that only the differential polarization was relevant and could be quantified according to the Berry phase [49]. Orbital magnetism in crystals has also found an elegant description in terms of geometrical quantities [50]. Soon after the experimental discovery of the quantum Hall effect, it was realized that the Hall conductance could be expressed as the flux of the Berry curvature [51] over the Brillouin zone. When the parameter space is a compact manifold, the integral of the Berry flux is quantized and it corresponds to the Chern number of the Berry connection over the Brillouin zone.

In Sec. 1.1, we introduce the concept of Berry phase, and the associated Berry connection and curvature. We also briefly introduce the reader to the field of fiber bundles and their topological properties. In Sec. 1.2, we introduce the quantum Hall effect and explain how the quantized Hall conductance is the expression of a non-trivial fiber bundle. Finally, in Sec. 1.3, we present the classification of the topological insulators according to their symmetries.

1.1 Berry phase, geometry and topology

We consider a system governed by the Hamiltonian $H(\mathbf{R})$ which depends on the values of several external parameters gathered in the vector $\mathbf{R} = (R_0, R_1, ...)$. We follow one eigenstate $|n(\mathbf{R})\rangle$ of the spectrum which is given by solving :

$$H(\mathbf{R})|n(\mathbf{R})\rangle = E_n(\mathbf{R})|n(\mathbf{R})\rangle, \tag{2.1}$$

where E_n is a non-degenerate level of the system. The parameters are now changed adiabatically such that $\mathbf{R} \equiv \mathbf{R}(t)$. The adiabatic approximation is valid when the characteristic time of evolution is much smaller than the time of transition between two states n and n'.

In this approximation, the system remains in an instantaneous eigenstate $|n(\mathbf{R}(t))\rangle$ of $H(\mathbf{R}(t))$, but its phase can change. Berry [43] showed that if the system is prepared in the state $|n(\mathbf{R}(0))\rangle$ at $t = 0$, and evolves in a closed loop C in parameter space, then its wavefunction at time $t = T$ will be :

$$|\Psi(\mathbf{R}(T))\rangle = e^{i\gamma_n(C)} e^{-\frac{i}{\hbar}\int_0^T dt E_n(\mathbf{R}(t))} |n(\mathbf{R}(0))\rangle, \tag{2.2}$$

where the path is parametrized by the variable $t \in [0, T]$ such that $\mathbf{R}(0) = \mathbf{R}(T)$. The second phase term is the dynamical phase, while the first term is called the Berry phase that reads :

$$\gamma_n(C) = \int_C d\mathbf{R}.\boldsymbol{\mathcal{A}}^n(\mathbf{R}), \tag{2.3}$$

where $\boldsymbol{\mathcal{A}}^n(\mathbf{R})$ is called the Berry connection. The Berry connection is defined as :

$$\boldsymbol{\mathcal{A}}^n(\mathbf{R}) = i\langle n(\mathbf{R})|\nabla_{\mathbf{R}}|n(\mathbf{R})\rangle. \tag{2.4}$$

We can see that the variable t used to parametrize the path has disappeared, and the Berry phase depends only on the shape of the path in parameter space. The Berry phase is therefore the circulation of the Berry connection along the closed path. The Berry connection is analogous to the vector potential of an electromagnetic field but in parameter space rather than in three-dimensional space. This connection is gauge dependent because the wavefunction of the electrons are defined up to a phase. Under a gauge transformation, the wavefunction and the Berry connection transform respectively as :

$$|n(\mathbf{R})\rangle \longrightarrow e^{i\chi(\mathbf{R})}|n(\mathbf{R})\rangle, \tag{2.5}$$

$$\boldsymbol{\mathcal{A}}^n(\mathbf{R}) \longrightarrow \boldsymbol{\mathcal{A}}^n(\mathbf{R}) - \boldsymbol{\nabla}_{\mathbf{R}}\chi(\mathbf{R}). \tag{2.6}$$

Because the Berry phase is defined over a loop, it is obvious that the Berry phase is gauge independent.

Once again, in analogy with electromagnetism, it is possible to define a magnetic field in parameter space as the curl of the Berry connection. This field is called the Berry curvature. Using Stokes' theorem, the Berry phase can be expressed as :

$$\gamma_n(C) = \int_\Sigma d\mathbf{S}.\boldsymbol{\mathcal{F}}^n(\mathbf{R}), \tag{2.7}$$

with :

$$\boldsymbol{\mathcal{F}}^n(\mathbf{R}) = \nabla_{\mathbf{R}} \times \boldsymbol{\mathcal{A}}^n(\mathbf{R}), \tag{2.8}$$

where $\boldsymbol{\mathcal{F}}^n(\mathbf{R})$ is the Berry curvature. The Berry phase of a path C in parameter space is therefore the flux of the Berry curvature through the surface Σ delimited by the path such that $C = \partial\Sigma$. When the parameter space is two-dimensional, such as in the case of a two-dimensional crystal, the Berry connection has only two components $\mathcal{A}^n_x$ and $\mathcal{A}^n_y$, and the Berry curvature of the band n is a one-component object :

$$\mathcal{F}^n_{xy}(\mathbf{k}) = \partial_{k_x}\mathcal{A}^n_y(\mathbf{k}) - \partial_{k_y}\mathcal{A}^n_x(\mathbf{k}). \tag{2.9}$$

We see that a geometrical structure analogous to a gauge vector potential has emerged in the parameter space. This geometrical structure is embedded in the mathematical field of fiber bundles. Fiber bundles are spaces that possess a geometrical structure and a topological structure, which will be useful in the case of Bloch Hamiltonian. We introduce very briefly the concepts of vector bundles. Introduction on fiber bundles in the context of geometrical phases can be found in the books [52] and [44] or in the thesis of Michel Fruchart [53].

A vector bundle E associates to each point of the base space X a vector field, called the fiber. In the case of a two-dimensional crystal, the base space X is the two-dimensional Brillouin zone torus $\mathbb{T}^2$, and the fiber is the Hilbert space $\mathbb{C}^N$ of the physical Bloch eigenstates $|u_{\mathbf{k}}\rangle \in \mathbb{C}^N$ of the $N \times N$ Bloch Hamiltonian. The total space E has the dimension of the product of the dimension of the base space X and the dimension of the fiber. Locally, it looks like the cartesian product $\mathbb{R}^2 \times \mathbb{C}^N$ but not necessarily globally. A choice of vector $|\mathbf{k}, u_{\mathbf{k}}\rangle$ (up to a gauge transformation) is thereby the fiber associated to the point $\mathbf{k}$ of the base manifold. If the projection map is smooth (continuous) from the bundle space E to the whole base space X, then the bundle is called trivial and is isomorphic to the space $\mathbb{T}^2 \times \mathbb{C}^N$ in our case. If it is not, the bundle has a non-trivial, or twisted, topology.

The connection describes the geometrical structure of the fiber bundle, and therefore encodes the global topological structure of the bundle. An example of a non-trivial fiber bundle is the Möbius bundle [54] which assigns to each point of the base space S^1 the fiber $\mathbb{R}$. Locally, this bundle is the direct product of $S^1 \times \mathbb{R}$, but not globally because when coming back to the origin point after a rotation of 2π in S^1, a point of coordinate x on the fiber is now located at $-x$. To define the bundle globally, one must separate the bundle in different sections that are locally the direct product of the base space S^1 and the fiber $\mathbb{R}$, and provide transition functions at the intersection between the sections.

It is possible to classify the topological properties of the fiber bundles according to their characteristic classes. Fiber bundles that belong to the same class have identical topological invariants that are integers. Later on, we will consider a topological invariant called the first Chern number, which is defined for even dimensional base spaces. For the case of vector bundles defined on a two-dimensional Brillouin zone, the first Chern number is an integer that has the expression :

$$C^n = \frac{1}{2\pi} \int_{BZ} d^2k \mathcal{F}^n_{xy}(\mathbf{k}). \tag{2.10}$$

After having introduced the mathematical background for the topological effects, we now turn on to physical realization in condensed matter systems such as the quantum Hall effect.

1.2 Quantum Hall effect

In 1980, von Klitzing, Dorda and Pepper [55] discovered experimentally that the Hall conductance of a 2D gas of electrons subjected to a perpendicular magnetic field was quantized in units of e^2/h. This phenomenon is called the quantum Hall effect (QHE), and the quantization of the transverse conductance was shown to be extremely accurate and independent of the shape of the edges and of the amount of disorder. It was therefore first advertised as a metrological way to measure the quantum of conductance e^2/h and to serve as a new definition of the Ohm in the metric system.

When subjected to a perpendicular magnetic field, the electrons confined in two dimensions form highly degenerate Landau levels. When the Fermi energy is between two Landau levels, the material is insulating, and the current is carried by states localized at the edges of the sample [56]. Because the material is confined by the vacuum, the edges are dispersing at the interfaces (see Fig 2.1.(a)). When the Fermi level is in a gap, the Hall conductance is given by :

$$G = \nu \frac{2e^2}{h}, \tag{2.11}$$

where ν is the number of filled Landau levels, and the factor 2 corresponds to the spin degeneracy. ν also coincides with the number of chiral edge states. There is one edge state per Landau level and each contributes to one unit of the quantum of conductance. These edge states are chiral in the sense that they propagate along one direction around the material. This can be understood qualitatively within the classical skipping orbit picture [Fig 2.1.(b)].

In their analysis of the QHE, Laughlin [57] and Halperin [56] considered a gas of massive electrons without taking into account the lattice periodicity. However, Hofstadter [38] showed than when the unit cell of a lattice is threaded by a rational magnetic flux $\phi = p/q$, a Bloch band splits into p subbands with periodicity qa along one direction, where

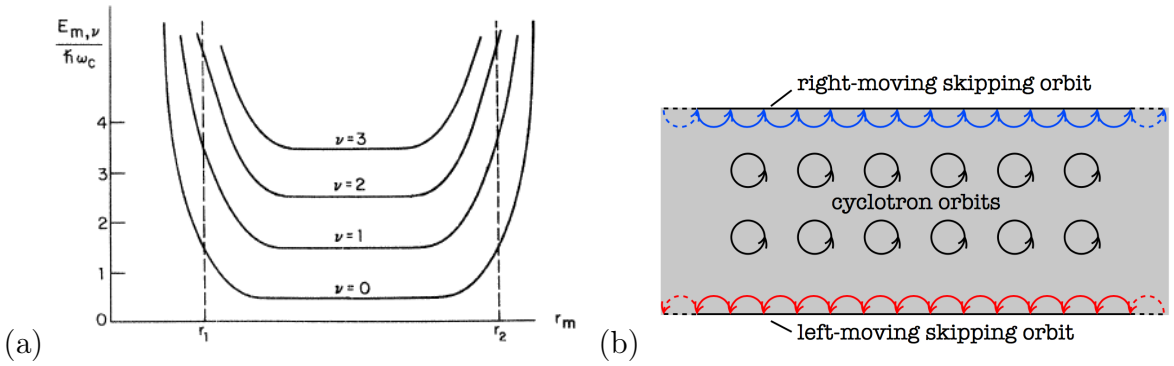

Figure 2.1 – (a) Landau levels in the Landau gauge of an infinite ribbon with width $r_2 - r_1$. In this gauge, the states belonging to a Landau level are degenerate and are labelled by the position of their center of motion. Close to the edge of the sample, the states disperse and generate a Hall response. Image taken from [56] (b) Skipping orbit picture. The electrons in the bulk have a cyclotron orbit motion, while the states close to the edge are reflected at the boundary and therefore propagate along the edge. We can see with this simple picture the chirality of the edge states, they are right-moving at the upper edge while they are left-moving at the

a is the lattice spacing. This scheme allows the definition of a magnetic Brillouin zone which is q times smaller than the normal Brillouin zone. Thouless, Kohmoto, Nightingale and den Nijs (TKNN) [6] showed that such a band possesses an integer quantum number, and that the Hall conductance of the band is quantized as $G = \nu e^2/h$, where ν is the sum of the Chern number of the filled bands. This TKNN integer relates the change of the phase of the wavefunction upon realizing a loop in the Brillouin zone. A remarkable property comes from the fact this integer characterizes an infinite system without edges, and is therefore independent of the edge shape. Also, this integer can only change if the gap closes.

It was soon realized by Avron, Seiler and Simon [58] that the Hall conductance quantization originated from a topological invariant, the Chern number, which is naturally an integer. Simon [59] established a connection between the Berry phase and the TKNN invariant. The phase of the wavefunction $u^n(\mathbf{k})$ attached to each point $\mathbf{k}$ of the Brillouin zone forms a $U(1)$ line bundle over the torus T^2. Using the Kubo formalism, the Hall conductance of the band n is found to be equal to [51] :

$$\sigma_H^n = \frac{e^2}{h} C^n, \tag{2.12}$$

where C^n is the Chern number defined in Eq. (2.10). The Berry connection $\mathbf{A}(\mathbf{k})$ introduced in Sec. 1.1 is defined in the Brillouin zone as :

$$\mathbf{A}^n(\mathbf{k}) = i\langle u^n(\mathbf{k})|\nabla_{\mathbf{k}}|u^n(\mathbf{k})\rangle, \tag{2.13}$$

where $|u^n(\mathbf{k})\rangle$ is the Bloch wavefunction of the band n. Applying Stokes' theorem to Eq. (2.10), one would naively expect the Hall conductance to vanish because the Brillouin zone torus has no boundary. However, because the phase is ill-defined at the zeros of the wavefunction, the Berry connection is not defined smoothly over the Brillouin zone and one needs to separate the Brillouin zone in different patches and apply a transition function at each interface. This obstruction is the expression of the non-triviality topology of the bundle.

We follow the simple example used in [51] to demonstrate the quantization of the Chern number. The Bloch wavefunction $|u^n(\mathbf{k})\rangle$ defined on the Brillouin zone torus $\mathbb{T}^2$ vanishes at only one point $\mathbf{k}_0$. The torus T^2 is divided in two pieces R_I and R_{II} such that $\mathbf{k}_0$ is located in R_{II}. One needs to apply a gauge transformation at the boundary between the two patches such that :

$$|u_I^n(\mathbf{k})\rangle = e^{i\xi(\mathbf{k})}|u_{II}^n(\mathbf{k})\rangle \tag{2.14}$$

$$\mathbf{A}_I^n(\mathbf{k}) = \mathbf{A}_{II}^n(\mathbf{k}) - \nabla_{\mathbf{k}}\xi(\mathbf{k}). \tag{2.15}$$

Using Stokes' theorem, the Chern number can therefore be rewritten as :

$$C^n = \frac{1}{2\pi}\Big\{ \int_{R_I} d^2k \left[\nabla_{\mathbf{k}} \times \mathbf{A}_I^n(\mathbf{k})\right]_z + \int_{R_{II}} d^2k \left[\nabla_{\mathbf{k}} \times \mathbf{A}_{II}^n(\mathbf{k})\right]_z \Big\} \tag{2.16}$$

$$= \frac{1}{2\pi} \int_{\partial R} d\mathbf{k} \left[\mathbf{A}_I^n(\mathbf{k}) - \mathbf{A}_{II}^n(\mathbf{k})\right] \tag{2.17}$$

$$= \frac{1}{2\pi} \int_{\partial R} d\mathbf{k} \nabla_{\mathbf{k}}\xi(\mathbf{k}), \tag{2.18}$$

where ∂R is the boundary between R_I and R_{II}. The phase change must be continuous along the closed path and is thus a multiple of 2π. Therefore, the Chern number must be an integer.

We have shown here the quantization of the Chern number in a simple case where the phase is ill-defined only in one point in the Brillouin zone. However, the phase of the wavefunction is usually more complex and can have several zeros.

In this section, we have analyzed the conductance of the quantum Hall effect, which is found to be quantized according to a topological number characterizing the fiber bundle defined over the Brillouin zone torus. However, the band structure of the quantum Hall effect, as described by Hofstadter, is very complex and depends critically on the rationality of the magnetic flux per plaquette ϕ. To compute the Chern number, one must work in the magnetic Brillouin zone, and have a very precise knowledge of the wavefunction.

A breakthrough discovery was to realize that such non-trivial topological phases existed intrinsically in crystal in the absence of an external magnetic field. Such materials are called topological insulators and are characterised by different kinds on topological invariants, including the Chern number. In the next section, we present a general classification of the topological insulators depending on their symmetries and the dimension of space.

1.3 Classification of topological insulators

We have seen that a new way of classifying phases of matter has emerged. These phases are characterized by topological invariants which are defined for a Bloch band of a gapped Hamiltonian. This invariant expresses the obstruction to define the phase of the Bloch wavefunction globally in the Brillouin zone. The first example of a non-trivial topological insulator is the integer quantum Hall effect (QHE), for which the Bloch bands are characterized by their Chern number. However, the QHE necessitates the application of an external magnetic field and relies on the Landau levels structure or magnetic bands. The anomalous quantum Hall effect, namely the Haldane model [30], is a model which breaks time-reversal symmetry and is also characterized by a non-zero Chern number. The Chern number is a topological invariant that characterizes two-dimensional crystals where time-reversal symmetry is broken and that belongs to the set $\mathbb{Z}$. In the anomalous

QHE, also called Chern insulator, the Hall conductance is proportional to the Chern number and is quantized in units of the quantum of conductance e^2/h.

The interest for topological insulators surged with the experimental discovery of the quantum spin Hall (QSH) effect [41]. The particularity of the QSH insulator is that it is time-reversal invariant. Because the Hall conductivity violates time-reversal symmetry, the Chern number vanishes in the QSH effect. However, one can picture the QSH effect as two copies of the Haldane model with opposite Chern number for each spin when one spin component is conserved. To characterize the topology of time-reversal invariant systems, Kane and Mele introduced a new kind of topological invariant, namely the $\mathbb{Z}_2$ invariant which can take only two values, 0 and 1 [60]. It was soon realized that such a topological invariant could be generalized to three dimensional materials [61, 62], which led to the rise of 3D topological insulators.

Depending on the presence or the absence of time-reversal symmetry, we see that two different kinds of topological order emerge, characterized by $\mathbb{Z}$ and $\mathbb{Z}_2$ invariants. One can ask the question if there exists a broader classification of topological invariants depending on the symmetries of the system. The characteristic of a topological insulators is that it possesses edge states which are topologically protected against disorder. More specifically, a topological invariant characterizes Hamiltonians that can be continuously deformed into each other as long as the gap remains closed. Altland and Zinbauer classified fermionic systems, including superconducting ones, in ten different classes [63] according to the presence of time-reversal symmetry ($\mathcal{T}$), charge conjugation ($\mathcal{C}$) and chiral symmetry ($\mathcal{S} = \mathcal{T}\mathcal{C}$). The antiunitary symmetries $\mathcal{T}$ and $\mathcal{C}$ symmetries can be present and square to +1 or −1, or be broken, which makes a total of nine possible classes. In the absence of both $\mathcal{C}$ and $\mathcal{T}$, the lattice can still have chiral symmetry, which makes the tenth class. The edge states of topological materials are robust against disorder, which means in particular that the topological phases are present even if space-inversion is broken. Therefore, only the "extremely generic" symmetries like $\mathcal{T}$, $\mathcal{C}$ and $\mathcal{S}$ allow to classify topological insulators. For example, the QSH state is protected by time-reversal symmetry. It is therefore possible to classify the topological insulators and superconductors in the "ten-fold way" [64, 65, 66]. Table 2.2 shows the classification of topological insulators and superconductors.

		TRS	PHS	SLS	d=1	d=2	d=3
Standard	A (unitary)	0	0	0	-	$\mathbb{Z}$	-
(Wigner-Dyson)	AI (orthogonal)	+1	0	0	-	-	-
	AII (symplectic)	−1	0	0	-	$\mathbb{Z}_2$	$\mathbb{Z}_2$
Chiral	AIII (chiral unitary)	0	0	1	$\mathbb{Z}$	-	$\mathbb{Z}$
(sublattice)	BDI (chiral orthogonal)	+1	+1	1	$\mathbb{Z}$	-	-
	CII (chiral symplectic)	−1	−1	1	$\mathbb{Z}$	-	$\mathbb{Z}_2$
BdG	D	0	+1	0	$\mathbb{Z}_2$	$\mathbb{Z}$	-
	C	0	−1	0	-	$\mathbb{Z}$	-
	DIII	−1	+1	1	$\mathbb{Z}_2$	$\mathbb{Z}_2$	$\mathbb{Z}$
	CI	+1	−1	1	-	-	$\mathbb{Z}$

Figure 2.2 – Periodic table of topological insulators and superconductors. The integers +1 and −1 represents how the time-reversal (TRS) and particle-hole (PHS) symmetry square. Image taken from [64].

The three classes A, AI and AII correspond to the standard Wigner-Dyson [67] classes which are defined by the absence of particle-hole symmetry. The unitary class A corresponds to systems when no symmetry is present, which is the case of the integer and anomalous quantum Hall effects in two-dimensions. The AI class is the orthogonal class for time-reversal invariant systems with $\mathcal{T}^2 = 1$ (spinless fermions). The AII class corresponds to symplectic systems where time-reversal is present with $\mathcal{T}^2 = -1$ (spinfull fermions). The QSH effect belongs to the symplectic class.

The classes AIII, BDI and CII corresponds to chiral systems which are usually implemented on a bipartite lattice. Graphene belongs to the BDI class if one considers spinless fermions. BDI corresponds to systems having sublattice chiral symmetry and time-reversal invariance with $T^2 = +1$. We see that no topological invariant exists in this class in two dimensions. The 4 other classes introduced by Altland and Zirnbauer occur generally for the Bogoliubov-de Gennes Hamiltonians of superconducting systems that we will not discuss here.

In the next section, we introduce the Haldane model as a representative of the class A, which presents a quantum Hall effect without Landau levels. This model is a band insulator with translational symmetry.

2 The Haldane model

In a seminal paper, Haldane [30] introduced a model that presents a quantized Hall conductance where time-reversal symmetry is broken but with a net zero magnetic flux per unit cell. Because the lattice periodicity is preserved, one can define a simple Brillouin zone in opposite with the QHE where one needs to define a magnetic Brillouin zone. The electronic structure is made of two bands, the valence and the conduction band. The total Chern number is zero, but the valence and the conduction band have a non-zero and opposite Chern numbers [54]. This model possesses a chiral edge state that propagates in one direction along the boundary. This edge state is topologically protected from backscattering and is therefore a characteristic feature of the non-trivial topology. Because of the features shared with the quantum Hall effect, this model was dubbed as quantum anomalous Hall effect.

This model hasn't been realized in graphene as originally introduced. However, it is a good starting point for understanding topological phases because of its simplicity. It also allows to visualize topological transitions by varying the parameters of the model. In the context of cold atoms, the Haldane model has been realized by modulating periodically a honeycomb optical lattice [40]. It was also realized in thin Bi_2Se_3 thin films[39] doped with chromium.

The Haldane model is defined on the honeycomb lattice (see Fig. 2.3), and its Hamiltonian is composed of three terms :

$$\mathcal{H}_{Hal} = \mathcal{H}_{gr} + \mathcal{H}_{\phi} + \mathcal{H}_{S}. \tag{2.19}$$

The first term is the usual bare graphene Hamiltonian given by Eq. (1.1). The second term is an on-site staggered potential with opposite sign on the A and B sublattice as seen in the previous chapter, which we call a Semenoff mass term [29] :

$$\mathcal{H}_S = M_S \sum_{\mathbf{r}_A,\mathbf{r}_B} \left(a^\dagger(\mathbf{r}_A) a(\mathbf{r}_A) - b^\dagger(\mathbf{r}_B) b(\mathbf{r}_B) \right), \tag{2.20}$$

while the third term corresponds to complex valued second neighbours hoppings :

$$\mathcal{H}_\phi = t_2 \sum_{\mathbf{r}_A} \sum_{i=1}^{3} a^\dagger(\mathbf{r}_A + \boldsymbol{a}_i) a(\mathbf{r}_A) e^{i\phi} + t_2 \sum_{\mathbf{r}_B} \sum_{i=1}^{3} b^\dagger(\mathbf{r}_B + \boldsymbol{a}_i) b(\mathbf{r}_B) e^{-i\phi} + \text{H.c.}. \tag{2.21}$$

The phases of the second neighbour hoppings are chosen according to the pattern of Fig. 2.3. The arrows on Fig. (2.3) represent the positive phase ϕ accumulated for second neighbour hoppings.

The Semenoff term breaks space inversion symmetry while the fluxes break time-reversal invariance. The non-trivial topological properties arise from the second-neighbour hopping with a complex phase with $\phi \neq 0$ and $\phi \neq \pi$. The Semenoff term doesn't generate a topological phase but allows us to visualize a topological transition by allowing a gap closing between a non-trivial topological phase and a trivial one.

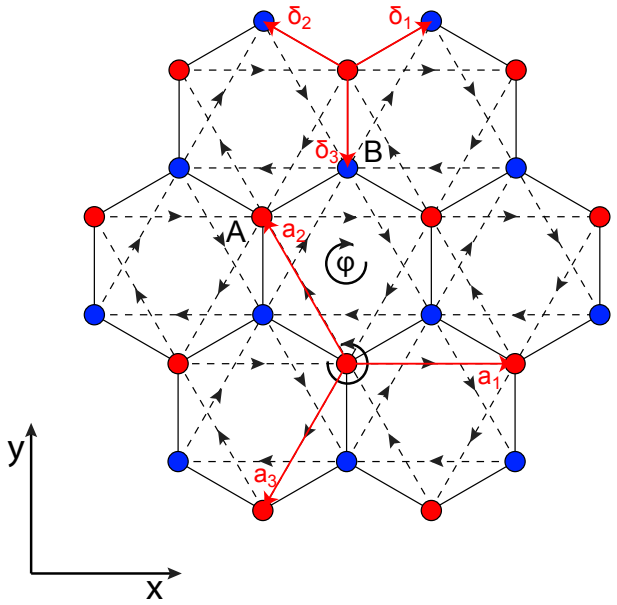

Figure 2.3 – Lattice of the Haldane model. The phase acquired during second neighbour hoppings is shown by the arrows on the dashed lines. The vectors $\mathbf{a}_1 = \sqrt{3}a\boldsymbol{e}_x$ and $\mathbf{a}_{2,3} = -\frac{\sqrt{3}a}{2}\boldsymbol{e}_x \pm \frac{3a}{2}\boldsymbol{e}_y$ are the vectors linking a site to its second neighbours.

Because the magnetic fluxes have the periodicity of the lattice, it is possible to apply Bloch theorem and define a Brillouin zone. Using the Fourier transform of the operators defined in Eq. (1.3), we obtain the Hamiltonian in $\mathbf{k}$ space :

$$\mathcal{H} = \sum_{\mathbf{k}} \Psi^\dagger(\mathbf{k}) \begin{pmatrix} M_S + 2t_2 \sum_i \cos(\mathbf{k}.\mathbf{a}_i + \phi) & t \sum_a e^{-i\mathbf{k}.\boldsymbol{\delta}_a} \\ t \sum_a e^{i\mathbf{k}.\boldsymbol{\delta}_a} & -M_S + 2t_2 \sum_i \cos(\mathbf{k}.\mathbf{a}_i - \phi) \end{pmatrix} \Psi(\mathbf{k}), \tag{2.22}$$

with $\Psi^\dagger(\mathbf{k}) = (a^\dagger(\mathbf{k}), b^\dagger(\mathbf{k}))$. Using the expression for a two-band Hamiltonian of Eq. (1.7), we find the expression of $d_0(\mathbf{k})$ and of the vector $\mathbf{d}(\mathbf{k})$:

$$d_0(\mathbf{k}) = 2t_2 \cos(\phi) \sum_i \cos(\mathbf{k}.\mathbf{a}_i), \tag{2.23}$$

$$\mathbf{d}(\mathbf{k}) = \begin{pmatrix} t \sum_\alpha \cos(\mathbf{k}.\boldsymbol{\delta}_\alpha) \\ t \sum_\alpha \sin(\mathbf{k}.\boldsymbol{\delta}_\alpha) \\ M_S - 2t_2 \sin(\phi) \sum_i \sin(\mathbf{k}.\mathbf{a}_i) \end{pmatrix}. \tag{2.24}$$

We can see that the second-neighbour couplings add two terms over the bare graphene Hamiltonian that depend on $\mathbf{k}$: the term $d_0(\mathbf{k})$ in $\cos(\phi)$ proportional to the identity, and the term $d_z(\mathbf{k})$ in $\sin(\phi)$ proportional σ_z that call we a Haldane mass term. In the case $M_S = 0$, these terms are even and odd in $\mathbf{k}$ respectively :

$$d_0(\mathbf{k}) = d_0(-\mathbf{k}) \tag{2.25}$$
$$d_z(\mathbf{k}) = -d_z(-\mathbf{k}) \tag{2.26}$$

Both terms break the chiral symmetry $\mathcal{S} = \sigma_z$. We observe two opposite situations :

- when $t_2 = 0$ and $M_S \neq 0$, the term $d_z(\mathbf{k})$ is even in $\mathbf{k}$ and therefore breaks space inversion according to Eq. (1.96) but preserves time-reversal invariance. Thereby, we recover the Semenoff mass term introduced in Sec. 4.1, which has the same sign in both valleys : $M_+ = M_-$.

- when $t_2 \neq 0$, $\phi \neq 0$ and $M_S = 0$, according to Eqs. (1.97) and (1.96), time-reversal is broken, space inversion symmetry is valid and the mass term is opposite in each valley : $M_+ = -M_-$. The dispersion relation is the same as for a Semenoff mass, however the difference is important in regard of the topological properties of the bands.

Fig. 2.4 shows the dispersion relation $E_\pm(\mathbf{k}) = \pm|\mathbf{d}(\mathbf{k})|$ for different sets of parameters. Because the Haldane mass term is odd in $\mathbf{k}$, the mass term can have a different value in the different valleys. In Fig. 2.4.(a), we observe a Dirac point in valley $\mathbf{K}$, while the valley $\mathbf{K'}$ is gapped. In Fig. 2.4.(c), we observe the opposite scenario, while in Fig 2.4.(b), the Semenoff mass is set to zero and the Haldane mass has opposite sign in the valleys, which however doesn't reflect on the spectrum.

To obtain the low-energy dispersion relation, we linearize around the Dirac points $\xi\mathbf{K}$ where $\xi = \pm$ is the valley index. Setting $\mathbf{k} = \xi\mathbf{K} + \mathbf{q}$ such that $\mathbf{q} \ll \mathbf{K}$ gives us :

$$d_0(\mathbf{q}) = -3\sqrt{3}t_2\cos(\phi) \tag{2.27}$$
$$\mathbf{d}_\xi(\mathbf{q}) = \begin{pmatrix} \xi q_x \\ q_y \\ M_\xi \end{pmatrix}, \tag{2.28}$$

where we have set $\hbar = v = 1$. We recover the massive Hamiltonian Dirac with the dispersion relation $E^2 = p^2 + M_\xi^2$ with a valley-dependent mass :

$$M_\xi = M_S + \xi 3\sqrt{3}t_2\sin(\phi) \tag{2.29}$$

When time-reversal symmetry and space-inversion are broken, the mass gap is not identical in both valleys. In fact, it is possible to have a single Dirac cone in the valley ξ when the condition :

$$M_S = -\xi 3\sqrt{3}t_2\sin(\phi) \tag{2.30}$$

is fulfilled.

We have shown here that the Haldane model allows for mass terms with opposite signs in the valley space. This fact has important consequences on the topological properties of this model which allows for a quantized Hall conductance. In the next section, we will study the geometrical and topological aspects of this model.

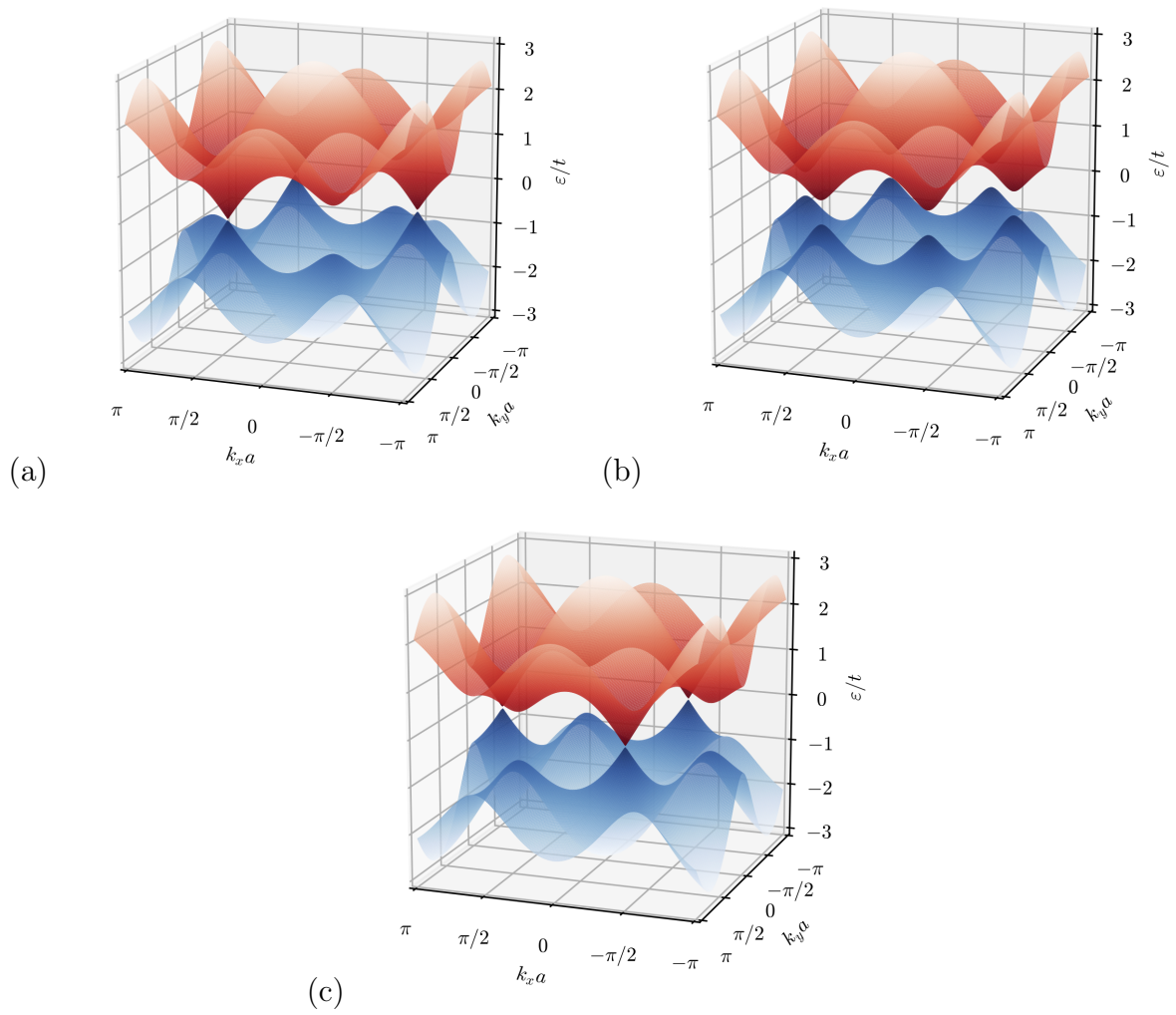

Figure 2.4 – Dispersion relation of the Haldane model for $\phi = \pi/2$ for : (a) $M_S = -3\sqrt{3}t_2$, (b) $M_S = 0$ and (c) $M_S = 3\sqrt{3}t_2$. In (a), we have $M_+ = 0$ and $M_- = 6\sqrt{3}t_2$, so that there is a band touching in valley K while valley K' is gapped. In (b), the Semenoff mass is zero, so the gap originates from the complex second neighbour hoppings. The sign of the mass is opposite in each valley such that $M_+ = -M_-$, however, this doesn't reflect on the spectrum. In (c), we observe the opposite situation as in (a) except that the gap vanishes in valley K' instead of K. (a) and (c) are located at topological transitions because there is a gap closing.

3 Berry phases and Chern number in the Haldane model

In this section, we analyze the geometrical properties of the Haldane model encoded in the Berry connection. Depending on the parameters M_S, t_2 and ϕ, this model allows to study different limiting cases such as massless graphene (semimetal), the Semenoff insulator (trivial insulator) and the Haldane insulator (non-trivial insulator).

In Sec. 3.1, we derive the expression of the Berry connection and curvature of a generic two-band Hamiltonian. In Sec. 3.2, we calculate the Chern number of the Haldane model. In Sec. 3.3, we analyze the constraints imposed by the symmetries of the model. In Sec. 3.4, we study the Berry connection of graphene where the mass term vanishes, and observe a winding of the phase around the Dirac points characteristic of chiral symmetric systems. In Sec. 3.5, we describe the Berry connection and curvature of a Semenoff

insulator ($t_2 = 0$). Finally, in Sec. 3.6, we study the Haldane insulator ($M_S = 0$).

3.1 Berry connection and curvature of a two-level system

To study these different phases, we consider first the generic Bloch Hamiltonian for a two-band model as described in Eq. (1.7) :

$$H(\mathbf{k}) = \mathbf{d}(\mathbf{k}).\boldsymbol{\sigma}. \tag{2.31}$$

The dispersion relation is given by $E(\mathbf{k}) = \pm \mathrm{d}(\mathbf{k})$ with $\mathrm{d}(\mathbf{k}) = |\mathbf{d}(\mathbf{k})|$, which describes an insulator if the condition $|\mathbf{d}(\mathbf{k})| \neq 0$ is satisfied everywhere in the Brillouin zone. In this case, the vector $\mathbf{d}(\mathbf{k})$ lives in the space $\mathbb{R}^3 - \{0\}$ which can be mapped onto the sphere S^2. We can therefore define the unit vector $\hat{\mathbf{d}}(\mathbf{k}) = \frac{\mathbf{d}(\mathbf{k})}{|\mathbf{d}(\mathbf{k})|}$ for all $\mathbf{k}$, and use the spherical angles θ and ϕ such that :

$$\hat{\mathbf{d}}(\mathbf{k}) = \begin{pmatrix} \sin\theta_{\mathbf{k}} \cos\varphi_{\mathbf{k}} \\ \sin\theta_{\mathbf{k}} \sin\varphi_{\mathbf{k}} \\ \cos\theta_{\mathbf{k}} \end{pmatrix}, \tag{2.32}$$

with :

$$\varphi_{\mathbf{k}} = \arctan\left(\frac{d_y(\mathbf{k})}{d_x(\mathbf{k})}\right), \quad \text{and} \quad \theta_{\mathbf{k}} = \arccos\left(\frac{d_z(\mathbf{k})}{d(\mathbf{k})}\right). \tag{2.33}$$

The eigenstates of this model have the expressions :

$$|u^-_{\mathbf{k}}\rangle = \begin{pmatrix} \sin\frac{\theta}{2} \\ -\cos\frac{\theta}{2} e^{i\varphi} \end{pmatrix}, \qquad |u^+_{\mathbf{k}}\rangle = \begin{pmatrix} \cos\frac{\theta}{2} \\ \sin\frac{\theta}{2} e^{i\varphi} \end{pmatrix}, \tag{2.34}$$

where $\pm$ is the band index, and we have dropped the index $\mathbf{k}$ for simplicity. These eigenstates are defined up to a gauge transformation. We can see that the eigenstates are independent of $\mathrm{d}(\mathbf{k})$ and are therefore characterized only by the angles θ and φ. The wavefunctions live on the two-dimensional sphere, so this model describes a S^2 bundle on the Brillouin zone torus T^2.

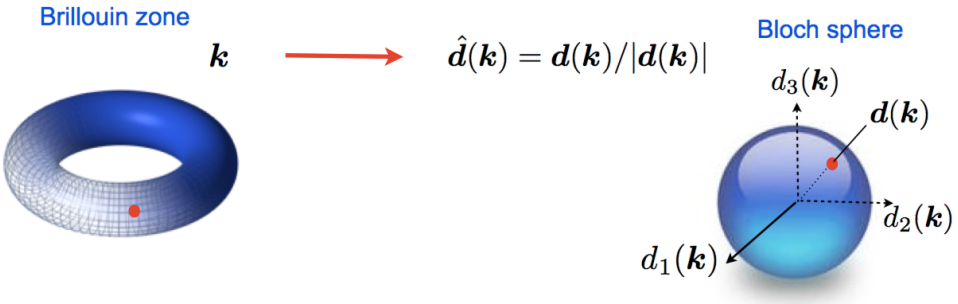

Figure 2.5 – Mapping from the Brillouin zone torus to the Bloch sphere $\hat{\mathbf{d}}(\mathbf{k}) = \mathbf{d}(\mathbf{k})/|\mathbf{d}(\mathbf{k})|$ of the eigenstates (2.34). Image taken from Cayssol [68].

We thus wish to describe the geometrical properties of the valence band with eigenstates $|u^-_{\mathbf{k}}\rangle$. We can see that the phase is ill-defined for $\theta = 0$. It is possible to make a gauge transformation by multiplying $|u^-_{\mathbf{k}}\rangle$ by $e^{-i\varphi}$, but then the phase would not be defined at $\theta = \pi$. We can already see that such a bundle has a non-trivial topology if both the poles $\theta_{\mathbf{k}} = 0$ and $\theta_{\mathbf{k}} = \pi$ are reached in the Brillouin zone. To describe the geometry of

the bundle, we separate the sphere into two hemisphere : north ($\theta \in \{0, \frac{\pi}{2} + \varepsilon\}$) and south ($\theta \in \{\frac{\pi}{2} - \varepsilon, \pi\}$) where $\varepsilon \ll 1$. We define the vectors $|u_{\mathbf{k}}^{N-}\rangle$ and $|u_{\mathbf{k}}^{S-}\rangle$:

$$|u_{\mathbf{k}}^{N-}\rangle = \begin{pmatrix} \sin\frac{\theta}{2} e^{-i\varphi} \\ -\cos\frac{\theta}{2} \end{pmatrix}, \qquad |u_{\mathbf{k}}^{S-}\rangle = \begin{pmatrix} \sin\frac{\theta}{2} \\ -\cos\frac{\theta}{2} e^{i\varphi} \end{pmatrix}, \tag{2.35}$$

The phase of $|u_{\mathbf{k}}^{N-}\rangle$ is well defined over the north hemisphere while the phase of $|u_{\mathbf{k}}^{S-}\rangle$ is well defined over the south hemisphere. The wavefunctions are related by the transition function $|u_{\mathbf{k}}^{N-}\rangle = t_{NS}|u_{\mathbf{k}}^{S-}\rangle$ at the equator $\theta = \frac{\pi}{2}$ with :

$$t_{NS} = e^{-i\varphi}. \tag{2.36}$$

This transition function is an element of the $U(1)$ group, which we will see later is related to the topology of the bundle. In the north pole, the Berry connection of the valence band in spherical coordinates has the expression :

$$\boldsymbol{\mathcal{A}}^{N-}(\mathbf{k}) = i\langle u_{\mathbf{k}}^{N-}|\nabla_{\mathbf{k}}|u_{\mathbf{k}}^{N-}\rangle = \sin^2\left(\frac{\theta_{\mathbf{k}}}{2}\right)\nabla_{\mathbf{k}}\varphi_{\mathbf{k}}. \tag{2.37}$$

In the south pole, we find :

$$\boldsymbol{\mathcal{A}}^{S-}(\mathbf{k}) = i\langle u_{\mathbf{k}}^{S-}|\nabla_{\mathbf{k}}|u_{\mathbf{k}}^{S-}\rangle = -\cos^2\left(\frac{\theta_{\mathbf{k}}}{2}\right)\nabla_{\mathbf{k}}\varphi_{\mathbf{k}}. \tag{2.38}$$

They are related by the gauge transformation :

$$\boldsymbol{\mathcal{A}}^{N-}(\mathbf{k}) = \boldsymbol{\mathcal{A}}^{S-}(\mathbf{k}) + it_{NS}^{-1}\nabla_{\mathbf{k}}t_{NS} = \boldsymbol{\mathcal{A}}^{S-}(\mathbf{k}) + \nabla_{\mathbf{k}}\varphi_{\mathbf{k}}. \tag{2.39}$$

A pole is reached when $\mathrm{d}_x(\mathbf{k}^*) = \mathrm{d}_y(\mathbf{k}^*) = 0$, and $\mathrm{d}_z(\mathbf{k}^*) \neq 0$. According to Eq. (2.28), we deduce that this condition is fulfilled at the Dirac points $\mathbf{k}^* = \mathbf{K}_\pm$. The sign of the mass at the Dirac point tells us which pole is reached :

$$\mathrm{d}_z(\mathbf{K}_\xi) = M_\xi > 0 \quad \Rightarrow \quad \theta_{\mathbf{K}_\xi} = 0 \tag{2.40}$$

$$\mathrm{d}_z(\mathbf{K}_\xi) = M_\xi < 0 \quad \Rightarrow \quad \theta_{\mathbf{K}_\xi} = \pi \tag{2.41}$$

When both poles are reached when scanning the Brillouin zone, it is not possible to define a continuous gauge over the Brillouin zone, and the bundle is not trivial. This is the case when the mass term has a different sign at the Dirac points. In that case, we need to separate the Brillouin zone in two parts and apply the transition function at the interface. From Eq. (2.9), we find that the Berry curvature has the expression :

$$\mathcal{F}_{xy}^{-}(\mathbf{k}) = \frac{1}{2}\sin\theta\left(\frac{\partial\theta_{\mathbf{k}}}{\partial k_x}\frac{\partial\phi_{\mathbf{k}}}{\partial k_y} - \frac{\partial\phi_{\mathbf{k}}}{\partial k_x}\frac{\partial\theta_{\mathbf{k}}}{\partial k_y}\right), \tag{2.42}$$

This quantity is gauge independent and can therefore be measured. To obtain the expression of the Berry connection and curvature in function of $\mathbf{k}$ we need the expression for the derivatives of the angles $\varphi_{\mathbf{k}}$ and $\theta_{\mathbf{k}}$ as a function of the vector $\mathbf{d}(\mathbf{k})$. We find :

$$\nabla_{\mathbf{k}}\varphi_{\mathbf{k}} = \frac{1}{d_x^2 + d_y^2}\left[(\nabla_{\mathbf{k}}d_y)d_x - (\nabla_{\mathbf{k}}d_x)d_y\right], \tag{2.43}$$

$$\nabla_{\mathbf{k}}\theta_{\mathbf{k}} = \frac{-1}{d\sqrt{d_x^2 + d_y^2}}\left[(\nabla_{\mathbf{k}}d_z)d - (\nabla_{\mathbf{k}}d)d_z\right], \tag{2.44}$$

3.2 Chern number

We have seen in Sec. 1.2 that, according to the Kubo formula, the Hall conductance of a filled band of a 2D material is proportionnal to the TKNN integer or equivalently the Chern number of the band. The Chern number is a topological invariant defined for two-dimensional materials where time-reversal symmetry is broken. It can be computed using different methods [54, 68, 69]. We present here two methods : first, the calculation of the Chern number as the integral of the Berry curvature over the whole Brillouin zone, as presented in Refs [51] or [54]. Second, we will see that the Chern number can be expressed as the winding number of the vector $\mathbf{d}(\mathbf{k})$ around the Bloch sphere.

The Hall conductivity of a filled valence band calculated using Kubo formalism given by (see Annex B) :

$$\sigma_{xy} = \frac{e^2}{h} C^-, \tag{2.45}$$

where C^- is the Chern number of the valence band defined as :

$$C^- = \frac{1}{2\pi} \int_{\mathrm{BZ}} d^2k \mathcal{F}^-_{xy}(\mathbf{k}) \tag{2.46}$$

such that :

$$\mathcal{F}^-_{xy}(\mathbf{k}) = \left[\nabla \times \mathcal{A}^-(\mathbf{k})\right]_z, \tag{2.47}$$

where $[...]_z$ corresponds to the z component of the vector. Using Stokes' theorem naively gives a vanishing Chern number because the Brillouin zone has no boundary. However, we have seen in Sec. 3 that it is impossible to define a continuous gauge over the whole Brillouin zone when the Dirac points have opposite mass. The procedure consists in separating the Brillouin zone in two parts U_N and U_S defined as :

$$\{\mathbf{k} \in U_N | \theta_{\mathbf{k}} \in \{0, \pi/2 + \varepsilon\}\} \tag{2.48}$$

$$\{\mathbf{k} \in U_S | \theta_{\mathbf{k}} \in \{\pi/2 - \varepsilon, \pi\}\} \tag{2.49}$$

We define the boundary ∂U between U_N and U_S as the ensemble of points $\mathbf{k} \in \partial U$ that obey the condition $\theta_{\mathbf{k}} = \pi/2$:

$$\{\mathbf{k} \in \partial U | \theta_{\mathbf{k}} = \frac{\pi}{2}\} \tag{2.50}$$

This ensemble corresponds to a closed loop in the Brillouin zone defined by $d_z(\mathbf{k}) = 0$. Using the expression for $d_z(\mathbf{k})$ from Eq. (2.24) with $M_S = 0$, we find that :

$$\theta_{\mathbf{k}} = \frac{\pi}{2} \quad \Leftrightarrow \quad k_y = \frac{k_x}{\sqrt{3}} \tag{2.51}$$

If the masses are opposite in the Dirac points $\mathrm{sign}(M_+) = -\mathrm{sign}(M_-)$, the Chern number of the valence band defined in Eq. (2.46) has the expression :

$$C^- = \frac{1}{2\pi} \int_{U_N} d^2k \left[\nabla \times \boldsymbol{\mathcal{A}}^{N-}(\mathbf{k})\right]_z + \frac{1}{2\pi} \int_{U_S} d^2k \left[\nabla \times \boldsymbol{\mathcal{A}}^{S-}(\mathbf{k})\right]_z, \tag{2.52}$$

$$= \frac{1}{2\pi} \int_{\partial U_N} d\mathbf{k}.\mathcal{A}^{N-}(\mathbf{k}) + \frac{1}{2\pi} \int_{\partial U_S} d\mathbf{k}.\mathcal{A}^{S-}(\mathbf{k}), \tag{2.53}$$

where the integral in the second line is operated along the equator of the Bloch sphere ∂U. It is operated anti-clockwise around the north pole and clockwise around the south pole. The boundaries ∂U_N and ∂U_S have opposite orientation, such that we can write :

$$C^- = \frac{1}{2\pi} \oint_{\partial U} d\mathbf{k} \left[\mathcal{A}^{N-}(\mathbf{k}) - \mathcal{A}^{S-}(\mathbf{k})\right], \tag{2.54}$$

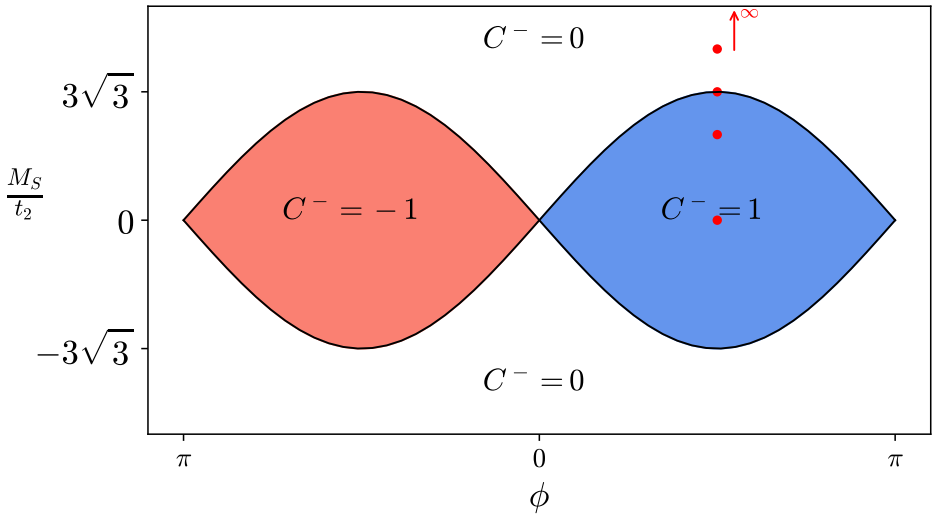

Figure 2.6 – Phase diagram of the Haldane model as a function of the parameters M_S, t_2 and ϕ calculated using Eq. (2.59). C^- denotes the Chern number of the occupied valence band. There are two non-trivial phases with Chern number +1 and −1 indicated in red and blue respectively. Outside these regions in parameter space, the Chern number is zero. The red dots correspond to the coordinates in parameter space of the plots of Fig. 2.10.

where we have set the convention that the integral is operated anti-clockwise along ∂U. Using Eq. (2.39), we find :

$$C^- = \frac{i}{2\pi}\int_{\partial U} d\mathbf{k} t_{NS}^{-1}\nabla_{\mathbf{k}} t_{NS}, \tag{2.55}$$

$$= \frac{i}{2\pi}\int d\log t_{NS}, \tag{2.56}$$

where t_{NS} is defined in Eq. (2.36). Therefore, the Chern number of the valence band can be expressed as the winding number of the $U(1)$ transition function t_{NS} between the two regions. Using the expression of the transition function for the case of the Haldane model (2.36), we find that the Chern number can be expressed as [69] :

$$C^- = \frac{1}{2}(\text{sign}(M_+) - \text{sign}(M_-)), \tag{2.57}$$

because the winding of the transition function along the equator depends on the orientation of the integral along the equator. If the mass is negative in valley K and positive in valley K', then the north hemisphere is located at the Dirac point K' and the integral along ∂U is performed anti-clockwise around K'. In the opposite scenario, the north hemisphere is at the Dirac point K, and the integral along ∂U is performed anti-clockwise around K and thus clockwise around K'. Thus, depending on the sign of the masses at the Dirac point, the phase winds in opposite directions along the equator.

We can see that each Dirac point carries a topological charge 1/2 and that depending on the sign of mass in each valley, we can define different phases. At first sight, there are 4 phases depending on the sign of the masses which are $(\text{sign}(M_+), \text{sign}(M_-)) = (1,1), (1,-1), (-1,1)$ and $(-1,-1)$. When the mass has opposite sign in the valleys, the Chern number is ±1, while if the mass has the same sign, the Chern number is zero. A

transition between these phases happens when the gap closes in one valley, namely :

$$\frac{M_S}{t_2} = \pm 3\sqrt{3}\sin\phi. \tag{2.58}$$

Fig. 2.6 shows the topological phase diagram of the Haldane model as a function of the parameters M_S, t_2 and ϕ such that :

$$C^{-} = \frac{1}{2}(\text{sign}(M_S + 3\sqrt{3}t_2\sin\phi) - \text{sign}(M_S - 3\sqrt{3}t_2\sin\phi)). \tag{2.59}$$

It is possible to obtain phases with higher Chern number by engineering models with additional Dirac points whose "topological charges" are equal to the sign of the masses at the corresponding Dirac point[69]. Another path to engineer phases with higher Chern number is to include distant neighbours hopping in the Haldane model [70].

There exist another formulation of the Chern number, which is the winding number of the vector $\hat{\mathbf{d}}(\mathbf{k}) = \mathbf{d}(\mathbf{k})/|\mathbf{d}(\mathbf{k})|$ around the Brillouin zone (see Ref. [69] and Annex B) :

$$C^{-} = \frac{1}{4\pi}\int_{BZ} d^2k(\partial_{k_x}\hat{\mathbf{d}}(\mathbf{k}) \times \partial_{k_y}\hat{\mathbf{d}}(\mathbf{k})).\hat{\mathbf{d}}(\mathbf{k}) \tag{2.60}$$

When integrating over a portion of the Brillouin zone, this formula gives the solid angle of the Bloch sphere traced by the vector $\hat{\mathbf{d}}(\mathbf{k})$. Thus, this formula counts the number of times the vector $\hat{\mathbf{d}}(\mathbf{k})$ wraps around the Bloch sphere when $\mathbf{k}$ is varied across the Brillouin zone. Because the Brillouin zone is periodic in $\mathbf{k}$, this number is an integer. This formula is useful in order to picture the non-triviality of a model by considering how the vector $\hat{\mathbf{d}}(\mathbf{k})$ winds around the Bloch sphere when the parameters are varied.

3.3 Symmetries

The presence of symmetries in the Hamiltonian of the system impose some constraints over the Berry connection and curvature. From the expression (1.58) of the time-reversed state, we find that if the system has time-reversal symmetry, the Berry connection and curvature must satisfy (see Annex A) :

$$\boldsymbol{\mathcal{A}}(\mathbf{k}) = \boldsymbol{\mathcal{A}}(-\mathbf{k}) + \nabla\zeta(\mathbf{k}), \tag{2.61}$$

$$\mathcal{F}_{xy}(\mathbf{k}) = -\mathcal{F}_{xy}(-\mathbf{k}), \tag{2.62}$$

which means that the Berry curvature must have opposite sign in each valley. From this argument, we can see that the Chern number, which is the integral of the Berry curvature over the Brillouin zone must vanish for a time-reversal symmetric system .

Using the same reasoning, we find that the Berry connection and curvature of a space-inversion invariant system must obey :

$$\boldsymbol{\mathcal{A}}(\mathbf{k}) = -\boldsymbol{\mathcal{A}}(-\mathbf{k}) + \nabla\zeta(\mathbf{k}), \tag{2.63}$$

$$\mathcal{F}_{xy}(\mathbf{k}) = \mathcal{F}_{xy}(-\mathbf{k}). \tag{2.64}$$

Therefore, in the case of a time-reversal and space-invariant system, which is the case of graphene, the Berry curvature must vanish everywhere in the Brillouin zone :

$$\mathcal{F}_{xy}(\mathbf{k}) = 0 \quad \forall \quad \mathbf{k} \in \text{BZ} \tag{2.65}$$

However, a system where time-reversal symmetry is broken can have a non-zero Chern number. We will see in the next section three special cases of the Haldane model as a function of the presence or absence of these symmetries.

3.4 Graphene

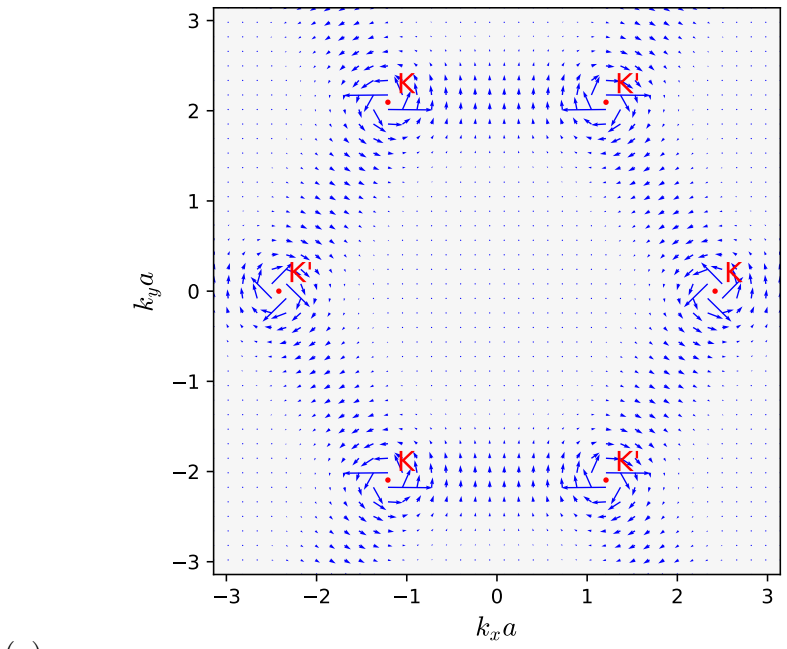

(a)

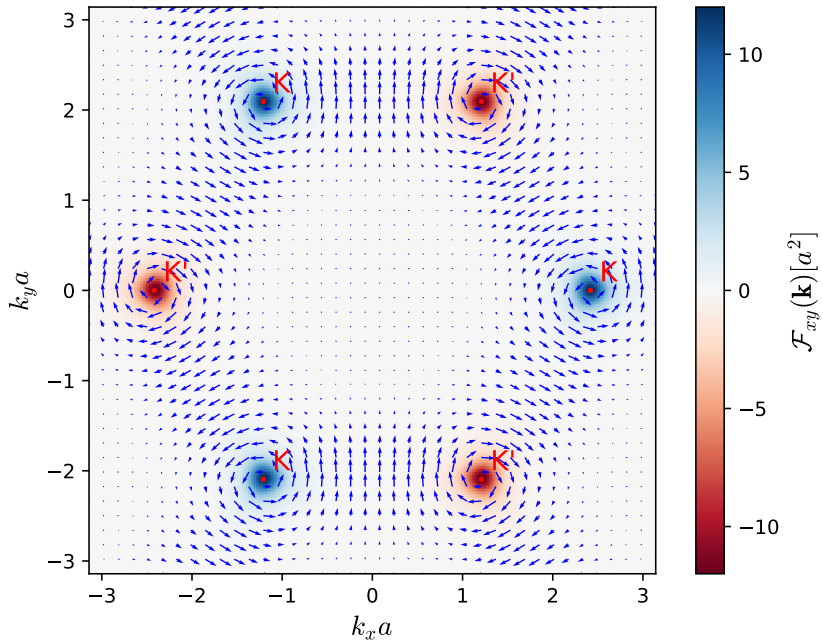

(b)

Figure 2.7 – Berry connection (blue arrows) and Berry connection (color coding) of (a) graphene and (b) the Haldane model with a positive Semenoff mass such that $M_S = 0.3t$ and $t_2 = 0$. The Berry connection is plotted in the north pole gauge using Eqs. (2.37) and (2.43). In the case of a Semenoff insulator with positive mass, the south pole defined by $\theta_{\mathbf{k}} = \pi$ is not reached and the north pole gauge is continuous over the Brillouin zone. The Berry connection winds around the Dirac points in opposite direction. The Berry curvature is peaked around the Dirac points and has opposite sign in the different valleys.

In the case of graphene, the lattice has chiral symmetry which means that the term in σ_z is forbidden. The Berry connection is thus restricted to the equator of the Bloch

sphere $\theta_{\mathbf{k}} = \pi/2$ and only one gauge is necessary to describe the Berry connection over the Brillouin zone. Fig. 2.7.(a) shows the Berry connection of graphene in the Brillouin zone in the north pole gauge using Eqs. (2.37) and (2.43) with $\theta_{\mathbf{k}} = \pi/2$. We can see that the Berry connection winds around the Dirac points in opposite direction in each valley. Because graphene has both time-reversal and space-inversion symmetry, the Berry curvature vanishes everywhere.

Using Eq. (2.28) for the expression for the vector $\mathbf{d}_\xi(\mathbf{q})$ around the Dirac points with the mass set to zero, Eq. (2.37) reduces to :

$$\boldsymbol{\mathcal{A}}_\xi^N(\mathbf{q}) = \frac{1}{2}\nabla_{\mathbf{q}}\varphi_{\mathbf{q}} = \frac{\xi}{2q}\mathbf{e}_\varphi, \tag{2.66}$$

$$\boldsymbol{\mathcal{A}}_\xi^S(\mathbf{q}) = -\frac{\xi}{2q}\mathbf{e}_\varphi, \tag{2.67}$$

where we have used the polar coordinates $(q,\varphi_{\mathbf{q}})$ centered on a Dirac point :

$$q = \sqrt{q_x^2 + q_y^2}, \tag{2.68}$$

$$\varphi_{\mathbf{q}} = \arctan(\xi q_y/q_x), \tag{2.69}$$

and $\mathbf{e}_\varphi$ is the polar unit vector corresponding to the angle φ around the Dirac point. The Berry connection winds around the Dirac point in opposite direction, and the direction of rotation depends on the gauge. We can see from Eq. (2.66) that in the north gauge, the Berry connection winds anti-clockwise around the Dirac point K and clockwise around K' which is consistent with Fig. 2.7.(a). The Berry connection diverges at the Dirac point, which is due to the fact that the Dirac point are degeneracy points between the conductance and valence band which means that the Berry connection is ill-defined at the Dirac points.

It is interesting to calculate the Berry phase around a path in momentum space close to the Dirac points. The Berry phase $\gamma(C)$ corresponding to the path C around the Dirac point ξ has the expression :

$$\gamma_\xi(C) = \int_C d\mathbf{q}.\boldsymbol{\mathcal{A}}_\xi(\mathbf{q}) = \pm\frac{1}{2}\int_C d\mathbf{q}.\nabla_{\mathbf{q}}\varphi_{\mathbf{q}} = \pm\frac{\xi}{2}\int_C d\varphi, \tag{2.70}$$

where the ± sign depends on the chosen gauge. Therefore, if the path encloses the Dirac point, the angle ϕ runs from 0 to 2π around the equator of the Bloch sphere, which gives a Berry phase of :

$$\gamma_\xi(C) = \pm\xi\pi, \tag{2.71}$$

whereas if it doesn't encloses the Dirac point we have $\gamma_\xi(C) = 0$. The Berry phase has opposite sign in both valleys, however, the sign depends on the gauge. The gauge freedom implies that the Berry phase is defined modulo 2π [71].

This Berry phase has a topological origin, because its value doesn't depend on the shape of the path, but rather on the presence or the absence of a Dirac point inside the loop. This topological property is named winding number, because it corresponds to the phase of the wavefunction accumulated when winding around a Dirac point. Due to chiral symmetry, a path in the Brillouin zone is restricted to the equator of the Bloch sphere, and the angle spanned by the vector $\mathbf{d}(\mathbf{k})$ is 0 if the path doesn't wind around the origin of the Bloch sphere or 2π if it winds around the origin. The winding number in graphene is at the origin of a zero-energy edge state linking both valleys [35]. In a ribbon

of graphene, this winding number can also be expressed as the zak phase of a closed line in the Brillouin zone characterized by a fixed momentum $k_\parallel$ parallel to the boundary [72] and expresses the presence or absence of an edge state at momentum $k_\parallel$.

When making a circle in two-dimensions enclosing a Dirac point, the electron acquires a phase of $\pm\pi$ independently to the shape of the path. This phase is analogous to the π phase acquired by an electron under a 2π rotation in real space. If we consider a path enclosing the two Dirac points, the total phase vanishes because the Dirac points have opposite velocities. Such a property is related to the Chern number that vanishes in the case of graphene.

Because graphene has both time-reversal and space inversion symmetry, the Berry curvature vanishes everywhere in the Brillouin zone. However, because the expression for the Berry phase can be expressed as the flux of the Berry curvature through the surface enclosed by the path, there must be a non-zero flux at the Dirac points. The Berry curvature of graphene can thus be expressed as :

$$\mathcal{F}^{-}_{xy}(\mathbf{k}) = \pm\pi(\delta(\mathbf{k}-\mathbf{K}) - \delta(\mathbf{k}-\mathbf{K}')), \tag{2.72}$$

which gives us the correct expression for the Berry phase (2.71) around a Dirac point. The Dirac points are degeneracy points between the valence and conduction bands and act therefore as source and sink of Berry curvature. Each Dirac point carries therefore a topological charge $\pm 1/2$, and the Berry connection is analogous to the field generated by a magnetic monopole located at the Dirac points [73, 71] in two dimensions.

3.5 Semenoff insulator

In the case of a Semenoff insulator, the second neighbour hopping are set to zero ($t_2 = 0$), and thus the presence of magnetic fluxes doesn't affect the electronic properties. In that case, time-reversal symmetry is present, however, due to the non-vanishing on-site potential (Semenoff mass), space-inversion is broken. In a Semenoff insulator, the sign of the mass is identical in both valleys and is equal to M_S. The image of a circle in $\mathbf{q}$-space centered on the Dirac point is a circle on the Bloch sphere at latitude θ such that $\cos\theta_{\mathbf{q}} = M_S/\sqrt{M_S^2+q^2}$. For a Semenoff mass with positive sign, the vector $\mathbf{d}(\mathbf{q})$ reaches the north pole $\theta_{\mathbf{q}} = 0$ at the Dirac points, but never reaches the south pole. Therefore, for a positive mass, we only need the expression of the Berry connection in the north pole gauge over the Brillouin zone.

Fig. 2.7.(b) shows the Berry connection vector field and the Berry curvature over the Brillouin zone calculated using the north pole gauge (2.37) for a Semenoff mass $M_S = 0.3t$. The Berry curvature for a Semenoff insulator was obtained analytically in [74]. We see that the Berry connection winds around the Dirac points with opposite direction, counter-clockwise in the valley K and clockwise in valley K'. Because the system is time-reversal symmetric, the Berry curvature has opposite sign in both valleys. The Berry curvature is located mainly around the Dirac points. When the Berry connection winds clockwise, the Berry curvature is negative, and inversely.

The Berry connection around the Dirac point ξ in the north pole gauge simplifies to :

$$\boldsymbol{\mathcal{A}}^N_\xi(\mathbf{q}) = \sin^2\left(\frac{\theta_{\mathbf{q}}}{2}\right)\nabla_{\mathbf{q}}\varphi_{\mathbf{q}}, = \frac{\xi}{2q}\left(1 - \frac{M_S}{\sqrt{q^2+M_S^2}}\right)\mathbf{e}_\varphi = \mathcal{A}_\varphi \mathbf{e}_\varphi, \tag{2.73}$$

where we have used the expression of the vector $\mathbf{d}_\xi(\mathbf{k})$ given in Eq. (2.28) and $\nabla\phi_{\mathbf{q}} = 1/q\mathbf{e}_\varphi$. At the Dirac points, the Berry connection vanishes which is consistent with the fact that

the phase of the wavefunction is zero at the Dirac point. Using polar coordinates (q, ϕ), we find that the Berry curvature equals :

$$\mathcal{F}^-_{xy}(\mathbf{q}) = \frac{1}{q}\frac{\partial(q\mathcal{A}_\varphi)}{\partial q} = -\xi\frac{M_S}{2}(q^2 + M_S^2)^{-3/2}. \tag{2.74}$$

in both gauges. Because the Dirac points are related by time-reversal symmetry, the Berry curvature has opposite sign in both valleys. The Berry curvature is maximal at the Dirac point and decreases away from it. The Berry curvature at a Dirac point equals $\mathcal{F}^-_{xy}(0) = -\xi M_S^2/2$.

We have seen that the Chern number is defined as the integral of the Berry curvature over the whole compact base space, namely the Brillouin zone. Although it is not mathematically exact, it is interesting to evaluate the Chern number c^-_ξ of the valence band carried by the Dirac point K_ξ :

$$c^-_\xi = \frac{1}{2\pi}\int_{\mathbb{R}^2} dS\mathcal{F}^-_{xy}(\mathbf{q}) \tag{2.75}$$

$$= \frac{1}{2\pi}\int_0^{2\pi} d\varphi \int_0^\infty dq\frac{\partial(q\mathcal{A}_\varphi)}{\partial q} \tag{2.76}$$

$$= \xi\frac{1}{2}\text{sign}(M_S), \tag{2.77}$$

Therefore, each Dirac point carries a Chern number 1/2 of opposite sign in both valleys whose sign depends on the sign of the mass term. Thus, when integrating over the Brillouin zone, the contribution from the two points vanishes and the Chern number is zero.

3.6 Haldane insulator

We name Haldane insulator a phase of the Haldane model where the Semenoff mass is set to zero ($M_S = 0$). In that phase, the system is invariant under space inversion, however due to non-vanishing magnetic fluxes ($t_2 \neq 0$), time-reversal symmetry is broken. In that case, the masses at the dirac points have opposite sign :

$$M_\xi = \xi 3\sqrt{3}t_2\sin(\phi) = \xi M_H, \tag{2.78}$$

such that $M_+ = -M_- \equiv M_H$, where $M_H = 3\sqrt{3}t_2\sin(\phi)$ is the Haldane mass defined as the mass in valley K. The sign of the masses at the Dirac point is given by the value of ϕ. For simplicity, we restrict ϕ to the interval $[-\pi, \pi]$. We have :

$$\phi \in [-\pi, 0] \quad \Rightarrow \quad M_+ < 0 \quad \text{and} \quad M_- > 0 \tag{2.79}$$

$$\phi \in [0, \pi] \quad \Rightarrow \quad M_+ > 0 \quad \text{and} \quad M_- < 0 \tag{2.80}$$

Because both poles are reached, one needs to use the two gauges defined by Eqs. (2.37) and (2.38). Fig. 2.8 shows the Berry connection and curvature over the Brillouin zone in both gauges for a flux of $\phi = \pi/2$ which corresponds to a positive Haldane mass M_H. In that case, the north pole is reached at K, while the south pole is reached at K'. We can see that in the north gauge [Fig. 2.8.(a)], the Berry connection diverges around K' while it vanishes at K which is consistent with the fact that the Berry connection is ill-defined at the Dirac point K'. The Berry connection winds counter-clockwise around K. In the

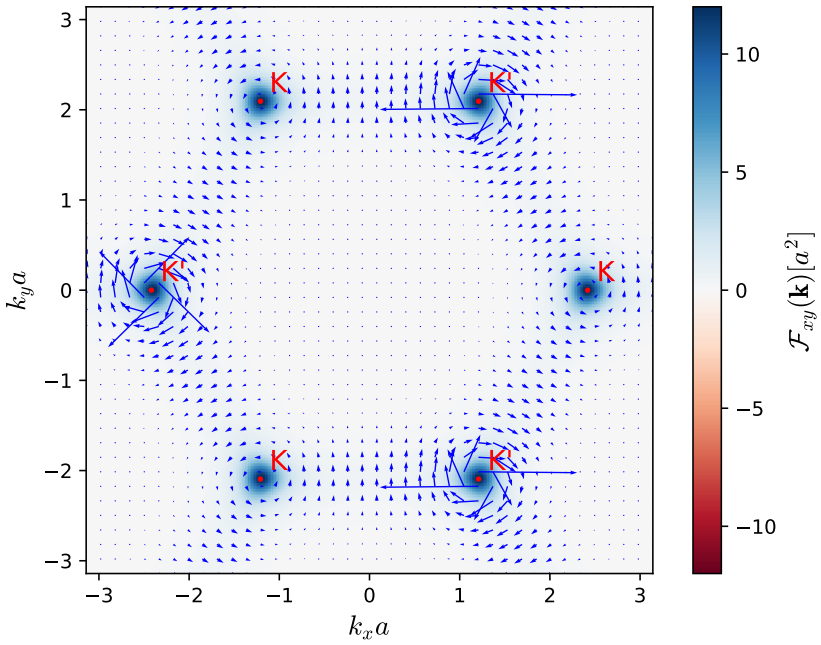

(a)

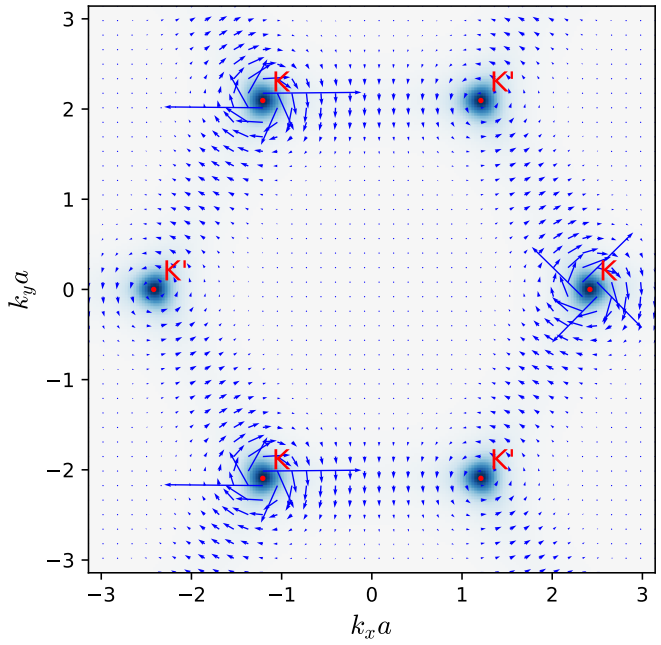

(b)

Figure 2.8 – Berry connection (vector field) and Berry curvature of the Haldane model for a Haldane mass $t_2 = 0.1/\sqrt{3}t$, $\phi = \pi/2$ and $M_S = 0$ over the Brillouin zone plotted using the expression of the Berry connection at : (a) the north pole (2.37) and (b) at the south pole (2.38). In the north pole gauge, the Berry phase winds anti-clockwise around the Dirac point $\mathbf{K}$, while it diverges at $\mathbf{K}'$. In contrary, in the south pole gauge, the Berry connection winds anti-clockwise around $\mathbf{K}'$ and diverges at $\mathbf{K}$. Thus, the Berry connection winds in the same direction around both Dirac points.

south gauge [Fig. 2.8.(a)], the scenario is opposite, but the Berry connection winds also counter-clockwise around K'. In the two gauges, the Berry connection around the Dirac

points is given by :

$$\boldsymbol{\mathcal{A}}_K^N(\mathbf{q}) = \sin^2\left(\frac{\theta_\mathbf{q}}{2}\right)\mathbf{e}_\varphi = \frac{1}{2q}\left(1 - \frac{M_H}{\sqrt{q^2 + M_S^2}}\right)\mathbf{e}_\varphi, \tag{2.81}$$

$$\boldsymbol{\mathcal{A}}_{K'}^S(\mathbf{q}) = \cos^2\left(\frac{\theta_\mathbf{q}}{2}\right)\mathbf{e}_\varphi = \frac{1}{2q}\left(1 - \frac{M_H}{\sqrt{q^2 + M_S^2}}\right)\mathbf{e}_\varphi, \tag{2.82}$$

which means that both Dirac point wind in the same direction in their own gauge and therefore add up when considering the total circulation of the Berry connection. If we reverse the sign of the flux, then the sign of the masses is reversed and so is the direction of rotation. The Berry curvature has the same value in both valleys, namely :

$$\mathcal{F}_{xy}^-(\mathbf{q}) = \frac{M_H}{2}(q^2 + M_H^2)^{-3/2}. \tag{2.83}$$

As we have done in the previous section, although it is not mathematically exact, we calculate the Chern number carried by a Dirac point :

$$c_\xi^- = \frac{1}{2}\text{sign}(M_H) \tag{2.84}$$

Thus, each Dirac point carries the Chern number 1/2, which leads to a total Chern number $C^- = +1$ in the case of a flux $\phi = \pi/2$. This is consistent with the value of the Chern number of Fig. 2.6.

4 Edge states

Topological insulators are classified according to their bulk topological invariants and a characteristic feature of a non-trivial topology is the presence of edge states at the boundary of the material. The edge states are topological solitons that live at the boundary between two topologically distinct regions. The first example of a solitonic edge state was introduced by Jackiw and Rebbi in the context of field theory in one-dimension [75]. Such a solitonic state has zero-energy and exists at the boundary between two regions with opposite mass scalar field. At the boundary, the sign of the mass changes and therefore closes locally the mass gap. In condensed matter, one-dimensional solitonic states exist in the Su, Shrieffer and Hegger model used to describe polyacetylene [76]. This model consists of a dimerized chain of atoms and a bound state exist at a the interface between two phases with a different dimerization scheme. In general, if the total space has dimension D, then the interface soliton has dimension D-1.

In two-dimensional topological insulators, one-dimensional metallic states exist at the interface between two regions with different topological invariants. When no symmetry is present, the topological invariant is the Chern number [65]. The vacuum is considered as a topologically trivial region, so the number of edge states at the boundary is equal to the topological invariant of the filled bands. The edge states are robust to moderate disorder because the topological invariant can only change if the bulk band gap closes. These edge states are related to the bulk topological invariant by the bulk-boundary correspondence, which is robust under disorder and certain types of interactions [37].

In the quantum Hall effect, the relation between the quantized Hall conductance and the presence of edge states was first shown by Halperin [56]. Thereafter, the correspondence between the bulk topological invariant and the number of edge states was proved

by Hatsugai [33, 34]. The edge states are chiral in the sense that they propagate along one-direction at the boundary. Backscattering is forbidden because there exist no state propagating in the opposite direction. In the quantum Hall effect, the number of edge states is proportional to the number of filled Landau levels.

The topology of the Haldane model is characterized by its Chern number. The Haldane model possesses one chiral edge state whose direction of propagation is dictated by the sign of the Chern number. The presence of such a metallic state can be understood by the fact that the sign of the mass is inverted in one valley and thus the gap has to close at the boundary. In this section, we wish to study the properties of the edge state of the Haldane model in relation with the bulk topological properties that we studied in the last section.

In Sec. 4.1, we calculate numerically the dispersion relation of a ribbon of the Haldane model in the tight-binding formalism. In Sec. 4.2, we calculate the dispersion relation of the edge states in the Haldane gap.

4.1 Tight-binding ribbon

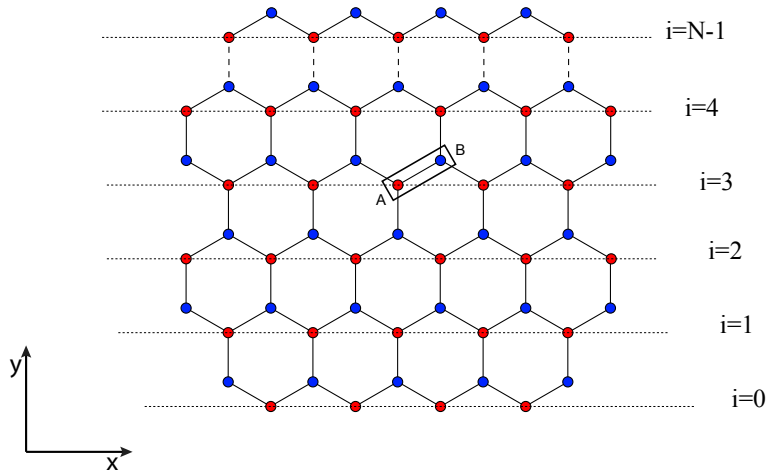

Figure 2.9 – Geometry of the zig-zag ribbon. The ribbon is infinite along the x direction and is made of N unit cells along y labelled by the index n. The edges are located at $y = 0$ and $y = N\frac{3a}{2}$

We consider a ribbon infinite along x and with boundaries at $y = 0$ and $y = W$ as shown in Fig. 2.9. We separate the ribbon in several layers along y labelled by the index n. In this geometry considered, because of the shape of the edges, the ribbon is called a zig-zag ribbon. The boundary conditions consists in cancelling the wavefunction at the missing spots at the edges namely $u_B(i = -1) = 0$ and $u_A(i = N) = 0$.

We consider the Haldane Hamiltonian in real space of Eq. (2.19) and operate the Fourier transform of the operators $a(\mathbf{r})$ and $b(\mathbf{r})$ along x such that :

$$a(\mathbf{r}) = \frac{1}{\sqrt{2\pi N}} \sum_{k_x} a_i(k_x) e^{-ik_x x} \quad \text{and,} \quad b(\mathbf{r}) = \frac{1}{\sqrt{2\pi N}} \sum_{k_x} b_i(k_x) e^{-ik_x x}, \tag{2.85}$$

where i labels the position of a site along the y direction, such that $r_{Ay} = i\frac{3a}{2}\mathbf{e}_y$ with $i \in \{0, N-1\}$ where N is the number of sites of the ribbon along y (see Fig. 2.9), and k_x

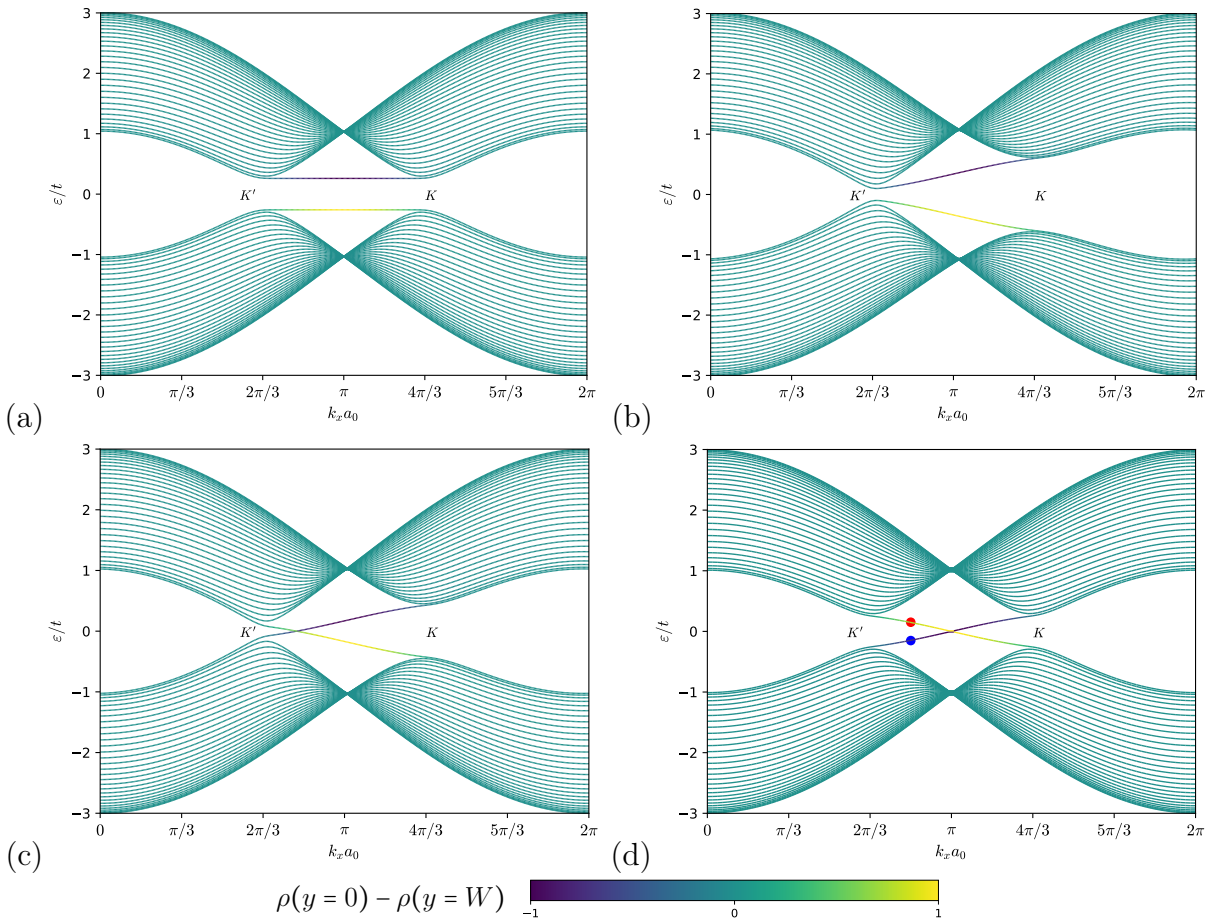

Figure 2.10 – Dispersion relation of tight-binding Haldane ribbons with $N = 30$ sites for different parameters indicated by the red dots in the phase diagram in Fig. 2.6. The phase is $\phi = \pi/2$ for all the plots. (a) $t_2 = 0$ and $M_S = 3\sqrt{3}\times 0.05t$. (b) $t_2 = 0.05t$ and $M_S = 4\sqrt{3}t_2$. (c) $t_2 = 0.05t$ and $M_S = 2\sqrt{3}t_2$. (d) $t_2 = 0.05t$ and $M_S = 0$. The colorbar represent the electronic probability density difference between the edge $\rho(y = 0) - \rho(y = W)$. A state colored in yellow is located at $y = 0$, while a state colored in indigo is located at $y = W$. Two edge states link the valleys **K** and **K**'. These edge states cross the gap in (c) and (d), and characterize a non-trivial topological phase. These plots represent a topological phase transition between a Semenoff insulator with $C = 0$ in (a) and a Haldane insulator with $C = +1$ in (d). The transition happens at $M_S = 3\sqrt{3}t_2$. The mass $M_- = M_S - 3\sqrt{3}t_2\sin(\phi)$ in the valley **K′** closes and reopens while changing of sign along the transition. The dots in (d) correspond to the edge state whose wavefunction is plotted on Fig. 2.11. The periodicity of the lattice along x is $a_0 = \sqrt{3}a$, so we have $k_x a_0 = \sqrt{3}k_x a$.

is the longitudinal momentum. Replacing expression (2.85) in Eq. (2.19), we obtain :

$$\begin{aligned}\mathcal{H} = t\sum_{k_x,i}\left[b_i^\dagger(k_x)a_i(k_x)2\cos\left(\frac{\sqrt{3}a}{2}k_x\right) + b_{i-1}^\dagger a_i + H.c.\right] \\ + \sum_{k_x,i}\left[a_i^\dagger(k_x)a_i(k_x)\left(\frac{M}{2} + t_2\cos(\sqrt{3}ak_x + \phi)\right) + a_{i+1}^\dagger(k_x)a_i(k_x)2t_2\cos\left(\frac{\sqrt{3}a}{2}k_x - \phi\right) + H.c.\right] \\ + \sum_{k_x,i}\left[b_i^\dagger(k_x)b_i(k_x)\left(-\frac{M}{2} + t_2\cos(\sqrt{3}ak_x - \phi)\right) + b_{i+1}^\dagger(k_x)b_i(k_x)2t_2\cos\left(\frac{\sqrt{3}a}{2}k_x + \phi\right) + H.c.\right],\end{aligned} \tag{2.86}$$

which can be expressed as :

$$\mathcal{H} = \sum_{k_x} \sum_{\alpha\beta} \sum_{ij} \Psi_i^{\dagger\alpha}(k_x) H_{ij}^{\alpha\beta}(k_x) \Psi_j^{\beta}(k_x), \tag{2.87}$$

where $\alpha, \beta = \{A, B\}$ is the sublattice index and $i, j \in \{0, N-1\}$. For a ribbon with N unit cells along the transverse direction, the Hamiltonian for each k_x has size $2N \times 2N$ because there are two sites per unit cell. The dispersion relation is obtained by diagonalizing the Hamiltonian numerically $H_{ij}^{\alpha\beta}(k_x)$ for each k_x in the Brillouin zone, and the boundary condition is automatically imposed because there is no hopping at the sites $n = -1$ and $n = N$. Fig. 2.10 shows the dispersion relation of Haldane ribbons for different sets of parameters. The color coding represents the difference of the density of probability of the electron wavefunction at the edges such that :

$$\rho(y = 0) = |u_A(i = 0)|^2 + |u_B(i = 0)|^2 \quad \text{and,} \tag{2.88}$$

$$\rho(y = W) = |u_A(i = N - 1)|^2 + |u_B(i = N - 1)|^2. \tag{2.89}$$

The states in green correspond to the bulk states, the yellow states are localized at the edge $y = 0$ while the indigo states are localized at the edge $y = W$. The dispersion relation of a ribbon is similar to the projection of the bulk dispersion relation on the axis of the longitudinal momentum (except for the presence of edge states). In a zig-zag ribbon the two valleys are projected at different longitudinal momentum k_x (see Fig. 1.2.(b)) and are located at $K'_x = 2\pi/3\sqrt{3}a$ and $K_x = 4\pi/3\sqrt{3}a$. Because the lattice has periodicity $a_0 = \sqrt{3}a$ along x, the Brillouin zone has periodicity $2\pi/a_0$. In the case of an armchair ribbon (edges along x) where k_y is a good quantum number, the two valleys project at the same momentum $K_y = 0$. We will not study this case, but the properties of the edge states are analogous (chirality, velocity).

In Fig. 2.10.(a), the mass is a purely Semenoff mass, and is identical in both valleys. We observe two flat states linking both valleys. Because these states don't appear in the bulk dispersion relation,we deduce that they are edge states. These edge states are analogous to the flat zero-energy states linking both valleys in graphene as we have seen in Sec. 3.4. They have a topological origin in the sense that the Berry phase around the Dirac points is opposite in both valleys, but their energy is non-zero because chiral symmetry is broken. These edge states don't cross the gap so they are not edge states that characterize a topological insulator.

In Fig. 2.10.(b), we have added a small coupling between next-nearest neighbours with a phase, which gives rise to a Haldane mass term. The masses in the valleys K and K' are different, however, because the Haldane mass is smaller than the Semenoff mass, the sign of the mass is identical in the valleys. Because there is no band inversion, the model is topologically trivial and doesn't possess metallic edge states in the gap.

In Fig. 2.10.(c), we can see that upon increasing second neighbour couplings, the Haldane mass increases and becomes more important than the Semenoff mass, which leads a different mass sign in the valleys. In that case, there is a band inversion and we can see that the edge state crosses the gap which signals a non-trivial topology. Finally, in Fig. 2.10.(d), the Semenoff mass is set to zero, and the mass is opposite in the valleys. In that case, the system is invariant under space inversion, and the edge states crosses the gap. This phase corresponds to the Haldane insulator with Chern number $C^- = +1$.

Fig. 2.11 shows the square modulus of the wavefunction corresponding to the edge states at energy and momentum indicated by the markers on Fig. 2.10.(d), which corresponds to the Haldane insulator. The group velocity of the edge state along the direction

x is given by :

$$v_x = \frac{1}{\hbar}\frac{\partial E(k_x)}{\partial k_x}, \tag{2.90}$$

The red circle on Fig. 2.10.(d) corresponds to the wavefunction of Fig. 2.11.(a). We can see that it is located at the lower edge $y = 0$. According to (2.90), the dispersion relation of the edge state indicates that it propagates in the direction $-x$. The blue circle on Fig. 2.10.(d) corresponds to the wavefunction of Fig. 2.11.(b) and is located at the upper edge $y = W$. This edge state propagate along the direction $+x$. We conclude from this analysis that for a Haldane insulator with Chern number +1, the edge state rotates clockwise along the boundary of the sample, while for a Chern number −1, the edge states rotates counterclockwise.

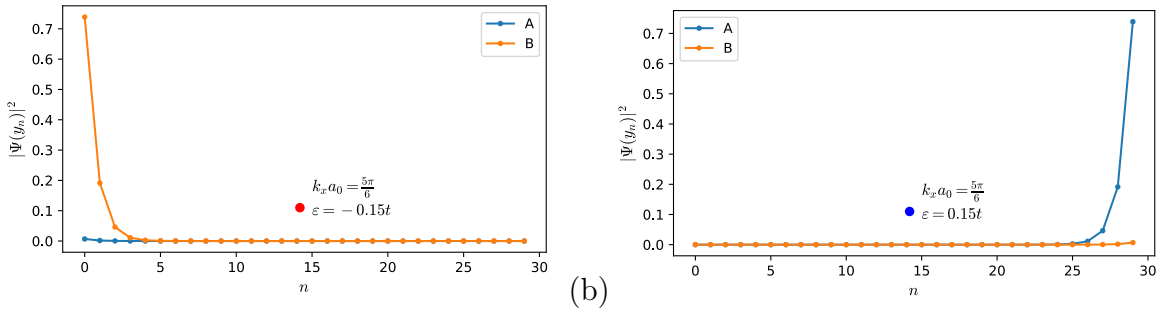

(a) (b)

Figure 2.11 – Square modulus of the wavefunctions of the edge states of the Haldane model with parameters $\phi = \pi/2$, $t_2 = 0.05t$ and $M_S = 0$ at momentum $k_x = 5\pi/6$. The absissa corresponds to the index of the site along y such that $y_n = n\frac{3a}{2}$ (see Fig. 2.9). The color indicates the wavefunction over sites A and B. (a) Edge state corresponding to the red dot on Fig. 2.10.(d). (b) Edge state corresponding to the blue dot on Fig. 2.10.(d). The edge states have opposite group velocity and are located at the opposite edge, which indicates that they are chiral. We can see that the edge state on the lower edge has a weight mainly on lattice B, while the upper edge has a weight mainly on lattice A.

In the next section, we compare this analysis with the case of a ribbon modelled by the Dirac equation with an inverted Haldane mass at the interface with a Semenoff insulator.

4.2 Ribbon in the Dirac equation

Another method to calculate the spectrum of a ribbon is to model the dispersion relation using the Dirac equation for the Haldane model and to choose appropriate boundary conditions. There exists several types of boundary conditions for the Dirac equation that can be classified according to their symmetries [77]. In the case of graphene, zero-energy edge states can exist depending on the orientation of the edge [78]. In the microscopic description of the honeycomb lattice, the boundary condition consists in setting the wavefunction to zero at the missing sites. However, there exist other types of boundary condition, such as the one introduced by Berry and Mondragon [79]. This boundary condition consists in confining the Dirac fermions by an infinite mass potential. In that case, the vacuum is considered as a Semenoff insulator with infinite gap, which corresponds to a topologically trivial material. We expect therefore to observe edge states at the boundary of the Haldane ribbon.

For a zig-zag ribbon with boundaries along y at $y = 0$ and $y = W$, the Berry-Mondragon boundary conditions can be expressed as a restriction on the spinors :

$$\Psi(y = W) = -\sigma_x \Psi(y = W) \tag{2.91}$$
$$\Psi(y = 0) = \sigma_x \Psi(y = 0), \tag{2.92}$$

which is consistent with [78].

In a ribbon infinite along x, the Dirac equation (for a Haldane ribbon) has the expression :

$$((\tau_z \sigma_x k_x - i\sigma_y \partial_y) + M_H \sigma_z \tau_z)\Psi(y) = \varepsilon \Psi(y), \tag{2.93}$$

where we have considered a Haldane mass $M_H \sigma_z \tau_z$ with opposite sign in the valleys and we have set $\hbar v = 1$. This model has a Chern number $C^- = \text{sign}(M_H)$. To obtain the dispersion relation of the edge states, we consider the edges separately. For the upper edge, we consider that the Haldane region is located at $y < 0$ and apply the boundary condition (2.91) at $y = 0$, while for the lower edge, we consider the Haldane region at $y > 0$ and apply the boundary condition (2.92) at $y = 0$.

Upper edge We first consider the upper edge at $y = 0$, such that the Haldane insulator is located at $y < 0$. In a first attempt, we look for the existence of a state located in the gap at $\varepsilon = k_x = 0$. The Dirac equation simplifies to :

$$i\sigma_y \partial_y \Psi(y) = M_H \sigma_z \tau_z \Psi(y), \tag{2.94}$$
$$\Rightarrow \quad \partial_y \Psi(y) = M_H \sigma_x \tau_z \Psi(y) \tag{2.95}$$

For the upper edge located at $y = 0$, the boundary condition is $\Psi(y = 0) = -\sigma_x \Psi(y = 0)$ which implies that $\Psi(y)$ must be an eigenstate of σ_x. Thus, we find that an edge state must obey the equation :

$$\partial_y \Psi(y) = -M_H \tau_z \Psi(y). \tag{2.96}$$

Therefore, a bounded state such that $\Psi(y \to -\infty) = 0$ exists only in the valley $\xi = -\text{sign}(M_H)$ with a wavefunction that is an eigenstate of σ_x with eigenvalue -1 :

$$\Psi(y) = c \begin{pmatrix} 1 \\ -1 \end{pmatrix} e^{|M_H| y}, \tag{2.97}$$

where c is a normalization factor. If we insert this expression for $\Psi(y)$ in Eq. (2.93), using $\tau_z \sigma_x \Psi(y) = \text{sign}(M_H)\Psi(y)$, we find that $\Psi(y)$ is still an eigenstate, which leads to the dispersion relation :

$$\varepsilon = \text{sign}(M_H) \hbar v k_x, \tag{2.98}$$

where we have reinserted $\hbar v$. For a positive Haldane mass, this edge state is located at the upper edge and has a positive velocity along x, which is consistent with the case of a tight-binding ribbon. Thus, for a Haldane model with Chern number +1, the edge state exists only in the valley K' because the band inversion occurs in the valley K'.

Lower edge To study the lower edge, we consider that the Haldane region is located at $y > 0$. For $\varepsilon = k_x = 0$, Eq. (2.95) still applies, but we apply the boundary condition $\Psi(y = 0) = \sigma_x \Psi(y = 0)$, such that we have the equation for the edge state :

$$\partial_y \Psi(y) = M_H \tau_z \Psi(y). \tag{2.99}$$

This time, the bounded state must exist at $y > 0$, which is satisfied only in the valley $\tau_z = -\text{sign}(M_H)$, and the wavefunction is the eigenstate of σ_x with eigenvalue +1 :

$$\Psi(y) = c \begin{pmatrix} 1 \\ 1 \end{pmatrix} e^{-|M_H|y}, \tag{2.100}$$

Reinserting this expression in Eq. (2.93), with $\tau_z \sigma_x \Psi(y) = -\Psi(y)$ we find that the dispersion is :

$$\varepsilon = -\text{sign}(M_H)\hbar v k_x, \tag{2.101}$$

This edge state located at the lower edge has a negative velocity along x and lives in the valley $\mathbf{K}'$.

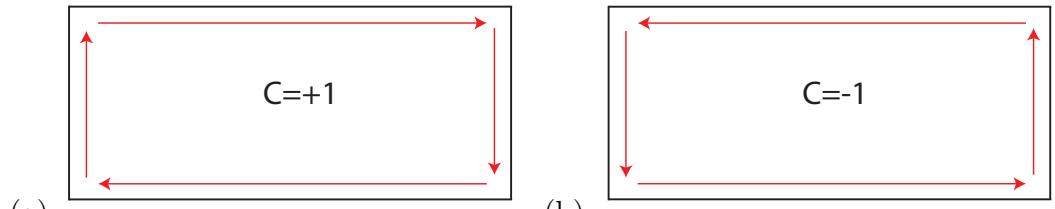

(a) (b)

Figure 2.12 – Direction of propagation of the edge states around a sample in the Haldane phase with Chern number (a) $C^- = +1$ and (b) $C^- = -1$. For a Chern number +1, the edge state rotates clockwise, while if the Chern number is −1, the rotation is anticlockwise.

We have studied the edge states of the Haldane ribbon modelled by the massive Dirac equation with opposite mass sign in the different valleys. The boundary conditions are modelled as an interface with a Semenoff insulator which corresponds to confinement by an infinite mass gap. When the Semenoff mass is positive, the Semenoff insulator is topologically equivalent to the vacuum. We find that an edge state exists in the valley with negative mass sign, which expresses the fact that the gap must close at the boundary between two topologically distinct regions. If the Haldane mass M_H is positive, the sign of the mass is negative in the valley K' and the edge state is polarized in the valley K'. In that case, according to Eq. (2.57), the Chern number of the valence band is $C^- = +1$ and the edge state rotates clockwise. If the Haldane mass is negative, the edge state is polarized in K, the Chern number is −1 and the edge state rotates anti-clockwise. This analysis is coherent with the direction of propagation of the edge state found by diagonalizing numerically ribbons.

From this analysis, we conclude that the two types of boundary conditions give similar physical results. The tight-binding boundary conditions consists in setting to zero the wavefunction on one sublattice for an edge and on the other sublattice on the opposite edge. The Berry-Mondragon boundary conditions impose a restriction on the spinor at the edge, and thus treats both sublattice on equal foot. The wavefunction has approximately the same weight on both sublattices while in a tight-binding ribbon the wavefunction is polarized on one sublattice. In the next chapter, we will use these two types of boundary conditions depending on the procedure used to obtain the dispersion relation of the edge states.

5 Conclusion

In this chapter, we have investigated the geometrical and topological properties of the Haldane model. In crystalline materials, due to Bloch theorem, one can label the states according to their quasi-momentum. This quasi-momentum belongs to the Brillouin zone which is periodic in reciprocal space. The Brillouin zone is a manifold that is topologically equivalent to a two-dimensional torus. To each point of this torus, from the expression of the Bloch states, it is possible to define the Berry connection and the Berry curvature in $\mathbf{k}$-space. These objects define a geometrical structure for the Bloch wavefunctions in the Brillouin zone. They are analogous to a gauge potential and a gauge field which are embedded in the mathematical field of fiber bundles. Besides their geometrical structure, fiber bundles also possess a topological structure. Topological insulators are materials that exhibit a Hall conductance quantized in units of a topological invariant defined for the fiber bundle of the Bloch Hamiltonian. Depending on the symmetries of the Hamiltonian, the topological invariant can be either the Chern number (when time-reversal symmetry is broken) or a $\mathbb{Z}_2$ invariant when time-reversal symmetry is present. The first example of a topological insulator is the quantum Hall effect, which however necessitates the application of an external magnetic field and one cannot apply easily the Bloch theorem.

We have analyzed the Haldane model, a model based on the graphene lattice where time-reversal symmetry is broken by the introduction of periodic magnetic fluxes with the period of the lattice. The valence band of this model possess a non-zero Chern number, and there exist a chiral edge state propagating around the sample. Because there are two sites per unit cell, the wavefunction of the electrons in the bands are spinors labelled by their quasi-momentum. The state of a two-level system can be described as a point on the Bloch sphere. The Bloch Hamiltonian characterizes therefore a mapping from the Brillouin zone to the Bloch sphere. In the Haldane model, the mass gap has opposite sign in both valley and the poles of the Bloch sphere are reached at the Dirac points, which signals that the phase of the Bloch wavefunction has a non-trivial winding around the whole Bloch sphere when the quasi-momentum spans the Brillouin zone.

We have then studied the edge states of this model. When the valence band is filled and the conduction band is empty, the Fermi level is in the gap and the material is an insulator. Because the mass gap is inverted in one valley, the gap has to close at the boundary and there are edge states that conduct current. Depending on the flux pattern in real space, the filled band can have a Chern number $+1$ or -1 and the edge states rotates clockwise or anti-clockwise around the sample. We have obtained the dispersion relation of the edge states in a ribbon geometry. First, we have diagonalized numerically a tight-binding ribbon, and second, we have considered the Dirac equation with boundary conditions corresponding to an interface with the vacuum as a trivial insulator. From these two procedure, we have obtained the direction of propagation of the edge states as a function of the sign of the Chern number.

Chapter 3

Floquet theory description of irradiated graphene

In crystalline materials, the eigenstates are labelled by their quasi-momentum. As we have seen in the previous chapter, the non-trivial winding of the wavefunction in the Brillouin zone characterizes topological phases like the Haldane insulator. However, the topological properties are defined for the bulk of the material and few external parameters allow to tune the topological properties. A topological phase transition happens only by closing the gap which requires fine tuning of several parameters. Driving the material with a periodic excitation leads to additional knobs that can be used to induce non-trivial topological properties in out-of-equilibrium matter. Tuning the parameters of the driving can lead to topological phases which do not exist at equilibrium. Such topological insulators are dubbed Floquet topological insulators [68] because the description of the bands is often studied within the Floquet formalism.

First, several studies have shown that irradiating graphene with circularly polarized electromagnetic wave at high-frequency compared to the bandwidth of graphene generates a Haldane mass at the Dirac points, which turns graphene into the quantum anomalous Hall phase [10, 80]. Second, it has been proven that driving a trivial two-band semiconductor with a frequency on resonance with the valence and conduction band generates a band inversion which leads to a non-zero Chern number of the bands [11]. Experimentally, signatures of Floquet-Bloch states have been observed at the surface of an irradiated topological insulator [81], and in photonic crystals [82].

When the Floquet band structure is gapped, it can be described by an effective time-independent Hamiltonian. It is possible to classify topologically this effective Hamiltonian according to the usual classification scheme of static Hamiltonians, and to have bands with non-zero topological invariants [83]. However, it was realized that some quasi-energy bands have a vanishing Chern number, while the material still possesses edge states crossing the gaps [83, 84]. This indicates that the bulk-edge correspondence works differently than at equilibrium. This fact led to an important research activity aiming at characterizing the topology of driven Hamiltonian beyond the effective static description [85, 86, 87, 88]. The topological characterization of the quasi-energy bands is not encoded in the Hamiltonian, but rather in the time-evolution operator $U(\mathbf{k}, t)$ and its winding during one period of the driving [85]. The resulting topological invariant is associated to a gap in the quasi-energy spectrum.

In Sec. 1, we introduce the Floquet theory for time-periodic Hamiltonian, deriving an expression for the Floquet Hamiltonian and the effective Hamiltonian at high frequency.

In Sec. 2, we apply these tools to the lattice description of graphene and observe the edge states characteristic of a Floquet topological insulator. In Sec. 3, we consider the low-energy description of graphene by the Dirac equation where the driving creates a set of nested gaps with associated edge states.

1 Floquet formalism

The electronic properties of the electrons in a crystal are encoded in the band structure. According to the Bloch theorem, the electrons are labelled by their quasi-momentum defined in a compact Brillouin zone. When the electrons are subjected to a periodic driving, energy is not a good quantum number anymore. Instead, according to Floquet theorem, each eigenstate is characterized by its quasi-energy, which lives inside a Floquet zone. Analogously with the Brillouin zone, the Floquet zone is periodic in quasi-energy and is therefore compact. If the lattice has space dimension D, the eigenstates live in the Floquet-Bloch space which has dimension D+1 [89], including the space of time-periodic and space-periodic functions. In this space, it is possible to define an effective Floquet-Bloch Hamiltonian, which can eventually have a non-trivial topology.

The presence of driving introduces several parameters that allow to have a more detailled tunability of the Floquet-Bloch band structure. In the high frequency-regime, the direct transitions are forbidden. It is thus possible to define an effective Hamiltonian for the electrons, which is the usual Bloch Hamiltonian renormalized by virtual photon absorption processes.

In Sec. 1.1, we present the Floquet theorem applied to time-periodic Hamiltonians. In Sec. 1.2, we derive the expression of the Floquet Hamiltonian in the Sambe space of time-periodic functions, while in Sec. 1.3, we derive an expression for the effective Hamiltonian in the case of high-frequency off-resonant driving.

1.1 Floquet theorem

The dynamical properties of a quantum system are encoded in its Hamiltonian. The time evolution of the system is ruled by the Schrödinger equation. If the Hamiltonian is time-independent, the time-evolution of a state with energy E consists in a phase factor $e^{-iEt/\hbar}$. However, when the Hamiltonian depends on the time variable, the time-evolution is usually more complex and there are no stationary states. Floquet theorem is the analogous of Bloch theorem for systems with a time-periodic Hamiltonian. Instead of energies, the quantum states are described by a quasi-energy which describes the "stroboscopic" evolution of the state on time scales larger than the period of the Hamiltonian.

We wish to obtain the eigenstates of a time-periodic Hamiltonian described by the time-dependent Schrödinger equation :

$$i\hbar\partial_t\Psi(t) = H(t)\Psi(t), \tag{3.1}$$

where $H(t+T) = H(t)$ with T the period of the driving. Floquet theorem [90] states that the eigenfunctions of the Schrödinger equation (3.1) can be expressed as [91] :

$$\Psi_\varepsilon(t) = e^{-i\varepsilon t/\hbar}u_\varepsilon(t), \tag{3.2}$$

where ε is the quasi-energy that characterizes the state $\Psi(t)$. This quasi-energy describes the evolution of the system over long time-scales such that a state acquires a phase $e^{-i\varepsilon T/\hbar}$

during one period of the driving. The quasi-energies are periodic with period ω. In analogy with a Bloch state, $u_\varepsilon(t)$ is a time-periodic function called a Floquet state. This function encodes the evolution of the system over short time-scales. Inserting the expression for the states (3.2) into Eq. (3.1) gives us the eigenvalue equation for ε_α :

$$H_F(t)|u_\alpha(t)\rangle = \varepsilon_\alpha|u_\alpha(t)\rangle, \tag{3.3}$$

where we have defined the Floquet Hamiltonian :

$$H_F(t) = H(t) - i\hbar\partial_t, \tag{3.4}$$

and α labels the eigenstates of the Hamiltonian. In the extended space of time-periodic functions, the scalar product is expressed as :

$$\langle\langle u_\alpha|u_\beta\rangle\rangle = \frac{1}{T}\int_0^T dt\langle u_\alpha(t)|u_\beta(t)\rangle, \tag{3.5}$$

and the average value of the operator $O(t)$ is $\langle\langle O(t)\rangle\rangle$.

We can see from Eq. (3.2) that it is always possible to redefine ε and $u(t)$ by the gauge transformation :

$$\varepsilon \to \varepsilon + q\hbar\omega, \tag{3.6a}$$
$$u(t) \to u(t)e^{iq\omega t}. \tag{3.6b}$$

This set of states represents physically equivalent states. Therefore, we can choose a gauge such that ε belongs to a Floquet zone defined by $\varepsilon \in [\varepsilon_0 - \hbar\omega/2, \varepsilon_0 + \hbar\omega/2)$ for any real number ε_0. It is possible to express the evolution operator over one period of driving as :

$$U(T) = e^{-iH_{\text{eff}}T}, \tag{3.7}$$

where H_{eff} is an effective Hamiltonian whose eigenvalues are the quasi-energies.

1.2 Sambe space

Because the Hamiltonian $H(t)$ and the Floquet states $u_\varepsilon(t)$ are periodic in time, it is possible and useful to develop them in Fourier series. We define the Fourier coefficients of the Hamiltonian and of the states as :

$$H(t) = \sum_{n=-\infty}^{\infty} H_n e^{in\omega t}, \tag{3.8}$$

$$u(t) = \sum_{n=-\infty}^{\infty} u_n e^{in\omega t}, \tag{3.9}$$

so that the eigenproblem Eq. (3.3) can be written as :

$$\sum_n (H_{m-n} + n\hbar\omega\delta_{mn}\mathbb{1})u_{\alpha,n} = \varepsilon_\alpha u_{\alpha,m}, \tag{3.10}$$

where $\mathbb{1}$ is the identity in the Hilbert space of the system. This equation is an infinite matrix equation whose eigenvalues are the quasi-energies, and whose eigenstates are composed of the Fourier components of the Floquet state $u_\alpha(t)$. In this representation, a Floquet state belongs to an extended Hilbert space $\mathcal{S} = \mathcal{T} \times \mathcal{H}$ composed of the Hilbert space $\mathcal{H}$ of the Hamiltonian $H(t)$, and the space $\mathcal{T}$ of time-periodic functions. We name

this extended Hilbert space Sambe space [92], and we rewrite Eq. (3.3) in a matrix equation :

$$\tilde{H}_F|\tilde{u}_\alpha\rangle = \varepsilon_\alpha|\tilde{u}_\alpha\rangle, \tag{3.11}$$

where $\tilde{H}_F$ is the Floquet Hamiltonian in Sambe space, and $|\tilde{u}_\alpha\rangle$ is a Floquet state in Sambe space. In matrix form, Eq. (3.11) can be expressed as :

$$\tilde{H}_F = \begin{pmatrix} \ddots & \vdots & \vdots & \vdots & \iddots \\ \cdots & H_0 + (p+1)\hbar\omega & H_1 & H_2 & \cdots \\ \cdots & H_{-1} & H_0 + p\hbar\omega & H_1 & \cdots \\ \cdots & H_{-2} & H_{-1} & H_0 + (p-1)\hbar\omega & \cdots \\ \iddots & \vdots & \vdots & \vdots & \ddots \end{pmatrix} \quad \text{and,} \quad |\tilde{u}_\alpha\rangle = \begin{pmatrix} \vdots \\ |u_{\alpha,p+1}\rangle \\ |u_{\alpha,p}\rangle \\ |u_{\alpha,p-1}\rangle \\ \vdots \end{pmatrix}. \tag{3.12}$$

Therefore, the full Floquet Hamiltonian in Sambe space $\tilde{H}_F$ consists in a set of the bare Hamiltonians H_0 on the diagonal which are "dressed" with p photons and are coupled to each other via the Fourier components H_n with $n \neq 0$ of the driving. We call these dressed Hamiltonians "Floquet replicas" because in absence of driving, those blocks simply duplicate H_0 with a shift $p\hbar\omega$. The quasi-energy spectrum repeats itself with period $\hbar\omega$. The quasi-energies are therefore redundant and one needs only the spectrum in a region of frequency $[-\hbar\omega/2, \hbar\omega/2]$. The first harmonic of the time-dependent Hamiltonian couples two Floquet replicas with a difference of one photon, the second harmonic couples Floquet replicas with a difference of two photons, etc... This Hamiltonian is infinite and in practice one needs to operate a truncation.

Finally, we note that the scalar product (3.5) in Sambe space can be expressed as :

$$\langle\langle u_\alpha|u_\beta\rangle\rangle = \langle\tilde{u}_\alpha|\tilde{u}_\beta\rangle = \sum_p \langle u_{\alpha,p}|u_{\beta,p}\rangle. \tag{3.13}$$

1.3 Effective Hamiltonian for high-frequency driving

The quasi-energies can be expressed as the eigenvalues of the Floquet Hamiltonian, however it is not easy to compute them because the matrix equation is infinite. In this section, we describe the expression of an effective Hamiltonian in the limit of high-frequency driving. We consider time-periodic driving potential with a frequency ω much larger than the characteristic energy scale U of the Hamiltonian $H(t)$ which allows us to define the small parameter :

$$\lambda = \frac{U}{\hbar\omega} \ll 1. \tag{3.14}$$

This condition allows us to avoid resonances between the eigenvalues of the bare Hamiltonian. In this limit, light does not excite electrons but dresses the states through emission and re-absorption of virtual photons. We can thus derive a time-independent effective Hamiltonian that describes the system.

To derive the expression of the effective Hamiltonian, we fix a gauge such that the quasi-energies are restricted to the domain $[-\hbar\omega/2, \hbar\omega/2)$. We can always obtain the quasi-energies and Floquet states in another gauge using Eq. (3.6). The eigenvalue problem (3.10) can be rewritten as :

$$\sum_n H_{m-n}u_n = (\varepsilon - m\hbar\omega)u_m \;\Rightarrow\; u_m = \frac{1}{\varepsilon - m\hbar\omega}\sum_n H_{m-n}u_n. \tag{3.15}$$

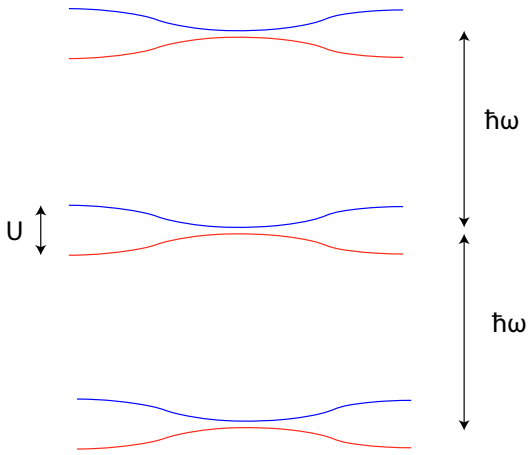

Figure 3.1 – Floquet replicas for high-frequency driving. The energy scale of the original bandwidth U of the Hamiltonian is much smaller than the frequency of the driving $\hbar\omega$. In that regime, the bare Hamiltonian is dressed by the driving and there is an infinite set of Floquet replicas at quasi-energy multiples of $\hbar\omega$.

We also consider that couplings between replicas with a difference of photons greater than one are negligible i.e. :

$$H_m = 0 \quad \forall\ |m| > 1, \tag{3.16}$$

The zeroth Fourier component of the Floquet state has therefore the expression :

$$u_0 = \frac{1}{\varepsilon}\sum_n H_{-n}u_n \approx \frac{1}{\varepsilon}\left(H_0u_0 + H_1u_{-1} + H_{-1}u_1\right) \quad \Rightarrow \quad u_0 \sim \lambda^0. \tag{3.17}$$

The first and second order components are given by :

$$u_{\pm1} \approx \mp\frac{1}{\hbar\omega}\left(H_{\pm1}u_0 + H_0u_{\pm1} + H_{\mp1}u_{\pm2}\right) \Rightarrow\ u_1 \sim \lambda^1, \tag{3.18}$$

$$u_{\pm2} \approx \mp\frac{1}{2\hbar\omega}\left(H_{\pm1}u_{\pm1} + H_0u_{\pm2} + H_{\mp1}u_{\pm3}\right) \Rightarrow\ u_2 \sim \lambda^2, \tag{3.19}$$

where we have used the condition :

$$\varepsilon \ll \hbar\omega, \tag{3.20}$$

which derives from Eq. (3.14). In the limit of high-frequency, combing Eqs. (3.17) and (3.18), and keeping only terms linear in λ leads to an approximate eigenvalue equation for the the zero component of the wavefunction :

$$\left(H_0 + \frac{[H_1, H_{-1}]}{\hbar\omega} + \mathcal{O}(\lambda^2)\right)u_0 = \varepsilon u_0. \tag{3.21}$$

Thus, we define the effective Hamiltonian as :

$$H_{\text{eff}}u_0 = \varepsilon u_0, \quad \text{with} \quad H_{\text{eff}} = H_0 + \frac{[H_1, H_{-1}]}{\hbar\omega}, \tag{3.22}$$

and the first harmonics of the Floquet state are given by :

$$u_{\pm1} = \mp\frac{H_{\pm1}}{\hbar\omega}u_0. \tag{3.23}$$

Therefore, in the regime given by Eqs. (3.14) and (3.16), the wavefunction is described by an effective Hamiltonian where the original Hamiltonian is "dressed" by the irradiation. In that case, no real electrons can be emitted or absorbed and the dressing arises from processes corresponding to emission and re-absorption of a virtual electron for $H_1 H_{-1}$ and the reverse process $H_{-1} H_1$. In the next section, we derive an expression for the effective Hamiltonian of graphene.

2 Irradiated graphene : lattice description

In this section, we apply the Floquet formalism introduced in the previous section to the case of graphene irradiated by an electromagnetic wave. In that case, it is possible to open a gap at quasi-energy $\varepsilon = 0$ and to manipulate the Dirac points using the amplitude and polarization of the wave [93, 94]. This opens the possibility to generate topological phases with non-zero Chern number. In the case of a circularly polarized electromagnetic wave, the high-frequency effective Hamiltonian is analogous to the Hamiltonian of the Haldane model [10, 80]. Hence, under circular polarization, graphene becomes insulating and possesses a chiral edge state crossing the gap, whose chirality depends on the polarization of the electromagnetic wave.

When the frequency is lowered, the driving couples the bands through emission and absorption of real photons and it is not easy to define a simple effective Hamiltonian. In this regime, the original Bloch bands are folded inside the first Floquet zone and some gaps open at the Floquet zone edges $\varepsilon = \pm\hbar\omega/2$ due to anti-crossing between the Bloch bands. If the reshuffled bands have a non-zero topological invariant, some edge states can eventually cross the gap at $\varepsilon = \hbar\omega/2$.

In this section, we analyze the graphene lattice irradiated by a circularly polarized electromagnetic wave. In Sec. 2.1, we derive the effective Hamiltonian for high-frequency driving, and obtain the expression for the Haldane mass gap. In Sec. 2.2, we diagonalize the Hamiltonian of an irradiated ribbon of graphene for any driving frequency and obtain edge states crossing the gaps at $\varepsilon = 0$ and $\varepsilon = \pm\hbar\omega/2$.

2.1 Effective Hamiltonian

We now derive the effective Hamiltonian introduced in Eq. (3.22) for the honeycomb lattice of graphene irradiated by a circularly polarized electromagnetic wave. The high-frequency condition (3.14) is valid if the frequency is larger than the bandwidth of graphene :

$$\hbar\omega \gg 6\tau, \tag{3.24}$$

where we have renamed the hopping parameter as τ to avoid confusion with the time parameter. The non-irradiated graphene Hamiltonian has the expression :

$$H_g(\mathbf{k}) = \begin{pmatrix} 0 & \rho(\mathbf{k}) \\ \rho^*(\mathbf{k}) & 0 \end{pmatrix}, \tag{3.25}$$

where $\rho(\mathbf{k}) = \tau \sum_\alpha e^{i\mathbf{k}.\boldsymbol{\delta}_\alpha}$. We consider irradiation by a circularly polarized electromagnetic wave described by the time-dependent vector potential $\mathbf{A}(t) = A_0(\cos(\omega t), \chi \sin(\omega t))$ where $\chi = \pm 1$ is the polarization of the EM wave. The electric field is given by $\mathbf{E}(t) = -\partial_t \mathbf{A}(t) = A_0\omega(\sin(\omega t), -\chi\cos(\omega t))$, which means that the polarization is left-handed for $\chi = +1$ and right-handed for $\chi = -1$. The coupling of electrons to light is introduced

through the Peierls substitution $\mathbf{k} \to \mathbf{k} + e\mathbf{A}(t)$, where we have set $\hbar \equiv 1$. The time-dependent Bloch Hamiltonian has therefore the expression :

$$H(\mathbf{k},t) = \begin{pmatrix} 0 & \rho(\mathbf{k},t) \\ \rho^*(\mathbf{k},t) & 0 \end{pmatrix}, \tag{3.26}$$

where $\rho(\mathbf{k},t) = \tau \sum_\alpha e^{i(\mathbf{k}+e\mathbf{A}(t)).\boldsymbol{\delta}_\alpha}$. The Fourier coefficients of the Hamiltonian (3.26) are :

$$H_q(\mathbf{k}) = \int_0^T \frac{dt}{T} H(\mathbf{k},t) e^{-iq\omega t} = \begin{pmatrix} 0 & \rho_q(\mathbf{k}) \\ \rho^*_{-q}(\mathbf{k}) & 0 \end{pmatrix}, \tag{3.27}$$

with :

$$\rho_q(\mathbf{k}) = \sum_\alpha e^{i\mathbf{k}.\boldsymbol{\delta}_\alpha} \tau_{\alpha,q}, \tag{3.28}$$

and :

$$\tau_{\alpha,q} = \tau \int_0^T \frac{dt}{T} e^{ie\mathbf{A}(t)\boldsymbol{\delta}_\alpha} e^{-iq\omega t}, \tag{3.29}$$

$$= \tau \int_0^T \frac{dt}{T} e^{ieA_0(\cos(\omega t)\delta_{\alpha,x} + \chi \sin(\omega t)\delta_{\alpha,y})} e^{-iq\omega t}, \tag{3.30}$$

are the Fourier components of the hopping amplitudes that depend on the bond. Using the Jacobi-Anger expansion for the exponential of sine and cosine function, we get :

$$\tau_{\alpha,q} = \tau i^q J_q(eA_0 a) e^{i\chi q\theta_\alpha}, \tag{3.31}$$

where $\theta_\alpha = \arctan\left(\frac{\delta_{\alpha y}}{\delta_{\alpha x}}\right)$ is the angle of the bond relative to the x axis, $J_n(x)$ is the Bessel function of the first kind, and we have used the identity :

$$\sum_m J_{m+q}(\alpha) J_m(\beta) e^{im\frac{\pi}{2}} = J_q(\sqrt{\alpha^2+\beta^2}) e^{-iq\arctan\left(\frac{\beta}{\alpha}\right)}, \tag{3.32}$$

introduced in Ref. [93]. We obtain finally :

$$\rho_q(\mathbf{k}) = \tau i^q J_q(eA_0 a) \sum_\alpha e^{i\mathbf{k}\boldsymbol{\delta}_\alpha} e^{i\chi q\theta_\alpha}. \tag{3.33}$$

In order to neglect higher order couplings, according to Eq. (3.16), the terms H_q with $q > 1$ must be negligible. The characteristic energy of the Hamiltonian H_q is $\tau J_q(\mathcal{A})$, where $\mathcal{A} = eA_0 a$ represents the dimensionless coupling strength. For weak driving $\mathcal{A} \ll 1$, we have $J_q(\mathcal{A}) \approx (\frac{\mathcal{A}}{2})^q$. Condition (3.16) is valid if couplings with higher order than unity are negligible :

$$J_q(\mathcal{A}) \ll 1 \quad \forall q > 1. \tag{3.34}$$

In the high frequency ($\hbar\omega \gg 6\tau$) and weak coupling ($\mathcal{A} \ll 1$) regime, the effective Hamiltonian (3.22) has the expression :

$$H_{\text{eff}}(\mathbf{k}) = H_0(\mathbf{k}) + d_z(\mathbf{k})\sigma_z, \tag{3.35}$$

where $H_0(\mathbf{k})$ is the graphene Hamiltonian with the hoppings renormalized by the field :

$$H_0(\mathbf{k}) = J_0(\mathcal{A}) H_g(\mathbf{k}). \tag{3.36}$$

Although for $\mathcal{A} \ll 1$, we have $J_0(\mathcal{A}) \approx 1$, we choose to keep the factor $J_0(\mathcal{A})$ in order to discuss the effect of the irradiation over the bare Hamiltonian. The function $d_z(\mathbf{k})$

is generated by the commutator $[H_1, H_{-1}]$ arising from the dressing of the bands by the irradiation :

$$d_z(\mathbf{k})\sigma_z = \frac{[H_1, H_{-1}]}{\hbar\omega} = \left(\frac{|\rho_1(\mathbf{k})|^2 - |\rho_{-1}(\mathbf{k})|^2}{\hbar\omega}\right)\sigma_z, \tag{3.37}$$

where $|\rho_{\pm1}(\mathbf{k})|^2$ are given by :

$$|\rho_{\pm1}(\mathbf{k})|^2 = \frac{\tau^2\mathcal{A}^2}{4}\left[3 + 2\sum_i \cos(\mathbf{k}.\mathbf{a}_i \mp \chi\frac{2\pi}{3})\right], \tag{3.38}$$

where we have used $J_1(\mathcal{A}) \approx \mathcal{A}/2$, the expression for the next nearest neighbour vectors $\mathbf{a}_1 = \boldsymbol{\delta}_1 - \boldsymbol{\delta}_2$, $\mathbf{a}_2 = \boldsymbol{\delta}_2 - \boldsymbol{\delta}_3$ and $\mathbf{a}_3 = \boldsymbol{\delta}_3 - \boldsymbol{\delta}_1$ and that $\theta_i - \theta_{i+1} = \frac{2\pi}{3}$. Replacing $|\rho_{\pm1}(\mathbf{k})|^2$ into (3.37) leads to :

$$d_z(\mathbf{k}) = \chi\frac{\sqrt{3}}{2}\frac{\tau^2\mathcal{A}^2}{\hbar\omega}\sum_i \sin(\mathbf{k}.\mathbf{a}_i). \tag{3.39}$$

This term is analogous to the term $d_z(\mathbf{k})$ in the Haldane model given in Eq. (2.24). Identifying with this term gives us :

$$t_2\sin(\phi) = -\chi\frac{\sqrt{3}}{4}\frac{\tau^2\mathcal{A}^2}{\hbar\omega}. \tag{3.40}$$

From the expression (2.29) for the mass at the Dirac point, we find that the effective mass term for irradiated graphene is equal to :

$$M_\xi^I = -\xi\chi\frac{9}{4}\frac{\tau^2\mathcal{A}^2}{\hbar\omega} = -\chi\xi\frac{(evA_0)^2}{\hbar\omega} \tag{3.41}$$

Because $d_z(\mathbf{k})$ is odd in $\mathbf{k}$, the irradiation generates a mass gap with opposite signs in the valleys, analogous to the Haldane model. The sign of the Haldane mass depends on the polarization of the EM wave. This term is proportional to the square of the dimensionless coupling and originates from the lifting of the degeneracy at the Dirac points due to second order exchange of virtual photons. In real space the term H_1H_{-1} is analogous to second neighbour hoppings between sites of the A sublattice with hopping amplitude $t_2 = \frac{\sqrt{3}}{4}\frac{\tau\mathcal{A}}{\hbar\omega}e^{i\phi}$ with $\phi = \frac{\pi}{2}$, while $H_{-1}H_1$ generate the same term with opposite phase on the B sublattice [80].

The Hamiltonian H_{eff} represents therefore a Chern insulator whose valence band Chern number is equal to :

$$C^- = \frac{1}{2}\left(\text{sign}(M_+^I) - \text{sign}(M_-^I)\right) = -\chi. \tag{3.42}$$

The Chern number is equal to +1 for a right-handed polarization and −1 for a left-handed polarization. Comparing the value of the Chern number and the direction of propagation of the edge state obtained in Sec. 4.1, we deduce that the edge state rotates around the sample in the same direction as the rotation of the electric field of the electromagnetic wave. In the limits $\hbar\omega \gg 6t$ and $\mathcal{A} \ll 1$, irradiated graphene is an insulator and possesses a chiral edge state at its boundaries whose direction depends on the polarization of the electromagnetic wave.

This mass term also exists for driving with smaller frequency, however, for frequencies smaller than the bandwidth, one needs to take into account real processes emerging from the coupling between the valence and the conduction band. In the next section, we analyze the effect of irradiated graphene in a ribbon geometry to study the edge states.

2.2 Dispersion relation of an irradiated graphene ribbon

We consider the same geometry of the zig-zag ribbon shown in Fig. 2.9, where the longitudinal wavevector k_x is a good quantum number. The tight-binding Hamiltonian for the irradiated honeycomb lattice is :

$$\mathcal{H}(t) = \tau \sum_{\mathbf{r}_a} \sum_{\alpha=1}^{3} b^\dagger(\mathbf{r}_A + \boldsymbol{\delta}_\alpha, t) a(\mathbf{r}_A, t) e^{ie\mathbf{A}(t)\boldsymbol{\delta}_\alpha} + H.c., \tag{3.43}$$

where the effect of the driving is introduced through the Peierls substitution $\tau \to \tau e^{ie\int_{\mathbf{r}_A}^{\mathbf{r}_A+\boldsymbol{\delta}_\alpha} \mathbf{A}(t)}$. We perform the Fourier expansion along the axis x as in Eq. (2.85) such that the Hamiltonian can be expressed as :

$$\mathcal{H}(t) = \sum_{k_x} \sum_{ij} \Psi_i^\dagger(k_x, t) H_{ij}(k_x, t) \Psi_j(k_x, t), \tag{3.44}$$

where $\Psi_i^\dagger(k_x, t) = (a_i^\dagger(k_x, t), b_i^\dagger(k_x, t))$ is the spinor in the basis $i \in [0, N-1]$ of the sites along the y direction. The Bloch Hamiltonian has the expression :

$$H_{ij}(k_x, t) = \begin{pmatrix} 0 & \rho_{ij}(k_x, t) \\ \rho_{ji}^*(k_x, t) & 0 \end{pmatrix}, \tag{3.45}$$

with :

$$\rho_{ij}(k_x, t) = \tau\big(e^{-i\frac{\sqrt{3}a}{2}k_x} e^{-ie\mathbf{A}(t)\boldsymbol{\delta}_1} + e^{i\frac{\sqrt{3}a}{2}k_x} e^{-ie\mathbf{A}(t)\boldsymbol{\delta}_2}\big)\delta_{ij} + \tau e^{-ie\mathbf{A}(t)\boldsymbol{\delta}_3}\delta_{ij+1} \tag{3.46}$$

In Sambe space, the Floquet Hamiltonian (3.10) has the expression :

$$\tilde{H}_{Fij}^{mn} = \begin{pmatrix} n\hbar\omega\delta^{mn}\delta_{ij} & \rho_{ij}^{m-n}(k_x) \\ \rho_{ji}^{*n-m}(k_x) & n\hbar\omega\delta^{mn}\delta_{ij} \end{pmatrix}, \tag{3.47}$$

where :

$$\rho_{ij}^q(k_x) = \tau J_q(\mathcal{A}) \left[2\cos\left(\frac{\sqrt{3}a}{2}k_x - \chi q \frac{2\pi}{3}\right)\delta_{ij} + (-1)^{\chi q}\delta_{i,j+1} \right], \tag{3.48}$$

is the Fourier component q of $\rho_{ij}(k_x, t)$ calculated using Eq. (3.31). In Sambe space, $\tilde{H}_F$ is an infinite matrix, so one needs to truncate it. In the truncation procedure, the gauge invariance (3.6) is broken and thus the spectrum is not periodic in ε. For small coupling strength $\mathcal{A}$, the coupling strength $J_{n-n'}(\mathcal{A})$ between replicas dressed with n and n' photons decreases with $n - n'$. If we consider $2M+1$ replicas such that $n \in [-M, M]$, the gauge invariance is almost restored around the replica $n = 0$ if $M \gg 1$. We focus therefore on the central replica $n = 0$ and choose a sufficient number of replicas so that the spectrum around $n = 0$ converges as we increase M.

For a ribbon with N sites along y, the matrix $\tilde{H}_F$ has size $2N(2M+1)\times 2N(2M+1)$ and there are $2N(2M+1)$ eigenstates. The quasi-energies on the $n = 0$ replicas are restricted to $\varepsilon \in [-\hbar\omega/2, \hbar\omega/2]$. In this first Floquet zone, there are $2N$ eigenstates for each value of k_x. In this procedure, we always check the convergence of the spectrum $n = 0$ with increasing M. We mention in the caption of the figures the number M of Floquet replicas used in the calculation.

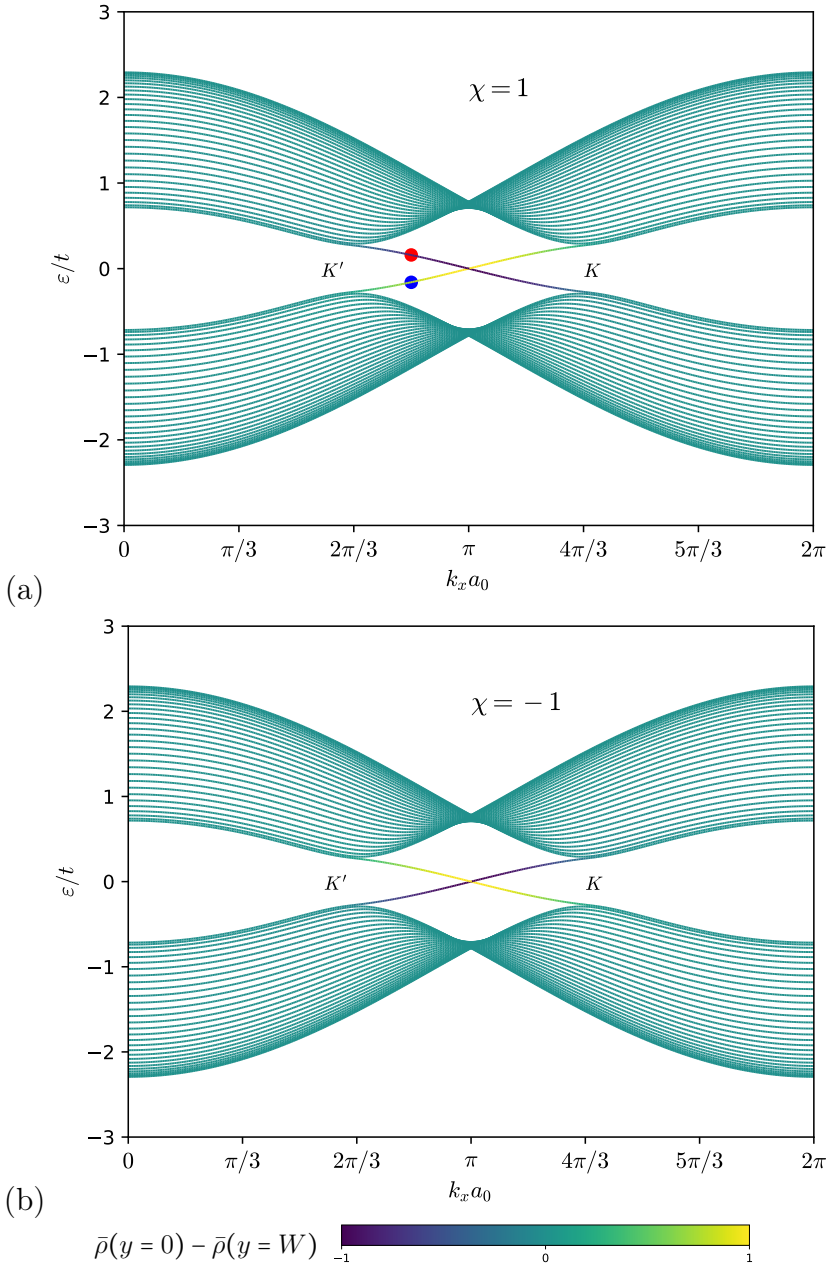

Figure 3.2 – Quasi-energy spectra of a zig-zag ribbon with $N = 30$ sites along y and $M = 1$ replicas, irradiated by a circularly polarized electromagnetic wave with frequency $\hbar\omega = 6t$, amplitude $\mathcal{A} = 1$ and polarization : (a) $\chi = +1$, (b) $\chi = -1$. Only the central replica $n = 0$ is represented. We can see that the driving generates a mass at the Dirac points, and we observe the presence of edge states crossing the gap which are characteristic of the Haldane model. The dots correspond to the wavefunction plotted on Fig. 3.3.

a) High-frequency limit

Fig. 3.2 shows the spectrum of irradiated graphene ribbons in the out-of-resonance frequency regime $\hbar\omega = 6t$ which corresponds to the case studied in Sec. 2.1. In that case, the first Floquet zone range is $[-\hbar\omega/2, \hbar\omega/2] = [-3t, 3t]$. We have plotted only the first Floquet zone. The color coding represents the time averaged electronic density at the

edges such that :

$$\bar{\rho}(y=0) = \langle\langle u_A(i=0)|u_A(i=0)\rangle\rangle + \langle\langle u_B(i=0)|u_B(i=0)\rangle\rangle, \tag{3.49}$$

and identically $\bar{\rho}(y=W)$ at the other edge $i = N-1$. For $\mathcal{A}=1$, we have $J_2(\mathcal{A}) \approx 0.1$ which means that the weak coupling approximation is still applicable.

We can compare the ribbon spectrum to the analytical spectrum obtained in Sec. 2.1. The spectrum is identical to the one of the effective Haldane model, with a mass given by Eq. (3.41). For $\mathcal{A}=1$ the value of the mass is equal to $|M^I| \approx 0.5t$. We observe two edge states crossing the gap, one at each edge of the ribbon. In Fig. 3.2.(a), the polarization of the wave is $\chi = 1$ which means that, according to Eq. (3.42), the Chern number of the valence band is $C^- = -1$. According to the color coding, we find that the edge states rotates counter-clockwise, which is coherent with the direction of rotation shown in Fig. 2.12.(b). When reversing the polarization of the driving, we see on Fig. 3.2.(b) that the direction of propagation of the edge states is reversed. This fact signals that the phases have opposite Chern number.

We can see that the bandwidth of graphene is significantly reduced. This is due to the fact that the zeroth order hopping parameters are renormalized by the driving and are equal to $\tau J_0(\mathcal{A})$. The bandwidth is thereby equal to $6\tau J_0(1) \approx 4.6\tau$ which is consistent with Fig. 3.2.

Fig. 3.3 shows the wavefunction of the edge state corresponding to the blue and the red dot in Fig. 3.2.(a) for $M=1$ replicas. In Sambe space, the wavefunction is a spinor with $2(2M+1)$ components, a two-component spinor for each replica. For an eigenstate α and $M=1$, the spinor has the expression : $\tilde{u}_\alpha^T = (u^1_{\alpha,A}, u^1_{\alpha,B}, u^0_{\alpha,A}, u^0_{\alpha,B}, u^{-1}_{\alpha,A}, u^{-1}_{\alpha,B})$. Eq. (3.22) tells us that the wavefunction u^0_α on the replica $n=0$ should be identical to the wavefunction of the Haldane model represented on Fig. 2.11, which means that it is mainly polarized on the B sublattice for the edge state at $y=0$ and the components on the replica $m=\pm 1$ of the A sublattice are given by Eq. (3.23) such that :

$$u^1_A = -\rho^1 u^0_B, \quad \text{and,} \quad u^{-1}_A = \rho^{-1} u^0_B, \tag{3.50}$$

in matrix notation, where $\rho^{\pm 1}$ is given by (3.48).

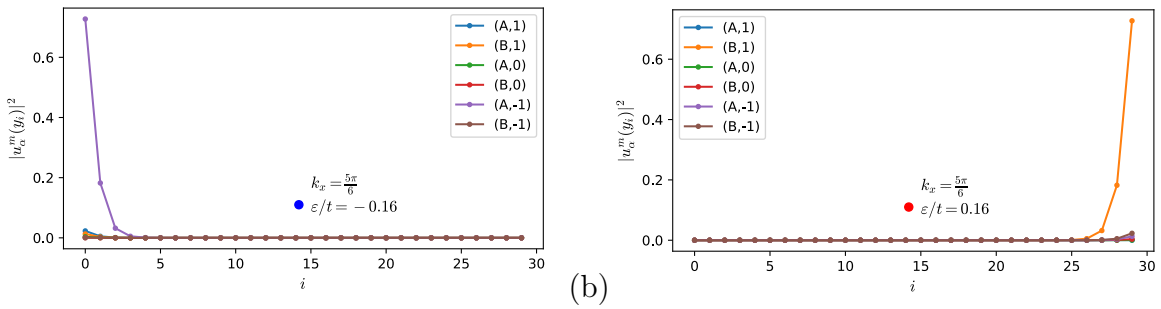

Figure 3.3 – Square modulus of the wavefunctions of the edge states of the graphene irradiated by an electromagnetic wave with frequency $\hbar\omega = 6t$, amplitude $\mathcal{A}=1$ polarization $\chi = 1$ corresponding to the dots on Fig. 3.2.

b) Resonant frequency

As the frequency is decreased, the Floquet sidebands get closer in quasi-energy. A topological phase transition happens when the gap at $\varepsilon = \hbar\omega/2$ closes. We have seen that

under irradiation, according to Eq. (3.14), the zeroth component of the nearest neighbour hoppings in the graphene Hamiltonian is renormalized by a factor $J_0(\mathcal{A})$. The band touching happens when the bandwidth equals the frequency of the irradiation, namely when $\hbar\omega = 6tJ_0(\mathcal{A})$. When the frequency further decreases, the gap reopens because of the allowed transitions between the bands. This gap closing corresponds thus to a topological transition.

Figs. 3.4 shows the quasi-energy spectra of irradiated graphene ribbon for a frequency smaller than the bandwidth of graphene. At $\varepsilon = 0$, we still observe the edge states characteristic of the effective Haldane model. However, the electromagnetic field is at resonance so the irradiation also couples the valence band and the conduction band of the Haldane model. At quasi-energy $\varepsilon = \pm\hbar\omega/2$, the original bands create an anti-crossing, which opens a gap. There are now two quasi-energy bands $\varepsilon_-(k_x)$ such that $-\hbar\omega/2 < \varepsilon_- < 0$ and $\varepsilon_+(k_x)$ restricted to $0 < \varepsilon_+ < \hbar\omega/2$. The spectrum possesses two non-equivalent gaps Δ_0 at $\varepsilon = 0$ and $\Delta_{\omega/2}$ at $\varepsilon = \hbar\omega/2$. In Figs. 3.4, two Floquet zones are shown in order to visualize the original bands and the dispersion of the edge states. We can see that the spectrum is identical in the range $[-\hbar\omega, 0]$ and in $[0, \hbar\omega]$, which expresses the fact that the Floquet quasi-energy spectra are invariant under the gauge transformation $\varepsilon \to \varepsilon + n\hbar\omega$.

In Fig. 3.4.(a), there is a band inversion occurring at $\varepsilon = \hbar\omega/2$ such the original bands are reshuffled. The quasi-energy band ε_+ is now a mixture of the original valence and conduction bands of graphene. This band inversion leads to an exchange of Chern number and the apparition of edge states at $\varepsilon = \hbar\omega/2$. We observe four edge state crossing the gap, two per edge. Because of this exchange of Chern number between the original graphene bands, one needs introduce a Floquet Chern number $C_F^{\pm}$ which characterizes the Floquet quasi-energy bands ε_+ and ε_-. Computing this Chern number is a difficult task since the bands are reshuffled and we don't have a bulk expression for the effective stroboscopic Hamiltonian. One needs to have a new topological invariant that takes into account the time-periodicity of the problem.

Such a new topological invariant was introduced by Rudner *et al.* [85] to characterize the topological phases of periodically driven systems. In this scheme, the Brillouin zone base space T^2 is extended to the circle S^1 of time-periodic functions, and the topological properties are encoded in the time-evolution operator $U(\mathbf{k}, t)$ in this three-dimensional space. This invariant is a winding number $W[U]$ that characterizes the mapping of the compact space $S^1 \times T^2$ to the space of unitary time-evolution operators $U(N)$. Rudner *et al.* showed that this winding number is defined for a gap in the quasi-energy spectrum and is equal to the number of chiral edge states $n_{\text{edge}}(\varepsilon)$ crossing the gap at quasi-energy ε. The winding numbers of the gaps at energy ε are related to the Chern number as :

$$C_{F,\varepsilon\varepsilon'} = W[U_{\varepsilon'}] - W[U_{\varepsilon}] = n_{\text{edge}}(\varepsilon') - n_{\text{edge}}(\varepsilon). \tag{3.51}$$

$C_{F,\varepsilon\varepsilon'}$ is the Chern number of the bands between the gaps around quasi-energies ε and ε'. We can see that according to Eq. (3.51), it is possible to have a vanishing Chern number if the number of chiral edge states is identical in the gaps Δ_0 and $\Delta_{\omega/2}$.

We now apply this expression to Figs. 3.4 in order to calculate the Chern number of the Floquet quasi-energy bands. In Fig. 3.4.(a), there is one chiral edge state crossing the gap Δ_0 which is the usual Haldane edge state. This edge state corresponds to a winding number of the gap $n_{\text{edge}}(\varepsilon = 0) = W_0 = 1$. In the gap $\Delta_{\omega/2}$, we observe two edge states whose chirality is opposite than the edge state at $\varepsilon = 0$. They contribute thus to a winding number $W_{\omega/2} = -2$. The Chern number of the band ε_+ is thus $C_F^+ = W_0 - W_{\omega/2} = 3$. Hence, because of the apparition of two edge states, the original conduction band has exchanged

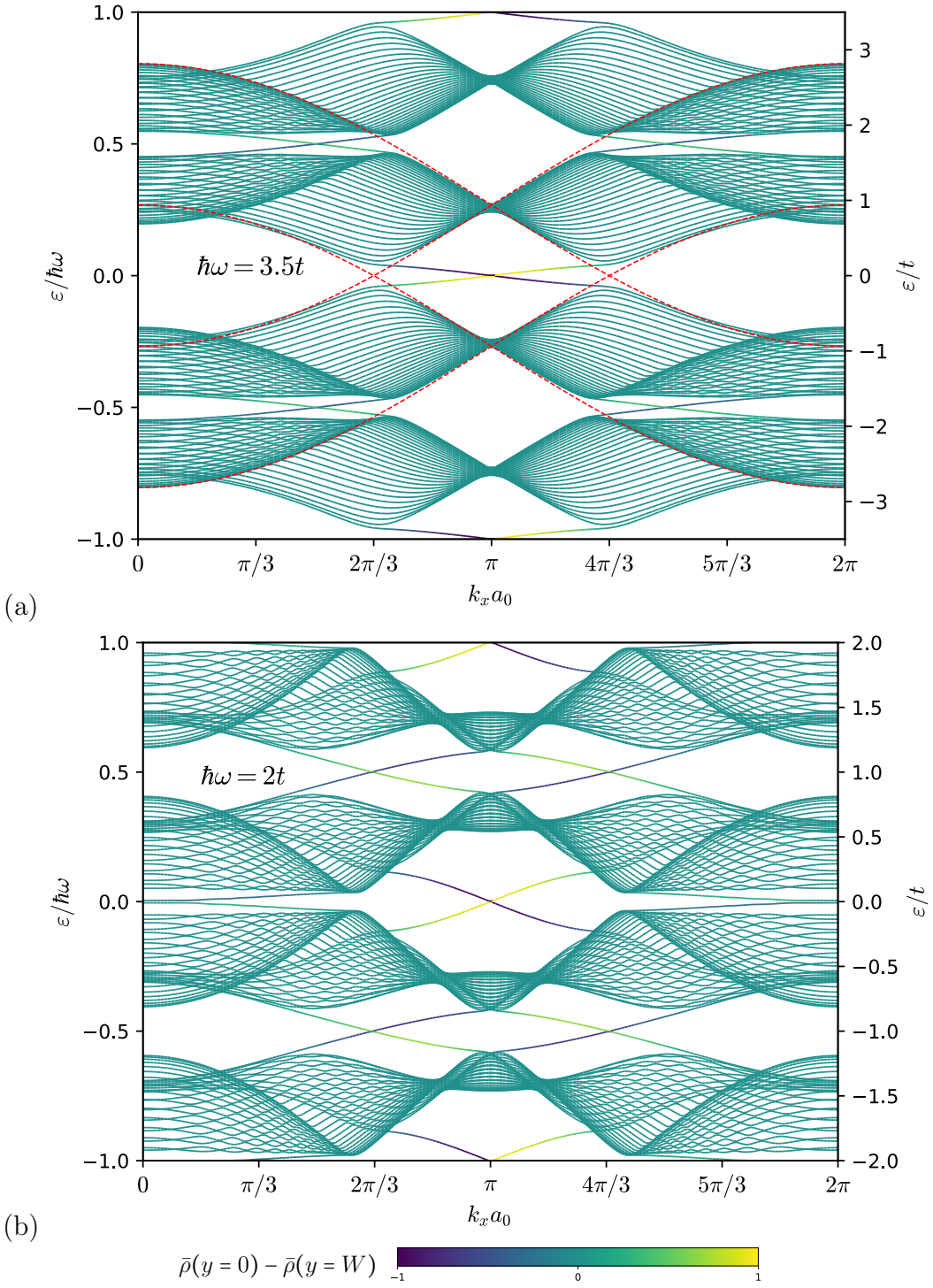

Figure 3.4 – Quasi-energy spectra of a zig-zag graphene ribbon with $N = 30$ sites irradiated by an EM wave amplitude $\mathcal{A} = 0.5$, polarization $\chi = 1$ and frequency : (a) $\hbar\omega = 3.5t$ (b) $\hbar\omega = 2t$. We have kept $M = 2$ replicas. The quasi-energy runs from $-\hbar\omega$ to $\hbar\omega$ which corresponds to two Floquet zones. The red lines on (a) demarcate the original bands of graphene renormalized by $J_0(\mathcal{A})$. We still observe the edge states of the effective Haldane model at $\varepsilon = 0$ and for (a), we see the appearence of two additional anti-chiral edge states at $\varepsilon = \hbar\omega/2$ and in (b), another edge state appears at $\varepsilon = 0$.

a Chern number of +2 with the valence band. Identically, the band ε_- has Chern number

$C_F^- = -3$.

Upon further decreasing the frequency of the driving (Fig. 3.4.(b)), another band inversion occurs at Δ_0. We observe the apparition of a new edge state crossing the $\varepsilon = 0$ gap. Because this edge state has opposite chirality than of the edge state at $\varepsilon = 0$ of Fig. 3.4.(b), it contributes to a winding number $W_0 = -1$. The total winding number of the gap Δ_0 is now $W_0 = 0$ and the band ε_+ has thus a Chern number $C_F^+ = 2$. The band ε_- has Chern number $C_F^- = -2$.

If we decrease further the frequency of the irradiation, the number of resonances between the valence band and the conduction band increases. This fact leads to a complex quasi-energy band structure where each band inversion leads to exchange of Chern number between the bands. Computing the Chern number is a difficult task when the frequency of the driving decreases. This calculation has been performed numerically for graphene by Gomez *et al.* [94]. The first steps are $|C_F| = 1$, $|C_F| = 3$ and $|C_F| = 2$ which is what we have deduced from the number and the chirality of the edge states plotted in Figs. 3.4. Our analysis gives results which are consistent with [94].

In this section, we have studied irradiated graphene in a ribbon geometry, and have observed the presence of edge states at the non-equivalent quasi-energy gaps $\varepsilon = 0$ and $\varepsilon = \hbar\omega/2$. We have seen that as the frequency of the driving is decreased, more resonances are allowed between the original conduction and valence band which lead to an increasingly complex quasi-energy spectrum. The Chern number of the quasi-energy bands can be computed by counting the edge states crossing the gaps. However, as the number of edge states increases, it becomes harder to count the number of edge states and one needs to use numerical methods to compute the edge states. In Sec. 3, we analyze the case of irradiated graphene for frequencies small compared to the bandwidth so that we can use the Dirac equation.

3 Irradiated graphene : continuum Dirac description

We have seen that upon decreasing the frequency of the electromagnetic wave in irradiated graphene, resonant transitions are allowed, which open gaps in the quasi-energy band structure at $\varepsilon = 0$ and $\varepsilon = \hbar\omega/2$. However, frequencies of the order of the bandwidth (in the ultraviolet range) cannot be matched experimentally by chemical potential variation. Our goal in the next chapter is to study the Floquet spectrum in an accessible range of energy using chemical potential variation. This is experimentally achievable using lasers with frequencies in the Terahertz or infrared, corresponding to 10 to 100 meV. In that range, graphene can be modelled using the Dirac equation. Due to multi-photon resonances, gaps open at frequencies multiple of $\hbar\omega/2$. Because of the linear dispersion of graphene, the quasi-energy spectrum is made of an infinite number of nested gaps as a function of the momentum [95] whose size depends on the number of photons involved in the resonance. These gaps host chiral edge states propagating at the boundaries of the sample [96].

In Sec. 3.1, we derive the effective Hamiltonian close to the Dirac points which is analogous to the Haldane Hamiltonian. In Sec. 3.2, we analyze the Floquet spectrum when the frequency is maller than to bandwidth of graphene. In Sec. 3.3, we study the nested gap structure. In Sec. 3.4, we derive an effective Hamiltonian near a band crossing, and compute the Chern number associated with this crossing. Finally, in Sec. 3.5, we plot the dispersion relation of the edge states in a ribbon geometry.

3.1 Effective Hamiltonian

The time-dependent Hamiltonian describing the Dirac fermions in the valley-isospin representation is written as :

$$H(\mathbf{k},t) = H_0(\mathbf{k}) + V(t)\,, \tag{3.52}$$

where H_0 is the bare graphene Hamiltonian and $V(t)$ is the coupling with the time-periodic driving. The vector potential $\mathbf{A}(t) = A_0(\cos\omega t, \chi \sin\omega t)$ couples to the electric charge via the Peierls substitution $\mathbf{p} \to \mathbf{p} - q\mathbf{A}(t)$, where $q = -e$ is the electron charge. The Hamiltonian for the coupling between electrons and the electromagnetic field can therefore be expressed as :

$$V(t) = (V_1 e^{i\omega t} + V_{-1} e^{-i\omega t}), \tag{3.53}$$

where the matrices V_1 and V_{-1} read :

$$V_1 = \frac{evA_0}{2}(\tau_z\sigma_x - i\chi\sigma_y), \quad \text{and} \quad V_{-1} = \frac{evA_0}{2}(\tau_z\sigma_x + i\chi\sigma_y). \tag{3.54}$$

Because of the linear dispersion relation of graphene, the irradiation generates only terms linear in the coupling strength. Therefore, a Floquet replica couples only to replicas with ±1 photons. This formulation is analogous to a one-dimensional lattice with nearest neighbour couplings in quasi-energy space.

In the high-frequency limit, we can derive the effective Hamiltonian given by Eq. (3.22) to obtain :

$$H_{\text{eff}}(\mathbf{k}) = H_0(\mathbf{k}) - \chi\frac{(evA_0)^2}{\hbar\omega}\sigma_z\tau_z, \tag{3.55}$$

where the second term comes from the commutator $[V_1, V_{-1}]$ and corresponds to a mass term with opposite sign in the valleys identical to the one given in Eq. (3.41). We see that in the high-frequency limit, the low-energy Hamiltonian is identical to the one obtained by linearising the lattice Hamiltonian near the Dirac points.

An important dimensionless parameter is :

$$\beta = \frac{evA_0}{\hbar\omega}\,, \tag{3.56}$$

which quantifies the electromagnetic driving strength. Following a simple quasi-classical argument, evA_0 is simply the energy gained by an electron traveling at speed v in an electric field $E_0 = \omega A_0$ during a period of the electromagnetic wave ($1/\omega$), while $\hbar\omega$ is the minimal energy quantum which can be absorbed by the electron.

3.2 Dirac-Floquet spectrum

The quasi-energy spectrum of an irradiated graphene sheet can be obtained by diagonalizing the Hamiltonian in Sambe space. The spectrum is made of an infinite number of Floquet replicas coupled to their nearest neighbours by the driving. In Sambe space, the matrix equation reads :

$$\sum_n H^{\xi}_{F,mn}u_n = \sum_n (H^{\xi}_{0F,mn} + V^{\xi}_{F,mn})u_n = \varepsilon u_m\,, \tag{3.57}$$

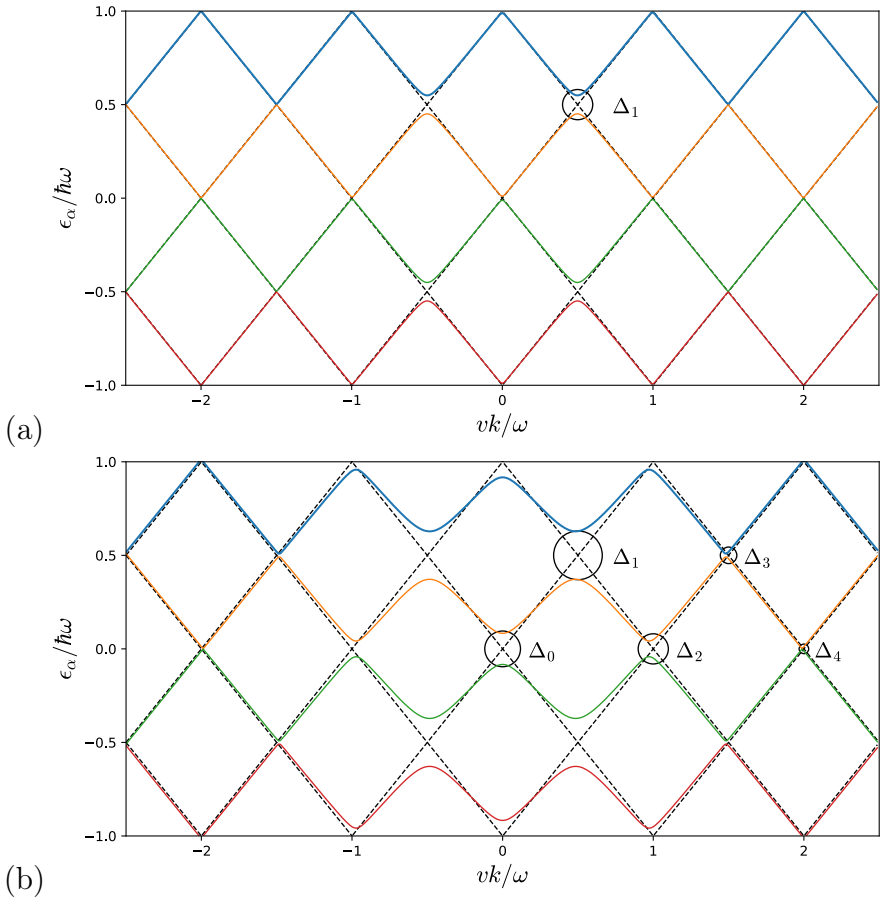

Figure 3.5 – Dispersion relation $\varepsilon_\alpha(k)$ ($k = |\mathbf{k}|$) of an infinite graphene sheet irradiated by an electromagnetic wave at driving strengths : (a) $\beta = 0.1$, (b) $\beta = 0.3$, using $N = 3$ Floquet replicas. The non-equivalent Floquet bands are $\varepsilon_+ \in [0, \hbar\omega/2]$ and $\varepsilon_- \in [-\hbar\omega/2, 0]$, the other bands are identical Floquet replicas. The dashed lines correspond to the non-irradiated case in the Floquet representation with dispersion $\varepsilon = \pm\hbar vk + n\hbar\omega$. The circles on (a) and (b) indicate the non-equivalent gaps Δ_m, located at momenta $k = m\omega/2v$, and at quasi-energies $\varepsilon = 0$ and $\varepsilon = \hbar\omega/2$, alternatively.

where $(m, n) \in \mathbb{Z}^2$ and $\xi = \pm 1$ is the valley index. The graphene Hamiltonian $H^\xi_{0F,mn}$ dressed with m photons is defined as :

$$H^\xi_{0F,mn} = (\hbar v(\xi\sigma_x k_x + k_y\sigma_y) + m\hbar\omega)\delta_{mn}, \tag{3.58}$$

which is diagonal in the Floquet basis. In contrast, the driving Hamiltonian $V^\xi_{F,mn}$,

$$V^\xi_{F,mn} = V^\xi_1\delta_{m,n-1} + V^\xi_{-1}\delta_{m,n+1}, \tag{3.59}$$

couples distinct Fourier components Φ_n. The matrices V^ξ_1 and V^ξ_{-1} defined in Eq. (3.54) read :

$$V^\xi_1 = \frac{evA_0}{2}\begin{pmatrix} 0 & \xi - \chi \\ \xi + \chi & 0 \end{pmatrix}, \quad \text{and,} \quad V^\xi_{-1} = \frac{evA_0}{2}\begin{pmatrix} 0 & \xi + \chi \\ \xi - \chi & 0 \end{pmatrix}. \tag{3.60}$$

In this Floquet representation, the wave function is an infinite vector containing all the different Fourier harmonics of the wave function. Since the Floquet matrix is infinite, we need to set a cut-off M in the number of Floquet replicas considered. The size of the

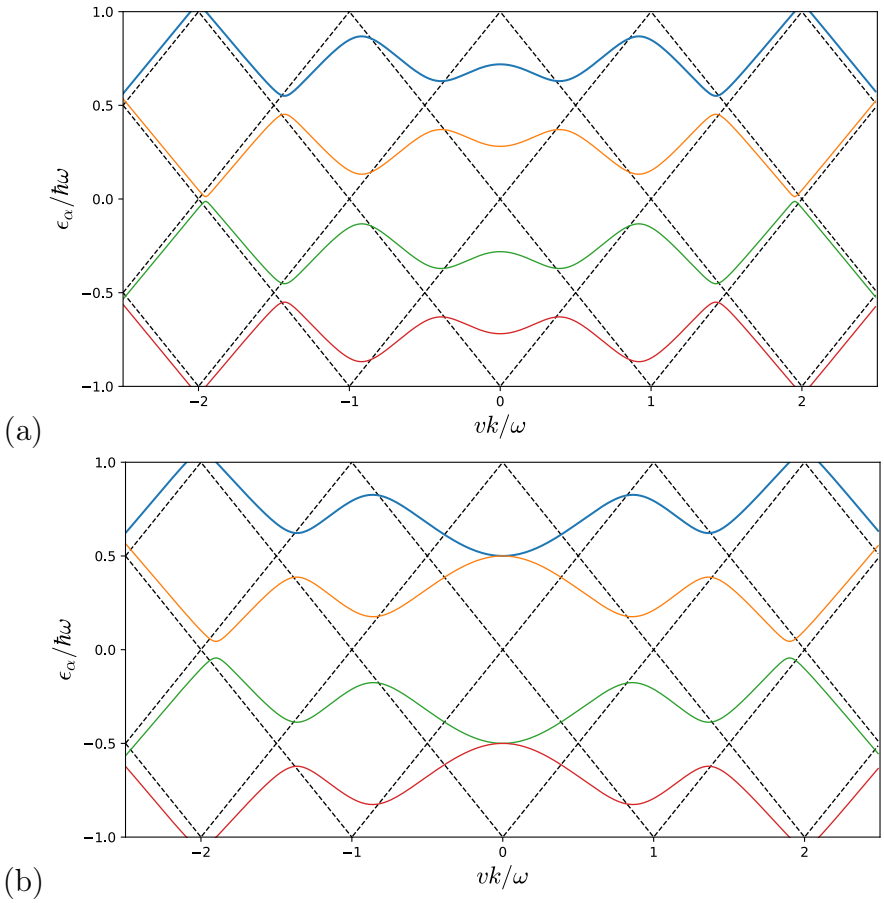

Figure 3.6 – Dispersion relation $\varepsilon_\alpha(k)$ ($k = |\mathbf{k}|$) of the irradiated graphene sheet at strong driving : (a) $\beta = 0.6$ and (b) $\beta = \sqrt{3}/2$ using $N = 3$ Floquet replicas. As β increases, the gap Δ_0 increases until it reaches $\Delta_0 = \hbar\omega$ for $\beta = \sqrt{3}/2$, which leads to a gap closing at $\varepsilon = \hbar\omega/2$

matrix is thus $2(2M+1) \times 2(2M+1)$ (taking into account the sublattice isospin index). Due to rotational invariance around $\mathbf{k} = 0$, the spectrum only depends on the norm $k = |\mathbf{k}|$ of the wave vector. The spectrum consists of $2(2M+1)$ bands having the dispersion relation $\varepsilon_\alpha(k)$ for $\alpha \in [1, 2(2M+1)]$.

The spectrum is periodic in energy (with period ω), so we restrict ourselves to the study of the reduced bands where $\varepsilon \in [-\hbar\omega/2, \hbar\omega/2]$. The gaps are located at different momenta because of the folding of the dispersion relation in the reduced Floquet zone $[-\hbar\omega/2, \hbar\omega/2]$. In this representation, there are two non-equivalent set of gaps centered at $\varepsilon = 0$ and at $\varepsilon = \hbar\omega/2$ [Fig. 3.5.(b)]. The gaps of even order (Δ_0,Δ_2,Δ_4...) are located at the center of the Floquet zone ($\varepsilon = 0$) and the even order ones (Δ_1,Δ_3...) are located at the edge ($\varepsilon = \pm\hbar\omega/2$) [Fig. 3.5.(b)].

For weak driving, $\beta = 0.1$ [Fig 3.5.(a)], the bands corresponding to the irradiated case (solid curves) follow closely the non-irradiated ones (dashed curves) except around the avoided crossing Δ_1 located at $k = \pm\omega/2v$ and centered around $\varepsilon = \pm\hbar\omega/2$. Upon increasing the driving, more gaps open at momenta $k_m = \pm m\omega/2v$, with m integer [Fig 3.5.(b)]. These gaps correspond to the anti-crossing of two Dirac bands dressed with n and n' photons such that $|n - n'| = m$. For example, at the gap Δ_3 in Fig. 3.5.(b), the electron is in a coherent superposition of a valence band electron dressed with 2 photons (having absorbed two quanta of the electromagnetic field) and a conduction band electron

dressed with −1 photon (meaning having emitted one quantum of the field).

For strong driving, multi-photon processes are more likely, leading to a strong modification of the quasi-energy spectrum [Fig. 3.6]. The gaps are bigger, and the location of the gaps get closer in momentum to $k = 0$ as β increases. For $\beta = \sqrt{3}/2$ [Fig. 3.6.(b)], the size of the gap Δ_0 reaches $\hbar\omega$ while the two gaps Δ_1 originally located at $k = \pm\omega/2v$ merge into one gap at $k = 0$, which leads to a band touching at the Floquet zone edges $\varepsilon = \pm\omega/2$.

3.3 Gap structure

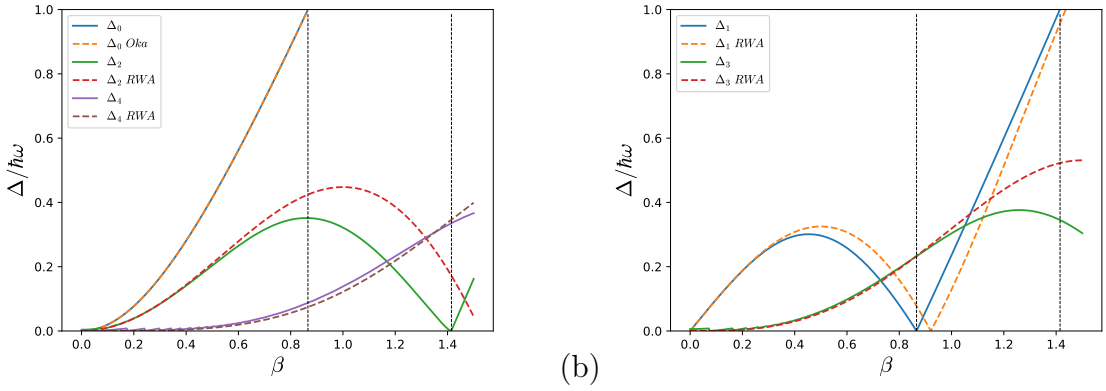

Figure 3.7 – Size of the gaps at (a) $\varepsilon = 0$ and (b) $\varepsilon = \hbar\omega/2$ as a function of the driving strength β calculated using the numerical Floquet method (solid lines) and the rotating wave approximation (RWA), namely Eqs. (3.61) and (3.62) (dashed curves). The numerical calculations (solid lines) agrees with RWA estimations for weak driving. The gap Δ_1 closes while the gap Δ_0 tends to $\hbar\omega$ for $\beta = \sqrt{3}/2$.

The Floquet spectrum has a very rich gap structure [95] that depends strongly on the driving strength β. In this section, we compare analytical expressions of the gap size obtained within the generalized rotating wave approximation scheme (see Annex D) and the results that we get from diagonalizing numerically in Floquet space. The RWA fits very well the numerics for low β, and describes qualitatively the size of the gaps for $\beta \lesssim 1$ (Fig. 3.7). The gap Δ_0 and the gaps Δ_m with $m \geqslant 1$ have different origins.

The central gap Δ_0 at quasi-energy $\varepsilon = 0$ and momentum $k = 0$ originates from the emission and re-absorption of virtual photons. Oka and Aoki [10] first discussed this gap and found that its size equals :

$$\frac{\Delta_0}{\hbar\omega} = \sqrt{1 + 4\beta^2} - 1 \approx 2\beta^2, \tag{3.61}$$

where the last approximation correspond to weak driving $\beta \ll 1$ and is consistent with Eq. (3.55) because the gap size equals twice the mass term : $\Delta_0 = 2M = 2\beta^2\hbar\omega$. The quadratic dependence in β for weak driving points out that this gap originates from a second order process in the coupling. The analytic expression Eq. (3.61) fits perfectly our numerics. For weak driving, the evolution is quadratic in β, and as the driving increases, it becomes linear until the gap size reaches the size of the Floquet zone $\Delta_0 = \hbar\omega$ for $\beta = \sqrt{3}/2$.

Multiphoton processes of order m induce the gaps Δ_m. For $m \geqslant 1$, the gap amplitudes have been derived within the generalized rotating wave approximation. When the driving

is at resonance with m photons, the gap size is found to be (see Annex D) :

$$\frac{\Delta_m}{\hbar\omega} \approx \beta|J_{m+1}(2\beta) - J_{m-1}(2\beta)| \approx \frac{\beta^m}{(m-1)!}\,, \tag{3.62}$$

where J_m is the m-th order Bessel function, and the last approximation is only valid for $\beta \ll 1$. For weak driving, the size of the gap Δ_m ($m \geqslant 1$) is strongly reduced upon increasing m. Increasing the driving strength β, the gaps evolve in a non-monotonic way and can also close.

For weak driving, the gap Δ_1 is located at wave-vector $k = \pm\omega/2v$, at quasi-energy $\varepsilon = \hbar\omega/2$ and has size $\Delta_1/\hbar\omega = \beta$ for weak driving. This gap originates from the anti-crossing of the bands $n = 1$ and $n' = 0$, and therefore it is a first order process in β (exchange of one photon). This explains why Δ_1 is the largest gap for weak driving (Figs. 3.5). The size of this gap first increases linearly with β, then it reaches a maximum value around $\beta \approx 0.5$, and starts decreasing until it reaches zero [Fig. 3.7.(b)]. We see that at the same value of β, the gap Δ_0 reaches $\hbar\omega$, and as we have seen earlier, this happens for $\beta = \sqrt{3}/2$ (first vertical dashed line on Fig. 3.7.(b)). We conclude that this value corresponds to a band touching at the Floquet zone edges $\varepsilon = \hbar\omega/2$. The corresponding spectrum is plotted on Fig. 3.6.(b). Upon increasing the driving strength, the gap Δ_1 reopens and is now centered at $k = 0$.

The gap Δ_2 originates from the anti-crossing of two Dirac bands dressed with $n = 1$ and $n' = -1$ photons. This is therefore a second order process in the coupling and is proportional to β^2 for weak driving, and the gap size is $\Delta_2/\hbar\omega = \beta^2$. Another band touching happens at $\varepsilon = 0$ when the gap Δ_2 vanishes while $\Delta_1 = \hbar\omega$. This band touching happens for $\beta \approx 1.42$ (second vertical dashed line).

The idea is the same for the gaps Δ_3 and Δ_4, they originate from the anti-crossing of bands dressed with a difference of 3 or 4 photons respectively. They are is thus proportional to β^3 and β^4 for weak driving. As driving strength increases, the same band touching scenario will occur with all the gaps. The gap Δ_m closes while the gap Δ_{m-1} reaches the Floquet zone size, which leads to a band touching. From expression (3.62), we see that the band touchings happen when :

$$\Delta_m = 0 \quad \Leftrightarrow \quad J_{m+1}(2\beta) \approx J_{m-1}(2\beta) \tag{3.63}$$

Our numerical diagonalizations go beyond the RWA estimations which are valid only at low β.

3.4 Berry curvature and Chern number

Irradiating graphene in the high frequency limit generates a Haldane mass term. Such a term leads to a non-trivial topology and the Chern number of the valence band equals $C^- = \pm 1$ depending on the polarization of the wave. Reducing the frequency of the electromagnetic wave generates band inversions which open gaps and host chiral edge states in the non-equivalent gaps $\varepsilon = 0$ and $\varepsilon = \hbar\omega/2$. In the regime of frequencies of the order of the bandwidth, $\hbar\omega \sim t$, calculating the Chern number and the number of edge states necessitates a more complicated numerical treatment because the number of anti-crossings between the original bands increases as the frequency decreases. If the frequency is small compared to the the bandwidth $\hbar\omega \ll t$, one can model low-energy graphene using the Dirac equation, and obtain spectra with rotational invariance around $\mathbf{q} = 0$. In that case, the original bands of graphene dressed by the electromagnetic wave

generate anti-crossings at momentum $q_n = n\omega/2v$, leading to dynamical gaps (see Figs. 3.5). Each of these anti-crossings corresponds to a band inversion and hosts chiral edge states [96]. In this section, we compute the Berry curvature and the Chern number of irradiated graphene at the different anti-crossings. In the Floquet formalism, the Berry curvature is now expressed as a time-averaged quantity [10] :

$$\boldsymbol{\mathcal{A}}^{\alpha}(\mathbf{k}) = i\langle\langle u^{\alpha}_{\mathbf{k}}|\nabla_{\mathbf{k}}|u^{\alpha}_{\mathbf{k}}\rangle\rangle = i\sum_{n}\langle u^{\alpha}_{\mathbf{k}n}|\nabla_{\mathbf{k}}|u^{\alpha}_{\mathbf{k}n}\rangle \tag{3.64}$$

In Sec. a), we compute the Berry curvature numerically as a function of the momentum $\mathbf{q}$ relative to the Dirac point. In Sec. b), we derive an effective two-band Hamiltonian close to the band crossing at $q = \hbar\omega/2v$ and calculate the associated Chern number.

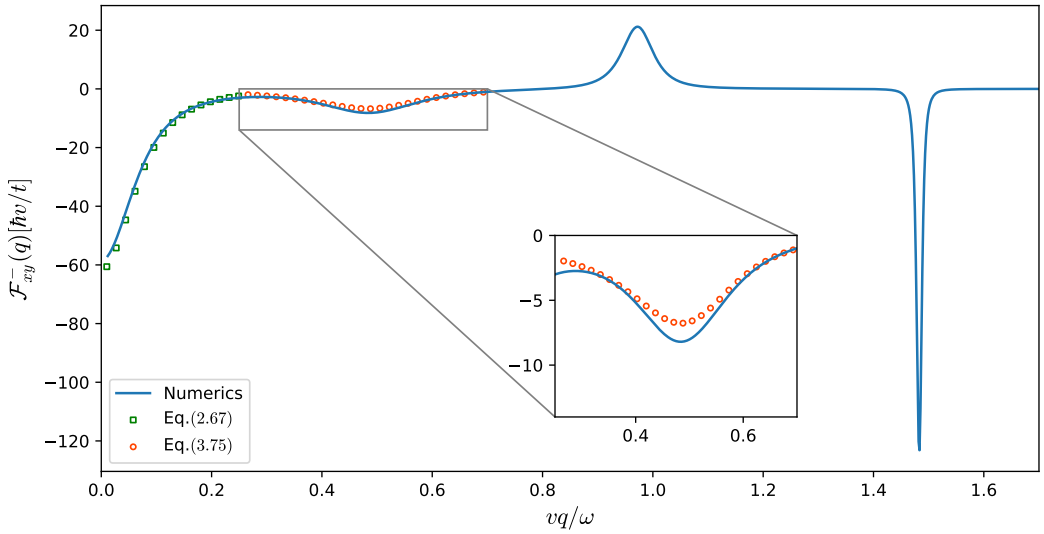

Figure 3.8 – Berry curvature of the quasi-energy band $\varepsilon_{-}(\mathbf{q})$ calculated numerically as a function of the modulus of the momentum $q = |\mathbf{q}|$ for polarization $\chi = +1$ and driving strength $\beta = 0.3$. The curve is identical for both valleys $\xi = \pm 1$. We can see that the Berry curvature is peaked at momentum $q_n = n\omega/2v$. The green squares corresponds to the Berry curvature associated with the Haldane gap at $\mathbf{q} = 0$ fitted using Eq. (2.83) with a Haldane mass $M_H/\hbar\omega = -\beta^2$. The red circles corresponds to the peak in the Berry curvature calculated with the effective Hamiltonian near the band crossing at $q = \omega/2v$ between the replicas $n = 0$ and $n = -1$ such that the Berry curvature equals Eq. (3.76).

a) Berry curvature around the Dirac point

Because the Hamiltonian has rotational symmetry around the Dirac point, it is convenient to use polar coordinates. In this system of coordinates, the Berry curvature can be expressed as :

$$\mathcal{F}^{-}_{\varphi q}(q,\varphi) = \frac{i}{q}\langle\langle\partial_{\varphi}u^{-}_{\mathbf{q}}|\partial_{q}u^{-}_{\mathbf{q}}\rangle\rangle - \frac{i}{q}\langle\langle\partial_{q}u^{-}_{\mathbf{q}}|\partial_{\varphi}u^{-}_{\mathbf{q}}\rangle\rangle \tag{3.65}$$

$$= \frac{2}{q}\mathrm{Im}\langle\langle\partial_{\varphi}u^{-}_{\mathbf{q}}|\partial_{q}u^{-}_{\mathbf{q}}\rangle\rangle \tag{3.66}$$

Fig. 3.8 shows the Berry curvature of the quasi-energy band $\varepsilon_-(\mathbf{q})$ as a function of the norm of the momentum $q = |\mathbf{q}|$. We observe a series of peaks when q is a multiple of $n\omega/2v$. The peak at $q = 0$ and at $q = n\omega/2v$ for $n \geq 1$ have different origins.

The peak at $q = 0$ corresponds to Berry curvature generated by the effective Haldane mass term in the Dirac equation that we studied in Chap. 2. The Berry curvature is peaked at the Dirac point and decreases away from it with a characteristic decay length $M_H/\hbar v$. The green empty squares on Fig. 3.8 are calculated using the expression for the Berry curvature of the Haldane model near a Dirac point as given by Eq. (2.83) with a Haldane mass :

$$M_H = -\beta^2 \hbar\omega \tag{3.67}$$

The sign of the Berry curvature at $q = 0$ indicates that the Haldane mass term is negative, which corresponds to a Chern number $c^- = -1/2$ per valley and therefore to a total Chern number $C = -1$ for polarization $\chi = +1$.

b) Effective Chern number near the band crossing Δ_1

The peaks at $n\omega/2v$ for $n \geq 1$ happen around the anti-crossings between the valence band and conduction bands of graphene dressed with $|n - n'|$ photons. To understand the origin of these peaks, we consider the peak at $q = \omega/2v$ which corresponds to the gap Δ_1 located at quasi-energy $\varepsilon = \hbar\omega/2$. For $q < \omega/2v$, the quasi-energy band $\varepsilon_+(q)$ is made of the original conduction band of graphene, while for $q > \omega/2v$, it is made of the valence band dressed with one photon. Thus, as q increases, the spinor switches from a conduction band spinor $(1, e^{i\varphi})^T$ to a valence band spinor $(1, -e^{i\varphi})^T$, which leads to a non-trivial winding of the wavefunction. The same mechanism happens for all the gaps : near an anti-crossing, the quasi-energy band switches from a valence-type band to a conduction-type band, or inversely, which in turn generates a non-zero Berry curvature. For weak driving, each of these peaks are well separated for each other and one can compute an effective Hamiltonian near a band crossing [95].

To picture this non-trivial winding of the vector $\mathbf{d}(\mathbf{q})$ near a band crossing, we derive an effective 2×2 Hamiltonian near the gap Δ_1 at $\varepsilon = \hbar\omega/2$. To do so, we keep only the replicas $m = 0$ and $m = 1$ of Eq. (3.57), hence a 4×4 Hamiltonian. Next, we rotate the Hamiltonian to its diagonal basis using the unitary operator :

$$P_\xi = \begin{pmatrix} 1 & 1 \\ e^{i\xi\varphi} & -e^{i\xi\varphi} \end{pmatrix}, \tag{3.68}$$

where $\varphi = \arctan(q_y/q_x)$. After these operations, the Hamiltonian is equal to :

$$\tilde{H}_\xi(\mathbf{q}) = P_\xi^\dagger H_\xi(\mathbf{q}) P_\xi = \begin{pmatrix} vq + \omega & 0 & \xi\frac{evA_0}{2}e^{-i\varphi} & \frac{evA_0}{2}e^{-i\varphi} \\ 0 & -vq + \omega & -\frac{evA_0}{2}e^{-i\varphi} & -\xi\frac{evA_0}{2}e^{-i\varphi} \\ \xi\frac{evA_0}{2}e^{i\varphi} & -\frac{evA_0}{2}e^{i\varphi} & vq & 0 \\ \frac{evA_0}{2}e^{i\varphi} & -\xi\frac{evA_0}{2}e^{i\varphi} & 0 & -vq \end{pmatrix}, \tag{3.69}$$

where $q = |\mathbf{q}|$. Around the gap Δ_1, the driving couples the bands at energy vq and $-vq + \omega$. We restrict ourselves to the two levels that cross at $q = \omega/2v$. Therefore, the effective Hamiltonian around Δ_1 is a 2×2 matrix which correspond to the subspace of these two bands coupled by the driving, namely :

$$H_{\text{eff}}(\mathbf{q}) = \begin{pmatrix} -vq + \omega & -\frac{evA_0}{2}e^{-i\varphi} \\ -\frac{evA_0}{2}e^{i\varphi} & vq \end{pmatrix}, \tag{3.70}$$

which is identical in both valleys. This Hamiltonian can be expressed as $H_{\text{eff}}(\mathbf{q}) = \varepsilon_0(\mathbf{q}) + \mathbf{d}(\mathbf{q}).\boldsymbol{\sigma}$ with :

$$\varepsilon_0(\mathbf{q}) = \frac{\hbar\omega}{2}, \quad \text{and} \quad \mathbf{d}(\mathbf{q}) = \begin{pmatrix} -\frac{evA_0}{2}\cos(\varphi_{\mathbf{q}}) \\ -\frac{evA_0}{2}\sin(\varphi_{\mathbf{q}}) \\ \frac{\omega}{2} - vq \end{pmatrix}. \tag{3.71}$$

The eigenvalues of this Hamiltonian are given by :

$$\varepsilon_{\pm}(\mathbf{q}) = \omega/2 \mp d(\mathbf{q}), \tag{3.72}$$

$$d(\mathbf{q}) = \sqrt{(vq - \omega/2)^2 + \left(\frac{evA_0}{2}\right)^2}, \tag{3.73}$$

where the minus sign in (3.72) originates from the fact that the conduction band of the effective Hamiltonian corresponds the quasi-energy band $\varepsilon_-(\mathbf{q})$, while the band with negative energy corresponds to $\varepsilon_+(\mathbf{q})$. This dispersion relation is analogous to a massive Dirac dispersion relation with a mass $M_{\text{eff}} = evA_0/2$. The effective mass is consistent with the size of the gap $\Delta_1 = 2M_{\text{eff}} = \beta\hbar\omega$ obtained in Sec. 3.3.

The effective vector $\mathbf{d}(\mathbf{q})$ can be parametrized by the angles $\theta_{\mathbf{q}}$ and $\varphi_{\mathbf{q}}$ of the Bloch sphere introduced in Eq. (2.32) in analogy with the Haldane model. When $q \to \infty$, we have $\cos(\theta_{\mathbf{q}}) = -1$ and the vector $\mathbf{d}(\mathbf{q})$ points towards the south pole. It is tempting to argue that when $q \to -\infty$, we have $\cos(\theta_{\mathbf{q}}) = 1$, so $\mathbf{d}(\mathbf{q})$ points towards the north pole, but of course, here, the limit $q \to -\infty$ is not relevant because we consider the modulus of the vector $\mathbf{q}$. However, in the limit $\beta \to 0$, the north pole is reached for $q < \omega/2v$ and the south pole for $q > \omega/2v$. For $q = \omega/2v$, the vector $\mathbf{d}(\mathbf{q})$ is at the equator. Thus, in the limit of vanishing β, we can see that the vector $\mathbf{d}(\mathbf{q})$ switches from the south pole to the north pole as q passes through $\omega/2v$. When the angle φ winds around the Dirac point at momentum q, the vector $\mathbf{d}(\mathbf{q})$ winds around the Bloch sphere at latitude $\cos\theta_{\mathbf{q}}$. Therefore, the effective Hamiltonian has a non-trivial winding around the sphere when varying $\mathbf{q}$. In the north gauge, the Bloch vector $|u^{-N}_{\mathbf{q}}\rangle$ of the quasi-energy band $\varepsilon_-(\mathbf{q})$ near this band crossing corresponds to the Bloch vector of the conduction band (2.34) of the effective Hamiltonian :

$$|u^{-N}_{\mathbf{q}}\rangle = \begin{pmatrix} \cos\frac{\theta}{2}e^{i\varphi} \\ \sin\frac{\theta}{2} \end{pmatrix}. \tag{3.74}$$

Thus the Berry connection in the north gauge has the expression :

$$\boldsymbol{\mathcal{A}}^{N-}(\mathbf{q}) = -\sin^2\left(\frac{\theta_{\mathbf{q}}}{2}\right)\nabla\varphi_{\mathbf{q}} = -\frac{1}{2q}\left(1 + \frac{vq - \omega/2}{\sqrt{(vq - \omega/2)^2 + (\beta/2)^2}}\right)\mathbf{e}_{\varphi}, \tag{3.75}$$

and the Berry curvature equals :

$$\mathcal{F}^{-}_{xy}(k) = -\frac{v}{2q}\left(\frac{\beta}{2}\right)^2\left((vq - \omega/2)^2 + \left(\frac{\beta}{2}\right)^2\right)^{-3/2}. \tag{3.76}$$

This expression is plotted as the red circles on Fig. 3.8. We can see that it fits approximately the numerical estimation (blue line) for the Berry curvature. As we have done earlier for the case of a single Dirac cone, we wish to derive an explicit expression for the Chern number of the effective Hamiltonian (3.70) considered as an isolated system, which

is the case for $\beta \to 0$. We find that the Chern number carried by the anti-crossing in the gap Δ_1 equals :

$$c^-_{1,\xi} = -\frac{1}{2}\left(1 + \frac{1}{\sqrt{1+\beta^2}}\right), \tag{3.77}$$

for which we find $c^-_{1,\xi} = -1$ to first order in β for polarization $\chi = 1$. This Chern number is identical in both valleys, and therefore, the total Chern number of the band $\varepsilon_-(\mathbf{q})$ associated to the gap Δ_1 is :

$$c^-_1 = -2. \tag{3.78}$$

We have seen that an anti-crossing generates a band inversion, which in turn leads to a winding of the vector $\mathbf{d}(\mathbf{q})$ around the Bloch sphere and a peak in the Berry curvature. We have considered the case of a single anti-crossing corresponding to the gap Δ_1 at $q = \omega/2v$. For $q < \omega/2v$, the quasi-energy $\varepsilon_-(\mathbf{q})$ band corresponds to the conduction band of graphene, and the vector $\mathbf{d}(\mathbf{q})$ points towards the north pole in the limit $\beta \to 0$. For $q > \omega/2v$, the quasi-energy band $\varepsilon_-(\mathbf{q})$ corresponds to the valence band of graphene dressed with one photon, and the vector $\mathbf{d}(\mathbf{q})$ points now towards the south pole.

Extending this reasoning to each anti-crossing of the quasi-energy band, we expect that for the crossings at quasi-energy $\varepsilon = \hbar\omega/2$, the vector $\mathbf{d}(\mathbf{q})$ switches from the north pole to the south pole, which leads to a negative peak in the Berry curvature and a local negative Chern number associated with the crossing. At the crossings at $\varepsilon = 0$, the vector $\mathbf{d}(\mathbf{q})$ switches from the south pole to the north pole, which leads to a positive peak in the Berry curvature, and we expect a positive Chern number associated with the crossing. This analysis is consistent with the numerical calculation of the Berry curvature as shown on Fig. 3.8. The calculation of the Chern number associated with each anti-crossing was done analytically in Ref. [95] using a projected green's function technique to obtain an effective Hamiltonian near each crossing. Our calculation for the first anti-crossing and the qualitative analysis for the next anti-crossings is consistent with their results.

3.5 Edge states

We now consider the edge states of the irradiated graphene sheet. At low-energy, it is relevant to use the Dirac equation to obtain the dispersion relation of the edge states. We use the Berry-Mondragon boundary conditions as introduced in Chap. 2 for the Haldane model.

We consider a ribbon of width W along y and infinite along x so the longitudinal wavevector k_x is a good quantum number. The procedure consists in fixing the momentum k_x and finding the energy of the eigenstates that satisfy the boundary conditions. We multiply the Hamiltonian (3.57) by σ_y and rearrange to obtain :

$$\sum_n \left[\left(\left(\varepsilon - m\hbar\omega\right)\sigma_y + i\xi\hbar v k_x \sigma_z\right)\delta_{mn} - \sigma_y V_1^\xi \delta_{m,n-1} - \sigma_y V_{-1}^\xi \delta_{m,n+1}\right] u_n^\alpha(y) = \hbar v q_\alpha u_m^\alpha(y), \tag{3.79}$$

where q_α represents the transverse wavevector that can be imaginary. A state corresponding to the wavevector q_α has the form $\Phi^\alpha(y,t)e^{ik_x x}$ with :

$$\Phi^\alpha(y,t) = e^{iq_\alpha y}\sum_n u_m^\alpha e^{im\omega t}, \tag{3.80}$$

As we have said previously, one needs to apply a cut-off in order to diagonalize Eq. (3.79). There exists therefore $2(2M+1)$ eigenstates, and a Floquet state with quasi-energy ε is

a superposition of these states with weights a_α such that :

$$\Psi_\varepsilon(y,t) = e^{-i\varepsilon t} \sum_{\alpha=1}^{2(2M+1)} a_\alpha e^{iq_\alpha y} \sum_m u_m^\alpha e^{im\omega t}, \tag{3.81}$$

and $\alpha \in [1, 2(2M+1)]$.

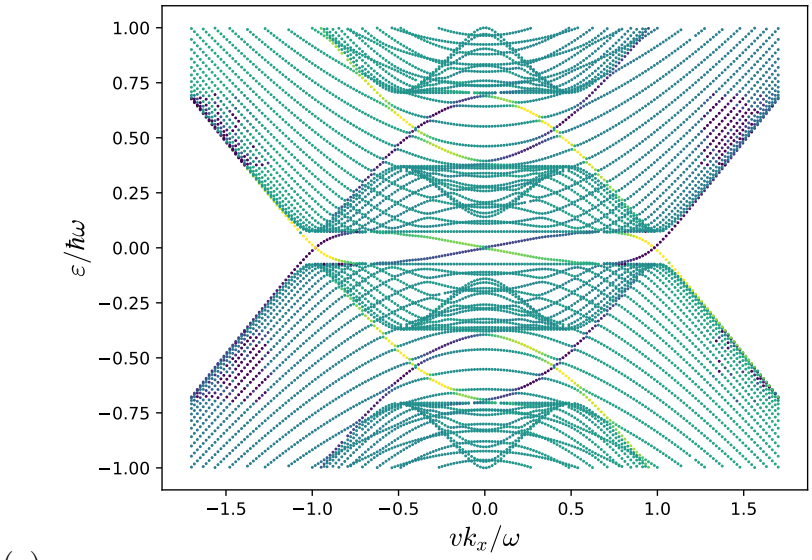

(a)

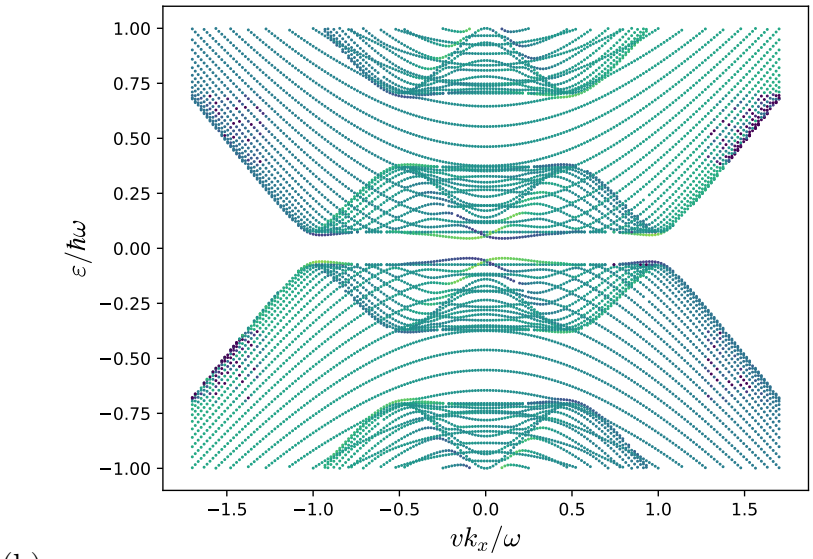

(b)

Figure 3.9 – Dispersion relation of graphene nanoribbons of width $W = 33l_\omega$ and driving strength $\beta = 0.4$ for polarization $\chi = 1$ using $M = 1$ Floquet replicas in (a) valley $\mathbf{K}'$ and (b) valley $\mathbf{K}$. We observe chiral edge states bridging the gaps $\varepsilon = 0$ and $\varepsilon = \hbar\omega/2$ in valley $\mathbf{K}'$.

To find the eigenstates, we need to impose the boundary conditions on Eq. (3.81). The Berry-Mondragon boundary conditions imply the following restriction on the spinors at the boundaries :

$$\Psi^A(y=0,t) = \Psi^B(y=0,t), \tag{3.82}$$
$$\Psi^A(y=W,t) = -\Psi^B(y=W,t), \tag{3.83}$$

which must be valid at any time t. Identifying to Fourier components of Eq. (3.81), we find :

$$\sum_\alpha a_\alpha (u_m^{A,\alpha} - u_m^{B,\alpha}) = 0, \tag{3.84a}$$

$$\sum_\alpha a_\alpha (u_m^{A,\alpha} + u_m^{B,\alpha}) e^{iq_\alpha W} = 0, \tag{3.84b}$$

which must be valid for all $m \in [-M, M]$. This is an homogeneous matrix equation with $2(2M+1)$ equations and $2(2M+1)$ unknown coefficients a_α. Eq. (3.84) can be written in matrix form :

$$M(\varepsilon, k_x)\mathbf{a} = 0, \tag{3.85}$$

where $\mathbf{a} = (a_1, ..., a_{2(2M+1)})$ is the vector composed of the coefficients a_α. ε is an eigenlevel when the determinant of the matrix $M(\varepsilon, k_x)$ is zero :

$$\det(M(\varepsilon, k_x)) = 0 \quad \Leftrightarrow \quad \varepsilon(k_x) \text{ is an eigenlevel} \tag{3.86}$$

The procedure to find the eigenstates and eigenvectors numerically consists in setting a longitudinal momentum k_x, and to vary ε.

Fig. 3.9 shows the dispersion relation of graphene nanoribbons with $M = 1$ Floquet replicas in the valleys K and K'. We observe the central replica $n = 0$ and the two sidebands dressed with $n = +1$ and $n = -1$ photons. We observe the gap Δ_0 at $k_x = 0$ with size $\Delta_0 \hbar\omega = 2\beta^2$ which originates from the second order process of emission and re-absorption of virtual photons. Also, at $\varepsilon = 0$, we observe the gap Δ_2 of size $\Delta_2/\hbar\omega = \beta^2$, which originates from the coupling of the $n = +1$ and $n = -1$ replicas. Finally, we observe the gaps at $\varepsilon = \pm\hbar\omega/2$, originating from the coupling between the $n = 0$ and $n = \pm 1$ replicas. Inside these gaps, we observe propagative states which correspond to bulk state of the $n = \pm 1$ replicas. These states have a small contribution on the time-average density of state $\bar{\rho}(\varepsilon) = \langle\langle \Psi_\varepsilon | \Psi_\varepsilon \rangle\rangle$. We haven't represented more replicas, because as we increase the number of replicas, there exists more propagative states that belong to the additional replicas.

For $\chi = 1$, we observe edge states only in valley K'. This can be understood using the same reasoning as explained for the edge states of the Haldane model. Berry-Mondragon boundary conditions correspond to an interface with a trivial insulator and if the gaps are inverted in valley K', then the edge states are polarized in this valley. We observe chiral edge states bridging the non equivalent gaps Δ_0 and $\Delta_{\hbar\omega/2}$. The edge states in the inequivalent gaps all have the same chirality, namely they rotate clockwise around the sample.

Figs. 3.10 shows the weight of the wavefunction on the nth Floquet replica for the different edge states corresponding to the red dot in the inset such that :

$$\Psi_m(y) = \sum_{\alpha=1}^{2(2M+1)} a_\alpha u_m^\alpha e^{iq_\alpha y} \tag{3.87}$$

In the gap at $\varepsilon = 0$ (Fig. 3.9), there are three edge states : one edge state centered on $k_x = 0$, and two lateral edge state that live close to the gap Δ_2 at $k_x = \pm\omega/v$. From the analysis of the Chern number carried by the gaps in Sec. 3.4, we can postulate that each edge state is associated to a band inversion.

The edge state centered on $k_x = 0$ that links the gaps at $k_x = \pm\omega/v$ originates from the inverted Haldane-like gap Δ_0 in the dispersion relation. There is only one edge state and

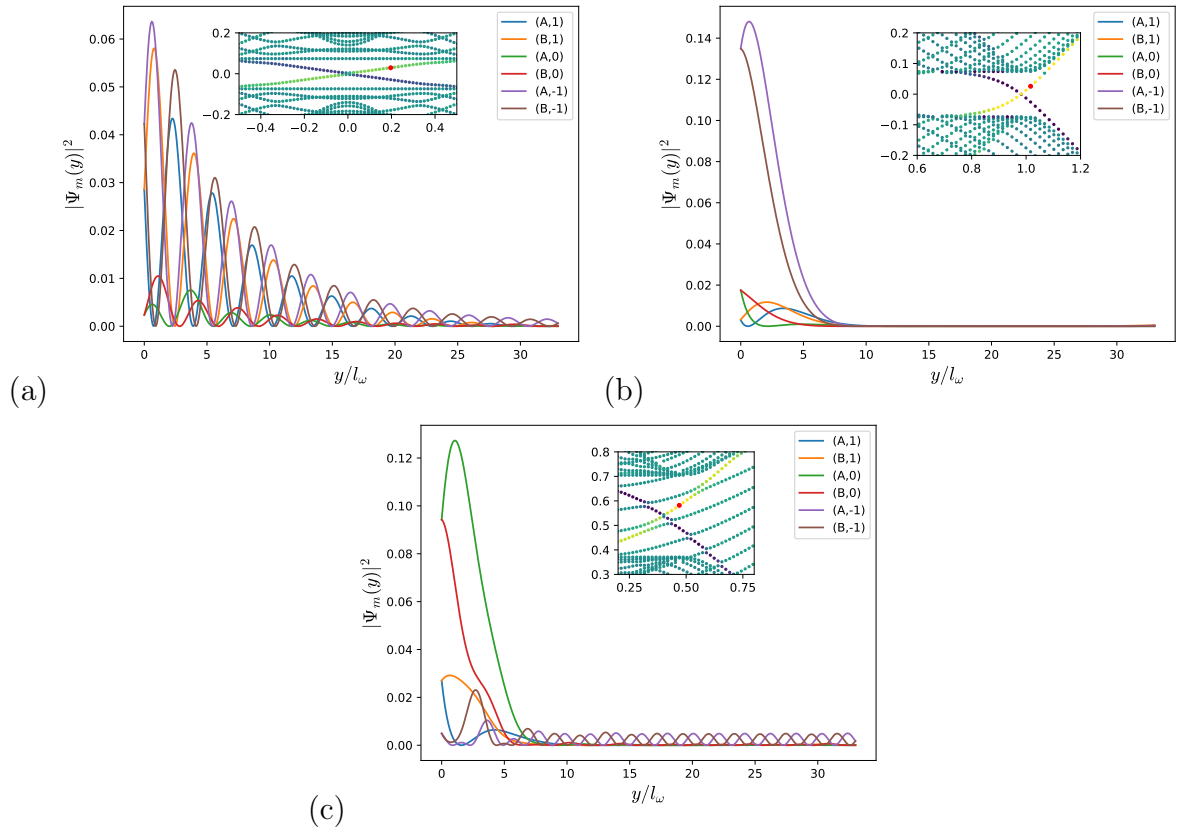

Figure 3.10 – Wavefunction $\Psi_m(y)$ of the edge states at the edge $y = 0$ for $W = 33l_\omega$ and $\beta = 0.4$ with energy and momentum corresponding to the red dot in the inset. The label (μ, m) correspond to the weight of the wavefunction on the sublattice $\mu = A, B$ and on the mth Floquet replica according to Eq. (3.87). For (a), the weight of the wavefunction is mainly on the replicas $n = +1$ and $n = -1$, it has long characteristic length and shows oscillations. For (b) the weight of the wavefunction is mainly on the replica $n = -1$. The wavfunction is localized much closer to the edge. For (c), the weight in mainly in the replica $n = 0$.

thus we expect this edge state to be associated with the Chern number $c_- = -1$ carried by the gap Δ_0. We can see from Fig. 3.10.(a) that this edge state has weight mainly on the $n = 1$ and $n = -1$ Floquet sidebands which is consistent with the fact that it originates from a second order process of emission and re-absorption of a virtual photon. This edge state presents an oscillatory behaviour, which means that the wavevectors q_α have a non-zero real part. Because they have a long penetration length, they are prone to backscattering between the edges.

The lateral edge states at quasi-energy $\varepsilon = 0$ and momentum $k_x = \pm\omega/v$ are associated to the gap Δ_2 of Fig. 3.5 which originates from the coupling between the $n = 1$ and $n = -1$ replicas. The weight of the edge state at $y = 0$ is located mainly over the $n = -1$ replica. We observe that the edge states located close to $k_x = -\omega/v$ has weight mainly on the $n = 1$ replica. These states are localized closer to the edge than the central edge state. They are associated with the band inversion that occurs at the anti-crossing between the $n = -1$ and $n = 1$ replicas.

Finally, the edge state in the gap Δ_1 at $\varepsilon = \hbar\omega/2$ and $k_x = \omega/2v$ is represented on Fig. 3.10.(c). We can see that the edge state at $y = 0$ has weight on the $n = 0$ sideband. The

other edge state at $y = W$ (not represented here) has weight on the $n = 1$ sideband. These edge states originate from the coupling between the $n = 0$ and $n = 1$ Floquet replicas and are associated to the gap Δ_1 in the spectrum. They present a similar shape as the lateral edge states at $\varepsilon = 0$, because they also originate from the band inversion occuring at $\varepsilon = \hbar\omega/2$ and $k = \pm\omega/2v$. The number of edge states correspond to the local Chern number $c_1 = -2$ calculated in Sec. 3.4.

4 Conclusion

In this chapter, we have considered irradiating graphene with a circularly polarized electromagnetic wave. We used the formalism of the Floquet theory to investigate the features of graphene under a periodic driving. Because the Hamiltonian is time-dependent, the energy is not a good quantum number. However, due to the time-periodicity of the Hamiltonian, one can define quasi-energies that are periodic in $\hbar\omega$. In the Floquet formalism, the electrons are dressed coherently by the photons which leads to an infinite number of sidebands separated by multiples of $\hbar\omega$. The driving couples these replicas, which in turn opens some gaps and one obtain reshuffled Floquet bands in the first Floquet zone $[-\hbar\omega/2, \hbar\omega/2]$.

For driving frequencies much larger than the bandwidth, it is possible to define an effective time-independent Hamiltonian dressed by the driving. For graphene, this Hamiltonian is similar to the Hamiltonian of the Haldane model, with a gap characterized by opposite sign in the valleys. The effective bands possess a non-zero Chern number which in turn leads to the appearance of topologically protected edge states bridging the gap. Upon decreasing the frequency, resonances between the valence and the conduction band are allowed and gaps open at $\varepsilon = \pm\hbar\omega/2$, leading to a band inversion. Due to these band inversions, there is an exchange of Chern number and additional edge states appear at the Floquet zone edges. For a frequency on-resonance with the bandwidth of graphene, the Floquet bands can be very complex with multiple edge states bridging the non-equivalent gaps $\varepsilon = 0$ and $\varepsilon = \hbar\omega$.

For irradiated system, a new kind of invariant was developed to characterize the topological properties of these systems. This invariant is defined for a gap and counts the number of edge states living inside this gap. The Chern number of the band is equal to the difference of the number of chiral edge states in the gaps above and below this band. Using this definition, we calculated the Chern number of irradiated graphene by plotting the dispersion relation of an irradiated ribbon of graphene and counting the number of edge states.

When the frequency is small compared to the bandwidth of graphene, it is possible to model graphene using the Dirac equation. In this scheme, the original Dirac cone dressed with different number of photons couples at $\varepsilon = 0$ and $\varepsilon = \hbar\omega/2$ and a set of nested gaps appear as a function of the momentum. Each gap is associated to an exchange of n photons and its size is proportional to β^n for weak driving where β is the driving strength. It is possible to define an effective Chern number for each gap, and we observe edge state associated with each gap. The wavefunction has weight mainly on the replicas which couple at the band crossing.

Chapter 4

Electronic transport in irradiated graphene

In this chapter, we suggest the use of DC transport measurements to investigate the features of the Floquet quasi-energy spectrum in coherent driven electronic graphene. We compute the conductance of graphene transistors driven by an electromagnetic wave, typically in the terahertz (THz) or infrared (IR) range. Indeed photon energies in the range $10 - 100$ meV can be matched by chemical potential variations in typical graphene samples. Recently, photon-assisted shot-noise has been studied experimentally in coherent diffusive graphene samples irradiated in the THz range [97]. Graphene is also a very promising platform for detection of light in a wide range of frequencies [98].

We consider a graphene based field effect transistor (gFET), whose conduction channel is irradiated by a circularly polarized electromagnetic wave at normal incidence (Fig. 4.1). The carrier density (in absence of irradiation) can be tuned using a DC electrostatic backgate. The source and drain leads are heavily doped and are not irradiated. The two-terminal differential conductance is studied as a function of the irradiation strength, chemical potential μ in the central region, and photon energy $\hbar\omega$ for various lengths L and widths W of the graphene ribbon.

To calculate the conductance of the sample in the presence of a scatterer, we use Landauer formalism. This formalism allows to obtain the conductance of a sample using the expression of the wavefunction of the electrons. In the scattering formalism, the reservoirs are modelled by semi-infinite leads with a much larger number of modes than the scattering region. By matching the wavefunctions of the states at the interfaces, it is possible to obtain the transmission probability of an electron through the scattering region. From these transmissions, it is possible to have the conductance.

In Sec. 1, we review the non-irradiated case following Ref. [99]. In Sec. 2, we explain the extension of the formalism used in the first section to the case of an irradiated ribbon. In Sec. 3, we present results for the minimal conductivity and the conductance as a function of the chemical potential for various values of the parameters of the system. Finally, in Sec. 4, we discuss the experimental range parameters required to observe these characteristic features.

1 Non-irradiated ribbon

We describe here the model used by Tworzydlo *et al.* [99] to obtain the conductance of a graphene sample as a function of the chemical potential. The scattering region consists

of a sheet of graphene of length L along the x direction and width W along y, with a chemical potential μ that can be tuned by a remote gate. The leads are modelled as highly-doped graphene at chemical potential μ_∞ such that $\mu_\infty \gg |\mu|$. The interfaces are located at $x = 0$ and $x = L$. The upper panel in Fig. 4.1 represents the 2D ribbon of graphene with the source and drain leads separated by the scattering region, while the lower panel represents the dispersion relation of the three region at the different chemical potentials.

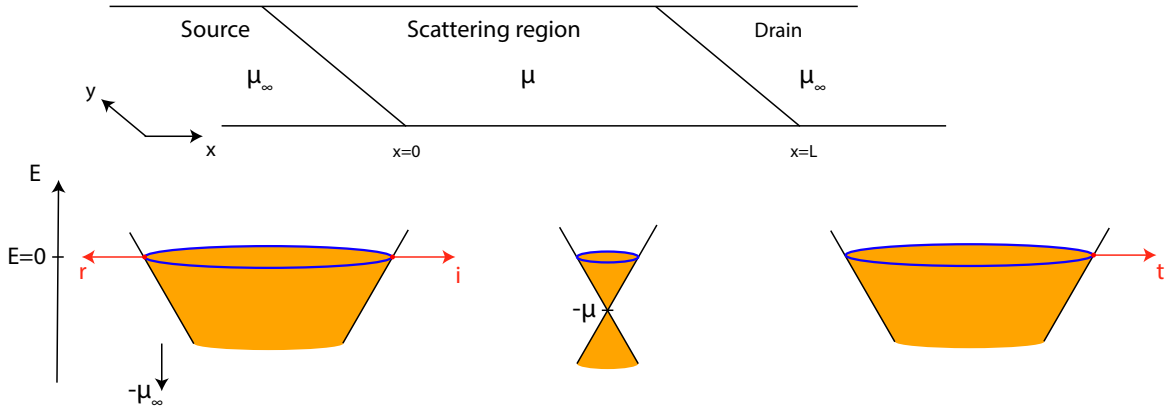

Figure 4.1 – Scattering model. The upper panel represents the three different regions of the ribbon with different chemical potential. The interfaces are located at $x = 0$ and $x = L$. The source and drain leads have chemical potential $\mu_\infty \gg \mu$, while the chemical potential μ of the central region can be tuned by a gate voltage.

We model graphene using the continuum description given by the Dirac equation. The solution of the Dirac equation corresponds to the envelope wavefunction of the electron relative to the Dirac point. We consider that the valleys are decoupled and spinless electrons. The total conductance will be four times the single valley and spin conductance.

In Sec. 1.1, we define the scattering states in the three regions. In Sec. 1.2, we match them to obtain the transmission and reflection probabilities. In Sec. 1.3, we obtain the conductance of the sample as a function of the chemical potential. Finally, in Sec. 1.4, we present the state of the art concerning transport in ballistic graphene.

1.1 Scattering states

The propagation of the electrons in the system is confined by the large but finite width of the sample along y. Depending on the detail of the microscopic boundary of the sheet, there exist different boundary conditions for the Dirac electrons that impose different quantization on the transverse wavevector. The detail of the boundary conditions has consequences when calculating the conductance of narrow ribbons [99]. However, we consider here a ribbon with a large width compared to the lattice spacing, so the microscopic details don't matter. Thus, for simplicity, we apply periodic boundary conditions along y, so the transversal wavevector k_y is a good quantum number. It is quantized as :

$$k_y = \frac{2\pi n_y}{W} \tag{4.1}$$

where $n_y \in \mathbb{Z}$. The scattering process doesn't mix the modes labelled by k_y so they can be considered as independent channels. In contrast to k_y and μ, the longitudinal wave-vector

k_x is not a good quantum number because the system is not translationally invariant along the x-axis. In the following, all the two-component wave functions are written as $\Phi(x,y,t) = \Phi(x,t)e^{ik_y y}$, and we will work with the $\Phi(x,t)$ wave functions (k_y being omitted) corresponding to the effective 1D transport problem at a given k_y. In order to calculate the two-terminal conductance, we need to match the wave functions at the interfaces $x = 0$ and $x = L$.

The wavefunction can be expressed in each region separately considering that the region is infinite. Thereby, although k_x is not conserved globally, we can still define it in each region separately. Moreover, k_x can be imaginary which corresponds to the case of an evanescent wave along x. According to Eq. (1.26), the eigenvectors of the Dirac equations are :

$$\Phi_s(x) = \begin{pmatrix} 1 \\ se^{i\varphi} \end{pmatrix} e^{ik_x x} \quad \text{with :} \quad \varphi = \arctan\left(\frac{k_y}{k_x}\right). \tag{4.2}$$

and $s = \pm$ is the band index. In the absence of inelastic scattering events, the energy of the electrons is conserved, all the physics happens thereby at the Fermi level. Here, the chemical potential μ allows us to tune the Fermi level, so we consider scattering happening at energy $E = 0$. From the eigenvalue equation (1.36), we obtain the relation :

$$\mu = \pm\hbar v k_F, \tag{4.3}$$

where $k_F = |\mathbf{k}|$ is the Fermi wavevector.

In the leads, at $E = 0$, we have the relation $\mu_\infty = \hbar v\sqrt{k_x^2 + k_y^2} \gg |\mu|$. However in the central region, we restrict ourselves to transverse momenta such that $k_y \sim \mu/\hbar v$, therefore, the scattering states in the leads have a longitudinal momentum :

$$k_x^\infty \approx \pm\frac{\mu_\infty}{\hbar v}. \tag{4.4}$$

Therefore, in the leads, the wavefunction for the right (+) and left (−) going solutions have the expression :

$$\Phi_{k_y}^{\pm}(x) = \frac{1}{\sqrt{2}}\begin{pmatrix} 1 \\ \pm 1 \end{pmatrix} e^{\pm ik_x^\infty x}. \tag{4.5}$$

We can see that the expression for the spinor is independent of k_y.

We consider a right-going electron originating from the left lead. It has the probability amplitude to be reflected equal to r, therefore the wavefunction of the electron in the left lead is :

$$\Psi^L(x) = \frac{1}{\sqrt{2}}\begin{pmatrix} 1 \\ 1 \end{pmatrix} e^{ik_x^\infty x} + \frac{r}{\sqrt{2}}\begin{pmatrix} 1 \\ -1 \end{pmatrix} e^{-ik_x^\infty x}, \tag{4.6}$$

where $k_x^\infty = \frac{\mu_\infty}{\hbar v}$. In the right lead, the wavefunction consists of a right going electron with transmission amplitude t :

$$\Psi^R(x) = \frac{t}{\sqrt{2}}\begin{pmatrix} 1 \\ 1 \end{pmatrix} e^{ik_x^\infty (x-L)}, \tag{4.7}$$

where we added the phase factor $e^{-ik_x^\infty L}$.

In the scattering region S, for a fixed k_y, the wavefunction is a superposition of a left and right going solutions with amplitudes a and b :

$$\Psi_{k_y}^S(x) = a\begin{pmatrix} 1 \\ e^{i\varphi} \end{pmatrix} e^{ik_x x} + b\begin{pmatrix} 1 \\ -e^{-i\varphi} \end{pmatrix} e^{-ik_x x}, \tag{4.8}$$

with $k_x^S = \sqrt{\left(\frac{\mu}{\hbar v}\right)^2 - k_y^2}$, and $\varphi = \arctan\left(\frac{k_y}{k_x}\right)$.

1.2 Transmission and reflection probabilities

Our goal is to obtain the transmission and reflection coefficients t and r. Because the Dirac equation is of first order in the space derivatives, only the wavefunction is needed at the boundaries, and not its derivative. However, because the wavefunction is a spinor, both its components need to be matched at the interfaces at $x = 0$ and $x = L$. At $x = 0$, we have $\Psi^L(x = 0) = \Psi^S(x = 0)$ which gives the equations :

$$1 + r = a + b, \tag{4.9}$$
$$1 - r = ae^{i\varphi} - be^{i\varphi}. \tag{4.10}$$

At $x = L$, we have $\Psi^S(x = L) = \Psi^R(x = L)$ gives us :

$$ae^{ik_xL} + be^{-ik_xL} = t, \tag{4.11}$$
$$ae^{ik_xL}e^{i\varphi} - be^{-ik_x^SL}e^{-i\varphi} = t. \tag{4.12}$$

Solving this non-homogeneous linear system of equation gives :

$$t = \frac{k_x}{k_x\cos(k_xL) - i\frac{\mu}{\hbar v}\sin(k_xL)}, \tag{4.13}$$
$$r = \frac{-k_y\sin(k_xL)}{k_x\cos(k_xL) - i\frac{\mu}{\hbar v}\sin(k_xL)}, \tag{4.14}$$

where we have used the fact that $\cos(\varphi) = \hbar v k_x/\mu$ and $\sin(\varphi) = \hbar v k_y/\mu$. The transmission probability is the modulus square of the transmission amplitude. The transmission and reflection probabilities for the propagative states are :

$$T_{k_y}^{(p)}(\mu) = |t|^2 = \frac{k_x^2}{k_x^2\cos(k_xL)^2 + \left(\frac{\mu}{\hbar v}\right)^2\sin(k_xL)^2} \text{ with : } k_x = \sqrt{\left(\frac{\mu}{\hbar v}\right)^2 - k_y^2}, \tag{4.15}$$
$$R_{k_y}^{(p)}(\mu) = |r|^2 = \frac{k_y^2\sin(k_xL)^2}{k_x^2\cos(k_xL)^2 + \left(\frac{\mu}{\hbar v}\right)^2\sin(k_xL)^2}. \tag{4.16}$$

Current conservation implies that for every k_y we must have $R_{k_y} + T_{k_y} = 1$, which can be easily checked. These probabilities corresponds to propagative states with real longitudinal wavevector k_x^S which is valid for $|\mu| > \hbar v|k_y|$. The case $\hbar v|k_y| > |\mu|$ corresponds to evanescent states in the scattering region such that $k_x^S = i\kappa = i\sqrt{k_y^2 - \left(\frac{\mu}{\hbar v}\right)^2}$. In that case, the transmission and reflection probabilities are obtained as :

$$T_{k_y}^{(e)}(\mu) = \frac{\kappa^2}{\kappa^2\cosh(\kappa L)^2 + \left(\frac{\mu}{\hbar v}\right)^2\sinh(\kappa L)^2} \text{ with : } \kappa = \sqrt{k_y^2 - \left(\frac{\mu}{\hbar v}\right)^2}, \tag{4.17}$$
$$R_{k_y}^{(e)}(\mu) = \frac{k_y^2\sinh(\kappa L)^2}{\kappa^2\cosh(\kappa L)^2 + \left(\frac{\mu}{\hbar v}\right)^2\sinh(\kappa L)^2}. \tag{4.18}$$

In Fig. 4.2, we plot the transmission probability as a function of the transverse momentum k_y for a short ribbon [Fig. 4.2.(a)] and for a long ribbon [Fig. 4.2.(b)]. The transmission is total at normal incidence which is a characteristic property of Dirac fermions for which backscattering is forbidden. When increasing $|k_y|$, the conductance decreases because of the imperfect matching between the scattering states in the leads and in the

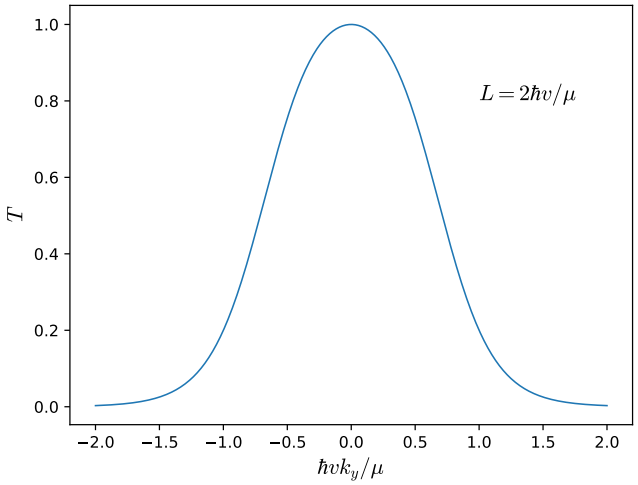

(a)

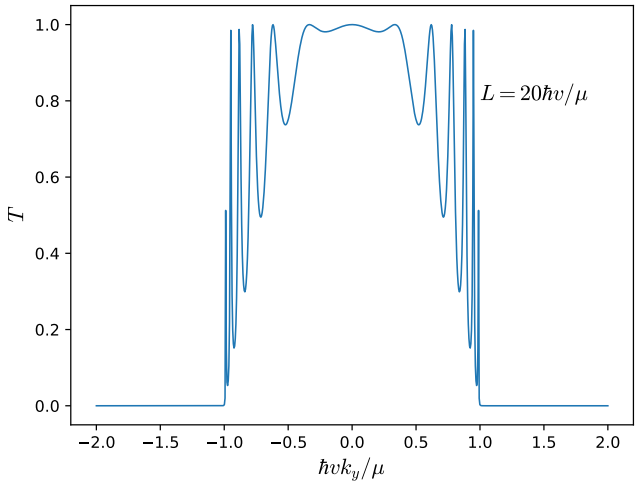

(b)

Figure 4.2 – Transmission probability of the graphene field effect transistor as a function of the transverse momentum k_y for : (a) a short ribbon of length $L = 2\hbar v/\mu$, and b) a longer ribbon of length $L = 20\hbar v/\mu$. We can see that, in both cases, the transmission is total at normal incidence ($k_y = 0$). For $\hbar v|k_y| > \mu$, the current is carried by evanescent states. For a short ribbon, some current is carried by evanescent states while for a longer ribbon, no evanescent states contribute to the conductance. The oscillations in (b) correspond to Fabry-Pérot interferences between propagative states.

scattering region. In the regions $\hbar v|k_y| > |\mu|$, there is no propagative states and the current is carried only by evanescent states with characteristic length is $1/\kappa$. We can see that for a short ribbon, the transmission is non-zero for $\hbar v|k_y| > |\mu|$, which means that some current is carried by evanescent states. For a longer ribbon, the current is carried only by propagative states. The interferences between the propagative states generate the oscillations in the transmission probability, where the graphene sheet act as a Fabry-Pérot interferometer.

1.3 Conductance of the ribbon

In the case of a ballistic conductor, the resistance originates from the interface between the sample and the contacts. Because the reservoirs have a much more important number of modes than the sample, there is a mismatch between the modes at the interfaces. The maximum current that a single mode can carry is given by the quantum of conductance equal to $G_s = e^2/h$. According to Landauer formalism, the conductance of the ribbon is the sum of the transmission probabilities of each mode and is expressed as :

$$G(\mu) = g\frac{e^2}{h}\sum_{k_y} T_{k_y}(\mu), \tag{4.19}$$

where $g = 4$ is the degeneracy factor, and the sum runs over all the channels k_y indexed by the number n from Eq. (4.1).

a) Conductance vs chemical potential

First, we present the conductance as a function of the chemical potential. Because of the quantization of the transverse wavevector k_y in units of $2\pi/W$, we express the chemical potential and wavevectors in units of $\hbar v/W$. In this choice of units, the conductance of the sample depends only on the ratio W/L. In Fig. 4.3, we plot the conductance of the sample as a function of μ for different aspect ratio. Fig.4.3.(b) corresponds to results originally found in [99] for the case of a short and wide ribbon. For a sample of width $W = 1\mu$m, we have $\hbar v/W \approx 1$meV, which means that the chemical potential runs from -40meV to 40meV, an experimentally achievable range.

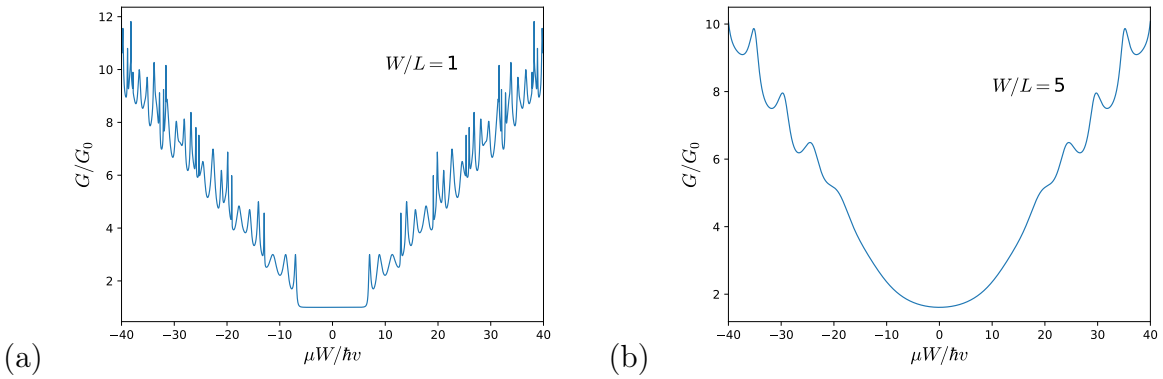

(a) (b)

Figure 4.3 – Conductivity of a graphene sheet of width W and length L as a function of the chemical potential μ, with $G_0 = 4e^2/h$ for : (a) a square graphene strip, and (b) a short and wide ribbon.

In both Figs. 4.3, the conductance increases approximatively linearly with the modulus of μ, and presents oscillations. For a square ribbon ($W/L = 1$), we can see a plateau centered on $\mu = 0$ at conductance $G = G_0$. When μ is very small, there is only one propagative state with transverse momentum $k_y = 0$ while the state at higher $|k_y|$ are evanescent. Because it is at normal incidence, this state has perfect transmission and therefore its conductance is equal to G_0. Upon increasing $|\mu|$, two more channels are opened. However, their transmission is not perfect and varies with μ due to interferences which is why the conductance oscillates. The conductance remains bounded below $3G_0$

because there are only three propagative states in this energy range. The same scenario occurs upon increasing the chemical potential, as more propagative states are open.

For the short and wide ribbon with $W/L = 5$ shown on Fig. 4.3.(b), the curve is smoother, and the Fabry-Pérot oscillations appear for higher values of the chemical potential. For a sample with a fixed width W, the length of the sample is shorter. The oscillations appear when the length of the sample is of the order of the Fermi wavevector, i.e. $L \approx 2\pi/k_F = 2\pi\hbar v/\mu$. For a ribbon with aspect ratio $W/L = 5$, this condition is satisfied for a value of the chemical potential such that $\mu W/\hbar v \approx 5 \times 2\pi \approx 30$. We can see on Fig. 4.3.(b) that this value corresponds approximately to the value at which the curve starts to oscillate. Below this value, the Fermi wavelength is longer than the length of the ribbon and thus doesn't generate interferences.

When the ribbon is long enough, so that we can neglect the contribution from the evanescent states, and wide enough so that the sum in Eq. (4.19) can be transformed to an integral, we obtain the formula for the conductance :

$$G(\mu) = \frac{G_0 W}{2\pi} \int_{-|\mu|/\hbar v}^{|\mu|/\hbar v} d_{ky} T_{k_y}^{(p)}(\mu), \tag{4.20}$$

$$= \frac{G_0 W}{\pi} \frac{|\mu|}{\hbar v} \int_0^1 dx \frac{1-x^2}{1-x^2\cos^2(\sqrt{1-x^2}k_F L)}, \tag{4.21}$$

$$\approx \frac{G_0}{4} \frac{|\mu| W}{\hbar v}, \quad \text{for } k_F L = \frac{\mu L}{\hbar v} \gg 1 \tag{4.22}$$

where we have used the change of variables $x = \frac{\hbar v k_y}{\mu}$ in the second line, and we find that the integral in the second line is equal to $\pi/4$ in the limit $\frac{\mu L}{\hbar v} \gg 1$ (see Appendix C).

We can see that the conductance is proportionnal to the width of the sample, because the number of channels increases with W, and is independent of L which is characteristic of a ballistic sample. This expression corresponds to the trend of the curve on Figs. 4.3, and doesn't take into account for the interference effects. We can see that this expression is consistent with the figures for which $G/G_0 \approx 10$ for $|\mu|W/\hbar v \approx 40$. The conductivity is equal thus to :

$$\sigma \approx \frac{e^2}{h}\sqrt{\pi n} L, \tag{4.23}$$

where we have used Eq. (1.34) for the chemical potential. The conductivity increases with the length of the sample, which is characteristic of a ballistic sample. When the length of the sample is greater than the mean free path l_e of a diffusive graphene sample, the conductivity reaches the value :

$$\sigma \approx \frac{2e^2}{h}\sqrt{\pi n} l_e. \tag{4.24}$$

b) Minimal conductivity

The minimal conductivity of graphene corresponds to the conductivity when the Fermi level is at the Dirac point ($\mu = 0$). At the Dirac point, the density of states vanishes and no propagating state exists. However, experimentally, the conductivity reaches a minimum which is non-zero. The value of the minimal conductivity of graphene has been the subject of an intensive theoretical effort which led to different values depending on the formalism used [100]. The value usually depends on the disorder landscape, where density fluctuations lead to propagative states at the Dirac point. We present here the calculation

of the minimal conductivity for clean and non-interacting graphene using the transport formalism presented in the previous sections, such as in Refs. [99].

For a wide enough sample $W \gg L$, the sum over the channels can be transformed to an integral :

$$G(\mu) = \frac{G_0 W}{2\pi} \int_{-k_\infty}^{k_\infty} dk_y T_{k_y}, \tag{4.25}$$

$$= \frac{G_0 W}{\pi} \left[\int_0^{\frac{|\mu|}{\hbar v}} dk_y T_{k_y}^{(p)} + \int_{\frac{|\mu|}{\hbar v}}^{k_\infty} dk_y T_{k_y}^{(e)} \right], \tag{4.26}$$

where $G_0 = 4e^2/h$ and $k_\infty = \frac{\mu_\infty}{\hbar v}$ is the (very large) Fermi wavevector in the leads. There is a competition between two contributions : for small μ, the transport will be dominated by evanescent modes, whereas the propagating ones dominate for large μ. At the Dirac point ($\mu = 0$), the conductance originates only from evanescent modes with transmission probability :

$$T_{k_y}^{(e)} = \frac{1}{\cosh^2(k_y L)}, \tag{4.27}$$

which leads to the minimal conductance :

$$G(\mu = 0) = \frac{G_0 W}{\pi} \int_0^{k_\infty} dk_y \frac{1}{\cosh^2(k_y L)} = \frac{G_0}{\pi} \frac{W}{L} \quad \text{for} \quad W \gg L \tag{4.28}$$

The conductivity of the 2D sheet is related to the conductance according to the formula :

$$\sigma = G \frac{L}{W} = \frac{G_0}{\pi}. \tag{4.29}$$

We can see that in the limit $W \gg L$, the conductivity of the sample reaches a universal value.

1.4 Ballistic graphene in experiments

The first transport experiments in graphene were realized by the group of Novoselov *et al.* in Manchester [1, 17]. They realized a field effect transistor made of a graphene layer on a silicon substrate in a multiterminal setup. They measured carrier mobilities μ_e up to $\approx 10000 \text{cm}^2/\text{V/s}$, which corresponds to a mean free path :

$$l_e = (h/2e)\mu_e \sqrt{n/\pi}, \tag{4.30}$$

of the order of 100nm for characteristic carrier concentration $n \approx 10^{12} \text{cm}^{-2}$. For sample sizes of the order of the micrometer, this regime is still diffusive. A first step towards ballistic conduction was achievedby the realization of suspended graphene devices. The suspension allowed to reduce scattering from substrate impurities. The mobilities gained an order of magnitude reaching $200000 \text{cm}^2/\text{V/s}$ [101, 102, 103], with a mean free path approaching the sample size, but without observing characteristic features of ballistic transport. However, devices made of suspended graphene are not easy to engineer and manipulate. Later on, hexagonal Boron Nitride (h-BN) was found to be a very clean substrate for high-quality graphene [104] with mobilities of the same order as suspended graphene but which allowed for a greater tunability compared to suspended samples. Ballistic conduction was finally achieved at room temperature in graphene samples encapsulated between two layers of h-BN [105, 106], which led to mobilities up to $500000 \text{cm}^2/\text{V/s}$, and a mean free path longer than the size of the sample. Finally, encapsulated samples with mobilities of three millions of $\text{cm}^2/\text{V/s}$ and a mean-free path reaching up to $28\mu m$ were realized [107].

2 Irradiated ribbon

In this section, we present the formalism developed to compute the 2-terminal conductance of a graphene-based transistor whose central 2D conducting channel is irradiated by circularly polarized light at normal incidence. The transmission and reflection coefficients are evaluated within the Landauer-Büttiker formalism extended to driven Floquet systems [108]. Note that the electromagnetic field is uniform in the central gated graphene region, while the leads are not irradiated.

We consider the same geometry as in Fig. 4.1, namely a rectangular ribbon of width W and length L connected by two non-irradiated leads. The Hamiltonian being time-dependent, the single electron energy is not conserved. However, due to the invariance under discrete translations of time T, the quasi-energy ε is still a good quantum number. In the scattering problem, we consider electrons incoming at energy $\varepsilon = 0$, which corresponds to the Fermi level of the leads. The electrons propagating inside the irradiated region can emit or absorb one or several photon(s) of energy $\hbar\omega$. These inelastic scattering events are described by a set of transmission (reflection) coefficients t_{n0} (r_{n0}) corresponding to the amplitude of being transmitted (reflected) with a final energy $\varepsilon+n\hbar\omega$.

In order to determine those Floquet scattering coefficients, we use periodic boundary conditions along the y direction. The transverse wave-vector k_y is quantized as in Eq. 4.1. Note that with such periodic boundary conditions, only bulk 2D states are investigated.

2.1 Spectrum

In the irradiated region ($0 < x < L$), we need to find the Floquet eigenstates Φ_m and the longitudinal wave-vector k_x corresponding to a given set (μ, k_y) (still having in mind the scattering problem for $\varepsilon = 0$ corresponding to an electron incident from the lead Fermi level). Multiplying Eq. (3.57) by $\xi\sigma_x$ and rearranging it allows to get both $k_x(\varepsilon)$ and Φ_m by solving the following equations:

$$\sum_n (K^{\xi}_{0F,mn} + K^{\xi}_{VF,mn})\Phi_n = \hbar v k_x \Phi_m, \tag{4.31}$$

where one has defined an infinite matrix K_{0F} with matrix elements:

$$K^{\xi}_{0F,mn} = \xi((\mu - m\hbar\omega)\sigma_x - i\sigma_z\hbar v k_y)\delta_{mn}, \tag{4.32}$$

and the infinite matrix K_{VF} by the matrix elements:

$$K^{\xi}_{VF,mn} = -\xi\sigma_x V_1^{\xi}\delta_{m,n-1} - \xi\sigma_x V_{-1}^{\xi}\delta_{m,n+1}, \tag{4.33}$$

describing the effect of the electromagnetic field.

Note that switching the valley index reverses the sign of k_x, and because the ribbon is space-inversion symmetric along the x direction, the eigenvalues k_x always come in pairs, therefore both valleys have the same contribution to the conductance. In practice, one can solve the scattering problem and compute the transport in a given valley, and multiply the single-valley result by 2 to get the total conductance.

Besides, $K_F = K_{0F} + K_{VF}$ being not Hermitian, the longitudinal momentum k_x can have an imaginary part, which corresponds to an evanescent state (Fig. 4.4). As we have seen before, we need to make a truncation in the number of Floquet side bands such that $m \in [-N, N]$. After numerical diagonalization, we obtain $2(2N+1)$ eigenvalues $k_x^{\alpha}(\varepsilon)$ and eigenvectors Φ_m^{α} with $\alpha \in \{1, 2(2N+1)\}$ labelling the different eigenmodes. The resulting

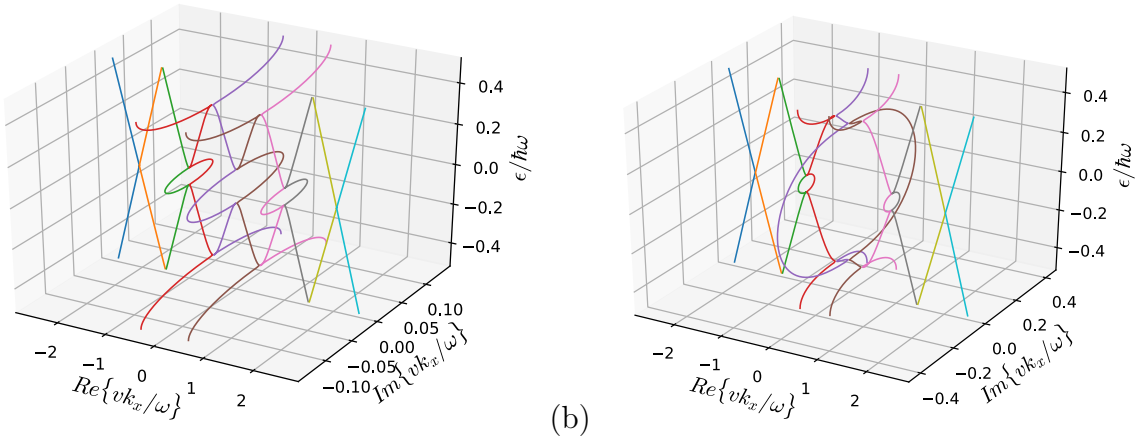

Figure 4.4 – Inverse dispersion relation $k_x^\alpha(\varepsilon)$ for $\beta = 0.3$ in the reduced Floquet zone for $N = 2$ with the real and imaginary parts of the wave vector k_x for (a) $k_y = 0$ and (b)$k_y = 0.4\omega/v$. Inside the gaps, the wavevector is imaginary which corresponds to an evanescent state.

2-component wave function is written as a superposition of the $2(2N+1)$ eigenmodes labelled by index α. The wave function of a given α-eigenmode is expressed as:

$$\Phi^\alpha(x,t) = e^{ik_x^\alpha x} \sum_{m=-N}^{N} \Phi_m^\alpha e^{-im\omega t}, \tag{4.34}$$

which is still a two-component spinor (attached to one valley, here $\xi = 1$).

When the Fermi level lies in the gap, $k_x^\alpha(\varepsilon)$ has a non-zero imaginary part which signals an evanescent state. For a ribbon with a finite length, these states will allow the current to tunnel through the gapped central region. The penetration lengths ξ are defined as the inverse of the imaginary part of the longitudinal wave-vector $k_x(\varepsilon)$ inside the gap (Fig. 4.4) :

$$\xi_\alpha = \frac{1}{|\Im\{k_x^\alpha\}|}. \tag{4.35}$$

For weak driving, $\beta \ll 1$, it is possible to associate each eigenmode (α) with a given anti-crossing between uncoupled Floquet replicas. Moreover, there is a direct relation between the length ξ and the size of the gaps :

$$\xi_m = \frac{\hbar v}{\Delta_m}. \tag{4.36}$$

As the size of the gap increases, the imaginary part of $k_x(\varepsilon)$ (where ε is in the gap) increases, thereby the characteristic length decreases. According to Eqs. (3.61) and (3.62), and for $\beta \ll 1$ the decay lengths are expressed as:

$$\xi_0 = \frac{l_\omega}{\sqrt{1+4\beta^2}-1} \approx \frac{l_\omega}{2\beta^2}, \tag{4.37}$$

$$\xi_m \approx \frac{(m-1)!}{\beta^m} l_\omega\,, \tag{4.38}$$

in terms of the length :

$$l_\omega = v/\omega\,, \tag{4.39}$$

corresponding to the distance travelled by an electron during one cycle of driving (divided by 2π). We compared the RWA method and the numerics and we see a good agreement between numerical diagonalisation and RWA even for $\beta \approx 1$.

2.2 Scattering states and transmission coefficients

To simplify the expression of the scattering states in the leads, we consider heavily n-doped leads, as we have done for the non-irradiated case in Sec. 1.1. The chemical potential in the leads is $\mu_\infty > 0$ for $x < 0$ and $x > L$ such that $\mu_\infty \gg |\mu|$.

In order to account for electrons leaving the scattering region with energy $\varepsilon + n\hbar\omega$, we use the Floquet theorem in the leads. However, because there is no driving, the Floquet replicas are decoupled. In the leads, for an infinite system, Eq. (3.57) with $\varepsilon = 0$ becomes :

$$\hbar v \left(\sigma_x k_x + \sigma_y k_y\right) \Phi_m(x) = (\mu_\infty - m\hbar\omega)\Phi_m(x). \tag{4.40}$$

For a given 2D wave-vector (k_x, k_y), there is an infinite amount of plane wave solutions labelled by their Floquet index m and their band index $s = \pm 1$:

$$\Phi_{m,s}(x) = \frac{1}{\sqrt{2}} \begin{pmatrix} s \\ e^{i\varphi} \end{pmatrix} e^{ik_x x}, \tag{4.41}$$

with $\mu_\infty = m\hbar\omega + s\hbar v\sqrt{k_x^2 + k_y^2}$ and $\cos\varphi = k_x/(\mu_\infty - m\hbar\omega)$, φ being the angle of incidence of the electron. Since $\mu_\infty \to \infty$, we have $\varphi \to 0, \pi$ and $s = \pm 1$ in both source and drain leads. Finally, the spinor in the leads is independent of m and we obtain one left $(+)$ and one right $(-)$ going solution :

$$\Phi_m^\pm(x) = \Phi^\pm e^{ik_x^\pm x}, \tag{4.42}$$

with $k_x^\pm = \pm\mu_\infty/\hbar v$, and

$$\Phi^\pm = \frac{1}{\sqrt{2}} \begin{pmatrix} 1 \\ \pm 1 \end{pmatrix}. \tag{4.43}$$

Using the expression of the eigenstates in the different regions, it is possible to construct the scattering states. We consider an incoming wave from the left lead at the quasi-energy $\varepsilon = 0$ and Floquet index $n = 0$. In the left lead, there will be $2N + 1$ waves reflected at energies $\varepsilon = n\hbar\omega$ with amplitude r_{n0}. The wave function in the left lead is then :

$$\Psi^L(x,t) = \left(\Phi^+ e^{ik_x^\infty x} + \sum_{n=-N}^{N} r_{n0}\Phi^- e^{-ik_x^\infty x} e^{in\omega t}\right) e^{-i\varepsilon t}, \tag{4.44}$$

where $k_x^\infty x = \mu_\infty - m\hbar\omega$. In the irradiated region, the wave function is a superposition of the eigenstates Φ^α with amplitudes a_α :

$$\begin{aligned} \Psi^I(x,t) &= \sum_\alpha a_\alpha \Phi^\alpha(x,t) e^{-i\varepsilon t} \\ &= \left(\sum_\alpha a_\alpha e^{ik_x^\alpha x} \sum_{n=-N}^{N} \Phi_n^\alpha e^{-in\omega t}\right) e^{-i\varepsilon t}. \end{aligned} \tag{4.45}$$

In the right lead, only the right going states with amplitude t_{n0} on the n's replica are chosen :

$$\Psi^R(x,t) = \left(\sum_{n=-N}^{N} t_{n0}\Phi_n^+ e^{ik_x^+(x-L)} e^{in\omega t}\right) e^{-i\varepsilon t}. \tag{4.46}$$

To calculate the reflected and transmitted amplitudes, we need to match the wave functions at the interfaces. The boundary condition at $x = 0$ is $\Psi^L(x = 0^-, t) = \Psi^I(x = 0^+, t)$:

$$\Phi^+ + \sum_{n=-N}^{N} r_{n0}\Phi_n^- e^{-in\omega t} = \sum_{\alpha}\sum_{n=-N}^{N} a_\alpha \Phi_n^\alpha e^{-in\omega t}, \tag{4.47}$$

and at $x = L$, the condition is $\Psi^I(x = L^-, y, t) = \Psi^R(x = L^+, t)$ so :

$$\sum_{\alpha}\sum_{n=-N}^{N} a_\alpha \Phi_n^\alpha e^{ik_x^\alpha L} e^{-in\omega t} = \sum_{n=-N}^{N} t_{n0}\Phi_n^+ e^{-in\omega t}\,. \tag{4.48}$$

These boundary conditions, at $x = 0$ and $x = L$, must be valid at any time t, so we can project them on the different Fourier harmonics to obtain the linear system of equations :

$$\Phi^+\delta_{n0} + r_{n0}\Phi^- = \sum_{\alpha} a_\alpha \Phi_n^\alpha, \tag{4.49}$$

$$\sum_{\alpha} a_\alpha \Phi_n^\alpha e^{ik_x^\alpha L} = t_{n0}\Phi^+. \tag{4.50}$$

On one hand, the number of unknown scattering parameters is $4(2N + 1)$ since we have $(2N + 1)$ reflection coefficients r_{n0}, $(2N + 1)$ transmission coefficients t_{n0}, and $2(2N + 1)$ coefficients a_α to determine. On the other hand, each matching condition represents $2N + 1$ spinor relations, hence there is a total of $4(2N + 1)$ linear relations between those coefficients.

2.3 Conductance formula

To calculate the conductance of the sample, we use the scattering theory extended to Floquet systems [108]. The scattering matrix element $t_{n0,k_y,\mu}(\varepsilon)$ is the probability amplitude for an electron entering from the left lead at energy ε and wave-vector k_y to exit in the right lead with energy $\varepsilon + n\hbar\omega$. The expression of the current through the sample is [108, 109] :

$$I = \frac{e}{h}\int_{-\infty}^{\infty} d\varepsilon \sum_{n=-N}^{N} \left(T_n(\varepsilon) f_L(\varepsilon) - T_n'(\varepsilon) f_R(\varepsilon)\right), \tag{4.51}$$

where $f_L(\varepsilon)$ and $f_R(\varepsilon)$ are the Fermi-Dirac distributions in the left and right leads at chemical potential μ_L and μ_R respectively. The transmission $T_n(\varepsilon)$ is the sum over all k_y channels of the transmission probabilities of electrons from energy ε in the left lead towards energy $\varepsilon + n\hbar\omega$ in the right lead :

$$T_n = \sum_{k_y} |t_{n0,k_y}|^2\,. \tag{4.52}$$

The current per channel flowing in the scatterer is conserved so the scattering matrix is unitary. This implies the relation :

$$\sum_{n=-N}^{n=N} \left(|t_{n0,k_y}|^2 + |r_{n0,k_y}|^2\right) = 1\,, \tag{4.53}$$

where $|r_{n0,k_y}|^2$ is the reflection probability of the transverse modes k_y :

$$R_n = \sum_{k_y} |r_{n0,k_y}|^2\,. \tag{4.54}$$

We checked that the unitary relation Eq.(4.53) is fulfilled in the numerical implementation. We can also notice that $T_n(\varepsilon) = T'_n(\varepsilon)$, $T'_n(\varepsilon)$ being the transmission probability defined similarly as $T_n(\varepsilon)$, but for the reversed scattering process (incident electron going from the right lead and transmitted to the left lead). The equality $T_n(\varepsilon) = T'_n(\varepsilon)$ ensures that there is no pumped current for zero bias. Therefore, at zero temperature, for small bias $V = (\mu_L - \mu_R)/e$ so that the transmission coefficient varies weakly, we obtain the conductance formula :

$$G(\mu) = \frac{\partial I}{\partial V} = G_0 \sum_{n=-N}^{N} T_n(\mu), \tag{4.55}$$

where $G_0 = \frac{4e^2}{h}$, where the factor 4 accounts for valley and spin degeneracy.

3 Conductance of the ribbon

In the previous section, we have presented the formalism which allows us to compute the two-terminal conductance of graphene-based transistors as a function of the chemical potential μ, radiation strength β, frequency ω, and geometrical parameters L and W (Fig. 4.1). We have considered the ballistic regime relevant for currently achievable high-mobility samples. In this section, we present our results for the conductance of this graphene transistor in different regimes. First, we analyse the conductance as the chemical potential is varied. In a second part, we detail the undoped case, namely when the Fermi energy is at the Dirac point.

3.1 Conductance-chemical potential curves

In this section, the dependence of the conductance upon the chemical potential is discussed for various irradiation strengths β. The main features consist in strong suppressions of the conductance in wide ranges of chemical potential, especially around $\mu = \pm\hbar\omega/2$. The suppression of the conductance originates from photo-induced gaps in the quasi-energy spectrum which lead to evanescent states. A simple phenomenological model is introduced which accounts for the residual conductance around $\mu = \pm\hbar\omega/2$. A crossover between 2D transport through bulk evanescent states and 1D edge transport is predicted, and shown to depend on the geometrical parameters L and W of the graphene ribbon.

a) Weak driving $\beta = 0.1$

In presence of electromagnetic radiation, the conductance (blue curves in Fig. 4.5) exhibits broad dips around chemical potentials $\mu = \pm\hbar\omega/2$. These dips mainly correspond to gaps centered at quasi-energy $\varepsilon = \pm\hbar\omega/2$, and located near $k = \pm\omega/2v$ in the quasi-energy dispersion relation (see Fig. 3.5.(a)). These gaps originate from one-photon resonances between the valence and the conduction band. The electromagnetic coupling leads to an avoided crossing and the opening of a gap Δ_1, associated to a typical decay length $\xi_1 = \hbar v/\Delta_1$. Besides this main gap, the quasi-energy spectrum of Fig. 3.5.(a) also contains a set of very tiny gaps located at higher wave-vectors, around $k = \pm 3\omega/2v, \pm 5\omega/2v...$, and also all nested around $\pm\hbar\omega/2$. However, for weak driving, the weight of the wave function on these states is negligible, and therefore their contribution to the conductance turns out to be far smaller (than the Δ_1 contribution) although their decay lengths are much larger (nearly propagating states).

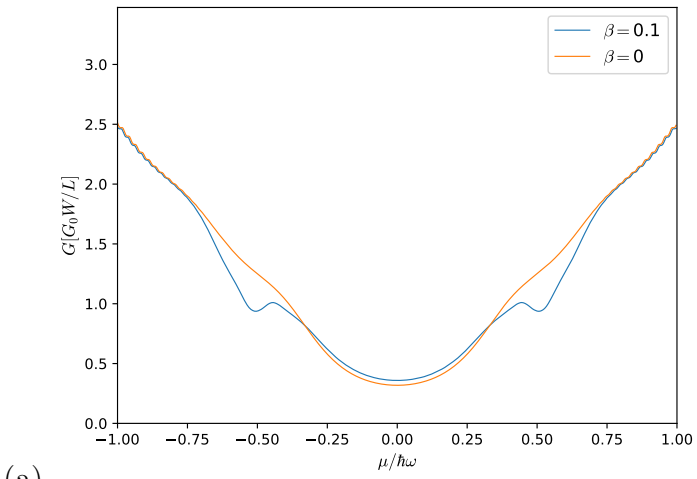

(a)

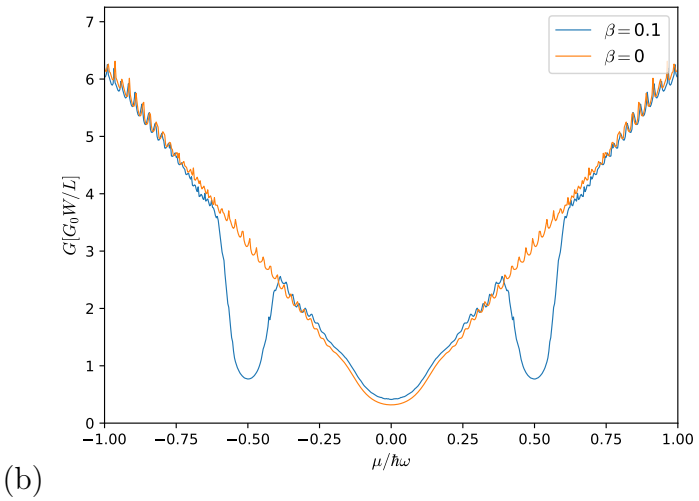

(b)

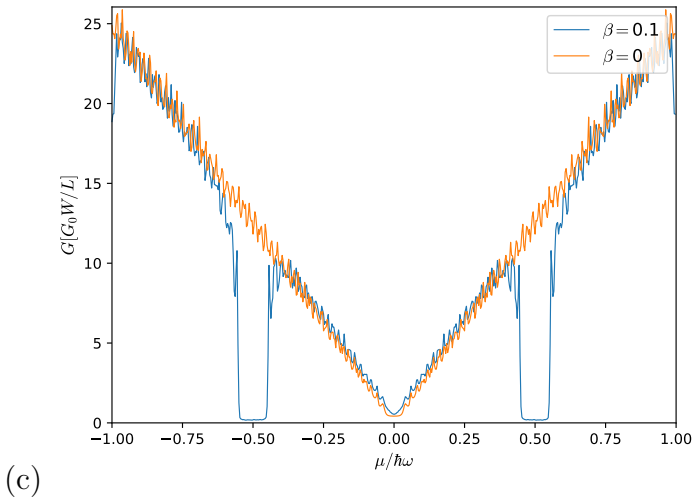

(c)

Figure 4.5 – Conductance of a rectangular graphene ribbon as a function of chemical potential for the non-irradiated case ($\beta = 0$ in orange) and for $\beta = 0.1$ in blue ($N = 2$) for a width $W = 250\, l_\omega$ and various lengths : (a) $L = 10\, l_\omega = \xi_1$, (b) $L = 25\, l_\omega = 2.5\, \xi_1$ and (c) $L = 100\, l_\omega = 10\, \xi_1$. For the irradiated case, some dips develop around filling $\mu = \pm\hbar\omega/2$ which corresponds to the gaps of order $m = 1$ at $k = \pm\omega/2v$ in Fig. 3.5.

The conductance at $\mu = \pm\hbar\omega/2$ is therefore controlled by the ratio between the sample

	Gaps at $\varepsilon = 0$		Gaps at $\varepsilon = \hbar\omega/2$	
	$m = 0$	$m = 2$	$m = 1$	$m = 3$
$\Delta_m/\hbar\omega$	0.02	0.01	0.1	0.0005
ξ_m/l_ω	50	100	10	2000

Table 4.1 – Table of the gap sizes and the characteristic length of the corresponding evanescent states for a driving strength of $\beta = 0.1$.

length L and the decay length ξ_1 of the evanescent state associated to the gap Δ_1, typically $\Delta_1 \simeq 0.1\,\hbar\omega$ and $\xi_1 = 10\,l_\omega$ for $\beta = 0.1$ according to Eq. (3.62) (see also table 4.1). Indeed the conductance dips become more pronounced and deeper as the length L increases. For $L = 10\,l_\omega = \xi_1$, the conductance is significantly suppressed (about 25 per cent less than the non irradiated sample conductance) around $\mu = \pm\hbar\omega/2$ [Fig. 4.5.(a)]. For $L = 25\,l_\omega = 2.5\,\xi_1$, the conductance is strongly reduced, roughly by a factor 4, with respect to the non-irradiated value [Fig. 4.5.(b)]. Finally when the length exceeds the penetration length by an order of magnitude, namely for $L = 100\,l_\omega = 10\,\xi_1$, the conductance dips are sharp and well defined [Fig. 4.5.(c)]. Besides, the width of the dips (which is well-defined only in Fig. 4.5.(c)) corresponds to the value of the gap Δ_1 : $\Delta_1 = 0.1\,\hbar\omega$ (see table 4.1). The remaining conductance originates from the states in the gap Δ_3 that have a very long characteristic length.

Away from these dips, the conductance of the irradiated ribbon follows approximately the non-irradiated one. Here, for $\beta = 0.1$, one can notice that the gaps around $\varepsilon = 0$ are very small so the characteristic length of the evanescent states in the gap are much larger than at $\pm\hbar\omega/2$ (Table 4.1), which means that even for $L = 100\,l_\omega$, the deviation from the non-irradiated curve keeps rather small. The conductance near the Dirac point, $\mu = 0$, is discussed in more detail in Section 3.2. We conclude that for weak driving, the effect of the driving on the conductance is mainly observable around $\mu = \pm\hbar\omega/2$.

Evanescent states in the gap at $\hbar\omega/2$: Fig. 4.6 shows the conductance of the ribbon as a function of the length of the ribbon when the chemical potential is in the gap $\mu = \hbar\omega/2$. Inside this gap, the bulk current is carried only by evanescent modes, thus, the conductance of the sample is expected to decrease exponentially with the length. At short length, the conductance is dominated by the evanescent modes coming from the gaps Δ_1, but for larger length, the modes originating from the gap Δ_3 will be dominant. Therefore, it is possible to express the conductivity in the gap with a simple model taking into account this interplay between states at gaps $\Delta_1$and Δ_3. First, we have checked that the conductance is proportional to W, and thus our ansatz reads :

$$G_{bulk} = G_0 W \left(a e^{-L/\xi_1} + b e^{-L/\xi_3} \right), \tag{4.56}$$

where ξ_1 and ξ_3 are given by Table 4.1, a and b being the only fitting parameters of our model that depend on β. The latter parameters (expressed in units of l_ω^{-1}) quantify the relative importance of the evanescent states in transport. For $\beta = 0.1$, using the rescaling by $G_0 W/L$, we obtain that the conductance inside the dips at $\mu = \pm\hbar\omega/2$ can be fitted by :

$$\frac{G}{G_0}\frac{L}{W} = L \left(a e^{-L/\xi_1} + b e^{-L/\xi_3} \right). \tag{4.57}$$

We can see that the ansatz fits well the conductance where the parameters a and b (expressed in units of l_ω^{-1}) quantify the relative importance of the evanescent states in transport. The peak with maximum around $L = 10\,l_\omega$ corresponds to the current carried

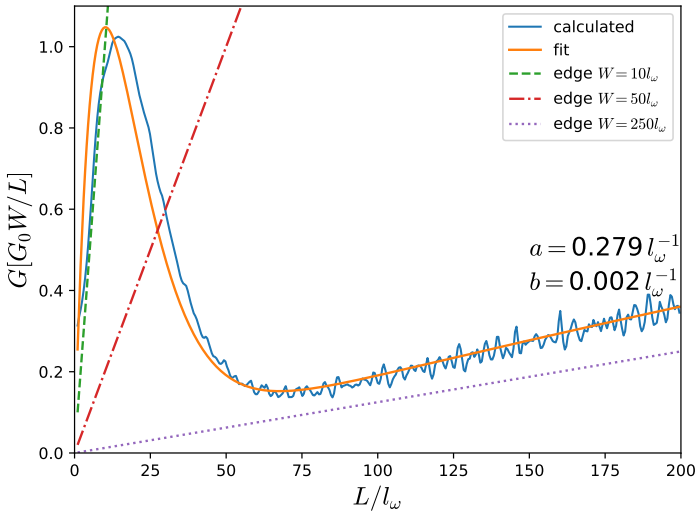

Figure 4.6 – Conductance of a ribbon as a function of the length L of the ribbon for driving strength $\beta = 0.1$ and chemical potential $\mu = \hbar\omega/2$ ($N = 3$) normalized by the ratio W/L (independent of the ribbon width W). The orange smooth curve corresponds to the fit in Eq. (4.57), and the resulting fitting parameters are a and b. For length $L \lesssim 70 l_\omega$, the conductance is carried mainly by the modes with characteristic length ξ_1 and for larger length, the modes with length ξ_3 dominate. Also plotted are the estimate of the conductance of the chiral edge state in dashed line for various widths of the sample.

by the evanescent modes carried mainly by the evanescent states originating from the first order side-band ($\xi_1 = 10 l_\omega$). The curve reaches a minimum around $L = 70\, l_\omega$ and then increases again as the states coming from the third order side-band become the dominant source of current. The parameter b is two orders of magnitude smaller than a, which indicates that for $\beta = 0.1$, the weight of the wave function on the evanescent states corresponding to the gap Δ_3 is very weak. This fact corroborates the approximation we made by considering only the evanescent states originating from the gaps Δ_1 and Δ_3.

Edge states : So far only transport through 2D bulk states (propagating or evanescent) has been evaluated and discussed. One can estimate the edge state contribution and compare it with the bulk contribution. The dotted lines on Fig. 4.6 corresponds to the edge state contribution. There is one edge state per valley that contributes to the dc conductance [110, 111, 95], taking into account for valley and spin degeneracy, the maximal conductance is equal to :

$$G_{edge}(\mu = \hbar\omega/2) = \frac{4e^2}{h}\,. \tag{4.58}$$

We said "maximal" conductance because the irradiation may reduce the conductance of the edge states. This effect has been studied by Aaron *et al.* [112] using the Bernevig-Hugues-Zhang model [8]. They found that the conductance is reduced by a Bessel factor with argument β, in the same fashion as in the photon-assisted transport problem. Here, as we consider weak driving, we will not take into account this reduced edge state conductance. Inter-edge scattering is neglected as only large sample widths W are considered. We have plotted the ratio $G_{edge} L/G_0 W$ for the edge states for different widths of the sample in Fig. 4.6. This demonstrates that the conductance is dominated by edge states only for long enough samples, namely when L exceeds the typical decay length of the bulk

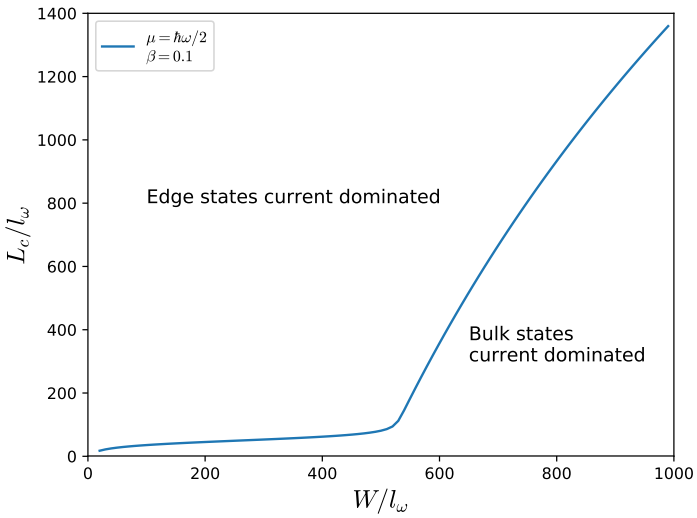

Figure 4.7 – Critical length L_c where bulk and edge have the same contribution to the current at $\mu = \hbar\omega/2$ for a driving strength $\beta = 0.1$. For lengths longer than L_c, the current is carried mainly by edge states whereas for shorter lengths, the current is dominated by the evanescent bulk states.

evanescent states. This crossover between 2D transport by evanescent states and 1D edge transport occurs at a typical length L_c which increases with the ribbon width W. Using the fit function (4.56) with the parameters a and b, it is possible to plot L_c as a function of W using the relation :

$$G_{bulk}(W, L_c) = G_{edge}\,. \tag{4.59}$$

The resulting $L_c(W)$ curve is plotted in Fig. 4.7. This "phase diagram" allows us to see the competition between bulk and edge current which depends on the shape of the sample and the frequency of irradiation (through l_ω). This curve shows that bulk transport dominates for short and wide graphene ribbons which can be understood qualitatively. Quantitatively, it gives a criterium needed to separate bulk and edge conductance in a particular experiment. There is a clear break in the curve around $W = 500 l_\omega$, where the edge conductivity becomes smaller than the conductivity carried by bulk evanescent states originating from the Δ_3 gap that have a very long penetration length.

b) Electromagnetic driving $\beta = 0.3$

For $\beta = 0.3$, the scenario is similar to the case with $\beta = 0.1$, except that some dips develop at $\mu = 0$ and $\pm\hbar\omega$ in addition to the dips at $\pm\hbar\omega/2$. Those dips correspond to the second order processes in β which are not negligible anymore. Table 4.2 shows the gaps sizes and the length of the corresponding evanescent states. As the length increases, the dips develop and are better defined.

Each gap is larger at $\beta = 0.3$ than its value at $\beta = 0.1$ case. Hence the corresponding evanescent state decay lengths have all decreased, thereby making the residual conductance smaller, provided L is kept constant. However, the weight of the wave-function on the higher order side-bands has increased, thus increasing the conductance in the gap Δ_1. In the gaps at $\mu = \pm\hbar\omega/2$, we can see in Fig. 4.8.(c) that the conductance is not zero anymore because the third order side-bands now carry some current. We can also see the presence of the gap Δ_3 at $\mu = \pm\hbar\omega/2$ inside the gap Δ_1 because there is a small dip in

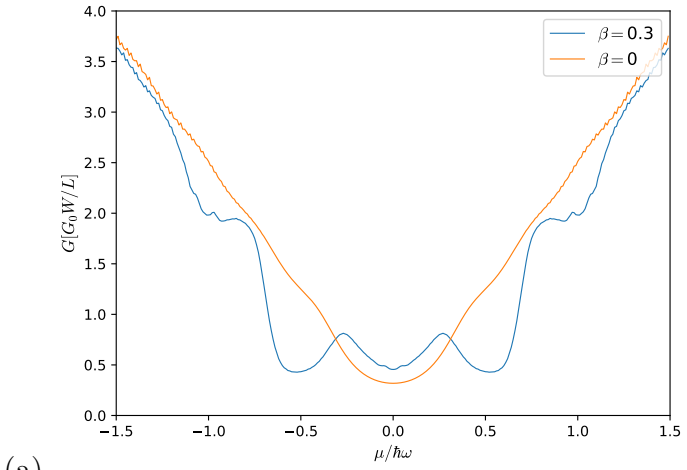

(a)

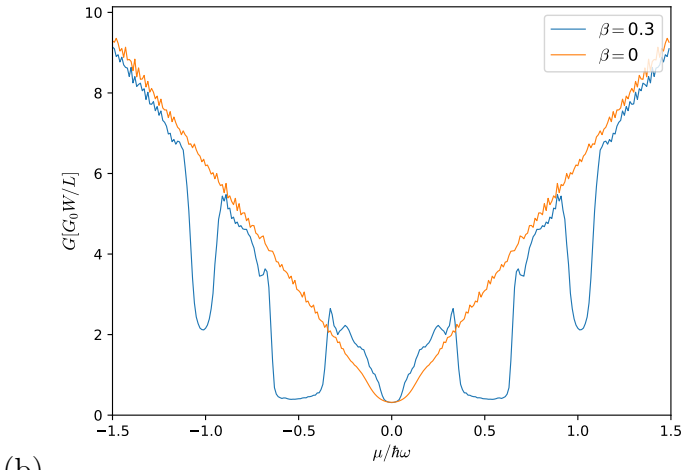

(b)

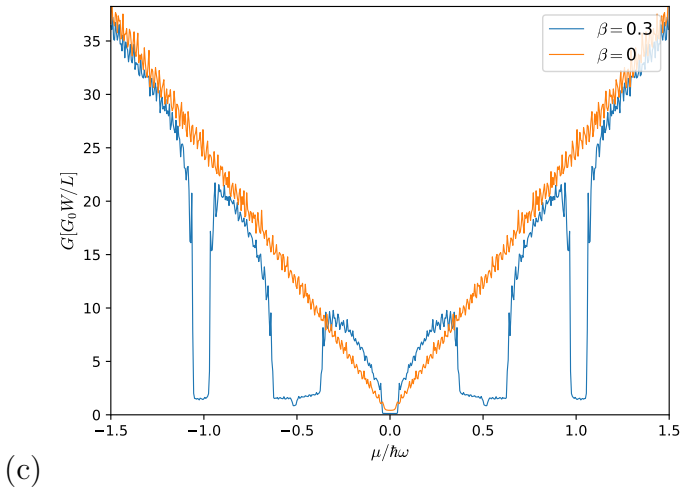

(c)

Figure 4.8 – Conductance of an irradiated graphene ribbon as a function of chemical potential for the non-irradiated case ($\beta = 0$, orange curve) and for $\beta = 0.3$ ($N = 2$, blue curve) for a width $W = 250l_\omega$ and a length : (a) $L = 10l_\omega$, (b) $L = 25l_\omega$ and (c) $L = 100l_\omega$. We can see the gap Δ_1 at $\hbar\omega/2$ which is larger than for $\beta = 0.1$. The residual conductance is more important because of the propagating states of the $n = 3$ replica. Additional dips develop around filling $\mu = 0$ and $\pm\hbar\omega$ which corresponds to the gap Δ_2 in fig. 3.5.

	Gaps at $\varepsilon = 0$			Gaps at $\varepsilon = \hbar\omega/2$	
	$m = 0$	$m = 2$	$m = 4$	$m = 1$	$m = 3$
$\Delta_m/\hbar\omega$	0.16	0.08	0.0013	0.3	0.0135
ξ_m/l_ω	6.25	12.5	761	3.33	74.1

Table 4.2 – Table of the gaps size and the characteristic length of the corresponding evanescent states for a driving strength of $\beta = 0.3$.

the middle inside the larger dip. Nevertheless, the gap at $\mu = 0$ is perfectly defined for $L = 100 l_\omega$ because the current carried by the fourth order side-bands is zero. In the gaps at $\mu = \pm\hbar\omega$, the current is not zero because the density of states is much higher than in the gap at $\mu = 0$.

3.2 Undoped graphene

In this section, we analyse more thoroughly the contribution of bulk states to the conductance when the chemical potential is equal to zero. We discuss the evolution of the conductance at the Dirac point as function of the irradiation strength β, and as a function of length L, comparing it with the edge contribution. We compare our results with those of Gu *et al.* [113].

a) Transmission probabilities

At zero doping $\mu = 0$, for $\beta = 0$, the current is carried by evanescent states that belongs to the elastic channel $n = 0$. Due to the semi-metallic nature of graphene, their decay length is infinite for $k_y = 0$ and decreases as $|k_y|$ increases (Eq. 4.27). For $\beta \neq 0$, the Floquet bands are coupled, so the inelastic channels with $m \neq 0$ are opened and the whole set of evanescent states located at wave-vector $k_x^m = \pm m\omega/v$ contribute to the current. The evanescent states in the gap at $k = 0$ that originate from the elastic channel $n = 0$ are now gapped, and their decay length decreases as β increases.

The total conductance corresponds to the sum of the transmission probability over all the transverse momenta k_y and over all the photon channels. As the driving strength increases, the coupling between the Floquet sidebands in the irradiated region increases, and the weight of the wavefunction spreads over the sidebands with higher number of photons. It is therefore interesting to plot the transmission probability T_m over the channel m which represents the probability of an electron entering the irradiated region at energy ε from the left lead to exit in the right lead at energy $\varepsilon + m\hbar\omega$. At $\varepsilon = 0$, the momentum $k_x^m = \pm m\omega/v$ corresponds to the anti-crossing between band dressed with m and $-m$ photons, and thus corresponds to the gap Δ_{2m} of order $2m$. Hence, for example, in the gap at $\varepsilon = 0$ and momentum ω/v, the transmission is carried by the channels $m = \pm 1$ with characteristic length $\xi_2 = l_\omega/2\beta^2$. Identically for higher order gaps, the transmission originating from the channels $T_{\pm m}$ is carried by evanescent states with characteristcs length ξ_{2m}.

Fig. 4.9 shows the transmission probability T_m carried by each replica when the chemical potential is at the Dirac point in the irradiated region for a weak driving strength. For $\beta = 0.2$, only the channels $m = 0$ and $|m| = 1$ contribute to the current, so only one Floquet replica is needed ($N = 1$). In both figures, we observe a narrow peak centered on $k_y = 0$ which corresponds to the current carried by the evanescent states of the central replica $m = 0$. This peak is narrow because there are very few state on the $m = 0$ replica

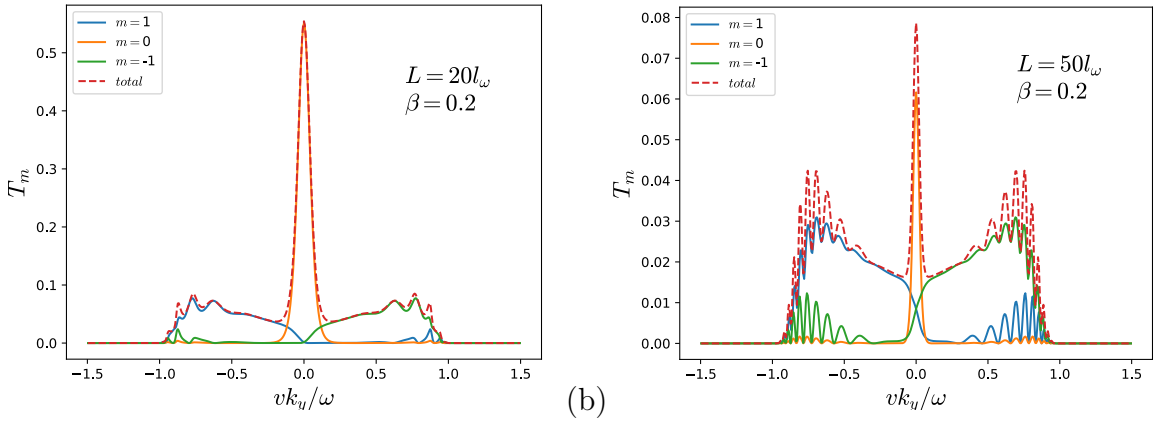

Figure 4.9 – Transmission probability T_m at zero doping $\mu = 0$ of a ribbon of length (a) $L = 20l_\omega$ and (b) $L = 50l_\omega$, for driving strength $\beta = 0.2$ as a function of the transverse momentum k_y. The current carried by the replica $m = 0$ is centered on $k_y = 0$ and is symmetric around $k_y = 0$, while the current carried by the replicas $m = \pm 1$ is carried mainly by the lateral sidebands.

at the Dirac point. However, the channels ± 1 contribute to the current in the region $-\omega/v < k_y < \omega/v$ because there exists a whole set of states over the Floquet sidebands ± 1 in this range of momentum. The current carried by the states on the $|m| = 1$ replicas is smaller than the current carried by the $m = 0$ channels because the weight of the wavefunction is smaller on the sidebands for weak driving strength.

For $\beta = 0.2$, the characteristic length of these states is $\xi_0 = 12.5l_\omega$ and $\xi_2 = 25l_\omega$. For the ribbon with length $L = 50l_\omega$, the transmission is smaller for all k_y than for $L = 20l_\omega$ which is coherent with the fact that the current is carried by evanescent states. However, the relative weight of the transmission over the channels $|m| = 1$ compared to the channel $m = 0$ is more important for the longer ribbon. This originates from the fact that the decay length of the evanescent states is longer on the $|m| = 1$ channel.

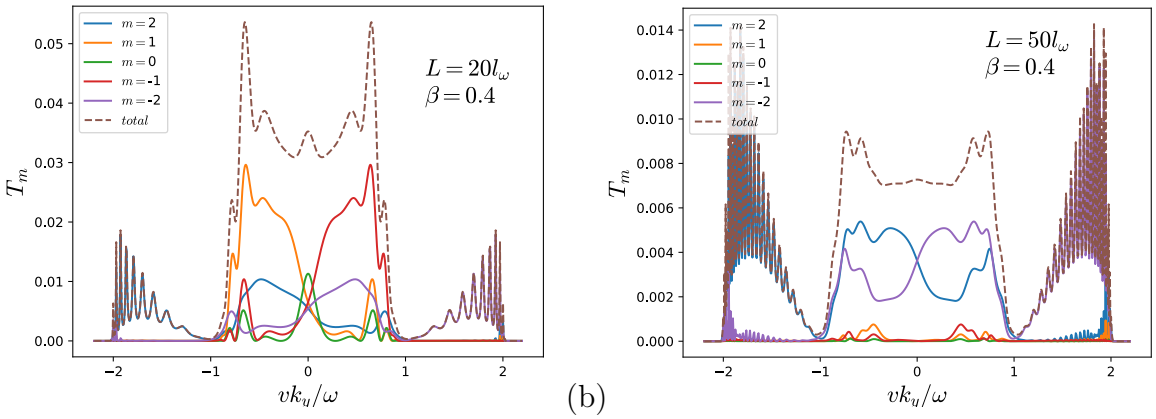

Figure 4.10 – Transmission probability T_m at zero doping $\mu = 0$ of a ribbon of length (a) $L = 20l_\omega$ and (b) $L = 50l_\omega$, for driving strength $\beta = 0.4$ as a function of the transverse momentum k_y. In (a), the current is carried mainly by states on the $|m| = 1$ channels, while in (b), the current is carried mostly by the channels $|m| = 2$.

Fig. 4.10 shows the transmission probabilities for driving strength $\beta = 0.4$. In that case, we considered $N = 2$ replicas because the weight of the wavefunction over the channels

$m = \pm 2$ is not negligible. We mention that the k_y range goes now from $-2\omega/v$ to $2\omega/v$, and that only the channels $m = \pm 2$ carry some current in the regions $|k_y| > \omega/v$ because no states are accessible for $|m| < 2$ in this region. For $\beta = 0.4$, the characteristic length of the evanescent states are $\xi_2 = 2\xi_0 \approx 6l_\omega$ and $\xi_4 \approx 234l_\omega$. For $L = 20l_\omega$, the current is carried mainly by the $|m| = 1$ channel, while for $L = 50l_\omega$, only the channel $|m| = 2$ carries some current because the length of the characteristic length of the channels $m = 0$ and $|m| = 1$ is negligible compared to the length of the sample, thereby they carry a negligible current.

We have seen that when varying the parameters β and L, there is a competition between the evanescent states carried by each channel. We will see in next section how the conductance carried by each channel evolves when varying the parameters.

b) Minimal conductivity vs driving strength

The minimal conductivity at the Dirac point reaches a universal value for short and wide ribbons, which is of the order of the quantum of conductance. When the driving is turned on, the whole set of evanescent states which belong to the set of Floquet replicas contributes to the current. We have seen that the driving strength and the length of the sample influences the transmission probabilities and therefore the conductance. The characteristic length of the evanescent states in the gap of order m is given by Eqs. (4.37) and (4.38). When β increases, their decay length decreases and therefore the current carried by the evanescent state with number of photon n should decrease. However, with increasing β, the amplitude of the wave function over states with higher number of photons n inside the irradiated region increases. There is a competition between these two effects that creates oscillations of the conductance at the Dirac point when varying β.

To understand this competition, it is useful to plot the conductivity G_m carried by each channel m, where m corresponds to the number of photons absorbed or emitted, defined as :

$$G_m = \frac{4e^2}{h}(T_m + T_{-m}) \tag{4.60}$$

evaluated at $\mu = 0$. The total transmission of a channel m is the sum over all the channels k_y. If the step between two k_y channels is shorter than the characteristic scale of variation of the transmission curve (see Figs. 4.9 and 4.10), the sum can be transformed to an integral : $\sum_{k_y} \to W/2\pi \int dk_y$, and the conductance is proportional to W. This is consistent with the fact that the density of states is proportional to $1/W$. However this curve depends on L because L has to be compared to the characteristic length ξ of the evanescent states (which are functions of β).

Fig. 4.11 shows the minimal conductance of the graphene sheet normalized by W/L which corresponds to the minimal conductivity. For $\beta = 0$, we recover the non-irradiated minimal conductance :

$$G(\mu = 0, \beta = 0) = \frac{G_0}{\pi}\frac{W}{L}\,. \tag{4.61}$$

On Fig. 4.11.(a), for weak β, the conductance carried by the channel $m = 0$ decreases as β increases because : *i*) the gap Δ_0 increases, so the characteristic length of the evanescent state decreases, and *ii*) the weight of the wave function on this channel decreases. We now turn to the current carried by the channel $n = 1$: for $\beta = 0$ it is zero because there is no irradiation, thus it necessarily increases with β because this channel is opened. We can see in Fig. 4.11 that the conductance G_1 increases faster than G_0 decreases, therefore the total conductance increases. The conductance G_1 reaches a maximum around $\beta = 0.25$. At this value, the characteristic length of the states on the channels $m = \pm 1$ equals

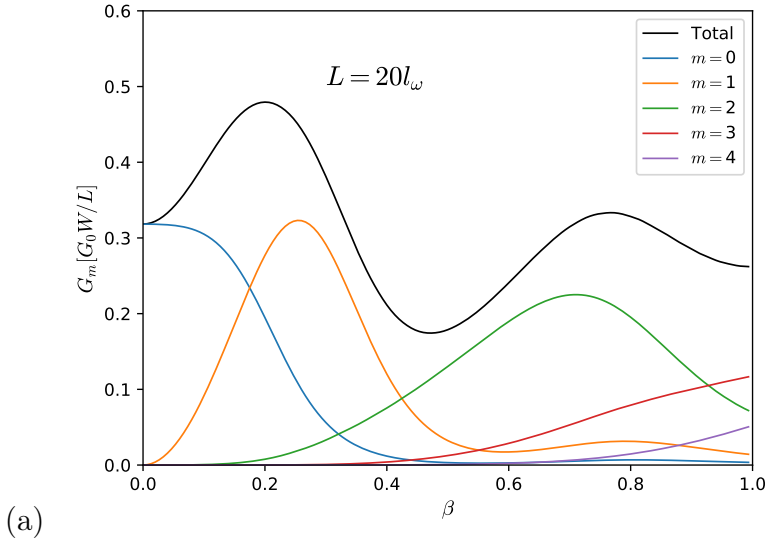

(a)

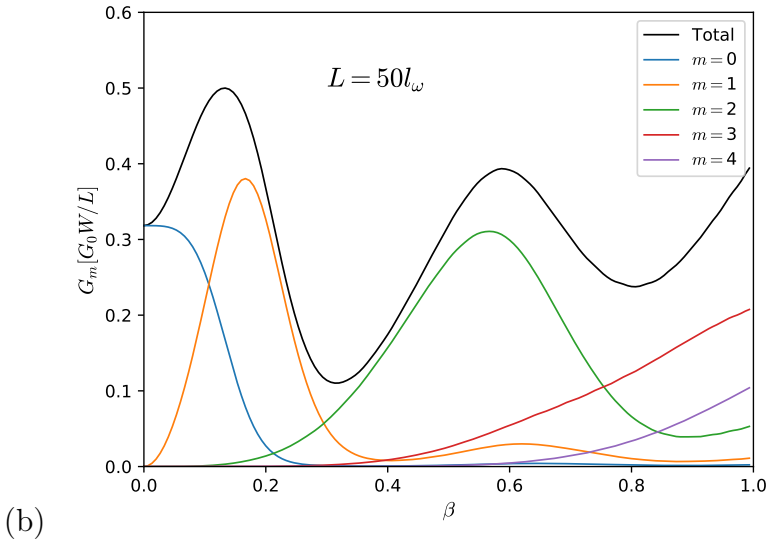

(b)

Figure 4.11 – Conductance G_m at the Dirac point carried by electrons having emitted or absorbed m photons in function of the driving strength for a length (a) $L = 20l_\omega$ and (b) $L = 50l_\omega$ and $N = 5$ Floquet replicas. G_m is defined by Eq. (4.60) in the text. The curves are independent on W as explained in the text. The competition between the decreasing characteristic length of the evanescent states and the increasing weight of the wave function over replicas with higher number of photons creates these oscillations.

$\xi_2 = l_\omega/\beta^2 \approx 16l_\omega$. Thus, the conductance G_1 starts decreasing when the characteristic length of the evanescent state is smaller than the length of the sample. At the same time, when β increases the weight of the wavefunction on the channel $|m| = 2$ increases and G_2 starts to contribute to the current. The conductance G_2 reaches a maximum around $\beta = 0.7$, which corresponds to a length $\xi_4 = 6l_\omega/\beta^4 = 25l_\omega$, which is of the order of the length of the sample.

Therefore, we see that the conductance G_m from the channel $|m|$ increases with β until it reaches a maximum when the characteristic length $\xi_{2|m|}$ of the evanescent states of this channel is of the same order as the length of the sample : $\xi_{2|m|} \approx L$. Above this value,

the conductance G_m decreases because it is $\xi_{2|m|}$ is too small compared to L, and the current is exponentially suppressed. The same scenario happens on Fig. 4.11.(b), except that the length of ribbon is longer, which means that the maxima of the conductance corresponding to each channel happens for smaller β.

c) Bulk vs edge state conductance

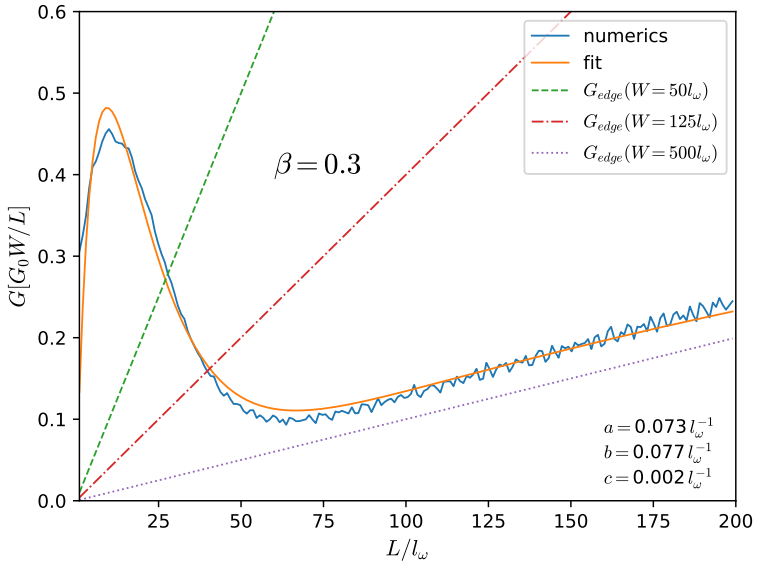

Figure 4.12 – Conductance of a ribbon as a function of the length L of the ribbon for driving strength $\beta = 0.3$ and chemical potential $\mu = 0$ ($N = 3$) normalized by the ratio W/L, which corresponds thus to the conductivity. The smooth orange curve corresponds to the fit in Eq. (4.62), and the resulting fitting parameters are a, b and c. The dashed lines corresponds to the edge state conductance given by Eq. (4.63), which are linear with respect to L because of they are protected topologically against backscattering.

We now turn on to the evolution of the conductance for a fixed β as a function of the length of the sample, and compare the contribution from the evanescent bulk states and an estimation of the current carried by the edge states. Fig. 4.12 shows the conductivity of the sample as a function of its length.

Bulk states : Similarly to the evanescent states conductivity in the gap at $\mu = \hbar\omega/2$, we find that the conductivity in the gap $\mu = 0$ can be fitted by a simple model including only 3 evanescent states (associated to 3 nested gaps around $\varepsilon = 0$ in Fig. 3.5.(a)) :

$$\frac{G}{G_0}\frac{L}{W} = L\left(ae^{-L/\xi_0} + be^{-L/\xi_2} + ce^{-L/\xi_4}\right), \tag{4.62}$$

where the fitting parameters a, b and c are shown on Fig. 4.12. For $\beta = 0.3$, the conductance originating from evanescent states that belong to the Δ_4 gap is very weak. We checked that adding the conductance states originating from the gap Δ_6 in the fitting function (4.62) doesn't change the results (for lengths smaller than $800l_\omega$, according to Table 4.2). We see that the fitting is accurate. Hence, the fitting function tells us that for ribbon of lengths shorter than ξ_0 and ξ_2, the current is dominated by evanescent states

originating from the gaps Δ_0 and Δ_2 with approximately equal weight. However, for ribbon with length longer than $50l_\omega$, the current originating from these states is exponentially suppressed and only the states of the gap Δ_4 contribute to the current. Extending this reasoning to ribbons with longer lengths, according to the length $\xi_4 = 761l_\omega$ given in Table4.2, we expect to find that for lengths longer than $800l_\omega$ the conductance originating from the gap Δ_6 will not be negligible.

Thus, in continuity with the analysis of the conductance as a function of the driving strength of the previous section, we deduce that for a certain driving strength, the conductance is mainly carried by states originating from one gap. As the length increases, the current originating from higher order gaps has a more important contribution, while the contribution from lower order gaps is exponentially suppressed. Therefore the scaling of the bulk conductance is quite different than the one obtained by Gu *et al.* [113]. Our model suggests that the bulk conductance is described by Eq. (4.62) where only the evanescent states with small m (m is the order of the anti-crossing) are required, whereas in Gu *et al.*, the whole set of evanescent states originating from the gaps Δ_m including those with high m has to be taken into account, resulting in an approximate power law behavior [113].

Edge state conductance : So far, only the bulk conductance has been evaluated and it is necessary to explicit the conditions upon which edge state contributions dominates. The dotted lines in Fig. 4.12 corresponds to the estimated edge state conductance for various width of the sample. There is one edge state linking the valleys that contributes to dc conductance [113, 95, 80, 111], therefore the maximal edge conductance is equal to :

$$G_{edge}(\mu = 0) = \frac{2e^2}{h} = G_0/2. \tag{4.63}$$

This situation is completely identical to the case studied in Sec. 3.1.a) except for the factor 1/2 in the edge conductance and the different expression for the bulk conductance (4.62). We don't take into account the non-quantization of the edge states due to the driving [112] but we know that the edge states are chiral and robust to disorder, so that their conductance is independent of the size of the sample. We apply the same procedure as in Sec. 3.1.a) to see the competition between edge and bulk states, and obtain the curve $L_c(W)$ for which the edge and the bulk states conductance is equal (Fig. 4.13).

4 Experimental parameters

In this section, we discuss the assumptions we made, and the restrictions they put on experimental realizations of such an irradiated graphene gFET. First, we investigate what the restrictions on the system parameters are necessary in order to have a ballistic conductor, meaning that dissipation occurs in the leads. In a second part, we consider the laser characteristics (frequency and power) that are needed to observe the particular effects predicted in this paper.

4.1 Dissipation

The Landauer-Büttiker formalism implicitly assumes that all the dissipation occurs in the leads. In the irradiated region, the electrons are coherently dressed by one or several quanta of the electromagnetic radiation, and the corresponding excess energy is dissipated in the drain electrode of the transistor. Clearly, this is only valid when the

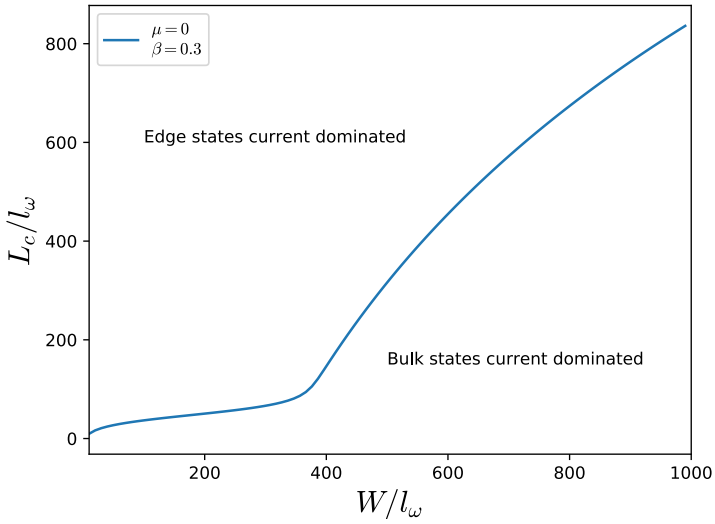

Figure 4.13 – Critical length L_c where bulk and edge have the same contribution to the current at $\mu = 0$ for a driving strength $\beta = 0.3$. For lengths longer than L_c, the current is carried mainly by edge states whereas for shorter lengths, the current is dominated by the evanescent bulk states.

irradiated region length L is short enough. If we consider coupling to a phonon bath, we have to compare the characteristic time for excited electrons to emit phonons to the passage time of the electron through the scattering region. We require

$$L < v\tau_{ph} \tag{4.64}$$

where τ_{ph} is the average time for an electron to decay into phonons. This gives an upper bound on the sample length, depending on which process dominates at the energy of the photons. The dominant process for relaxation of excited electrons is the emission of optical phonons of energy 194 or 330 meV [114]. The characteristic time for this process is $\tau_{opt} \approx 1$ps, which limits the sample length to $L < 1\mu$m. For electrons with smaller energy, the only dissipating channel is the acoustic phonon [115, 116], which is a much slower process that takes place on a timescale of the order of a nanosecond [116]. This channel limits the length to $L < 1$ mm.

Finally, the assumption of a ballistic conductor requires the length of the sample to be smaller than the mean free path l_e of scattering of electrons by impurities, which in high-quality graphene is $l_e \approx$ 1-10μm.

In order to safely neglect the effect of dissipation by scattering of electrons by optical phonons, we then need electron energies $\hbar\omega$ smaller than 200 meV. In this regime, the two remaining dissipation processes that limit the sample size are scattering by impurities and acoustic phonons. Since the acoustic phonon scattering time is very long, the only remaining process restricting the size of the sample for electron energies $\hbar\omega < 200$ meV is impurity scattering. At these typical energies, the photon energy is much smaller than the bandwidth of graphene, so the Dirac equation approximation is valid.

4.2 Observability

Accounting for the restriction on the photon energies in the last section, we consider photon energies ranging from 10 to 100 meV. Experimentally, the typical electron densities

that can be reached in graphene are around $5 \cdot 10^{12}$cm.s^{-1} which corresponds to Fermi energies up to 250 meV. With the electron energies considered, it is experimentally feasible to reach the energy dips at $\pm\hbar\omega/2$.

Photons with energy from 10 to 100 meV corresponds to Terahertz frequencies ranging from 2.5 to 25 THz. This frequency window corresponds to characteristic lengths l_ω = 6 nm to 0.6 nm. The typical electric field can be expressed as:

$$E_0 = \beta \frac{\hbar\omega}{e l_\omega}, \tag{4.65}$$

which means that the electric field intensity E_0 required to reach $\beta = 0.1$ range from 10^5 to 10^7V/m.

5 Conclusions

The two-terminal conductance of a rectangular graphene ribbon irradiated by an electromagnetic wave (frequency ω) has been studied using the Floquet theory for experimentally realizable setups. In the ballistic regime our numerical calculations confirm that the coherent dressing of the original Dirac cone leads to the opening of a set of two non-equivalent photo-induced gaps in the Floquet zone, around quasi-energies $\varepsilon = 0$ and $\varepsilon = \hbar\omega/2$. The size of the gaps are found to be in good agreement with RWA estimations [117] at low irradiation β. When the chemical potential is tuned inside one of these photo-induced gaps, the conductance of the sample decreases drastically because the current is now carried by evanescent states (rather than propagating states when $\beta = 0$). The conductance curve as a function of the chemical follows closely the non-irradiated one except at integer multiples of $\hbar\omega/2$ where broad dips appear. For weak driving, the main effect on the conductance is seen at doping $\mu = \hbar\omega/2$, while for stronger driving additional dips also develop around $\mu = \hbar\omega$. The effect of the irradiation is also effective at the Dirac point where it modulates the value of bulk minimal conductance. The widths of these dips (on the axis of chemical potential) correspond to the sizes of the gaps in the Floquet spectrum, while the depth of these dips (on the conductance axis) depends on the length of the sample. The residual conductance in dips originate from the set of evanescent states corresponding to the set of nested gaps. Depending on the driving strength, this conductance can been fitted by assuming that the current is carried by a few evanescent states characterized by distinct decay lengths.

Besides the transport by 2D bulk states, electrons may also propagate through photo-induced 1D edge states. We have shown that the edge state contribution to the total conductance can be neglected for short enough samples, and quantitative criteria to be in the bulk transport regime have been given.

Chapter 5

Irradiated quantum spin Hall edge state

In this chapter, we consider electronic transport through the helical edge state of a quantum spin Hall (QSH) insulator irradiated by an electromagnetic wave. In the adiabatic limit, irradiating such a system leads to a charge pumping mechanism which has a topological origin [118, 12]. The photocurrent has been investigated in the presence of dissipation through coupling with an environment [119]. In previous studies, the pumped current has been investigated for an infinite system. In our work, we consider a geometry where the irradiated edge state is coupled to leads which is always the case in any experiment.

In Sec. 1, we review the properties the QSH state. In Sec. 2, we present the Hamiltonian of the helical edge state. In Sec. 3, we develop the formalism of the electronic transport in this system and compute the pumped charge of the irradiated edge state coupled to leads. In Sec. 4, we analyse the topological properties of the system in the adiabatic regime.

1 Quantum Spin Hall insulator

In the previous chapters, we have discussed the Chern insulators in which time-reversal symmetry is broken. In time-reversal invariant systems, the Hall conductivity (and the Chern number) vanishes. However, in the presence of time-reversal symmetry, another kind of topological insulator exists, namely the quantum spin Hall (QSH) insulator which belongs to the class AIII. A model for such a time-reversal invariant topological insulator was first introduced by Kane and Mele [7] for graphene in the presence of spin-orbit coupling. The spin-orbit interaction respects time-reversal symmetry, and in the low-energy description of graphene, it generates a spin-dependent Haldane mass term with opposite sign for each spin. Therefore, a QSH insulator can be pictured as two copies of the Haldane model with opposite Chern number for the two spin projections. The total Chern number is zero, and no charge current is generated along the edges. However, because each spin has opposite Chern number, there is a non-zero spin Hall conductivity, carried by two edge states that counter-propagate along the edge with opposite spin. Because of this spin-momentum locking, these edge states are called helical. There exists therefore a helical one-dimensional metal along the edges.

In graphene, the spin-orbit coupling is weak and the gap induced by spin-orbit is too small for the quantum spin Hall effect to be observed experimentally. Following the theoretical model of the QSH effect in graphene by Kane and Mele, other model systems with stronger spin-orbit coupling strength were suggested to exhibit the QSH effect, such as

paramagnetic semiconductors [37] or semiconductors under a strain gradient [9]. However, the crucial step was made by Bernevig, Hugues and Zhang [8] who predicted in 2006 the existence of the QSH effect in HgTe/CdTe quantum wells that possess strong spin-orbit coupling. The QSH effect in such structures was shortly after observed experimentally by Laurens Molenkamp's group [41]. In a simple model, HgTe possesses a valence band corresponding to the s orbitals and a conduction band made of p orbitals. In contrast, CdTe has s above p. A layer of HgTe is sandwiched between two layer of CdTe, and when the thickness of the HgTe layer is higher than a critical thickness d_c, the p orbitals rise above the s orbitals, which leads to an inverted band structure. In that case, the HgTe quantum well is topologically non-trivial and presents counter-propagating edge states. The thickness of the layer allows to engineer a topological phase transition. The same mechanism was predicted to exist in InAs/GaSb quantum wells [120], in which robust helical edge states were observed later on [121]. More recently, the QSH effect was observed in a transition metal dichalcogenide, WTe_2 [42, 122], where the bulk band gap was found to be of the order of 50-100meV.

As we have seen in Chap. 1, time-reversal invariance implies :

$$H(\mathbf{k})|u_{\mathbf{k}}\rangle = E(\mathbf{k})|u_{\mathbf{k}}\rangle \quad \Rightarrow \quad H(-\mathbf{k})\mathcal{T}|u_{\mathbf{k}}\rangle = E(\mathbf{k})\mathcal{T}|u_{\mathbf{k}}\rangle, \tag{5.1}$$

which means that a state $|u_{\mathbf{k}}\rangle$ and its time-reversed $\mathcal{T}|u_{\mathbf{k}}\rangle$ are degenerate. In the case of spinful particles, we have seen that the time-reversal operation has the property $\mathcal{T}^2 = -1$. This property has an important consequence in the case of time-reversal invariant systems, which is the Kramer's degeneracy. Kramer's theorem states that for half-integer spin particles, a state and its time-reversed state are orthogonal. In the case of Bloch electrons, the time-reversed state of a state momentum $\mathbf{k}$ is a state at momentum $-\mathbf{k}$, and therefore, backscattering between these two states is forbidden.

The QSH insulator is characterized by a $\mathbb{Z}_2$ invariant which takes only two values 0, or 1. This invariant counts the parity of the number of Kramer's partners of edge states that cross the Fermi energy [4]. If this is an even number, backscattering is allowed between states that are not Kramer's partners, while if there is an odd number, there is always a protected pair which is left. There exists several expressions used to compute this topological invariant [7, 123, 62, 124].

2 Helical edge state

The QSH edge states can be pictured as a helical liquid [125] with a linear dispersion close to the crossing that respects time-reversal invariance. In a 1D lattice model that respects time-reversal symmetry, the fermion doubling theorem states that the lattice model must have an even number of Dirac fermions at low-energy [126]. However, in the topological phase, there is only one fermion branch, and thus, this fermion branch exists only as a holographic metal at the edge of a QSH insulator. This edge state is robust to weak interactions and disorder [127].

We introduce here the properties of the helical edge state of the QSH insulator. The Hamiltonian is composed of a pair of Kramer's partners such that states with opposite momenta have opposite spins. Because the two edge states are Kramer's partners at momentum $\mathbf{k}$ and $-\mathbf{k}$, backscattering is forbidden as long as time-reversal symmetry is preserved. Transport through these edge states is therefore ballistic even in the presence of disorder that respects time-reversal invariance.

The helical edge states is described by the Hamiltonian [125] :

$$\mathcal{H}_0 = \hbar v \int dx(\psi^\dagger_{R,\uparrow} i\partial_x \psi_{R,\uparrow} - \psi^\dagger_{L,\downarrow} i\partial_x \psi_{L,\downarrow}), \tag{5.2}$$

where the right (left) movers $\psi_{R,\uparrow}(\psi_{L,\downarrow})$ annihilation operators carry spin up (down) and v is the Fermi velocity of the edge state. For a system invariant by translation, we can make a Fourier transform of the field operators :

$$\psi_\alpha(x) = \int \frac{dk}{\sqrt{2\pi}} c_\alpha(k) e^{-ikx}, \tag{5.3}$$

where k is the quasi-momentum of the edge state along x, $\alpha = \{\uparrow, \downarrow\}$, and we have dropped the right/left index because it is pinned to the spin. Inserting Eq. (5.3) into (5.2), we obtain the Hamiltonian :

$$\mathcal{H}_0 = \hbar v \int dk k(c^\dagger_\uparrow(k) c_\uparrow(k) - c^\dagger_\downarrow(k) c_\downarrow(k)), \tag{5.4}$$

which can be recast as :

$$\mathcal{H}_0 = \int dk \Psi^\dagger(k) H_0(k) \Psi(k), \tag{5.5}$$

where $\Psi^\dagger(k) = (c^\dagger_\uparrow(k), c^\dagger_\downarrow(k))$ and $H_0(k)$ is the first quantized Bloch Hamiltonian which has the form :

$$H_0(k) = \hbar v k \sigma_z, \tag{5.6}$$

where σ_z is the Pauli matrix acting on spin space. Here, the Pauli matrices act on the real spin.

3 Transport through the irradiated edge state

In this section, we consider the same transport formalism as in Chap. 4 applied to the irradiated helical edge state. Because the edge state is one-dimensional, there is only one channel. First, we calculate the spectrum and wavefunction of a topological insulator edge state irradiated by a circularly polarized electromagnetic wave. The total Bloch Hamiltonian is :

$$H(k,t) = H_0(k) + V(t) \ , \tag{5.7}$$

where H_0 is the bare Hamiltonian and $V(t)$ corresponds to the coupling with the electromagnetic wave. We focus on the light-matter coupling through the Zeeman effect between the spin magnetic moment and the magnetic field of the EM wave $\mathbf{B}(t) = B_0(\cos(\omega t)\mathbf{e}_x + \sin(\omega t)\mathbf{e}_y)$. Because the magnetic field couples to the spin of the electrons, it allows transitions between the two spin projections. To neglect the coupling of the electrons with the electric field, we consider the semi-classical argument described in [12]. The orbital coupling strength is evA_0, with $A_0 = E_0/\omega$, where E_0 the electric field strength. The electric field can be neglected when the coupling strength is negligible compared to the quantum of energy $\hbar\omega$ that can be absorbed, namely $evE_0/\omega \ll \hbar\omega$. Moreover, $\hbar\omega$ must be smaller than the bulk band gap of the QSH insulator. For a band gap of 100meV [122], this restricts the frequencies to lower than 20THz.

The Hamiltonian of the interaction is :

$$V(t) = -\boldsymbol{\mu}\mathbf{B}(t) = \mu_B g_{\text{eff}} B_0 \left(\sigma_x \cos(\omega t) + \sigma_y \sin(\omega t)\right), \tag{5.8}$$

$$= g(\sigma_+ e^{-i\omega t} + \sigma_- e^{i\omega t}) \ , \tag{5.9}$$

where $\boldsymbol{\mu}$ is the magnetic moment of the electron spin, μ_B is the Bohr magneton, g_{eff} is the effective g-factor, $g = \mu_B g_{\text{eff}} B_0$ is the total coupling constant, and $\sigma_\pm = \sigma_x \pm i\sigma_y$.

In Sec. 3.1, we derive the expression for the spectrum and the eigenstates of this system using Floquet formalism. In Sec. 3.2, we calculate the scattering coefficients by matching the wavefunctions at the interfaces. Finally, in Sec. 3.3, we present the results for the pumped current in the absence of potential difference.

3.1 Spectrum and eigenstates

Due to the peculiar form of the interaction presented above, it is possible to have an analytical expression for the eigenstates of this system. In Sambe space, the quasi-energy eigenvalue equation given by Eq. (3.10) can be written as :

$$(vk\sigma_z + n\omega)\,\Phi_{\alpha,n} + g\sigma_-\Phi_{\alpha,n-1} + g\sigma_+\Phi_{\alpha,n+1} = \varepsilon_\alpha \Phi_{\alpha,n}, \tag{5.10}$$

where $\Phi_{\alpha,n}$ is the nth Fourier component of the eigenstate α such that $\Psi_\alpha(t) = e^{-i\varepsilon_\alpha t}\sum_n \Phi_{\alpha,n} e^{in\omega t}$, and $\hbar = 1$. Setting $\Phi_n = (u_n, v_n)^T$, where u_n and v_n are the weight of the wavefunction of the up and down spins respectively, we obtain the system of equations :

$$(vk + n\omega)\,u_n + g v_{n+1} = \varepsilon u_n, \tag{5.11}$$

$$g u_{n-1} + (-vk + n\omega)\,v_n = \varepsilon v_n. \tag{5.12}$$

We can see that u_n is only coupled to v_{n+1}, which means that if we set n, we can obtain the quasi-energies and the corresponding eigenvectors. Solving this system (of equations) gives us the quasi-energies :

$$\varepsilon_{\alpha,n} = n\omega + \frac{\omega}{2} + \alpha\lambda, \quad \text{for} \quad \Phi_{\alpha,n} = \begin{pmatrix} u_{\alpha,n} \\ v_{\alpha,n+1} \end{pmatrix} \tag{5.13}$$

where $\alpha = \pm$ and $\lambda = \sqrt{(vk - \omega/2)^2 + g^2}$. Fig. 5.1 shows the dispersion relation of the $n = 0$ and $n = -1$ Floquet replicas. A gap of size $2g$ opens in the dispersion relation at momentum $k = \omega/2$ and quasi-energy $\varepsilon = n\omega + \omega/2$. For weak driving ($g < \omega/2$), this gap is located at $\varepsilon = \omega/2$ on the $n = 0$ replica, while it is located at $\varepsilon = -\omega/2$, on the $n = -1$ replica. This gap is thus located at the edges of the first Floquet zone. As the driving increases (frequency decreases), the band $(\alpha, n) = (+, -1)$ rises above the band $(-, 0)$ and a gap opens at the Floquet zone center $\varepsilon = 0$. This gap opening happens at $g = \omega/2$. Of course, there is an infinite set of replicas that are not represented on Fig. 5.1, but we plot only the replicas $n = 0$ and $n = -1$ which are the only replicas relevant for transport as we will see later.

Using Eqs. (5.11), (5.12) and (5.13), we find that the wavefunction of the electron is :

$$\Psi_{\alpha,n}(x,t) = e^{-i\varepsilon_{\alpha,n}t}\frac{1}{\sqrt{2\lambda}}\begin{pmatrix} \sqrt{\lambda + \alpha(vk - \omega/2)}\,e^{in\omega t} \\ \alpha\sqrt{\lambda - \alpha(vk - \omega/2)}\,e^{i(n+1)\omega t} \end{pmatrix} e^{ikx}. \tag{5.14}$$

3.2 Scattering formalism and transmission probabilities

In this section, we calculate the transmission and reflections probabilities using Landauer-Büttiker formalism in the same manner as for the case of graphene in the previous chapter. We consider irradiating the edge state over a length L from $x = 0$ to $x = L$. In the transport formalism, we consider electrons incoming at energy $\varepsilon \equiv \varepsilon_{\alpha,n}$. Due to the coupling with

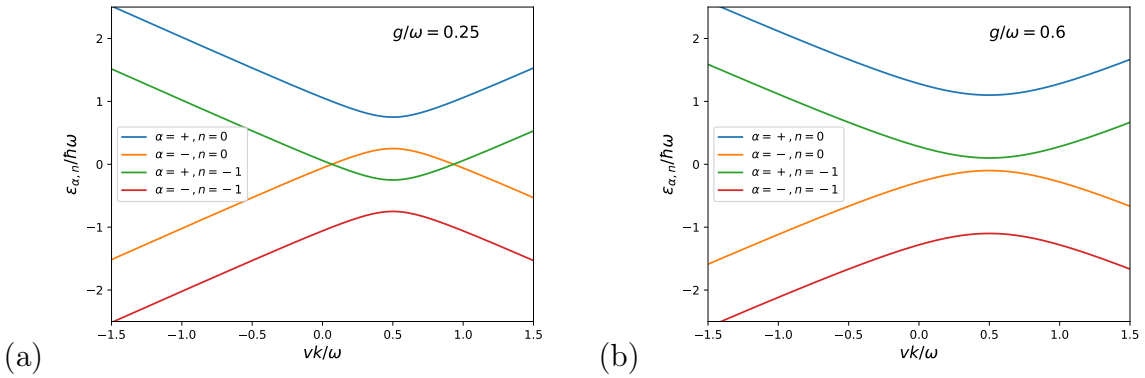

Figure 5.1 – Dispersion relation of the irradiated edge state given by Eq. (1.13) for (a) $g/\hbar\omega = 0.25$ and (b) $g/\omega = 0.6$ of the (α, n) band such that $\alpha = +, -$ labels the band index (valence or conduction) and n the number of photons. We plot only the $n = 0$ and $n = -1$ Floquet replicas. For $g < \omega/2$, we observe two gaps at $\varepsilon = \hbar\omega/2$ and $-\hbar\omega/2$, while for $g > \omega/2$, gap opens at $\varepsilon = 0$.

light, electrons can absorb or emit photons and exit with energy $\varepsilon + n\omega$. The transport can happen through propagative states, or evanescent states when the energy is inside the gap. We invert the dispersion relation (5.13) as :

$$k_{\alpha,n}(\varepsilon) = \frac{\omega}{2} + \alpha\sqrt{\gamma_n^2 - g^2}, \tag{5.15}$$

$$= \frac{\omega}{2} + \alpha K_n, \tag{5.16}$$

where $\gamma_n = (\varepsilon - n\omega - \omega/2)$, $K_n = \sqrt{\gamma_n^2 - g^2}$ is a wavevector that can be imaginary. Note that we have set $\hbar = v = 1$. In the scattering region, the wavefunction is a sum of the eigenstates at energy ε and wavevector $k_{\alpha,n}(\varepsilon)$:

$$\Psi_I(x,t) = e^{-i\varepsilon t}\left(\sum_n a_n \Phi_{+,n}(t)e^{ik_{+,n}x} + b_n\Phi_{-,n}(t)e^{ik_{-,n}x}\right), \tag{5.17}$$

where $\Phi_{\alpha,n}(t)$ is given by Eq. (5.14). In order to account for the possibility of an electron to absorb or emit photons, we apply the Floquet theorem in the leads, but without coupling to the irradiation. If we consider an electron coming from the left lead, the wavefunction is :

$$\Psi_L(x,t) = e^{-i\varepsilon t}\left(\phi^+ e^{ik_n x} + \sum_n r_n \phi^- e^{-ik_n x}e^{in\omega t}\right), \tag{5.18}$$

where $vk_n = \varepsilon - n\omega$, $\sigma_z\phi^\pm = \pm\phi^\pm$ are the left/right $(+/-)$ movers and r_n are the reflection coefficients for electrons exiting with energy $\varepsilon + n\omega$. The wavefunction in the right lead is expressed as :

$$\Psi_R(x,t) = e^{-i\varepsilon t}\sum_n t_n \phi^+ e^{ik_n(x-L)}e^{in\omega t}, \tag{5.19}$$

where t_n are the transmission coefficients. We match the spinors at the interfaces so that $\Psi_L(x = 0, t) = \Psi_I(x = 0, t)$ and $\Psi_I(x = L, t) = \Psi_R(x = L, t)$. This gives us a system of linear equations. We find that the only non-vanishing coefficients are t_0 and r_1, which means that an electron entering the irradiated region can only be transmitted at the same

energy or reflected while absorbing one photon. For a circular left-handed polarization, a photon has an angular momentum $J_z = -\hbar$ along the positive z axis. A spin-up electron has an angular momentum $J_z = \hbar/2$ and energy $\varepsilon = \hbar v k$, which means that after absorbing a photon, it becomes a spin-down electron with angular momentum $J_z = -\hbar/2$ and energy $\varepsilon = -\hbar v k + \hbar\omega$. Energy conservation implies that this process happens at quasi-energy $\varepsilon = \hbar\omega/2$.

Solving this linear system gives us :

$$t_0 = \frac{iK_0 e^{i\frac{\omega}{2v}L}}{(\varepsilon - \omega/2)\sin(K_0 L) + iK_0\cos(K_0 L)}, \tag{5.20}$$

$$r_1 = \frac{g\sin(K_0 L)}{(\varepsilon - \omega/2)\sin(K_0 L) + iK_0\cos(K_0 L)}, \tag{5.21}$$

where $K_0^2 = (\varepsilon - \omega/2)^2 - g^2$. Thus, the transmission and reflection probabilities for the propagative states are :

$$T_p(\varepsilon) = |t_0|^2 = \frac{K_0^2}{K_0^2 + g^2\sin^2(K_0 L)}, \tag{5.22}$$

$$R_p(\varepsilon) = |r_1|^2 = \frac{g^2\sin^2(K_0 L)}{K_0^2 + g^2\sin^2(K_0 L)}. \tag{5.23}$$

When the energy is in the gap, $(\varepsilon - \omega/2)^2 < g^2$, K_0 is imaginary : $K_0 = i\kappa_0 = i\sqrt{g^2 - (\varepsilon - \omega/2)^2}$. Using the relations $\sin(ix) = i\sinh(x)$ and $\cos(ix) = \cosh(x)$, we obtain finally the transmission and reflection probabilities for the evanescent states :

$$T_e(\varepsilon) = |t_0|^2 = \frac{\kappa_0^2}{\kappa_0^2 + g^2\sinh^2(\kappa_0 L)}, \tag{5.24}$$

$$R_e(\varepsilon) = |r_1|^2 = \frac{g^2\sinh^2(\kappa_0 L)}{\kappa_0^2 + g^2\sinh^2(\kappa_0 L)}. \tag{5.25}$$

Fig. 5.2 shows the transmission probability as a function of the incoming electron energy. We observe a dip in the transmission probability at $\varepsilon = \hbar\omega/2$ which corresponds to the one photon resonance between the conduction band and the valence band. For a short ribbon, the transmission probability in the gap is reduced but doesn't vanish, which means that the current is carried by evanescent states. As the length of the ribbon is increased, the dip gets sharper and no evanescent states contribute to the current. The oscillations correspond to Fabry-Pérot interferences.

We consider now the reverse process, namely electrons incoming from the right lead. Applying the same formalism, we find the transmission and reflection probabilities :

$$T'(\varepsilon) = |t_0'|^2 = \frac{K_{-1}^2}{K_{-1}^2 + g^2\sin^2(K_{-1} L)}, \tag{5.26}$$

$$R'(\varepsilon) = |r_{-1}'|^2 = \frac{g^2\sin^2(K_{-1} L)}{K_{-1}^2 + g^2\sin^2(K_{-1} L)}, \tag{5.27}$$

where $K_{-1}^2 = (\varepsilon + \omega/2)^2 - g^2$. The probabilities are identical to the one for electrons incoming from the left lead except for the shift $\hbar\omega$ in energy, which translates to :

$$T(\varepsilon + \omega/2) = T'(\varepsilon - \omega/2), \tag{5.28}$$

$$R(\varepsilon + \omega/2) = R'(\varepsilon - \omega/2), \tag{5.29}$$

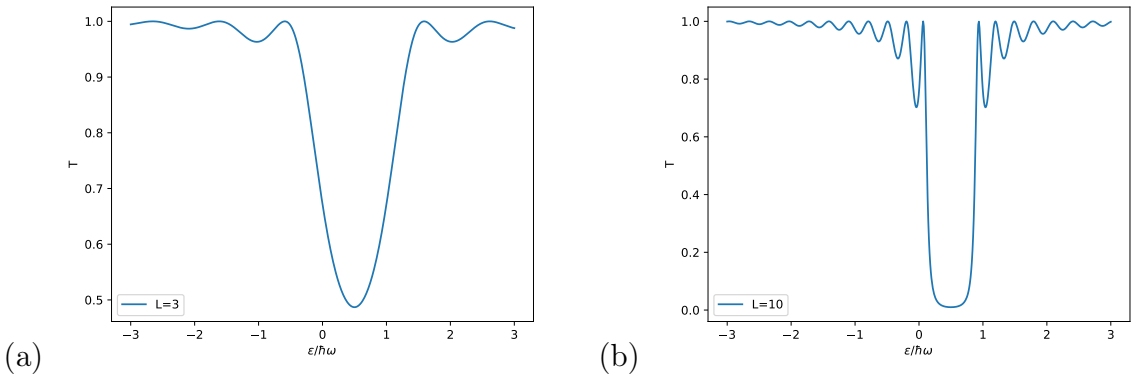

(a) (b)

Figure 5.2 – Transmission probability from the left lead to the right lead as a function of ε for a driving strength $g = 0.3\hbar\omega$ and for a ribbon of length (a) $L = 3\hbar v/\omega$, and (b) $L = 10\hbar v/\omega$.. We observe a dip of size $2g$ in the transmission around $\varepsilon = \hbar\omega/2$, which corresponds to the reflection of an electron having absorbed an electron.

3.3 Pumped current

Because time-reversal symmetry is broken (due to the circularly polarized light), the transmission probabilities from electrons incoming from the left and right leads are not identical. Such an asymmetry allows for the generation of a pumped current in the absence of a potential difference between the leads. According to the Landauer-Buttiker formalism extended to Floquet systems, the DC current through the irradiated edge state is equal to [108] :

$$I(\mu) = \frac{e}{h}\int_{-\Lambda}^{\Lambda} d\varepsilon \sum_n \left(T_n(\varepsilon) f_L(\varepsilon) - T'_n(\varepsilon) f_R(\varepsilon)\right), \tag{5.30}$$

where $T_n(\varepsilon)$ is the probability of an electron incoming from the left lead to be transmitted in the right lead having absorbed n photons, and $T'_n(\varepsilon)$ is the reversed process. $f_L(\varepsilon)$ and $f_R(\varepsilon)$ are the Fermi distributions at chemical potential μ in the left and right leads respectively. Λ is a cut-off in the integral that represents the bandwidth of the edge state, namely the size of the bulk gap of the material. Because the electrons can only be transmitted in the channel $n = 0$, we have $T_n(\varepsilon) = T(\varepsilon)$ and $T'_n(\varepsilon) = T'(\varepsilon)$. At zero bias and zero temperature, we obtain the photo-current :

$$I(\mu) = \frac{e}{h}\int_{-\Lambda}^{\mu} d\varepsilon \left(T(\varepsilon) - T'(\varepsilon)\right). \tag{5.31}$$

The pumped current is therefore the difference between transmission from the left to the right lead and the reverse process. The function $T(\varepsilon)$ and $T'(\varepsilon)$ are identical except for the shift $\pm\hbar\omega/2$ in energy. In order to simplify the expression for the current, we make a change of variable $\pm\hbar\omega/2$ in each integral, and define the function :

$$f(\varepsilon) \equiv T(\varepsilon + \hbar\omega/2) = T'(\varepsilon - \hbar\omega/2) = \frac{\varepsilon^2 - g^2}{\varepsilon^2 - g^2 + g^2 \sin^2\left(\sqrt{\varepsilon^2 - g^2}L\right)}, \tag{5.32}$$

The current has the expression :

$$I(\mu) = \frac{e}{h}\int_{-\Lambda}^{\mu} d\varepsilon T(\varepsilon) - \frac{e}{h}\int_{-\Lambda}^{\mu} d\varepsilon T'(\varepsilon) \tag{5.33a}$$

$$= \frac{e}{h}\int_{-\Lambda-\hbar\omega/2}^{\mu-\hbar\omega/2} d\varepsilon T(\varepsilon+\hbar\omega/2) - \frac{e}{h}\int_{-\Lambda+\hbar\omega/2}^{\mu+\hbar\omega/2} d\varepsilon T'(\varepsilon-\omega/2) \tag{5.33b}$$

$$= \frac{e}{h}\int_{-\Lambda-\hbar\omega/2}^{-\Lambda+\hbar\omega/2} d\varepsilon f(\varepsilon) - \frac{e}{h}\int_{\mu-\hbar\omega/2}^{\mu+\hbar\omega/2} d\varepsilon f(\varepsilon). \tag{5.33c}$$

We can see that in the limit $\Lambda \to \infty$, we have $f(\varepsilon \to -\infty) = 1$, thus :

$$I(\mu) = \frac{e\omega}{2\pi} - \frac{e}{h}\int_{\mu-\hbar\omega/2}^{\mu+\hbar\omega/2} d\varepsilon f(\varepsilon). \tag{5.34}$$

The function $f(\varepsilon)$ is plotted in Fig. 5.3 for various ribbon length. The curves have a dip centered on $\varepsilon = 0$ of width $2g$. For a long ribbon, the dip is well defined and corresponds to the gap of size g in the dispersion relation. The pumped current is the sum of two terms. The first term corresponds to a quantized charge pumping per unit cycle such that $\int_0^T I dt = e$. We can see from Eqs. (5.33) that this term originates from states located deep in the band of the edge state. This term has a topological origin [68] which is related to Thouless's charge pumping mechanism [13]. For a long length and a small frequency, the second term in Eq. (5.34) vanishes, this means that the quantized charge pumping happens in the adiabatic limit. For a left circular polarization, this current is directed along the positive x axis. As the frequency is increased such that $\hbar\omega/2 > g$, the second term generates a pumped current in the opposite direction. This current is carried by propagative states close the Fermi level such that incoming states can absorb or emit a quantum $\hbar\omega$.

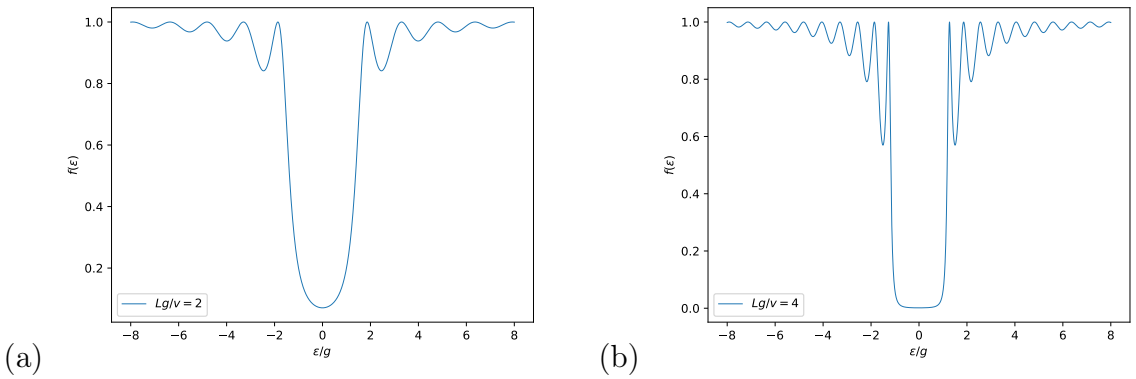

(a) (b)

Figure 5.3 – Function $f(\varepsilon)$ to integrate from $-\hbar\omega/2$ to $\hbar\omega/2$, for different length L of the irradiated region : (a) $L = 2\hbar v/g$ and (b) $L = 4\hbar v/g$

a) Pumped current at zero doping

We consider the current when the Fermi energy is located at the band crossing, namely $\mu = 0$. The pumped current becomes :

$$I_{\mu=0} = \frac{e\omega}{2\pi} - \frac{e}{h}\int_{-\hbar\omega/2}^{\hbar\omega/2} d\varepsilon f(\varepsilon), \tag{5.35}$$

$$= \frac{e\omega}{2\pi} - 2\frac{e}{h}\int_{0}^{\hbar\omega/2} d\varepsilon f(\varepsilon), \tag{5.36}$$

where we have used the fact that $f(\varepsilon)$ is even in ε. Fig. 5.4 shows the current as a function of the irradiation frequency for short ribbons. We observe the linear dependence for frequencies below $2g$ until it increases sublinearly above $2g$. We observe oscillations characteristic of Fabri-Pérot interference. At high-frequencies, the curve reaches a maximum which is independent of the frequency.

We consider now the pumped current when the irradiated region is long compared to the characteristic length of the evanescent states in the gap.

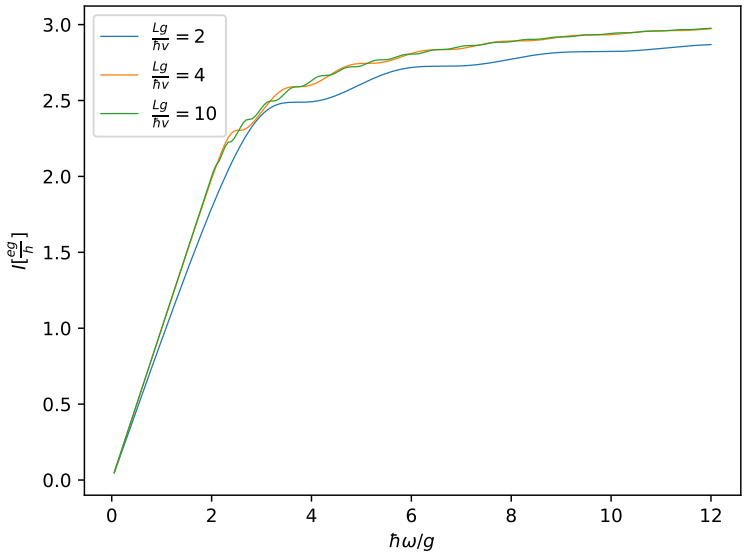

Figure 5.4 – Pumped current as a function of the driving frequency for different length L. Some small oscillations due to Fabry-Pérot interferences appear for $\omega/g \gtrsim 2$.

Long irradiated region : In the interval $0 < \varepsilon < g$, we have $\sin(\sqrt{\varepsilon^2 - g^2}L) = \sinh(\sqrt{g^2 - \varepsilon^2}L) = \sinh(\kappa L)$, where κ is the wavevector of the evanescent state in the gap. For $\kappa L \gg 1$, we have $f(\varepsilon) = 0$, therefore, the pumped current at the Dirac point is :

$$I_{\mu=0} = \frac{e\omega}{2\pi} \qquad \text{for} \quad \hbar\omega < 2g, \tag{5.37}$$

$$= \frac{e\omega}{2\pi} - 2\frac{e}{h}\int_{g}^{\hbar\omega/2} d\varepsilon f(\varepsilon) \qquad \text{for} \quad \hbar\omega > 2g. \tag{5.38}$$

For $\hbar\omega > 2g$, we can rewrite the current as :

$$I_{\mu=0} = \frac{e\omega}{2\pi} - 2\frac{e}{h}\int_g^{\hbar\omega/2} d\varepsilon + 2\frac{e}{h}\int_g^{\hbar\omega/2} d\varepsilon(1-f(\varepsilon)), \tag{5.39}$$

$$= \frac{e\omega}{2\pi} - 2\frac{e}{h}\left(\frac{\hbar\omega}{2} - g\right) + 2\frac{e}{h}\int_g^{\hbar\omega/2g} d\varepsilon(1-f(\varepsilon)), \tag{5.40}$$

$$= 2\frac{eg}{h} + 2\frac{e}{h}\int_g^{\hbar\omega/2} d\varepsilon(1-f(\varepsilon)), \tag{5.41}$$

From Fig. 5.3, we can see that the function $1-f(\varepsilon)$ tends to 0 as ω tends to infinity. Hence, the second term in Eq. 5.41 converges. Finally, we can rewrite the pumped current as :

$$I_{\mu=0} = I_{Adiabatic} \qquad \text{for} \quad \hbar\omega < 2g, \tag{5.42}$$

$$= I_{LR} + I_{Interf} \qquad \text{for} \quad \hbar\omega > 2g. \tag{5.43}$$

where $I_{Adiabatic}$ is the pumped current in the low-frequency regime, where one charge is pumped per cycle :

$$I_{Adiabatic} = \frac{e\omega}{2\pi}, \tag{5.44}$$

such that $\int_0^T I_{Adiabatic}dt = e$. I_{LR} is the pumped current in the weak driving case that can be regarded as the linear response to the current in g [12], and is equal to :

$$I_{LR} = 2\frac{eg}{h}. \tag{5.45}$$

Finally, I_{Interf} is an interference term that originates from the presence of the coupling with leads. Fig. 5.5 shows the pumped current as a function of the frequency of the driving for a long irradiated region. We compare our results with Dora *et al.* [12] where the current is calculated for the infinite system. We obtain the same result at low frequencies for the adiabatic charge pumping. They considered the filling of the bands according to the average energy $\bar{E}_\alpha = \langle\langle u_\alpha|H(t)|u_\alpha\rangle\rangle$, which is different from our setup where only states below the Fermi energy contribute to the current. At high-frequency, we find the same limiting behaviour except for the presence of an interference term originating from the leads. Our result is also very similar to Vajna *et al.* [119], where dissipation is taken into account by coupling the edge state to a bosonic bath. In our model, dissipation happens in the leads, namely in the external fermionic baths.

High frequency limit : We can see from Fig. 5.5 that the current seems to reach a plateau with increasing ω when the length is long enough. We can also see from Fig. 5.3 that this value is bounded. We now wish to perform the integral in Eq. (5.41) in the case $\hbar\omega/g \to \infty$ and $Lg/\hbar v \gg 1$. We make the change of variable $x^2 = (\varepsilon/g)^2 - 1$ and $\tilde{L} = Lg/v$ to get :

$$\lim_{\hbar\omega\to\infty} I_{Interf} = 2\frac{eg}{h}\int_0^\infty dx \frac{x}{\sqrt{x^2+1}}\frac{\sin^2(x\tilde{L})}{x^2+\sin^2(x\tilde{L})} \tag{5.46}$$

This integral can be performed analytically in the limit $\tilde{L} \gg 1$, we find (see Appendix C) :

$$\lim_{\hbar\omega/g, L\to\infty} I_{\mu=0} = \pi\frac{eg}{h} \tag{5.47}$$

Thus, we observe two different regimes. When the frequency is smaller than the Zeeman gap, we observe a current corresponding to one electron per period of the driving.

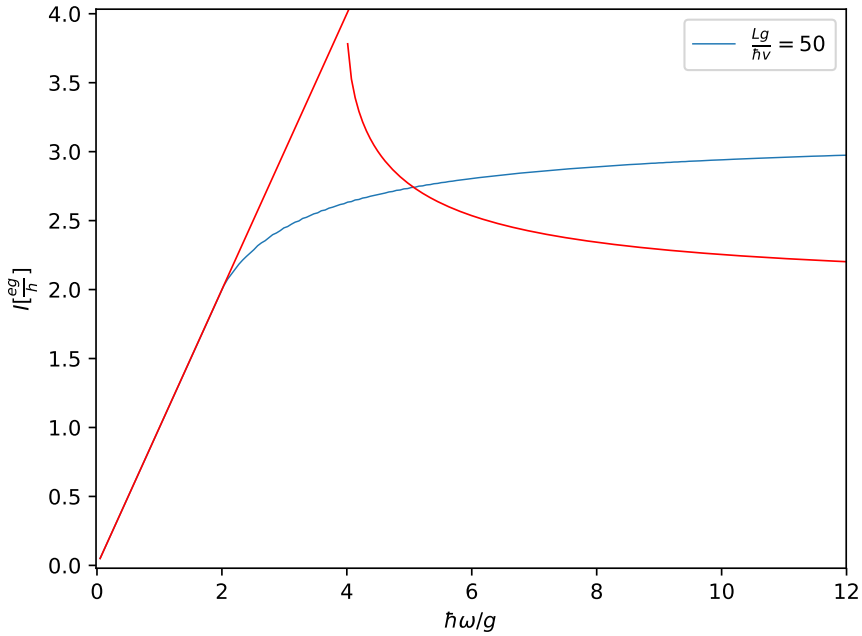

Figure 5.5 – Pumped current for a long irradiated region as a function of the driving frequency(blue curve), compared with Dora et al. [12] (red curve). For frequencies $\hbar\omega < 2g$, the current is proportional to ω, which corresponds to the adiabatic quantized charge pumping. For $\hbar\omega > 2g$, the current increases and reaches $\pi\frac{eg}{h}$ as $\omega \to \infty$.

This current is carried by states deep in the valence band and has a topological origin as we will see in Sec. 4. When the frequency is greater than the Zeeman gap, propagative states in the range $[-\hbar\omega/2, g]$ and $[g, \hbar\omega/2]$ generate a current in the opposite direction. In the limit $\hbar\omega \gg g$, this current reaches a limit which is independent of the frequency. In this limit, the pumped charge per unit cycle is equal to :

$$c = \int_0^T dt I = \pi e \frac{g}{\hbar\omega} \tag{5.48}$$

and is therefore inversely proportional to the frequency.

In the next section, we explain the topological origin of the quantized charge pumping mechanism.

4 Quantized adiabatic charge pumping

Berry's phase finds a broad range of applications in physical systems. We have seen that it plays an important role in the case of the quantized Hall conductivity of Chern insulators. Just before the introduction of such a phase for adiabatic and cyclic processes, Thouless [13] introduced the concept of quantized adiabatic charge pumping. In a time-periodic one dimensional model with translational invariance, Thouless said that the pumped charge per cycle has an expression similar of the expression for the TKNN integer for the quantum Hall conductivity, which is the integral of the Berry curvature over the Brillouin zone. The eigenstates of a Hamiltonian with translational symmetry can be

labelled by their quasi-momentum k such that they have the Bloch form $e^{ikx}|u_k^n\rangle$, where n is the band index. When the Hamiltonian is subjected to a time-periodic excitation such that $H(t) = H(t+T)$, the eigenstates are now time-dependent. In the adiabatic approximation, the velocity of the electrons can be expressed as [71] :

$$v_n(k) = \frac{\partial \varepsilon_n(k)}{\hbar \partial k} - \mathcal{F}^n_{qt}, \tag{5.49}$$

where the second term is an anomalous velocity which can be expressed as the Berry curvature in paramater space (k,t) :

$$\mathcal{F}^n_{kt}(k,t) = i\left\langle \frac{\partial u_k^n(t)}{\partial k} \middle| \frac{\partial u_k^n(t)}{\partial t} \right\rangle - i\left\langle \frac{\partial u_k^n(t)}{\partial t} \middle| \frac{\partial u_k^n(t)}{\partial k} \right\rangle \tag{5.50}$$

The pumped current carried by the filled band n is given by :

$$j^n = e\int \frac{dk}{2\pi}\mathcal{F}^n_{kt}(k,t), \tag{5.51}$$

where the first term in (5.49) vanishes because the full valence band doesn't generate any current. The pumped charge per cycle is given by :

$$C^n = \frac{1}{2\pi}\int_0^T dt \int dk \mathcal{F}^n_{kt}(k,t) \tag{5.52}$$

which is nothing else than the Chern number carried by the band n in parameter space (k,t). The pumped charge per unit cycle is thus quantized.

The application of a magnetic field on the helical edge state breaks time-reversal symmetry, which in turn couples the two spin species, leading to the opening of a gap in the dispersion relation of the edge state. When the edge state is irradiated with an electromagnetic wave, the magnetic field creates a closed loop in parameter space. If we consider the coupling between the EM wave and the helical edge state through the Zeeman interaction, the model realizes Thouless's topological charge pumping mechanism and presents also bound fractional charges at magnetic domain walls [118]. We will consider here the topological properties of this charge pumping mechanism.

We consider a setup identical to the one in Ref. [12], where the edge state lies along the x axis. It is irradiated by an elliptically polarized electromagnetic wave with frequency ω and wavevector k_0 such that its vector potential is $\mathbf{A}(t) = A_0(\cos(\omega t - k_0 z), \chi \sin(\omega t - k_0 z))$, where $\chi = \pm$ is the polarization of electromagnetic wave. The Hamiltonian of the system is :

$$H(k,t) = v\sigma_z(k - eA_x(t)) - \mu_B \mathbf{B}(t)\boldsymbol{\sigma}, \tag{5.53}$$

where $\mathbf{B}(t) = \nabla \times \mathbf{A}(t) = B_0(\cos(\omega t - k_0 z), \chi \sin(\omega t - k_0 z), 0)$ is the magnetic field of the electromagnetic wave such that $B_0 = -\omega/cA_0$, and we have set $g_s/2 = 1$, where $g_s \approx 2$ is the gyromagnetic ratio of the electron. If we parametrize the path by the angle φ corresponding to the angle of the vector $\mathbf{B}$ relative to the x axis such that $\varphi = \omega t$, we express the Hamiltonian as $H(k,\varphi) = \mathbf{d}(k,\varphi)\boldsymbol{\sigma}$, where the vector $\mathbf{d}(k,\varphi)$ is :

$$\mathbf{d}(k,\varphi) = \begin{pmatrix} g\cos(\varphi) \\ \chi g \sin(\varphi) \\ v(k - eA_{0x}\cos(\varphi)) \end{pmatrix}, \tag{5.54}$$

where we have set $g = -\mu_B B_0$. The vector $\mathbf{d}(k,\varphi)$ represents a mapping from the parameter space (k,t) to the Bloch sphere. We can see that this vector has a similar form as for

the case of the band crossing in graphene from Eq. (3.71). This vector points towards the north pole for $k \to +\infty$ and towards the south pole for $k \to -\infty$, and it rotates around the Bloch sphere as the magnetic field rotates in the xy plane around the origin. We can see that there is a non trivial winding of the vector $\mathbf{d}(k,\varphi)$ around the Bloch sphere, which signals a non-trivial topology.

The dispersion relation is :

$$\varepsilon_{\pm}(k,\varphi) = \pm|\mathbf{d}| = \sqrt{g^2 + v^2(k - eA_0\cos(\varphi))^2}, \tag{5.55}$$

We can see that the effect of the orbital coupling is only to shift the dispersion relation along the k axis. Using the parametrization of the eigenstates as Eq. (2.35), the Berry connection of the valence band in the north gauge has the expression :

$$\mathcal{A}_{\varphi}^{N^-}(k,\phi) = i\langle u_{k\varphi}^{N^-}|\partial_{\varphi}|u_{k\varphi}^{N^-}\rangle = \frac{1}{2}\left(1 - \frac{v(k - eA_0\cos(\varphi))}{\sqrt{g^2 + v^2(k - eA_0\cos(\varphi))^2}}\right) \tag{5.56}$$

$$\mathcal{A}_{k}^{N^-}(k,\phi) = 0 \tag{5.57}$$

The pumped charge of the filled valence band can be expressed in parameter space (k,φ) as :

$$C^- = \frac{1}{2\pi}\int d\varphi dk \mathcal{F}_{k\varphi}^-(k,\varphi), \tag{5.58}$$

where the Berry curvature is :

$$\mathcal{F}_{k\varphi}^-(k,\varphi) = \partial_k \mathcal{A}_{\varphi}^{N^-}(k,\phi) = g^2\left[g^2 + v^2(k - eA_0\cos(\varphi))^2\right]^{-3/2}. \tag{5.59}$$

The Berry curvature is peaked around momentum $eA_0\cos\varphi$ and decreases away from it. Finally, the pumped charge per unit cycle equals :

$$C^- = \frac{1}{2\pi}\int d\varphi dk \partial_k \mathcal{A}_{\varphi}^{N^-}(k,\varphi) \tag{5.60}$$

$$= \frac{1}{2\pi}\int d\varphi \left[\mathcal{A}_{\varphi}^{N^-}(\infty,\varphi) - \mathcal{A}_{\varphi}^{N^-}(-\infty,\varphi)\right] \tag{5.61}$$

$$= -\chi, \tag{5.62}$$

where χ is the polarization of the EM wave, which is left-handed for $\chi = 1$ and right-handed for $\chi = -1$. Therefore, the pumped charge per unit cycle is quantized as long as the path in parameter space encloses the origin. We see from the expression for the Chern number that the calculation is independent of the orbital coupling because the integration over k goes from $-\infty$ to $+\infty$ and the orbital coupling only acts as a shift in momentum. Therefore the orbital coupling doesn't contribute to the charge pumping. Hence, the average current can be expressed as :

$$j = \frac{e}{T}C^- = -\chi\frac{e\omega}{2\pi} \tag{5.63}$$

We see that this expression is identical to the one obtained in the previous section for $\hbar\omega < 2g$ in the transport formalism. As we have seen in Sec. 3.1, the gap at $\varepsilon = 0$ closes when $\hbar\omega = 2g$, the valence and conduction bands are not well defined which signals that the Chern number is ill-defined for $\hbar\omega > 2g$. Thus, we obtain that the pumped current in the adiabatic regime originates from a topological property of the valence band in the presence of a magnetic field rotating in parameter space.

5 Experimental parameters

We wish to find the regime of the laser parameters for which these two charge pumping regimes can be observed experimentally. The first constraint is that the laser frequency must be smaller than the bulk band gap of the material. Typical gaps are of the order of 50-100meV [42, 122], which puts an upper bound on the laser frequency of the order of 10Thz. For a laser power of 1W focused on an area of 1mm^2, the typical electric field strength is $E_0 = 10^3\text{V/m}$. The Zeeman coupling constant is thus of the order $g = g_{\text{eff}}\mu_B B_0 = g_{\text{eff}}\mu_B E_0/c \approx 10^{-9}\text{eV}$, where the effective g-factor which can be enhanced ($g_{\text{eff}} \approx 20 - 50$) in materials with strong spin-orbit coupling like HgTe/CdTe [12]. For a laser frequency of 1Thz, we are in the weak coupling $g \ll \hbar\omega$ (high-frequency) regime, and the pumped current is thus of the order of $I = \pi eg/h = 1\text{pA}$.

6 Conclusion and perspectives

In this chapter, we have considered transport through a QSH helical edge state irradiated by a circularly polarized electromagnetic wave. We have neglected the orbital coupling which is negligible compared to the Zeeman coupling in the regime $evE_0 \ll \hbar\omega$. In this regime, only transitions between spin up and spin down are allowed meaning that an incoming electron can only absorb or emit one photon. The dissipation is expected to happen in the leads. The particular form of the Hamiltonian allows to obtain the transmission and reflection probabilities analytically using Floquet formalism. In the absence of a potential difference between the leads, a pumped current is generated.

In the adiabatic regime, the valence band and conduction bands are separated by a gap. In this regime, there is a unit charge pumped during one period of the driving, which corresponds to Thouless's charge pumping mechanism. This quantized pumped charge is directly related to the Chern number of the valence band in the parameter space (k, t) of time periodic one-dimensional systems. The pumped charge is therefore carried by states deep in the valence band. In this regime, the orbital coupling has no effect on the pumped current.

For higher frequencies, the valence band and the conduction band are not well defined and the pumped charge is not quantized. In this regime of high-frequency and small coupling, the pumped charge is the sum of two contribution, a current analogous to the linear response of the system and an interference term due to the presence of leads. We compared our results with Dora *et al.* [12] and found that the presence of leads contributes to an additional pumped current compared to the system without leads. We also found similar results with Vajna *et al.* [119] where they considered dissipation happening through coupling with a bosonic bath.

This preliminary work opens the possibility to expand the analysis of this system to different regimes of parameters. It would be interesting to study the effect of the application of a potential difference between the leads and see how it competes with the pumped current. This work could also be extended to take into account the orbital coupling with light and the effect of the chemical potential of the edge state. Another interesting path would be to study the noise in this system.

Conclusion

This thesis is based on two basic ingredients, namely graphene and topological insulators. The link between these elements was to induce non-trivial topological phases in graphene through periodic driving by an electromagnetic wave. Chapters 1, 2 and 3 were dedicated to introducing these systems. Our main work was to study transport in irradiated graphene (Chap. 4), and the irradiated helical edge state of a quantum spin Hall insulator (Chap. 5).

Graphene is a good playground for studying topological phases of matter. It is a Dirac material with a linear dispersion relation at low-energy around the Dirac points. These points are protected by the presence of time-reversal and space-inversion symmetries, and breaking one of these symmetries opens a mass gap in the low-energy spectrum. In particular, we have seen that breaking time-reversal symmetry can generate a topological phase with a non-zero Chern number. The non-trivial topological properties derive from the fact that it is impossible to define a continuous gauge for the eigenstates over the whole Brillouin zone. We have considered two models based on the graphene lattice that present a non-zero Chern number :

- the Haldane model where time-reversal symmetry is broken through the presence of complex second neighbour hoppings with a magnetic flux pattern threading the unit cell. Modulating the parameters of the model allows to visualize a topological phase transition. We have discussed the characteristic chiral edge states that cross the gap and their chirality as a function of the Chern number of the filled valence band.

- graphene irradiated by a circularly polarized electromagnetic wave. In that case, the periodic driving breaks time-reversal symmetry. We have paid a particular attention to the Chern number of the bands and the chiral edge states bridging the non-equivalent gaps in the quasi-energy spectrum in three different regimes :

  - in the high-frequency regime, irradiated graphene is identical to the Haldane model. We have shown that the chirality of the edge states depends on the helicity of the electromagnetic wave.
  - when the frequency is of the order of the bandwidth and on resonance, we have calculated the Chern number of the Floquet bands by couting the number of edge states crossing the non-equivalent gaps in the quasi-energy spectrum.
  - in the low frequency regime where graphene is modelled by Dirac equation. In that case, we can assign an effective Hamiltonian at a band crossing and an associated Chern number. We have derived an effective Hamiltonian at a band-crossing with its associated Chern number. We have developed a procedure to obtain the dispersion relation of the edge states, their chirality and their wavefunctions.

In chapter 4, we have considered ballistic transport through an irradiated graphene sheet in a two-terminal setting. The graphene sheet is connected to two leads and we have obtained the conductance of the ribbon using the Landauer-Buttiker formalism extended to Floquet theory. The electrons are dressed by the photons and can be transmitted or reflected by absorbing or emitting one or more photons. The Floquet spectrum possesses a nested gap structure at the two non-equivalent gaps at quasi-energy $\varepsilon = 0$ and $\varepsilon = \hbar\omega$. The chemical potential can be tuned by an electrostatic gate. The conductance as a function of the chemical potential follows closely the non irradiated curve similar to Ref. [99] except at multiples of $\hbar\omega/2$ where we observe dips in the conductance. The residual conductance in the gap originates from the set of evanescent states with different characteristic lengths, which compete as the driving strength and the length of the ribbon are varied. This work has been published in Phys. Rev. B [128].

Another material that presents a different kind of non-trivial topological order is the quantum spin Hall effect. In these materials, time-reversal symmetry is conserved and the topological properties are encoded into a $\mathbb{Z}_2$ topological invariant. Such a model can be defined on the graphene lattice by introducing spin-orbit coupling and it possesses two counter-propagating edge states with the spin locked to the momentum. Chapter 5 presents a preliminary work concerning the transport properties of the helical edge state of the quantum spin Hall effect under irradiation. We have obtained the expression of the charge pumped due to the irradiation when the Fermi energy is at the Dirac point. We have found that there exists two regimes : at low frequency (compared to the coupling strength), the pumped charge per unit cycle is quantized, while at high frequency the charge is not quantized and is the sum of two contributions, one corresponding to a term analogous to a linear response mechanism, and a second one originating from the presence of leads. This work will be extended to a larger set of parameters and will be the subject of a second publication.

Appendix A

Symmetry constraints on the Berry phase properties

We wish to find the constraints imposed by time-reversal and space inversion on the Berry connection and Berry curvature. We denote respectively $\mathcal{A}^U(\mathbf{k})$ and $\mathcal{F}^U_{xy}(\mathbf{k})$ the resulting berry connection and curvature under the transformation U. If the system is symmetric under the transformation, then we must have :

$$\mathcal{A}^U(\mathbf{k}) = \mathcal{A}(\mathbf{k}) + \nabla\zeta(\mathbf{k}) \tag{A.1}$$
$$\mathcal{F}^U_{xy}(\mathbf{k}) = \mathcal{F}_{xy}(\mathbf{k}) \tag{A.2}$$

where we have allowed for a gauge freedom upon the action of the symmetry transformation for the Berry connection which is defined up to a gauge transformation.

1 Time-reversal symmetry

Under time-reversal, the Berry connection for spinless particles transforms as :

$$\mathcal{A}^T(\mathbf{k}) = i\langle u^T_{\mathbf{k}}|\nabla_{\mathbf{k}}|u^T_{\mathbf{k}}\rangle, \tag{A.3}$$
$$= i\langle u^*_{-\mathbf{k}}|\nabla_{\mathbf{k}}|u^*_{-\mathbf{k}}\rangle, \tag{A.4}$$
$$= i\int d^2x u_{-\mathbf{k}}(\mathbf{x})\partial_{\mathbf{k}}u^*_{-\mathbf{k}}(\mathbf{x}) \tag{A.5}$$

We integrate by parts to obtain :

$$\mathcal{A}^T(\mathbf{k}) = -i\int d^2x \partial_{\mathbf{k}}u_{-\mathbf{k}}(\mathbf{x})u^*_{-\mathbf{k}}(\mathbf{x}) \tag{A.6}$$
$$= -i\int d^2x u^*_{-\mathbf{k}}(\mathbf{x})\partial_{\mathbf{k}}u_{-\mathbf{k}}(\mathbf{x}) \tag{A.7}$$
$$= i\int d^2x u^*_{-\mathbf{k}}(\mathbf{x})\partial_{-\mathbf{k}}u_{-\mathbf{k}}(\mathbf{x}) \tag{A.8}$$
$$= i\langle u_{-\mathbf{k}}|\nabla_{-\mathbf{k}}|u_{-\mathbf{k}}\rangle, \tag{A.9}$$
$$= \mathcal{A}(-\mathbf{k}) \tag{A.10}$$

The Berry curvature transforms as :

$$\mathcal{F}^T_{xy}(\mathbf{k}) = \partial_{k_x}\mathcal{A}^T_y(\mathbf{k}) - \partial_{k_y}\mathcal{A}^T_x(\mathbf{k}), \tag{A.11}$$
$$= -(\partial_{-k_x}\mathcal{A}_y(-\mathbf{k}) - \partial_{-k_y}\mathcal{A}_x(-\mathbf{k})), \tag{A.12}$$
$$= -\mathcal{F}_{xy}(-\mathbf{k}) \tag{A.13}$$

Thereby, if the system is time-reversal invariant, we have :

$$\boldsymbol{\mathcal{A}}(\mathbf{k}) = \boldsymbol{\mathcal{A}}(-\mathbf{k}) + \nabla\zeta(\mathbf{k}) \tag{A.14}$$
$$\mathcal{F}_{xy}(\mathbf{k}) = -\mathcal{F}_{xy}(-\mathbf{k}) \tag{A.15}$$

2 Space-inversion symmetry

Under space inversion, the Berry connection transforms as :

$$\mathcal{A}^P(\mathbf{k}) = i\langle u^P_{\mathbf{k}}|\nabla_{\mathbf{k}}|u^P_{\mathbf{k}}\rangle, \tag{A.16}$$
$$= i\langle u_{-\mathbf{k}}|\sigma_x\nabla_{\mathbf{k}}\sigma_x|u_{-\mathbf{k}}\rangle, \tag{A.17}$$
$$= -i\langle u_{-\mathbf{k}}|\sigma_x\nabla_{-\mathbf{k}}\sigma_x|u_{-\mathbf{k}}\rangle, \tag{A.18}$$
$$= -\mathcal{A}(-\mathbf{k}) \tag{A.19}$$

The Berry curvature transforms as :

$$\mathcal{F}^T_{xy}(\mathbf{k}) = \partial_{k_x}\mathcal{A}^T_y(\mathbf{k}) - \partial_{k_y}\mathcal{A}^T_x(\mathbf{k}), \tag{A.20}$$
$$= (\partial_{-k_x}\mathcal{A}_y(-\mathbf{k}) - \partial_{-k_y}\mathcal{A}_x(-\mathbf{k})), \tag{A.21}$$
$$= \mathcal{F}_{xy}(-\mathbf{k}) \tag{A.22}$$

Thus, if the system is space-inversion invariant, we have :

$$\boldsymbol{\mathcal{A}}(\mathbf{k}) = -\boldsymbol{\mathcal{A}}(-\mathbf{k}) + \nabla\zeta(\mathbf{k}) \tag{A.23}$$
$$\mathcal{F}_{xy}(\mathbf{k}) = \mathcal{F}_{xy}(-\mathbf{k}) \tag{A.24}$$

Appendix B

Kubo formula for the Hall conductivity

1 General derivation

We follow here the derivation given in the lectures by David Tong (Cambridge) on the Quantum Hall Effect, however we take into account the distribution function for the electrons in the eigenstates of the system.

We consider a general time-independent Hamiltonian H_0 whose spectrum is know and given by the eigenvalue equation : $H_0|n\rangle = E_n|n\rangle$. This system is coupled to an external monochromatic electric field $\mathbf{E}(t) = \mathbf{E}e^{-i\omega t}$ with pulsation ω in the gauge $\mathbf{E} = -\partial_t \mathbf{A}$. The system couples to the fields via its current operator $\mathbf{J}$:

$$V(t) = -\mathbf{J}\mathbf{A}(t) \ , \tag{B.1}$$

with $A(t) = \frac{\mathbf{E}}{i\omega}e^{-i\omega t}$. We wish to calculate the average current when the field is present. We consider switching on the field at $t = t_0$. The average current along the direction i in the presence of driving is given by :

$$\langle J_i \rangle(t) = Tr\left[\rho(t) J_i\right] \tag{B.2}$$

where $\rho(t)$ is the density matrix at time t that obeys to the equation :

$$i\partial_t \rho(t) + \left[\rho(t), H_0 + V(t)\right]. \tag{B.3}$$

We switch to the interaction representation such that $\rho_I(t) = e^{iH_0 t}\rho(t)e^{-iH_0 t}$ and $V_I(t) = e^{iH_0 t}V(t)e^{-iH_0 t}$. Eq. (B.3) becomes :

$$i\partial_t \rho_I(t) + \left[\rho_I(t), V_I(t)\right]. \tag{B.4}$$

At $t = -\infty$, the system is at equilibrium : $\rho_I(-\infty) = \rho_F = \sum_n p_n |n\rangle\langle n|$, where p_n is the occupation probability ot the state $|n\rangle$ in the absence of driving. Integrating this equation formally gives us :

$$\rho_I(t) = \rho_F + i\int_{-\infty}^{t} dt' \left[\rho_I(t'), V_I(t')\right] \tag{B.5}$$

$$= \rho_F + i\int_{-\infty}^{t} dt' \left[\rho_F, V_I(t')\right], \tag{B.6}$$

where in the second line we have considered that the interaction is weak so that we neglect the second order terms in V. In the interaction representation, the average value of the current operator can be expressed as :

$$\langle J_i \rangle(t) = Tr\left[\rho_I(t) J_{i,I}(t)\right], \tag{B.7}$$

where $J_{i,I}(t)$ is the operator J_i in the interaction picture. Inserting the expression for the density matrix in Eq. (B.7), we obtain :

$$\langle J_i\rangle(t) = \langle J_i\rangle_0 - i\int_{-\infty}^{t} dt' Tr\{[\rho_F, V_I(t')]\, J_{i,I}(t)\}, \tag{B.8}$$

where $\langle J_i\rangle_0 = Tr\{\rho_F J_{i,I}(t)\}$ is the average current in the absence of driving. The current originating from the driving can be expressed as :

$$\langle J_i\rangle(t) = i\int_{-\infty}^{t} dt' Tr\{[\rho_F, J_{j,I}(t')]\, J_{i,I}(t)\}A_j(t') \tag{B.9}$$

$$= i\int_{-\infty}^{t} dt' Tr\{\rho_F\,[J_{j,I}(t'), J_{i,I}(t)]\}A_j(t') \tag{B.10}$$

$$= \frac{1}{\omega}\int_{-\infty}^{t} dt' \langle [J_{j,I}(t'), J_{i,I}(t)]\rangle_0 E_j e^{-i\omega t'}, \tag{B.11}$$

where we have used the invariance under cyclic permutation of the trace operation in the second line, and we have replaced $A(t)$ by it expression as a function of the electric field. The average value $\langle\ldots\rangle_0$ is taken at equilibrium. Because the system is invariant under time translations, the correlation function depends only on $t'' = t - t'$. We can rewrite the formula above as :

$$\langle J_i\rangle(t) = \frac{1}{\omega}\left(\int_0^{\infty} dt'' e^{i\omega t''}\langle [J_{j,I}(0), J_{i,I}(t'')]\rangle_0\right) E_j e^{-i\omega t}. \tag{B.12}$$

From the relation $\mathbf{J}(t) = \overline{\overline{\sigma}}\mathbf{E}(t)$, where $\overline{\overline{\sigma}}$ is the optical conductivity tensor, we find the coefficients of the conductivity tensor :

$$\sigma_{ij}(\omega) = \frac{1}{\omega}\int_0^{\infty} dt e^{i\omega t}\langle [J_{j,I}(0), J_{i,I}(t)]\rangle_0. \tag{B.13}$$

The current-current correlation fuction can be expressed in the bare Hamiltonian eigenstates basis $|n\rangle$:

$$\langle [J_{j,I}(0), J_{i,I}(t)]\rangle_0 = \sum_n p_n \langle n|J_j e^{iH_0 t} J_i e^{-iH_0 t}|n\rangle - \langle n|e^{iH_0 t} J_i e^{-iH_0 t} J_j|n\rangle \tag{B.14}$$

$$= \sum_{n,m} p_n \langle n|J_j|m\rangle\langle m|J_i|n\rangle e^{i(E_m - E_n)t} - p_n\langle n|J_i|m\rangle\langle m|J_j|n\rangle e^{i(E_n - E_m)t} \tag{B.15}$$

$$= \sum_{n,m} (p_n - p_m)\langle n|J_j|m\rangle\langle m|J_i|n\rangle e^{i(E_m - E_n)t}, \tag{B.16}$$

where we have inserted the closing relation $\sum_m |m\rangle\langle m| = \mathbb{1}$ in the second line. Inserting the expression above in Eq. (B.13), we obtain :

$$\sigma_{ij}(\omega) = \frac{1}{\omega}\sum_{n,m}(p_n - p_m)\langle n|J_j|m\rangle\langle m|J_i|n\rangle \int_0^{\infty} dt e^{i(\omega + E_m - E_n)t} \tag{B.17}$$

By integration in the complex plane, replacing ω by $\omega + i\delta$, where $\delta \to 0^+$, we find the Hall conductivity :

$$\sigma_{xy}(\omega) = -\frac{i}{\omega}\sum_{n,m}(p_n - p_m)\frac{\langle n|J_y|m\rangle\langle m|J_x|n\rangle}{\omega + E_m - E_n} \tag{B.18}$$

In order to obtain the DC component of the Hall conductivity, we take the limit $\omega \to 0$. We reinsert the factor $\hbar$, and expand the denominator as :

$$\frac{1}{\hbar\omega + E_m - E_n} \approx \frac{1}{E_m - E_n} - \frac{\hbar\omega}{(E_m - E_n)^2} + o(\omega^2) \tag{B.19}$$

The first term seems divergent, however, in the case of the Hall conductivity, this term vanishes. This can be shown from gauge invariance or equivalently from the conservation of current (not proved here). In the DC limit, the Hall conductivity has the expression :

$$\sigma_{xy} = i\hbar \sum_{n,m} (p_n - p_m) \frac{\langle n|J_y|m\rangle\langle m|J_x|n\rangle}{(E_m - E_n)^2} \tag{B.20}$$

2 Application to a two band system

We will here study the simple example of a two-level system in the Bloch bands of a crystal. For simplicity, we will focus here on a gapped system where the two bands are separated in order to avoid the problem of degeneracies. The single particle Hamiltonian of a two band system can be written as :

$$H(\mathbf{k}) = \mathbf{d}(\mathbf{k})\boldsymbol{\sigma}, \tag{B.21}$$

where $\mathbf{k}$ is the quasi-momentum of the electron, and $\boldsymbol{\sigma}$ is the vector composed of the three Pauli matrices. The eigenvectors of this Hamiltonian are the spinors :

$$|n\rangle = |u^s_{\mathbf{k}}\rangle, \tag{B.22}$$

where $s = \pm$ is the band index, with eigenvalues :

$$E_s(\mathbf{k}) = sd(\mathbf{k}), \tag{B.23}$$

where $d(\mathbf{k}) = |\mathbf{d}(\mathbf{k})|$. The condition for the system to be gapped $|\mathbf{d}(\mathbf{k})| \neq 0$ has to be satisfied for every $\mathbf{k}$. The current operator has the expression :

$$J_i(\mathbf{k}) = \frac{e}{\hbar}\frac{\partial h(\mathbf{k})}{\partial k_i} \tag{B.24}$$

2.1 Hall conductance as a Chern number

The operator J_i is diagonal in $\mathbf{k}$ so we can rewrite the Hall conductance as :

$$\sigma_{xy} = i\hbar \sum_{\mathbf{k}} \sum_{s,t=\pm} (f_s(\mathbf{k}) - f_t(\mathbf{k})) \frac{\langle u^s_{\mathbf{k}}|J_y(\mathbf{k})|u^t_{\mathbf{k}}\rangle\langle u^t_{\mathbf{k}}|J_x(\mathbf{k})|u^s_{\mathbf{k}}\rangle}{(E_s(\mathbf{k}) - E_t(\mathbf{k}))^2} \tag{B.25}$$

$$= i\hbar \sum_{\mathbf{k}} (f_+(\mathbf{k}) - f_-(\mathbf{k})) \left[\frac{\langle u^+_{\mathbf{k}}|J_y(\mathbf{k})|u^-_{\mathbf{k}}\rangle\langle u^-_{\mathbf{k}}|J_x(\mathbf{k})|u^+_{\mathbf{k}}\rangle}{(E_+(\mathbf{k}) - E_-(\mathbf{k}))^2} - \frac{\langle u^-_{\mathbf{k}}|J_y(\mathbf{k})|u^+_{\mathbf{k}}\rangle\langle u^+_{\mathbf{k}}|J_x(\mathbf{k})|u^-_{\mathbf{k}}\rangle}{(E_-(\mathbf{k}) - E_+(\mathbf{k}))^2} \right] \tag{B.26}$$

$$= i\frac{e^2}{\hbar} \sum_{\mathbf{k}} (f_+(\mathbf{k}) - f_-(\mathbf{k})) \left[\frac{\langle u^-_{\mathbf{k}}|\partial_{k_x} h(\mathbf{k})|u^+_{\mathbf{k}}\rangle\langle u^+_{\mathbf{k}}|\partial_{k_y} h(\mathbf{k})|u^-_{\mathbf{k}}\rangle}{(E_+(\mathbf{k}) - E_-(\mathbf{k}))^2} - \frac{\langle u^-_{\mathbf{k}}|\partial_{k_y} h(\mathbf{k})|u^+_{\mathbf{k}}\rangle\langle u^+_{\mathbf{k}}|\partial_{k_x} h(\mathbf{k})|u^-_{\mathbf{k}}\rangle}{(E_+(\mathbf{k}) - E_-(\mathbf{k}))^2} \right] \tag{B.27}$$

Now we can use the formula :

$$\langle u^{\alpha}_{\mathbf{k}}|\partial_{k_i}h(\mathbf{k})|u^{\beta}_{\mathbf{k}}\rangle = \langle u^{\alpha}_{\mathbf{k}}|\partial_{k_i}(h(\mathbf{k})|u^{\beta}_{\mathbf{k}}\rangle) - \langle u^{\alpha}_{\mathbf{k}}|h(\mathbf{k})|\partial_{k_i}u^{\beta}_{\mathbf{k}}\rangle \tag{B.28}$$

$$= (E_{\beta}(\mathbf{k}) - E_{\alpha}(\mathbf{k}))\langle u^{\alpha}_{\mathbf{k}}|\partial_{k_i}u^{\beta}_{\mathbf{k}}\rangle \tag{B.29}$$

$$= (E_{\alpha}(\mathbf{k}) - E_{\beta}(\mathbf{k}))\langle \partial_{k_i}u^{\alpha}_{\mathbf{k}}|u^{\beta}_{\mathbf{k}}\rangle, \tag{B.30}$$

where $\{\alpha,\beta\} = \{+,-\}$ to obtain :

$$\sigma_{xy} = i\frac{e^2}{\hbar}\sum_{\mathbf{k}}(f_+(\mathbf{k}) - f_-(\mathbf{k}))\left[\langle\partial_{k_x}u^-_{\mathbf{k}}|u^+_{\mathbf{k}}\rangle\langle u^+_{\mathbf{k}}|\partial_{k_y}u^-_{\mathbf{k}}\rangle - \langle\partial_{k_y}u^-_{\mathbf{k}}|u^+_{\mathbf{k}}\rangle\langle u^+_{\mathbf{k}}|\partial_{k_x}u^-_{\mathbf{k}}\rangle\right]. \tag{B.31}$$

Using the closing relation $|u^+_{\mathbf{k}}\rangle\langle u^+_{\mathbf{k}}| = 1 - |u^-_{\mathbf{k}}\rangle\langle u^-_{\mathbf{k}}|$, we obtain :

$$\sigma_{xy} = i\frac{e^2}{\hbar}\sum_{\mathbf{k}}(f_+(\mathbf{k}) - f_-(\mathbf{k}))\left[\langle\partial_{k_x}u^-_{\mathbf{k}}|\partial_{k_y}u^-_{\mathbf{k}}\rangle - \langle\partial_{k_x}u^-_{\mathbf{k}}|u^-_{\mathbf{k}}\rangle\langle u^-_{\mathbf{k}}|\partial_{k_y}u^-_{\mathbf{k}}\rangle\right.$$
$$\left. -\langle\partial_{k_y}u^-_{\mathbf{k}}|\partial_{k_x}u^-_{\mathbf{k}}\rangle + \langle\partial_{k_y}u^-_{\mathbf{k}}|u^-_{\mathbf{k}}\rangle\langle u^-_{\mathbf{k}}|\partial_{k_x}u^-_{\mathbf{k}}\rangle\right]. \tag{B.32}$$

Using the fact that $\langle u^-_{\mathbf{k}}|\partial_{k_\alpha}u^-_{\mathbf{k}}\rangle = -\langle\partial_{k_\alpha}u^-_{\mathbf{k}}|u^-_{\mathbf{k}}\rangle$, the second and the third term in the sum cancel each other so we get :

$$\sigma_{xy} = i\frac{e^2}{\hbar}\sum_{\mathbf{k}}(f_+(\mathbf{k}) - f_-(\mathbf{k}))\left[\langle\partial_{k_x}u^-_{\mathbf{k}}|\partial_{k_y}u^-_{\mathbf{k}}\rangle - \langle\partial_{k_y}u^-_{\mathbf{k}}|\partial_{k_x}u^-_{\mathbf{k}}\rangle\right]. \tag{B.33}$$

If we consider a gapped system where the valence band is filled ($f_+(\mathbf{k}) = 0$) and the conduction band is empty($f_-(\mathbf{k}) = 1$), we get the expression :

$$\sigma_{xy} = i\frac{e^2}{\hbar}\int\frac{d\mathbf{k}}{(2\pi)^2}\left(\langle\partial_{k_y}u^-_{\mathbf{k}}|\partial_{k_x}u^-_{\mathbf{k}}\rangle - \langle\partial_{k_x}u^-_{\mathbf{k}}|\partial_{k_y}u^-_{\mathbf{k}}\rangle\right). \tag{B.34}$$

The precedent equation can be written as :

$$\sigma_{xy} = \frac{e^2}{h}C_-, \tag{B.35}$$

where C_- is called the Chern number of the valence ($-$) band and is defined as :

$$C_- = \frac{1}{2\pi}\int_{BZ}d^2k\mathcal{F}^-_{xy}. \tag{B.36}$$

We have here introduced the mathematical object $\mathcal{F}^-_{xy}$ called the Berry curvature that is equal to :

$$\mathcal{F}^-_{xy} = i\langle\partial_{k_y}u^-_{\mathbf{k}}|\partial_{k_x}u^-_{\mathbf{k}}\rangle - i\langle\partial_{k_x}u^-_{\mathbf{k}}|\partial_{k_y}u^-_{\mathbf{k}}\rangle. \tag{B.37}$$

The Berry curvature can be expressed as the curl of the Berry vector potential $\mathcal{A}^n_\alpha$:

$$\mathcal{F}^n_{xy} = \partial_{k_x}\mathcal{A}^n_y - \partial_{k_y}\mathcal{A}^n_x, \tag{B.38}$$

where n is the band index and :

$$\mathcal{A}^s_\alpha(\mathbf{k}) = i\langle u^n_{\mathbf{k}}|\frac{\partial}{\partial k_\alpha}|u^n_{\mathbf{k}}\rangle, \tag{B.39}$$

with $\alpha \in \{x,y\}$.

The Chern number we introduced here is a number that corresponds to the Berry flux threading the whole Brillouin zone. This Chern number was originally introduced as the TKNN invariant[6] (due to the authors Thouless, Kohmoto, Nightingale and den Nijs). Due to the periodicity of the quasi-momentum of electrons in a crystal by translation of a reciprocal lattice unit vector, the Brillouin zone is topologically equivalent to a torus.

2.2 Hall conductance as a winding number

The current operator is expressed as :

$$J_i(\mathbf{k}) = \frac{e}{\hbar}\frac{\partial d_\alpha(\mathbf{k})}{\partial k_i}\sigma_\alpha, \tag{B.40}$$

where the summation over the indices $\alpha = \{x, y, z\}$ is implicit. We can rewrite Eq. (B.26) as :

$$\sigma_{xy} = i\hbar \sum_{\mathbf{k}} \frac{f_+(\mathbf{k}) - f_-(\mathbf{k})}{4d(\mathbf{k})^2} \left(Tr\left[J_y(\mathbf{k})P_-(\mathbf{k})J_x(\mathbf{k})P_+(\mathbf{k})\right] - c.c.\right) \tag{B.41}$$

$$= -2\hbar \sum_{\mathbf{k}} \frac{f_+(\mathbf{k}) - f_-(\mathbf{k})}{4d(\mathbf{k})^2} Im\{Tr\left[J_x(\mathbf{k})P_+(\mathbf{k})J_y(\mathbf{k})P_-(\mathbf{k})\right]\}, \tag{B.42}$$

where we have used the invariance of the trace operation under cyclic permutations, and introduced the projection operator $P_-(\mathbf{k})$ ($P_+(\mathbf{k})$) over the valence (conduction) band, that is defined as :

$$P_s(\mathbf{k}) = \frac{1}{2}\left[1 + s\frac{\mathbf{d}(\mathbf{k})\boldsymbol{\sigma}}{|\mathbf{d}(\mathbf{k})|}\right] = \frac{1}{2}\left[1 + s\hat{d}_\alpha(\mathbf{k})\sigma_\alpha\right], \tag{B.43}$$

where $\hat{\mathbf{d}}(\mathbf{k}) = \mathbf{d}(\mathbf{k})/d(\mathbf{k})$ is the unit vector spanning the Bloch sphere. Plugging Eqs. (B.40) and (B.43) into (B.42), we obtain :

$$\sigma_{xy} = -\frac{e^2}{8\hbar}\sum_{\mathbf{k}}(f_+(\mathbf{k}) - f_-(\mathbf{k}))\mathrm{Im}\{Tr\left[\frac{\partial \hat{d}_\alpha(\mathbf{k})}{\partial k_x}\sigma_\alpha(1 + \hat{d}_\beta(\mathbf{k})\sigma_\beta)\frac{\partial \hat{d}_\gamma(\mathbf{k})}{\partial k_y}\sigma_\gamma(1 - \hat{d}_\delta(\mathbf{k})\sigma_\delta)\right]\}. \tag{B.44}$$

The properties of the trace operation over a product of Pauli matrices tells us that the only imaginary trace is the one containing three Pauli matrices :

$$Tr\left[\sigma_a\sigma_b\sigma_c\right] = 2i\varepsilon_{abc}, \tag{B.45}$$

where ε_{abc} is the totally antisymmetric tensor. We can thus express Eq. (B.44) as :

$$\sigma_{xy} = -\frac{e^2}{2\hbar}\sum_{\mathbf{k}}(f_+(\mathbf{k}) - f_-(\mathbf{k}))\varepsilon_{\alpha\beta\gamma}\frac{\partial \hat{d}_\alpha}{\partial k_x}\frac{\partial \hat{d}_\beta}{\partial k_y}\hat{d}_\gamma. \tag{B.46}$$

Once again we consider an insulator in which the valence band is filled and the conducation band empty, and we replace the sum over the Brillouin zone by a integral, we get :

$$\sigma_{xy} = \frac{e^2}{2\hbar}\int_{BZ}\frac{d^2k}{(2\pi)^2}\varepsilon_{\alpha\beta\gamma}\frac{\partial \hat{d}_\alpha}{\partial k_x}\frac{\partial \hat{d}_\beta}{\partial k_y}\hat{d}_\gamma. \tag{B.47}$$

$$= \frac{e^2}{h}n_w, \tag{B.48}$$

where n_w is the winding number of the mapping $\mathbf{k} \to \hat{\mathbf{d}}(\mathbf{k})$, and is defined as :

$$n_w = \frac{1}{4\pi}\int_{BZ} d^2k\left(\frac{\partial \hat{\mathbf{d}}(\mathbf{k})}{\partial_{k_x}} \times \frac{\partial \hat{\mathbf{d}}(\mathbf{k})}{\partial_{k_y}}\right).\hat{\mathbf{d}}(\mathbf{k}) \tag{B.49}$$

Appendix C

Oscillating integrals

We wish to obtain an approximate value for oscillating integrals arising in conductance calculations for long scattering lengths compared to the Fermi wavelength $\lambda_F = 2\pi/k_F$. The idea is to separate the fast oscillating component from the slow component compared to the oscillation period.

1 Integral (4.21)

The integral from Eq. (4.21) has the expression :

$$I = \int_0^1 dx \frac{1-x^2}{1-x^2\cos^2(\sqrt{1-x^2}k_F L)}, \tag{C.1}$$

where we take the limit $k_F L \gg 1$. In first place, we make the change of variable $y^2 = 1-x^2$ to get the expression :

$$I = \int_0^1 dy \frac{y}{\sqrt{1-y^2}} \frac{y^2}{1-(1-y)^2\cos^2(k_F L y)}. \tag{C.2}$$

The integrand oscillates with a period $2\pi/k_F L$, so we separate the variable y in two parts : $y = y_n + \delta y$ with $y_n = \frac{2\pi n}{k_F L}$ and $\delta_y \in [0, \frac{2\pi}{k_F L}]$ so that we have :

$$I = \sum_{n=0}^{\mathrm{Int}\left(\frac{k_F L}{2\pi}\right)} \frac{y_n^3}{\sqrt{1-y_n^2}} \int_0^{\frac{2\pi}{k_F L}} d\delta y \frac{1}{1-(1-y_n)^2\cos^2(k_F L \delta y)}, \tag{C.3}$$

where we have neglected the variable δy in the variables outside the cosine function. The integral runs now over one period of oscillation. We find :

$$I = \sum_{n=0}^{\mathrm{Int}\left(\frac{k_F L}{2\pi}\right)} \frac{y_n^3}{\sqrt{1-y_n^2}} \frac{2\pi}{k_F L y_n} = \frac{2\pi}{k_F L} \sum_{n=0}^{\mathrm{Int}\left(\frac{k_F L}{2\pi}\right)} \frac{y_n^2}{\sqrt{1-y_n^2}}, \tag{C.4}$$

If we now transform the expression back to an integral form, we get :

$$I = \int_0^1 \frac{y^2}{\sqrt{1-y^2}} = \frac{\pi}{4} \tag{C.5}$$

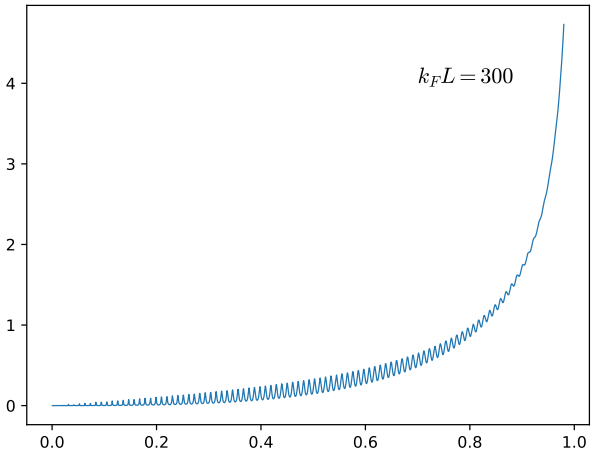

Figure C.1 – Integrand of Eq. (C.2). We can see that for $k_F L \gg 1$, the function varies slowly over one period of the oscillation.

2 Integral (5.46)

In order to calculate the integral (5.46) for $\tilde{L} \gg 1$, we separate the slowly varying function and the rapidly oscillating part. The function $1 - f(\varepsilon)$ to integrate fro g to ∞ is shown in Fig. C.2.

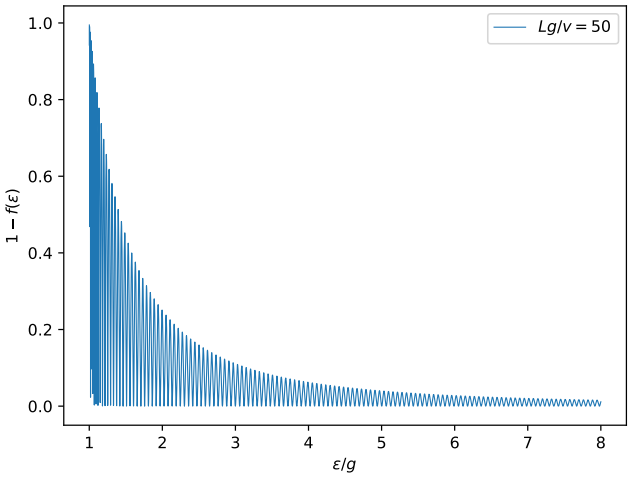

Figure C.2 – Integrand of Eq. (5.46). We can see that for $Lg/v \gg 1$, the function varies slowly over one period of the oscillation.

We make the change of variable $x = x_n + \bar{x}$, where $x_n = \frac{2\Pi n}{L}$ is the discrete points that stays constant during one period of oscillation, and $\bar{x}$ is the variable that we integrate

during one period. In the limit, $L \to \infty$, the separation of the scales is exact, therefore :

$$\lim_{\hbar\omega/g, L\to\infty} I_{Interf} = 2\frac{eg}{h}\sum_{n=0}^{\infty}\frac{x_n}{\sqrt{x_n^2+1}}\int_0^{2\pi/L} d\bar{x}\frac{\sin^2((x_n+\bar{x})\tilde{L})}{x_n^2+\sin^2((x_n+\bar{x}\tilde{L})} \quad \text{with} \quad x_n = \frac{2\pi n}{L} \tag{C.6}$$

$$= 2\frac{eg}{h}\sum_{n=0}^{\infty}\frac{x_n}{\sqrt{x_n^2+1}}\int_0^{2\pi}\frac{dy}{L}\frac{\sin^2(y)}{x_n^2+\sin^2(y)}, \quad \text{where} \quad y = \bar{x}\tilde{L} \tag{C.7}$$

$$= 2\frac{eg}{h}\sum_{n=0}^{\infty}\frac{x_n}{\sqrt{x_n^2+1}}\left[\frac{2\pi}{L}\left(1-\frac{x_n}{\sqrt{x_n^2+1}}\right)\right] \tag{C.8}$$

$$= 2\frac{eg}{h}\int_0^{\infty} dx\frac{x}{\sqrt{x^2+1}}\left(1-\frac{x}{\sqrt{x^2+1}}\right) \tag{C.9}$$

$$= 2\frac{eg}{h}\left(\frac{\pi}{2}-1\right) \tag{C.10}$$

Appendix D

generalized rotatating wave approximation for graphene

The low-energy dispersion of graphene is described by the Dirac equation. For each value of the momentum $\mathbf{k}$, there is a two-level system, so we can use the rotating wave approximation (RWA) to obtain the shift of the quasi-energy levels depending on the detuning of the laser close to the resonances. Graphene subjected to a circularly polarized electromagnetic wave $\mathbf{A} = A_0(\cos\omega t, \sin\omega t)$ is described by the Hamiltonian :

$$H(\mathbf{q},t) = H_0(\mathbf{q}) + V(t), \text{ where :} \tag{D.1a}$$

$$H_0(\mathbf{q}) = \hbar v \boldsymbol{\sigma}.\mathbf{q} \tag{D.1b}$$

$$V(t) = evA_0 \begin{pmatrix} 0 & e^{-i\omega t} \\ e^{i\omega t} & 0 \end{pmatrix} \tag{D.1c}$$

To be able to apply the RWA, we need to rotate the bare Hamiltonian H_0 to its diagonal basis. For that, we change of basis using the matrix :

$$U = \begin{pmatrix} 1 & 1 \\ e^{i\theta} & -e^{i\theta} \end{pmatrix} \tag{D.2}$$

where $\tan\theta = q_y/q_x$. In the rotated basis, we get :

$$\begin{aligned} \tilde{H}(\mathbf{q},t) &= U^{-1}H(\mathbf{q},t)U \\ &= \hbar v q \sigma_z + evA_0(\cos(\theta-\omega t)\sigma_0 + \sin(\theta-\omega t)\sigma_y) \end{aligned} \tag{D.3}$$

where $q = |\mathbf{q}|$, and σ_0 is the 2x2 identity matrix. The Hamiltonian H_0 is now diagonal and there is a time-dependent diagonal part, and a non-diagonal one. We introduce $\omega_0(q) = 2vq$, the resonant frequency at momentum q, and we express the wavefunction as : $\Psi(t) = (a(t), b(t))^T$. The Schrödinger equation can be written as :

$$\begin{aligned} i\hbar \begin{pmatrix} \dot{a}(t) \\ \dot{b}(t) \end{pmatrix} &= \begin{pmatrix} [\hbar\omega_0/2 + evA_0\cos(\theta-\omega t)]a(t) \\ [-\hbar\omega_0/2 + evA_0\cos(\theta-\omega t)]b(t) \end{pmatrix} \\ &+ \begin{pmatrix} -ievA_0\sin(\theta-\omega t)b(t) \\ ievA_0\sin(\theta-\omega t)a(t) \end{pmatrix}, \end{aligned} \tag{D.4}$$

and we introduce the variables $\tilde{a}(t)$ and $\tilde{b}(t)$ defined by :

$$\tilde{a}(t) = a(t)e^{i\omega_0 t/2 + i(evA_0/\hbar\omega)\sin(\theta-\omega t)} \tag{D.5}$$

$$\tilde{b}(t) = b(t)e^{-i\omega_0 t/2 - i(evA_0/\hbar\omega)\sin(\theta-\omega t)} \tag{D.6}$$

. Therefore :

$$\begin{aligned} i\hbar\dot{\tilde{a}}(t) &= -ievA_0\sin(\theta-\omega t)e^{i\omega_0 t+i2(evA_0/\hbar\omega)\sin(\theta-\omega t)}\tilde{b}(t) \\ i\hbar\dot{\tilde{b}}(t) &= ievA_0\sin(\theta-\omega t)e^{-i\omega_0 t-i2(evA_0/\hbar\omega)\sin(\theta-\omega t)}\tilde{a}(t) \end{aligned} \tag{D.7}$$

Using the Jacobi-Anger formula and setting $\beta = evA_0/\hbar\omega$, we find :

$$\begin{aligned} \dot{\tilde{a}}(t) = -\frac{\beta\hbar\omega}{2i}\sum_n J_n(2\beta)(&e^{i(\omega_0-(n+1)\omega)t+i(n+1)\theta} \\ &-e^{i(\omega_0-(n-1)\omega)t+i(n-1)\theta})\tilde{b}(t) \end{aligned} \tag{D.8}$$

$$\begin{aligned} \dot{\tilde{b}}(t) = \frac{\beta\hbar\omega}{2i}\sum_n J_n(2\beta)(&e^{-i(\omega_0-(n-1)\omega)t-i(n-1)\theta} \\ &-e^{-i(\omega_0-(n+1)\omega)t-i(n+1)\theta})\tilde{a}(t) \end{aligned} \tag{D.9}$$

We can now apply the generalized rotating wave approximation, which means that we keep only the slowly varying terms such that $\omega_0 \approx m\omega$ corresponding to m photons processes :

$$\dot{\tilde{a}}(t) = i\frac{\beta\hbar\omega}{2}(J_{m-1}(2\beta) - J_{m+1}(2\beta))e^{i(\omega_0-m\omega)t+im\theta}\tilde{b}(t) \tag{D.10}$$

$$\dot{\tilde{b}}(t) = -i\frac{\beta\hbar\omega}{2}(J_{m+1}(2\beta) - J_{m-1}(2\beta))e^{-i(\omega_0-m\omega)t-im\theta}\tilde{a}(t) \tag{D.11}$$

Deriving eq. (D.10) and substituting (D.11) into it gives :

$$\begin{aligned} &\ddot{\tilde{a}}(t) - i(\omega_0 - m\omega)\dot{\tilde{a}}(t) \\ &\quad + \left(\frac{\beta\hbar\omega}{2}\right)^2 (J_{m+1}(2\beta) - J_{m-1}(2\beta))^2\tilde{a}(t) = 0 \end{aligned}$$

Solving this equation for $\tilde{a}(t)$ and using eq. (D.5), we find two solutions :

$$a_\pm(t) = e^{-i\omega_\pm^m t}\sum_n J_n(\beta)e^{in\omega t-in\theta} \tag{D.12}$$

where $\omega_\pm^m$ is the quasi-energy equal to :

$$\omega_\pm^m = \frac{m\omega}{2} \pm \frac{1}{2}\sqrt{\delta_m^2 + \Omega_m^2} \tag{D.13}$$

where $\delta_m = \omega_0 - m\omega$ is the laser detuning such that $\delta_m \ll \omega_0$, and Ω_m is the Rabi frequency given by :

$$\Omega_m = \beta\hbar\omega|J_{m+1}(2\beta) - J_{m-1}(2\beta)| \tag{D.14}$$

This quasi-energy $\omega_\pm^m$ represents a two band model with an anti-crossing at momentum $q = m\omega/2v$ and energy $\varepsilon = m\hbar\omega/2$. When the driving is at resonance ($\delta_m = 0$), there is a gap of size Ω_m between the two quasi-energy bands.

Bibliography

[1] K. S. Novoselov, A. K. Geim, S. V. Morozov, D. Jiang, Y. Zhang, S. V. Dubonos, I. V. Grigorieva, and A. A. Firsov. Electric field effect in atomically thin carbon films. *Science*, 306(5696):666–669, 2004.

[2] Phaedon Avouris and Christos Dimitrakopoulos. Graphene: synthesis and applications. *Materials Today*, 15(3):86 – 97, 2012.

[3] A. H. Castro Neto, F. Guinea, N. M. R. Peres, K. S. Novoselov, and A. K. Geim. The electronic properties of graphene. *Rev. Mod. Phys.*, 81:109–162, Jan 2009.

[4] M. Z. Hasan and C. L. Kane. Colloquium : Topological insulators. *Rev. Mod. Phys.*, 82:3045–3067, Nov 2010.

[5] Xiao-Liang Qi and Shou-Cheng Zhang. Topological insulators and superconductors. *Rev. Mod. Phys.*, 83:1057–1110, Oct 2011.

[6] D. J. Thouless, M. Kohmoto, M. P. Nightingale, and M. den Nijs. Quantized hall conductance in a two-dimensional periodic potential. *Phys. Rev. Lett.*, 49:405–408, Aug 1982.

[7] C. L. Kane and E. J. Mele. Quantum spin hall effect in graphene. *Phys. Rev. Lett.*, 95:226801, Nov 2005.

[8] B. Andrei Bernevig, Taylor L. Hughes, and Shou-Cheng Zhang. Quantum spin hall effect and topological phase transition in hgte quantum wells. *Science*, 314(5806):1757–1761, 2006.

[9] B. Andrei Bernevig and Shou-Cheng Zhang. Quantum spin hall effect. *Phys. Rev. Lett.*, 96:106802, Mar 2006.

[10] Takashi Oka and Hideo Aoki. Photovoltaic hall effect in graphene. *Phys. Rev. B*, 79:081406, Feb 2009.

[11] Netanel H. Lindner, Gil Refael, and Victor Galitski. Floquet topological insulator in semiconductor quantum wells. *Nat Phys*, 7(6):490–495, 06 2011.

[12] Balázs Dóra, Jérôme Cayssol, Ferenc Simon, and Roderich Moessner. Optically engineering the topological properties of a spin hall insulator. *Phys. Rev. Lett.*, 108:056602, Jan 2012.

[13] D. J. Thouless. Quantization of particle transport. *Phys. Rev. B*, 27:6083–6087, May 1983.

[14] A. K. Geim and K. S. Novoselov. The rise of graphene. *Nature Materials*, 6:183 EP –, 03 2007.

[15] A. K. Geim and I. V. Grigorieva. Van der waals heterostructures. *Nature*, 499:419 EP –, 07 2013.

[16] P. R. Wallace. The band theory of graphite. *Phys. Rev.*, 71:622–634, May 1947.

[17] K. S. Novoselov, A. K. Geim, S. V. Morozov, D. Jiang, M. I. Katsnelson, I. V. Grigorieva, S. V. Dubonos, and A. A. Firsov. Two-dimensional gas of massless dirac fermions in graphene. *Nature*, 438:197 EP –, 11 2005.

[18] M.I. Katsnelson and K.S. Novoselov. Graphene: New bridge between condensed matter physics and quantum electrodynamics. *Solid State Communications*, 143(1):3 – 13, 2007. Exploring graphene.

[19] M V Berry. Classical adiabatic angles and quantal adiabatic phase. *Journal of Physics A: Mathematical and General*, 18(1):15, 1985.

[20] S. Reich, J. Maultzsch, C. Thomsen, and P. Ordejón. Tight-binding description of graphene. *Phys. Rev. B*, 66:035412, Jul 2002.

[21] Cristina Bena and Gilles Montambaux. Remarks on the tight-binding model of graphene. *New Journal of Physics*, 11(9):095003, 2009.

[22] P.A.M Dirac. The quantum theory of the electron. *Proceedings of the Royal Society of London A: Mathematical, Physical and Engineering Sciences*, 117(778):610–624, 1928.

[23] Hermann Weyl. Elektron und gravitation. i. *Zeitschrift für Physik*, 56(5):330–352, May 1929.

[24] Quentin Wilmart. *Engineering doping profils in graphene : from Dirac fermion oprtics to high frequency electronics*. PhD thesis, 2015. 2015ENSU0044.

[25] S. Das Sarma, Shaffique Adam, E. H. Hwang, and Enrico Rossi. Electronic transport in two-dimensional graphene. *Rev. Mod. Phys.*, 83:407–470, May 2011.

[26] B.A. Bernevig and T.L. Hughes. *Topological Insulators and Topological Superconductors*. Princeton University Press, 2013.

[27] Shinsei Ryu, Christopher Mudry, Chang-Yu Hou, and Claudio Chamon. Masses in graphenelike two-dimensional electronic systems: Topological defects in order parameters and their fractional exchange statistics. *Phys. Rev. B*, 80:205319, Nov 2009.

[28] J. L. Mañes, F. Guinea, and María A. H. Vozmediano. Existence and topological stability of fermi points in multilayered graphene. *Phys. Rev. B*, 75:155424, Apr 2007.

[29] Gordon W. Semenoff. Condensed-matter simulation of a three-dimensional anomaly. *Phys. Rev. Lett.*, 53:2449–2452, Dec 1984.

[30] F. D. M. Haldane. Model for a quantum hall effect without landau levels: Condensed-matter realization of the "parity anomaly". *Phys. Rev. Lett.*, 61:2015–2018, Oct 1988.

[31] L. D. Landau. On the theory of phase transitions. *Zh. Eksp. Teor. Fiz.*, 7:19–32, 1937. [Ukr. J. Phys.53,25(2008)].

[32] Felix Bloch. Über die quantenmechanik der elektronen in kristallgittern. *Zeitschrift für Physik*, 52(7):555–600, Jul 1929.

[33] Yasuhiro Hatsugai. Edge states in the integer quantum hall effect and the riemann surface of the bloch function. *Phys. Rev. B*, 48:11851–11862, Oct 1993.

[34] Yasuhiro Hatsugai. Chern number and edge states in the integer quantum hall effect. *Phys. Rev. Lett.*, 71:3697–3700, Nov 1993.

[35] Shinsei Ryu and Yasuhiro Hatsugai. Topological origin of zero-energy edge states in particle-hole symmetric systems. *Phys. Rev. Lett.*, 89:077002, Jul 2002.

[36] Roger S. K. Mong and Vasudha Shivamoggi. Edge states and the bulk-boundary correspondence in dirac hamiltonians. *Phys. Rev. B*, 83:125109, Mar 2011.

[37] Xiao-Liang Qi, Yong-Shi Wu, and Shou-Cheng Zhang. General theorem relating the bulk topological number to edge states in two-dimensional insulators. *Phys. Rev. B*, 74:045125, Jul 2006.

[38] Douglas R. Hofstadter. Energy levels and wave functions of bloch electrons in rational and irrational magnetic fields. *Phys. Rev. B*, 14:2239–2249, Sep 1976.

[39] Cui-Zu Chang, Jinsong Zhang, Xiao Feng, Jie Shen, Zuocheng Zhang, Minghua Guo, Kang Li, Yunbo Ou, Pang Wei, Li-Li Wang, Zhong-Qing Ji, Yang Feng, Shuaihua Ji, Xi Chen, Jinfeng Jia, Xi Dai, Zhong Fang, Shou-Cheng Zhang, Ke He, Yayu Wang, Li Lu, Xu-Cun Ma, and Qi-Kun Xue. Experimental observation of the quantum anomalous hall effect in a magnetic topological insulator. *Science*, 340(6129):167–170, 2013.

[40] Gregor Jotzu, Michael Messer, Remi Desbuquois, Martin Lebrat, Thomas Uehlinger, Daniel Greif, and Tilman Esslinger. Experimental realization of the topological haldane model with ultracold fermions. *Nature*, 515(7526):237–240, 11 2014.

[41] Markus König, Steffen Wiedmann, Christoph Brüne, Andreas Roth, Hartmut Buhmann, Laurens W. Molenkamp, Xiao-Liang Qi, and Shou-Cheng Zhang. Quantum spin hall insulator state in hgte quantum wells. *Science*, 318(5851):766, 11 2007.

[42] Shujie Tang, Chaofan Zhang, Dillon Wong, Zahra Pedramrazi, Hsin-Zon Tsai, Chunjing Jia, Brian Moritz, Martin Claassen, Hyejin Ryu, Salman Kahn, Juan Jiang, Hao Yan, Makoto Hashimoto, Donghui Lu, Robert G. Moore, Chan-Cuk Hwang, Choongyu Hwang, Zahid Hussain, Yulin Chen, Miguel M. Ugeda, Zhi Liu, Xiaoming Xie, Thomas P. Devereaux, Michael F. Crommie, Sung-Kwan Mo, and Zhi-Xun Shen. Quantum spin hall state in monolayer 1t'-wte2. *Nature Physics*, 13:683 EP –, 06 2017.

[43] M.W. Berry. Quantal phase factors accompanying adiabatic changes. *Proceedings of the Royal Society of London A: Mathematical, Physical and Engineering Sciences*, 392(1802):45–57, 1984.

[44] D. Chruscinski and A. Jamiolkowski. *Geometric Phases in Classical and Quantum Mechanics*. Progress in Mathematical Physics. Birkhäuser Boston, 2012.

[45] Akira Tomita and Raymond Y. Chiao. Observation of berry's topological phase by use of an optical fiber. *Phys. Rev. Lett.*, 57:937–940, Aug 1986.

[46] Dieter Suter, Gerard C. Chingas, Robert A. Harris, and Alexander Pines. Berry's phase in magnetic resonance. *Molecular Physics*, 61(6):1327–1340, 1987.

[47] Robert Tycko. Adiabatic rotational splittings and berry's phase in nuclear quadrupole resonance. *Phys. Rev. Lett.*, 58:2281–2284, Jun 1987.

[48] J. Zak. Berry's phase for energy bands in solids. *Phys. Rev. Lett.*, 62:2747–2750, Jun 1989.

[49] Raffaele Resta. Macroscopic polarization in crystalline dielectrics: the geometric phase approach. *Rev. Mod. Phys.*, 66:899–915, Jul 1994.

[50] Arnaud Raoux. *Orbital magnetism and geometrical aspects of band theory*. Theses, Université Paris-Saclay, February 2017.

[51] Mahito Kohmoto. Topological invariant and the quantization of the hall conductance. *Annals of Physics*, 160(2):343 – 354, 1985.

[52] A. Bohm, A. Mostafazadeh, H. Koizumi, Q. Niu, and J. Zwanziger. *The Geometric Phase in Quantum Systems: Foundations, Mathematical Concepts, and Applications in Molecular and Condensed Matter Physics*. Theoretical and Mathematical Physics. Springer Berlin Heidelberg, 2013.

[53] Michel Fruchart. *Topological phases of periodically driven crystals*. Theses, Université de Lyon, October 2016.

[54] Michel Fruchart and David Carpentier. An introduction to topological insulators. *Comptes Rendus Physique*, 14(9):779 – 815, 2013. Topological insulators / Isolants topologiques.

[55] K. v. Klitzing, G. Dorda, and M. Pepper. New method for high-accuracy determination of the fine-structure constant based on quantized hall resistance. *Phys. Rev. Lett.*, 45:494–497, Aug 1980.

[56] B. I. Halperin. Quantized hall conductance, current-carrying edge states, and the existence of extended states in a two-dimensional disordered potential. *Phys. Rev. B*, 25:2185–2190, Feb 1982.

[57] R. B. Laughlin. Quantized hall conductivity in two dimensions. *Phys. Rev. B*, 23:5632–5633, May 1981.

[58] J. E. Avron, R. Seiler, and B. Simon. Homotopy and quantization in condensed matter physics. *Phys. Rev. Lett.*, 51:51–53, Jul 1983.

[59] Barry Simon. Holonomy, the quantum adiabatic theorem, and berry's phase. *Phys. Rev. Lett.*, 51:2167–2170, Dec 1983.

[60] C. L. Kane and E. J. Mele. Z_2 topological order and the quantum spin hall effect. *Phys. Rev. Lett.*, 95:146802, Sep 2005.

[61] J. E. Moore and L. Balents. Topological invariants of time-reversal-invariant band structures. *Phys. Rev. B*, 75:121306, Mar 2007.

[62] Liang Fu, C. L. Kane, and E. J. Mele. Topological insulators in three dimensions. *Phys. Rev. Lett.*, 98:106803, Mar 2007.

[63] Alexander Altland and Martin R. Zirnbauer. Nonstandard symmetry classes in mesoscopic normal-superconducting hybrid structures. *Phys. Rev. B*, 55:1142–1161, Jan 1997.

[64] Andreas P. Schnyder, Shinsei Ryu, Akira Furusaki, and Andreas W. W. Ludwig. Classification of topological insulators and superconductors in three spatial dimensions. *Phys. Rev. B*, 78:195125, Nov 2008.

[65] Andreas P. Schnyder, Shinsei Ryu, Akira Furusaki, and Andreas W. W. Ludwig. Classification of topological insulators and superconductors. *AIP Conference Proceedings*, 1134(1):10–21, 2009.

[66] Shinsei Ryu, Andreas P Schnyder, Akira Furusaki, and Andreas W W Ludwig. Topological insulators and superconductors: tenfold way and dimensional hierarchy. *New Journal of Physics*, 12(6):065010, 2010.

[67] Freeman J. Dyson. Statistical theory of the energy levels of complex systems. i. *Journal of Mathematical Physics*, 3(1):140–156, 1962.

[68] Jérôme Cayssol, Balázs Dóra, Ferenc Simon, and Roderich Moessner. Floquet topological insulators. *physica status solidi (RRL) – Rapid Research Letters*, 7(1-2):101–108, 2013.

[69] Doru Sticlet, Frederic Piéchon, Jean-Noël Fuchs, Pavel Kalugin, and Pascal Simon. Geometrical engineering of a two-band chern insulator in two dimensions with arbitrary topological index. *Phys. Rev. B*, 85:165456, Apr 2012.

[70] Doru Sticlet and Frédéric Piéchon. Distant-neighbor hopping in graphene and haldane models. *Phys. Rev. B*, 87:115402, Mar 2013.

[71] Di Xiao, Ming-Che Chang, and Qian Niu. Berry phase effects on electronic properties. *Rev. Mod. Phys.*, 82:1959–2007, Jul 2010.

[72] P. Delplace, D. Ullmo, and G. Montambaux. Zak phase and the existence of edge states in graphene. *Phys. Rev. B*, 84:195452, Nov 2011.

[73] P.A.M Dirac. Quantised singularities in the electromagnetic field,. *Proceedings of the Royal Society of London A: Mathematical, Physical and Engineering Sciences*, 133(821):60–72, 1931.

[74] Piéchon F. Goerbig M. Fuchs, J. Topological berry phase and semiclassical quantization of cyclotron orbits for two dimensional electrons in coupled band models. *Eur. Phys. J. B*, 77:351, 2010.

[75] R. Jackiw and C. Rebbi. Solitons with fermion number $\frac{1}{2}$. *Phys. Rev. D*, 13:3398–3409, Jun 1976.

[76] A. J. Heeger, S. Kivelson, J. R. Schrieffer, and W. P. Su. Solitons in conducting polymers. *Rev. Mod. Phys.*, 60:781–850, Jul 1988.

[77] Edward McCann and Vladimir I Fal'ko. Symmetry of boundary conditions of the dirac equation for electrons in carbon nanotubes. *Journal of Physics: Condensed Matter*, 16(13):2371, 2004.

[78] A. R. Akhmerov and C. W. J. Beenakker. Boundary conditions for dirac fermions on a terminated honeycomb lattice. *Phys. Rev. B*, 77:085423, Feb 2008.

[79] M. V. Berry and R. J. Mondragon. Neutrino billiards: Time-reversal symmetry-breaking without magnetic fields. *Proceedings of the Royal Society of London. A. Mathematical and Physical Sciences*, 412(1842):53–74, 1987.

[80] Takuya Kitagawa, Takashi Oka, Arne Brataas, Liang Fu, and Eugene Demler. Transport properties of nonequilibrium systems under the application of light: Photoinduced quantum hall insulators without landau levels. *Phys. Rev. B*, 84:235108, Dec 2011.

[81] Y. H. Wang, H. Steinberg, P. Jarillo-Herrero, and N. Gedik. Observation of floquet-bloch states on the surface of a topological insulator. *Science*, 342(6157):453–457, 2013.

[82] Mikael C. Rechtsman, Julia M. Zeuner, Yonatan Plotnik, Yaakov Lumer, Daniel Podolsky, Felix Dreisow, Stefan Nolte, Mordechai Segev, and Alexander Szameit. Photonic floquet topological insulators. *Nature*, 496(7444):196–200, 04 2013.

[83] Takuya Kitagawa, Erez Berg, Mark Rudner, and Eugene Demler. Topological characterization of periodically driven quantum systems. *Phys. Rev. B*, 82:235114, Dec 2010.

[84] Liang Jiang, Takuya Kitagawa, Jason Alicea, A. R. Akhmerov, David Pekker, Gil Refael, J. Ignacio Cirac, Eugene Demler, Mikhail D. Lukin, and Peter Zoller. Majorana fermions in equilibrium and in driven cold-atom quantum wires. *Phys. Rev. Lett.*, 106:220402, Jun 2011.

[85] Mark S. Rudner, Netanel H. Lindner, Erez Berg, and Michael Levin. Anomalous edge states and the bulk-edge correspondence for periodically driven two-dimensional systems. *Phys. Rev. X*, 3:031005, Jul 2013.

[86] Frederik Nathan and Mark S Rudner. Topological singularities and the general classification of floquet–bloch systems. *New Journal of Physics*, 17(12):125014, 2015.

[87] David Carpentier, Pierre Delplace, Michel Fruchart, and Krzysztof Gawędzki. Topological index for periodically driven time-reversal invariant 2d systems. *Phys. Rev. Lett.*, 114:106806, Mar 2015.

[88] Michel Fruchart. Complex classes of periodically driven topological lattice systems. *Phys. Rev. B*, 93:115429, Mar 2016.

[89] A. Gómez-León and G. Platero. Floquet-bloch theory and topology in periodically driven lattices. *Phys. Rev. Lett.*, 110:200403, May 2013.

[90] Gaston Floquet. Sur les equations differentielles lineaires. *Ann. ENS [2]*, 12(1883):47–88, 1883.

[91] Jon H. Shirley. Solution of the schrödinger equation with a hamiltonian periodic in time. *Phys. Rev.*, 138:B979–B987, May 1965.

[92] Hideo Sambe. Steady states and quasienergies of a quantum-mechanical system in an oscillating field. *Phys. Rev. A*, 7:2203–2213, Jun 1973.

[93] Pierre Delplace, Álvaro Gómez-León, and Gloria Platero. Merging of dirac points and floquet topological transitions in ac-driven graphene. *Phys. Rev. B*, 88:245422, Dec 2013.

[94] Álvaro Gómez-León, Pierre Delplace, and Gloria Platero. Engineering anomalous quantum hall plateaus and antichiral states with ac fields. *Phys. Rev. B*, 89:205408, May 2014.

[95] P. M. Perez-Piskunow, L. E. F. Foa Torres, and Gonzalo Usaj. Hierarchy of floquet gaps and edge states for driven honeycomb lattices. *Phys. Rev. A*, 91:043625, Apr 2015.

[96] P. M. Perez-Piskunow, Gonzalo Usaj, C. A. Balseiro, and L. E. F. Foa Torres. Floquet chiral edge states in graphene. *Phys. Rev. B*, 89:121401, Mar 2014.

[97] F. D. Parmentier, L. N. Serkovic-Loli, P. Roulleau, and D. C. Glattli. Photon-assisted shot noise in graphene in the terahertz range. *Phys. Rev. Lett.*, 116:227401, Jun 2016.

[98] F. H. L. Koppens, T. Mueller, Ph. Avouris, A. C. Ferrari, M. S. Vitiello, and M. Polini. Photodetectors based on graphene, other two-dimensional materials and hybrid systems. *Nature Nanotechnology*, 9:780 EP –, 10 2014.

[99] J. Tworzydło, B. Trauzettel, M. Titov, A. Rycerz, and C. W. J. Beenakker. Sub-poissonian shot noise in graphene. *Phys. Rev. Lett.*, 96:246802, Jun 2006.

[100] S. Das Sarma, Shaffique Adam, E. H. Hwang, and Enrico Rossi. Electronic transport in two-dimensional graphene. *Rev. Mod. Phys.*, 83:407–470, May 2011.

[101] K.I. Bolotin, K.J. Sikes, Z. Jiang, M. Klima, G. Fudenberg, J. Hone, P. Kim, and H.L. Stormer. Ultrahigh electron mobility in suspended graphene. *Solid State Communications*, 146(9):351 – 355, 2008.

[102] K. I. Bolotin, K. J. Sikes, J. Hone, H. L. Stormer, and P. Kim. Temperature-dependent transport in suspended graphene. *Phys. Rev. Lett.*, 101:096802, Aug 2008.

[103] Xu Du, Ivan Skachko, Anthony Barker, and Eva Y. Andrei. Approaching ballistic transport in suspended graphene. *Nature Nanotechnology*, 3:491 EP –, 07 2008.

[104] C. R. Dean, A. F. Young, I. Meric, C. Lee, L. Wang, S. Sorgenfrei, K. Watanabe, T. Taniguchi, P. Kim, K. L. Shepard, and J. Hone. Boron nitride substrates for high-quality graphene electronics. *Nature Nanotechnology*, 5:722 EP –, 08 2010.

[105] Alexander S. Mayorov, Roman V. Gorbachev, Sergey V. Morozov, Liam Britnell, Rashid Jalil, Leonid A. Ponomarenko, Peter Blake, Kostya S. Novoselov, Kenji Watanabe, Takashi Taniguchi, and A. K. Geim. Micrometer-scale ballistic transport in encapsulated graphene at room temperature. *Nano Letters*, 11(6):2396–2399, 2011. PMID: 21574627.

[106] L. Wang, I. Meric, P. Y. Huang, Q. Gao, Y. Gao, H. Tran, T. Taniguchi, K. Watanabe, L. M. Campos, D. A. Muller, J. Guo, P. Kim, J. Hone, K. L. Shepard, and C. R. Dean. One-dimensional electrical contact to a two-dimensional material. *Science*, 342(6158):614–617, 2013.

[107] Luca Banszerus, Michael Schmitz, Stephan Engels, Matthias Goldsche, Kenji Watanabe, Takashi Taniguchi, Bernd Beschoten, and Christoph Stampfer. Ballistic transport exceeding 28 μ m in cvd grown graphene. *Nano Letters*, 16(2):1387–1391, 2016. PMID: 26761190.

[108] M. Moskalets and M. Büttiker. Floquet scattering theory of quantum pumps. *Phys. Rev. B*, 66:205320, Nov 2002.

[109] Sigmund Kohler, Jörg Lehmann, and Peter Hänggi. Driven quantum transport on the nanoscale. *Physics Reports*, 406(6):379 – 443, 2005.

[110] Gonzalo Usaj, P. M. Perez-Piskunow, L. E. F. Foa Torres, and C. A. Balseiro. Irradiated graphene as a tunable floquet topological insulator. *Phys. Rev. B*, 90:115423, Sep 2014.

[111] L. E. F. Foa Torres, P. M. Perez-Piskunow, C. A. Balseiro, and Gonzalo Usaj. Multiterminal conductance of a floquet topological insulator. *Phys. Rev. Lett.*, 113:266801, Dec 2014.

[112] Aaron Farrell and T. Pereg-Barnea. Photon-inhibited topological transport in quantum well heterostructures. *Phys. Rev. Lett.*, 115:106403, Sep 2015.

[113] Zhenghao Gu, H. A. Fertig, Daniel P. Arovas, and Assa Auerbach. Floquet spectrum and transport through an irradiated graphene ribbon. *Phys. Rev. Lett.*, 107:216601, Nov 2011.

[114] Dong Sun, Zong-Kwei Wu, Charles Divin, Xuebin Li, Claire Berger, Walt A. de Heer, Phillip N. First, and Theodore B. Norris. Ultrafast relaxation of excited dirac fermions in epitaxial graphene using optical differential transmission spectroscopy. *Phys. Rev. Lett.*, 101:157402, Oct 2008.

[115] Wang-Kong Tse and S. Das Sarma. Energy relaxation of hot dirac fermions in graphene. *Phys. Rev. B*, 79:235406, Jun 2009.

[116] R. Bistritzer and A. H. MacDonald. Electronic cooling in graphene. *Phys. Rev. Lett.*, 102:206410, May 2009.

[117] Y. Zhou and M. W. Wu. Optical response of graphene under intense terahertz fields. *Phys. Rev. B*, 83:245436, Jun 2011.

[118] Xiao-Liang Qi, Taylor L. Hughes, and Shou-Cheng Zhang. Fractional charge and quantized current in the quantum spin hall state. *Nature Physics*, 4:273 EP –, 03 2008.

[119] Szabolcs Vajna, Baruch Horovitz, Balázs Dóra, and Gergely Zaránd. Floquet topological phases coupled to environments and the induced photocurrent. *Phys. Rev. B*, 94:115145, Sep 2016.

[120] Chaoxing Liu, Taylor L. Hughes, Xiao-Liang Qi, Kang Wang, and Shou-Cheng Zhang. Quantum spin hall effect in inverted type-ii semiconductors. *Phys. Rev. Lett.*, 100:236601, Jun 2008.

[121] Lingjie Du, Ivan Knez, Gerard Sullivan, and Rui-Rui Du. Robust helical edge transport in gated InAs/GaSb bilayers. *Phys. Rev. Lett.*, 114:096802, Mar 2015.

[122] Sanfeng Wu, Valla Fatemi, Quinn D. Gibson, Kenji Watanabe, Takashi Taniguchi, Robert J. Cava, and Pablo Jarillo-Herrero. Observation of the quantum spin hall effect up to 100 kelvin in a monolayer crystal. *Science*, 359(6371):76–79, 2018.

[123] Liang Fu and C. L. Kane. Time reversal polarization and a Z_2 adiabatic spin pump. *Phys. Rev. B*, 74:195312, Nov 2006.

[124] Takahiro Fukui and Yasuhiro Hatsugai. Topological aspects of the quantum spin-hall effect in graphene: z_2 topological order and spin chern number. *Phys. Rev. B*, 75:121403, Mar 2007.

[125] Congjun Wu, B. Andrei Bernevig, and Shou-Cheng Zhang. Helical liquid and the edge of quantum spin hall systems. *Phys. Rev. Lett.*, 96:106401, Mar 2006.

[126] H.B. Nielsen and M. Ninomiya. Absence of neutrinos on a lattice: (i). proof by homotopy theory. *Nuclear Physics B*, 185(1):20 – 40, 1981.

[127] Cenke Xu and J. E. Moore. Stability of the quantum spin hall effect: Effects of interactions, disorder, and $\mathbb{z}_2$ topology. *Phys. Rev. B*, 73:045322, Jan 2006.

[128] Jonathan Atteia, Jens H. Bardarson, and Jérôme Cayssol. Ballistic transport through irradiated graphene. *Phys. Rev. B*, 96:245404, Dec 2017.